Experimental Investigation of Detonation Re-initiation Mechanisms Following a Mach Reflection of a Quenched Detonation

by

Rohit Ranjan Bhattacharjee

Thesis submitted to the Faculty of Graduate and Postdoctoral Studies
in partial fulfillment of the requirements for the degree of

MASTER OF APPLIED SCIENCE
in
Mechanical Engineering

Ottawa-Carleton Institute for Mechanical and Aerospace Engineering
University of Ottawa
Ottawa, Canada

© Rohit Ranjan Bhattacharjee, Ottawa, Canada, 2013

Abstract

Detonation waves are supersonic combustion waves that have a multi-shock front structure followed by a spatially non-uniform reaction zone. During propagation, a de-coupled shock-flame complex is periodically re-initiated into an overdriven detonation following a transient Mach reflection process. Past researchers have identified mechanisms that can increase combustion rates and cause localized hot spot re-ignition behind the Mach shock. But due to the small length scales and stochastic behaviour of detonation waves, the important mechanisms that can lead to re-initiation into a detonation requires further clarification.

If a detonation is allowed to diffract behind an obstacle, it can quench to form a de-coupled shock-flame complex and if allowed to form a Mach reflection, re-initiation of a detonation can occur. The use of this approach permits the study of re-initiation mechanisms reproducibly with relatively large length scales. The objective of this study is to experimentally elucidate the key mechanisms that can increase chemical reaction rates and sequentially lead to re-initiation of a de-coupled shock-flame complex into an overdriven detonation wave following a Mach reflection.

All experiments were carried out in a thin rectangular channel using a stoichiometric mixture of oxy-methane. Three different types of obstacles were used - a half-cylinder, a roughness plate along with the half-cylinder and a full-cylinder. Schlieren visualization was achieved by using a Z-configuration setup, a high speed camera and a high intensity light source.

Results indicate that forward jetting of the slip line behind the Mach stem can potentially increase combustion rates by entraining hot burned gas into unburned gas. Following ignition and jet entrainment, a detonation wave first appears along the Mach stem. The transverse wave can form a detonation wave due to rapid combustion of unburned gas which may be attributed to shock interaction with the unburned gas. Alternatively, the Kelvin-Helmholtz instability can produce vortices along the slipline that may lead to mixing between burned-unburned gases and potentially increase combustion rates near the transverse wave. However, the mechanism(s) that causes the transverse wave to re-initiate into a detonation wave remains to be satisfactorily resolved.

Acknowledgements

Firstly, I am very grateful to my supervisor Dr. Matei I. Radulescu for his guidance, thought provoking ideas and considerable patience with me. I thank Dr. Radulescu for giving me the opportunity to work in the Detonation and Reactive Dynamics Laboratory and for introducing me to the fascinating world of detonation studies. I also thank my supervisor for giving me the opportunity to present at the 2012 Canadian Section Combustion Institute conference in Toronto. I wish to acknowledge NSERC for their financial support to Dr. Radulescu through a Discovery Grant and the H2CAN Strategic Network of Excellence.

My sincerest gratitude to Logan Maley whose profound experimental know-how and selfless support over the years have made a deep impact on my work. I would also like to thank Geoff Maines, Louis Leblanc and Kadeem Dennis for their assistance in the laboratory.

I would like to acknowledge the helpful staff at the Department of Mechanical Engineering Machine Shop, particularly James MacDermid for designing the cylindrical obstacles used in all my experiments.

I am lucky to have made a wonderful group of friends through uOMEGA - Christina Vanderwel, Laura Brown, Stephen Baskey, Mishaal Azhar and many more. I am also glad to have met other enthusiastic graduate students - Brian Maxwell, Justin Tang, Daniel MacDonald, Ruben Fernandez, Jean-Louis Pelletier, Deliang Goudl and many others. They all have contributed in many ways to make my overall experience very enriching and fun. Thank you everyone, it's been a blast!

I am blessed beyond measure to have parents whose support and encouragement, during the lowest of lows and the highest of highs, fuels me every moment; I dedicate this work to my parents. Finally, a big thank you to uncle Colin, aunty Diana, Kevin and Neil for their heart warming generosity throughout my graduate studies.

Contents

1 Introduction **1**

1.1 The ideal detonation wave 1

1.2 The detonation cellular structure 2

1.3 Present state of knowledge 3

1.3.1 Reactive shock reflections 3

1.3.2 Detonation diffraction around obstacles 6

1.3.3 Summary of current state of knowledge 7

1.4 Problem definition and research objective 8

1.5 Thesis outline 8

2 Experimental Setup **13**

2.1 Flow facility 13

2.2 Measuring and data acquisition systems 14

2.3 Flow visualization systems 15

2.3.1 High speed Schlieren videos 16

2.3.2 Double-frame Schlieren photographs 16

2.4 Methods for gas ignition 17

2.4.1 High voltage ignition (HVI) system 17

2.4.2 Shock tube with a diaphragm method 18

2.5 Experimental procedure 18

2.5.1 Shock tube with a diaphragm installed 18

2.5.2 Shock tube without a diaphragm installed 19

2.6 First experimental series using a 305 mm diameter half-cylinder 19

2.7 Second experimental series using a 305 mm diameter half-cylinder followed by a roughness plate 19

2.8 Third experimental series using a 152 mm diameter full-cylinder 20

2.9 Sensitivity of the gas mixture 20

2.10 Interpretating the Schlieren images 21

3 Cellular Detonation Waves **33**

3.1 The detonation cellular structure 33

3.2 The stochastic behaviour of a cellular detonation wave 34

4 Mach Reflection Process Behind An Obstacle - Results **38**

4.1 Detonation diffraction around obstacles 38

4.2 Detonation failure 39

4.2.1 A comparison of the events following a Mach reflection with and without an obstacle 41

4.3 Experiments using the half-cylinder and roughness plate 42

4.4 Hot spot re-ignition behind the Mach stem 43

4.5 Re-initiation into a detonation along the Mach shock and transverse shock 48

4.6 Summary 52

5 Analyses and Discussions **92**

5.1 Sequence of the re-initiation process into a detonation wave 92

5.2 Predicting ignition delay in smooth wall tests 93

5.3 Predicting ignition delay in the roughness tests 96

5.4 Flame speed calculations 99

5.4.1 Absolute flame speed measurements 99

5.4.2 Post Mach shock estimations 100

5.4.3 Burning flame velocity 100

5.5 Mechanisms that cause mixing between burned and unburned gases . . . 101

5.5.1 Forward jetting slip line 101

5.5.2 Hydrodynamic instabilities 103

5.6 Summary 103

6 Conclusions and Recommendations **112**

6.1 Conclusions 112

6.2 Recommendations for future work 113

A Uncertainty Estimation **115**

B High Voltage Igniter (HVI) System **117**

B.1 Description 117

B.2 Specifications 118

B.3 Operation 118

B.3.1 Charging the capacitor 119

B.3.2 Discharging (firing) the capacitor 119

B.3.3 Guidelines for high voltage work 119

B.4 Testing 120

B.5 Spark Energy 123

C NASA Chemical Equilibrium Application Program (CEA) **127**

D Cantera and the GRI mechanism (GRI-Mech) version 3.0 **132**

D.1 Ignition delay following adiabatic shock compression 133

D.2 Adiabatic flame speed 134

E Constant pressure-enthalpy combustion **137**

F Flame Speed Calculations **138**

F.1 Measurements 138

F.2 Initial state conditions 141

F.3 Post-shock conditions and burning velocity of the flame tip 141

G Additional Schlieren Images **143**

G.1 Remaining frames from the high speed Schlieren video results 144

G.2 High speed Schlieren videos obtained from other experiments 156

G.2.1 Detonation failure regime using the half-cylinder obstacle 157

G.2.2 Experiments using the half-cylinder with the roughness plate . . . 161

G.2.3 Hot spot re-ignition regime using the half-cylinder obstacle 165

G.2.4 Detonation re-initiation regime using the half-cylinder obstacle . . 168

G.2.5 Detonation failure regime using the full-cylinder obstacle 174

G.2.6 Hot spot re-ignition regime using the full-cylinder obstacle 178

G.2.7 Detonation re-initiation regime using the full-cylinder obstacle . . 185

G.3 Schlieren images obtained from other experiments using the dual frame camera 185

G.3.1 Detonation failure regime using the half-cylinder obstacle 186

G.3.2 Hot spot re-ignition regime using the half-cylinder obstacle 189

G.3.3 Detonation re-initiation regime using the half-cylinder obstacle . . 191

References **197**

List of Tables

5.1 Theoretical $\tau_{ig_{th}}$ values for Fig. 4.10 prior to and following localized ignition behind the Mach shock using the half-cylinder obstacle. 94

5.2 Theoretical $\tau_{ig_{th}}$ values for Fig. 4.20 prior to and following localized ignition behind the Mach shock using the full-cylinder obstacle. 95

5.3 Theoretical $\tau_{ig_{th}}$ values for Fig. 4.7 prior to and following localized ignition behind the Mach shock using the half-cylinder and roughness plate. . . . 97

5.4 Temperature, pressure and density behind the Mach shock of known strength. 98

5.5 Conditions behind Mach shock after equilibrating at constant pressure-enthalpy. 98

5.6 Final volume of the gas pocket after equilibrating at constant pressure-enthalpy. 98

B.1 Discharge characteristics of the HVI system 125

F.1 Estimation of the the averaged absolute flame speed (u_F) and the angle (θ_F) it makes with the horizontal (θ_F), using the PCC application. . . . 139

F.2 The components of the averaged absolute flame speed (u_F) in the Y (vertical) and X (horizontal) axes. 139

F.3 Image calibration in Adobe Illustrator (AI). 140

F.4 Estimation of the Mach shock strength (u_M) and the direction in which it acts (θ_M) for several measurements. 140

F.5 Table summarizing the initial conditions. 141

F.6 A summary of the post shock conditions behind the Mach shock and the final averaged vertical flame speed for each measurement obtained from experiment. 142

List of Figures

1.1 A schematic diagram showing a Z-N-D detonation model propagating towards the right and temperature, pressure and density profile across the detonation wave. 9

1.2 Figure (a) shows a shadowgraph of a detonation front propagating from left to right in a channel in C_2H_4+3O_2+6N_2 at an initial pressure $p_0 = 20$ kPa. Figure (b) shows a soot foil from another experiment showing the irregular cellular pattern in C_2H_4+3O_2+5N_2 at an initial pressure $p_0 = 20$ kPa indicating that the cell width (λ) is 15 mm. 10

1.3 A schematic diagram illustrating the sequence of events in a single cell cycle for a propagating cellular detonation wave with the direction of propagation for each shock wave shown: (1) strong Mach stems; (2) weak incident wave; (3) transverse waves traveling towards each other; (4) weak incident waves; (5) overdriven Mach stem; (6) transverse waves traveling away from each other. Also labeled are the Kelvin-Helmholtz (K-H) instability and, the triple point path which is not observed in the Schlieren images 10

1.4 A schematic diagram of a reactive single Mach reflection, propagating towards the right, identifying the key features - the Mach stem, the incident wave, the transverse wave, a slip line, a triple point and the reaction zone. 11

1.5 A schematic diagram showing the diffraction of a detonation wave behind a full-cylinder obstacle to form two de-coupled shock-flame complexes, which forms a Mach reflection after interacting with each other. Description of the labels are as follows: (I) - Incident wave, (M) - Mach stem, (T) - Transverse wave, (Tr) - Triple point, (s) - slip line, (R) - Reaction zone (or flame interface) 12

2.1 A schematic diagram of the shock tube showing the pertinent dimensions and identifying the different sections. Also shown is the half-cylinder obstacle placed in the window section. 23

2.2 A schematic diagram showing the direction of the gas flow between the gas panel and the shock tube. 24

2.3 Photographs of different obstacles used for all experiments, shown with dimensions: top view (a1) and front view (a2) of the half-cylinder obstacle; top view (b1) and front view (b2) of the full-cylinder obstacle; top view (c1) and front view (c2) of the roughness plate. 25

2.4 Photographs of the PCB pressure sensor aluminum plug. Figure (a) shows the back view of the PCB pressure sensor housed inside the aluminum gauge plug. Figure (b) shows the front view of the PCB pressure sensor with its diaphragm placed flush against the surface of the aluminum gauge plug. 25

2.5 A schematic diagram showing the Z-configuration Schlieren setup used for experimental visualization. The high speed camera shown is the pco.2000 double frame camera and the high intensity light source shown is the two-spark PalFlash 501 light source. 26

2.6 A photograph of the vertical knife edge, which resolves the horizontal density gradients in the all Schlieren results obtained. 26

2.7 A photograph of the side view of the Phantom V1210 high speed camera. 27

2.8 A photograph of the high intensity LED light source, the focusing lens and the knife edge pin hole. 27

2.9 A photograph of the side view of the pco.2000 double frame high speed camera. Photograph courtesy of L. Maley. 28

2.10 A photograph of the two-spark PalFlash 501 high intensity light source, which uses argon gas, the focusing lens and the knife edge pin hole. Photograph courtesy of L. Maley. 28

2.11 A photograph of the High Voltage Igniter (HVI) system. 28

2.12 An electrical circuit diagram of the HVI system. 29

2.13 A photograph of a wiremesh installed to accelerate the flame in the driver section and cause rapid initiation of a detonation wave. 29

2.14 A schematic diagram of the shock tube shown with the diaphragm placed between the driver and driven sections. 30

2.15 A photograph showing the position of the half-cylinder obstacle in the shock tube for the first series of experiments. 31

2.16 A photograph showing the position of the half-cylinder and the roughness plate in the shock tube for the second series of experiments. 31

2.17 A photograph showing the position of the full-cylinder obstacle in the shock tube for the third series of experiments. 31

2.18 Variation of detonation cell width with initial pressure in CH_4+$2O_2$. The black vertical lines represent the range of initial pressures used for this work while the dashed line is a fitted trendline given by $\lambda = 831.64{p_0}^{-1.215}$. As expected, by increasing the initial pressure of the test mixture, the detonability (sensitivity of the mixture to detonation) increases, which is quantified by a decreasing cell width λ. 32

2.19 Figure a) shows a typical Schlieren image of a quenched detonation wave after it has diffracted behind the half-cylinder obstacle to form a de-coupled shock-flame complex. Figure b) shows a simple schematic diagram of the Schlieren image shown in Fig. a). 32

3.1 Schlieren images of a self-propagating detonation wave in stoichimetric oxy-methane mixture, at an initial pressure and temperature of $p_0 = 3.5$ kPa and $T_0 = 300$K respectively, showing: (a) - (c) a weakening incident wave with the reaction zone de-coupled from it and the two triple points approaching each other. Shown also are the stronger Mach stems, in the adjoining (half) cells, with the reaction zone closely coupled to their respective shock fronts; (d) - (f) the triple points are about to collide and then form an irregular (Mach) reflection immediately after collision while the failed incident wave has re-initiated into an overdriven Mach stem. The channel height is 203.2 mm and the inter-frame delay is 11.53 μsec. *Test ID: CH4+O2-08-24-12(0.5psiTEST1)* 35

3.2 A continuation of the evolution of the flow field from Fig. 3.1 now showing: (g) - (i) an overdriven Mach shock with the reaction zone closely coupled to it and the two triple points moving away from each other. Note the neighbouring cells are now weaker incident waves with their reaction zones de-coupled from the front; (j) - (l) the Mach stem rapidly expanding as the triple points move away from each other. The inter-frame delay is 11.53 μsec. 36

3.3 Figures (a1)-(c1) were obtained from a test using stoichiometric mixture of methane-oxygen with an initial pressure of 3.5 kPa and an initial temperature of 300K. Figs. (a2)-(c2) was taken from a separate test using the same conditions but shows a very different cellular pattern thus shedding light on the stochasticity of self-propagating cellular detonations waves . 37

4.1 A sequence of Schlieren images of a self-propagating cellular detonation in stoichiometric methane-oxygen mixture, at an initial pressure and temperature of 8.4 kPa and 300K, respectively, showing how it diffracts around a 152.4 mm diameter full-cylinder obstacle to form a de-coupled shock-flame complex devoid any triple point structure across its front. Also observed are shock structures (white lines) that reflect off the full-cylinder and the confining wall and propagate back. The channel height is 203.2 mm with an inter-frame delay of 23.06 μsec. *Test ID: CH4+O2-08-22-12(1.2psiTEST3)* 54

4.2 Schlieren images showing the evolution of a flow field of inert shock reflections of a quenched detonation wave behind the half-cylinder obstacle. The initial pressure and temperature was 5.5 kPa and 300K. Each image represents a different experiment at the same initial conditions using the dual-frame camera. *(a)Test ID: CH4+O2 - 08-4-11(0.85psi)6; (b)Test ID: CH4+O2 - 08-12-11(0.85psi)1; (c)Test ID: CH4+O2 - 08-28-11(0.85psi)3; (d)Test ID: CH4+O2 - 07-31-11(0.85psi)1; (e)Test ID: CH4+O2 - 01-15-11(0.8psi)1a; (f)Test ID: CH4+O2 - 07-31-11(0.85psi)3* 55

4.3 General velocity trend of the incident and Mach shock for the detonation failure case with the half-cylinder; the solid line shows the CEA calculated C-J Velocity for $p_0 = 5.5$ kPa, $T_0 = 300$K. Note that each data point was obtained from different experiments. 56

4.4 A flow field evolution showing a quenched detonation wave failing behind the full-cylinder obstacle. Since the detonation structure has quenched, there is no energy release in the vicinity of the shock front. Shown clearly is the transition of this shock-flame complex from a regular reflection to a Mach reflection with the important features identified. The initial pressure and temperature was 3.5 kPa and 300K. See Fig. G.8 for remaining frames. *Test ID: CH4+O2-08-20-12(0.5psiTEST1)* 57

4.5 Continuation of the flow field evolution shown in Fig. 4.4. The images show trailing pockets of unburned gas as well as the K-H instability and forward jet along the slip line. The initial pressure and temperature was 3.5 kPa and 300K. *Test ID: CH4+O2-08-20-12(0.5psiTEST1)* 58

4.6 Velocimetry of the incident shock (top and bottom walls) and Mach shock (centerline) of a flow field showing inert shock reflections behind the full-cylinder obstacle. These values were obtained from the experiment shown in Figs. 4.4 and 4.5. 59

4.7 Flow field evolution showing re-ignition behind the Mach shock where a layer of burned gas is formed over the roughness plate obstacle (Images courtesy of L. Maley and K. Dennis). As the burned gas expands we also observe the slip line jetting forward. The initial pressure was 7 kPa. All frames were obtained from the same experiment using the high speed video camera and the remaining frames are shown in Figures G.6 and G.7. *Test ID: CH4+O2-07-13-12(1.0psi)roughness* 60

4.8 Continuation of the flow field evolution shown in Fig. 4.7. Shown here is the burned gas being entrained with cooler reactants to form a vortex behind the Mach shock. Also shown is a back propagating shock wave, which propagates through unburned gas behind the transverse wave. In addition corrugation of the unburned gas, punctuated by hot spot formation, behind this shock wave is clearly seen. The initial pressure was 7 kPa. *Test ID: CH4+O2-07-13-12(1.0psi)roughness* 61

4.9 Velocity profile of the incident shock (top wall) and Mach shock (bottom wall) for the roughness test, where localized ignition events were observed behind the Mach shock. These values were obtained from the experiment shown in Figs. 4.7 and 4.8. 62

4.10 An evolution of a flow field showing re-ignition first at the foot of the Mach shock for a smooth wall test using the half-cylinder obstacle. The initial pressure was 10.3 kPa. All frames were obtained from the same experiment using the high speed video camera and the remaining frames are shown in Fig. G.1. *Test ID: CH4+O2-07-27-12(1.47psiTEST7)* . . . 63

4.11 A continuation of the flow field evolution shown in Fig. 4.10. The flame formed behind the Mach shock eventually evolves in time to couple with the entire Mach shock front. Also observable are the unburned gas pockets along the bottom wall and the K-H instability along the slip line. The initial pressure was 10.3 kPa. *Test ID: CH4+O2-07-27-12(1.47psiTEST7)* 64

4.12 Velocimetry of the incident shock (top wall) and Mach shock (bottom wall) obtained from the experiment shown in Figs. 4.10 and 4.11. The solid line shows the CEA calculated C-J velocity for $p_0 = 10.3$ kPa. . . . 65

4.13 Two sequential frames showing corrugation of the tongue of unburned gas due to hot spot formation as well as thinning out of the volute of the K-H instability along the slip line for $p_0 = 10.5$ kPa. Both frames were obtained from the same experiment using the dual-frame camera. *Test ID: CH4+O2 - 05-11-11(1.49psi3)* 65

4.14 Flow field evolution showing an spontaneous re-ignition event behind the Mach shock, rather that a gradual sequence as seen in Fig. 4.10 for $p_0 = 9.8$ kPa. All frames shown were obtained from the same experiment using the high speed video camera and the remaining frames are shown in Fig. G.2. *Test ID: CH4+O2-07-27-12(1.4psiTEST3)* 66

4.15 Velocimetry of the incident shock (top wall) and Mach shock (bottom wall) of a flow field showing spontaneous ignition following a Mach reflection; the solid line shows the CEA calculated C-J velocity for $p_0 = 9.8$ kPa. These values were obtained from the experiment shown in Fig. 4.14. . . . 67

4.16 Sequence of images showing localized hot spot re-ignition behind the foot of the Mach shock for a smooth wall test using the half-cylinder obstacle. The initial pressure was 12.3 kPa. All frames were obtained from the same experiment using the high speed video camera and the remaining frames are shown in Fig. G.5. *Test ID: CH4+O2-07-24-12(1.75psiTEST4)* . . . 68

4.17 A continuation of the flow field evolution immediately after Fig. 4.16(f). Following re-ignition behind the Mach shock, the hot gas products appear to be entrained by the forward jetting slip line. Also observable is a backward propagating shock wave. The initial pressure was 12.3 kPa. *Test ID: CH4+O2-07-24-12(1.75psiTEST4)* 69

4.18 Velocimetry of the incident shock (top wall) and Mach shock (bottom wall) of a flow field showing re-ignition following a Mach reflection. These values were obtained from the experiment shown in Figs. 4.16 and 4.17. . 70

4.19 A general evolution of a flow field showing re-ignition of the Mach shock following jet entrainment of hot burned gas with unburned gas behind the Mach stem, for $p_0 = 10.4$ kPa. Each image represents a different experiment at the same initial conditions using the dual-frame camera. *(a)Test ID: CH4+O2 - 08-3-11(1.49psi)3; (b)Test ID: CH4+O2 - 08-2-11(1.49psi)2* 70

4.20 A flow field evolving in time showing re-ignition behind the Mach shock. The sequence of images indicate the development of the forward jetting slip line as the flame front approaches the Mach shock front. The initial pressure was 8.4 kPa. All frames were obtained from the same experiment using the high speed video camera and the remaining frames are shown in Fig. G.9. *Test ID: CH4+O2-08-14-12(1.2psiTEST1)* 71

4.21 A continuation of the flow field evolution shown in Fig. 4.20. Following the earlier sequence of events, a strong coupling of the flame with the Mach shock front is observed. Also shown is a strong bifurcation of the Mach shock to form two new triple points that are moving away from each other. The initial pressure was 8.4 kPa. *Test ID: CH4+O2-08-14-12(1.2psiTEST1)* 72

4.22 Velocimetry of the incident shock (top and bottom walls) and Mach shock (centerline) of a flow field showing re-ignition events following a Mach reflection behind the full-cylinder obstacle. These values were obtained from the experiment shown in Fig. 4.20 and 4.21. 73

4.23 A sequence of Schlieren images showing that following a Mach reflection, distinct density gradients are observed behind the Mach shock. Also the flame interface, near the lower slip line, begins to approach the Mach shock front. The initial pressure was 10.5 kPa. See Figs. G.10 and G.11 for remaining frames. *Test ID: CH4+O2-08-03-12(1.49psiTEST4)* 74

4.24 A continuation of the flow field shown in Fig. 4.23 where we observe re-ignition behind the Mach shock. Here the familiar forward jet effect of the slip line is seen along with the flame front until it couples with the Mach shock. The initial pressure 10.5 kPa. *Test ID: CH4+O2-08-03-12(1.49psiTEST4)* 75

4.25 Velocimetry of the incident shock (top and bottom walls) and Mach shock (centerline) of a flow field showing re-ignition events following a Mach reflection behind the full-cylinder obstacle. These values were obtained from the experiment shown in Figs. 4.23 and 4.24. 76

4.26 An evolution of a flow field showing spontaneous re-ignition behind the Mach shock, instead of a gradual process as observed in Fig. 4.23 for the same initial conditions. The initial pressure was 10.5 kPa. All frames were obtained from the same experiment using the high speed video camera and the remaining frames are shown in Fig. G.12. *Test ID: CH4+O2-08-03-12(1.49psiTEST2)* 77

4.27 Velocimetry of the incident shock (top and bottom walls) and Mach shock (centerline) of a flow field showing spontaneous re-ignition events following a Mach reflection behind the full-cylinder obstacle. These values were obtained from the experiment shown in Figure 4.26. 78

4.28 Sequence of images showing detonation re-initiation of the Mach shock at its foot for $p_0 = 12.3$ kPa. All frames were obtained from the same experiment using the high speed video camera and the remaining frames are shown in Fig. G.4. *Test ID: CH4+O2-07-25-12(1.75psiTEST6)* . . . 79

4.29 A continuation of the sequence of images shown in Fig. 4.28. Following detonation re-initiation of the Mach shock rapid exothermic reactions near the transverse shock is observed. This is followed by a transverse detonation wave. The initial pressure is $p_0 = 12.3$ kPa. *Test ID: CH4+O2-07-25-12(1.75psiTEST6)* 80

4.30 Velocimetry of the incident shock (top wall), Mach shock (bottom wall) and triple point phase velocity of a flow field showing re-initiation following a Mach reflection. These values were obtained from the experiment shown in Figs. 4.28 and 4.29. 81

4.31 A general evolution of a flow field showing re-initiation of the Mach shock followed by re-initiation of the transverse wave. Also clearly observable are strong inert shock waves formed after detonation re-initiation on the Mach and transverse shock, indicative of rapid chemical reaction rates. The initial pressure was 10.4 kPa. Each image represents a different experiment at the same initial conditions using the double frame camera. *(a)Test ID: CH4+O2 - 08-3-11(1.49psi)1; (b)Test ID: CH4+O2 - 08-2-11(1.49psi)1* . 81

4.32 A reproducible flow field evolution showing a re-initiated Mach shock and transverse wave propagating towards the right and up. The initial pressure was 12.0 kPa. Each image represents a different experiment at the same initial conditions using the dual-frame camera. *(a) Test ID: CH4+O2 - 03-12-11(1.72psi)4; (b)Test ID: CH4+O2 - 03-12-11(1.72psi)6* 82

4.33 Flow field evolution showing rapid re-initiation first at the foot of the Mach shock. This is followed by a violent detonation re-initiation event on the transverse shock. The initial pressure was $p_0 = 10.5$ kPa. All frames were obtained from the same experiment using the high speed video camera and the remaining frames are shown in Fig. G.3. *Test ID: CH4+O2-07-27-12(1.5psiTEST2)* 83

4.34 Velocimetry of the incident shock (top wall), Mach shock (bottom wall) and phase velocity of the triple point for a flow field evolution showing re-initiation following a Mach reflection; the solid line shows the CEA calculated C-J velocity for $p_0 = 10.5$ kPa, $T_0 = 300$K. These values were obtained from the experiment shown in Fig. 4.33. 84

4.35 A flow field evolution showing simultaneous detonation re-initiation of the Mach shock and transverse wave for $p_0 = 16.8$ kPa. All frames were obtained from the same experiment using the high speed video camera and the remaining frames are shown in Fig. G.13. *Test ID: CH4+O2-08-01-12(2.4psiTEST4)* 85

4.36 A continuation of the flow field evolution shown in Fig. 4.35 for $p_0 = 16.8$ kPa. *Test ID: CH4+O2-08-01-12(2.4psiTEST4)* 86

4.37 Velocimetry of the incident shock (top and bottom walls), Mach shock (centerline) and triple point phase velocity of a flow field showing re-initiation following a Mach reflection behind the full-cylinder obstacle. These values were obtained from the experiment shown in Figs. 4.35 and 4.36. The initial pressure and temperature is 16.8 kPa and 300K. 87

4.38 A flow field showing first a Mach reflection of a de-coupled shock-flame complex. A spontaneous event occurs near the Mach shock, which cannot be well resolved. The initial pressure and temperature was 16.8 kPa and 300K. All frames were obtained from the same experiment using the high speed video camera. *Test ID: CH4+O2-08-01-12(2.4psiTEST5)* 88

4.39 A continuation of the flow field immediately following the event shown in Fig. 4.38(d). At a later time detonation re-initiation occurs at the Mach shock. However an unusual case is observed where detonation re-initiation only occurs along the lower transverse wave while the upper transverse shock remains non-reactive. This is indicated by the long trailing unburned pockets of gas. The initial pressure and temperature was 16.8 kPa and 300K. *Test ID: CH4+O2-08-01-12(2.4psiTEST5)* 89

4.40 A summary of all experiments showing the different gas dynamic behaviours observed for different initial pressures. 90

4.41 A histogram summary of all experiments illustrating the different detonation regimes observed using only the half-cylinder obstacle. Note that experiments using the roughness plate have been excluded. 90

4.42 A histogram summary of all experiments illustrating the different detonation regimes observed using only the full-cylinder obstacle. 91

5.1 A schematic diagram illustrating a possible sequence of events leading to re-initiation of the Mach stem and transverse shock into a detonation. Note for simplicity the reflected shock wave has been omitted. Label descriptions: incident shock (I); Mach stem (M); transverse shock (T); triple point (Tr); slip line (s); reaction zone or flame interface (R); Kelvin Helmholtz (K-H) instability; forward jet (FwJ); kink (k'); entrained products and reactants (1). 105

5.2 A continuation from Fig. 5.1. Label descriptions: Mach detonation (D1); transverse detonation (D2); rapid exothermic reaction (2); back propagating shock (3). 105

5.3 Figure showing the height of a layer of burned gas, measured from the bottom surface of the groove, after it has expanded. 106

5.4 Two sequential Schlieren images showing a flame growth behind the Mach shock over the roughness plate behind the half-cylinder obstacle. The initial pressure and temperature was 7 kPa and 300K. Both successive images are 10μsec apart and were recorded using the high speed video camera. 106

5.5 A Schlieren image showing the measured velocity component vectors of the flame tip along the vertical and horizontal directions. 107

5.6 A modified Schlieren image wherein two sequential frames (Fig. 5.4) are superimposed with the lighter density gradients subtracted. Also shown is the selected point on the Mach shock front that is approximately close to the flame tip. 108

5.7 The modified Schlieren image now showing the perpendicular drawn to the tangent on the first point that meets the second Mach shock front. These two points were used to measure the displacement and hence calculate the local velocity of the Mach shock in the vicinity of the flame tip. 109

5.8 A Schlieren numerical image showing the bifurcation of the Mach stem. . 109

5.9 A schematic diagram showing a Mach reflection of an inert shock over a compressive ramp used in the bifurcating Mach shock study by P. Mach . 110

5.10 The Schlieren image on the left was taken from Fig. 4.20. The schematic diagram on the right shows typical features of a reactive Mach reflection of a de-coupled shock-flame complex. Labels shown are as follows: incident wave (I), triple point (TR), Mach stem (M), transverse wave (T) and the de-coupled reaction zone or flame trailing behind. 110

5.11 Figure (a) shows a schematic diagram that illustrates the Mach reflection process with pertinent parameters labeled. Figure (b) shows a schematic diagram that illustrates the same Mach reflection as Fig. (a) after rotating counter-clockwise by angle θ_I. For simplicity the reflected shock wave has been omitted from the schematic diagram. 110

5.12 A Schlieren numerical simulation showing the forward jet effect of the slip line behind the Mach shock. The input parameters are: $M_I = 3$, $\theta_w = 30^\circ$ and $\gamma = 1.2$. Here, the forward jet is not strong enough to cause a distinct Mach shock bifurcation. Image courtesy of S. S. Lau-Chapdelaine. 111

5.13 A Schlieren numerical simulation showing the forward jet effect of the slip line behind the Mach shock. The input parameters are: $M_I = 4$, $\theta_w = 30^\circ$ and $\gamma = 1.2$. Here, the forward jet appears strong enough to cause a kink in the Mach shock. Image courtesy of S. S. Lau-Chapdelaine. 111

B.1 Current Waveform ($V_0 = 20$kV) 121

B.2 Voltage Waveform ($V_0 = 20$kV) 121

B.3 Current Waveform ($V_0 = 25$kV) 122

B.4 Voltage Waveform ($V_0 = 25$kV) 122

B.5 Current Waveform ($V_0 = 30$kV) 123

B.6 Voltage Waveform ($V_0 = 30$kV) 123

B.7 (a) Ignition Circuit Components Diagram; (b) Equivalent RLC Circuit . 124

B.8 Current Waveform shorted and open spark gap ($V_0 = 20$kV) 125

B.9 Current Waveform shorted and open spark gap ($V_0 = 25$kV) 126

B.10 Current Waveform shorted and open spark gap ($V_0 = 30$kV) 126

G.1 Schlieren images of a flow field evolution showing re-ignition behind the Mach shock. The initial pressure and temperature was 10.3 kPa and 300K. All frames were obtained from the same experiment using the high speed video format with an inter-frame delay of 12.97 μsec. *Test ID: CH4+O2-07-27-12(1.47psiTEST7)* 144

G.2 Schlieren images of a flow field evolution showing re-ignition behind the Mach shock. The initial pressure and temperature was 9.8 kPa and 300K. All frames were obtained from the same experiment using the high speed video format with an inter-frame delay of 12.97 μsec. *Test ID: CH4+O2-07-27-12(1.4psiTEST3)* 145

G.3 Schlieren images of a flow field evolution showing re-initiation behind the Mach and transverse shock. The initial pressure and temperature was 10.5 kPa and 300K. All frames were obtained from the same experiment using the high speed video format with an inter-frame delay of 12.97 μsec. *Test ID: CH4+O2-07-27-12(1.5psiTEST2)* 146

G.4 Schlieren images of a flow field evolution showing detonation re-initiation of the Mach shock and transverse wave, following an increase in chemical reaction rates behind the Mach shock. The initial pressure and temperature was 12.3 kPa and 300K. All frames were obtained from the same experiment using the high speed video format with an inter-frame delay of 12.97 μsec. *Test ID: CH4+O2-07-25-12(1.75psiTEST6)* 147

G.5 Schlieren images of a flow field evolution showing re-ignition behind the Mach shock following jet entrainment potentially due to forward jetting of the slipline. The initial pressure and temperature was 12.3 kPa and 300K. All frames were obtained from the same experiment using the high speed video format with an inter-frame delay of 12.97 μsec. *Test ID: CH4+O2-07-24-12(1.75psiTEST4)* 148

G.6 Schlieren images of a flow field evolution showing re-ignition behind the Mach shock, following jet entrainment of hot burned gas with unburned gas over the roughness plate obstacle. The initial pressure and temperature was 7 kPa and 300K. All frames were obtained from the same experiment using the high speed video format with an inter-frame delay of 10 μsec. *Test ID: CH4+O2-07-13-12(1.0psi)roughness* 149

G.7 Continuation of the flow field evolution shown in Figure G.6 above now showing a back propagating shock wave. *Test ID: CH4+O2-07-13-12(1.0psi)roughness* 150

G.8 Schlieren images of a flow field evolution showing inert shock reflections of a quenched detonation wave behind the full-cylinder obstacle. The initial pressure and temperature was 3.5 kPa and 300K. All frames were obtained from the same experiment using the high speed video format with an inter-frame delay of 11.53 μsec. *Test ID: CH4+O2-08-20-12(0.5psiTEST1)* . . 151

G.9 Schlieren images of a flow field evolution showing re-ignition behind the Mach shock following jet entrainment potentially due to forward jetting of the slipline. The initial pressure and temperature was 8.4 kPa and 300K. All frames were obtained from the same experiment using the high speed video format with an inter-frame delay of 12.91 μsec. *Test ID: CH4+O2-08-14-12(1.2psiTEST1)* 152

G.10 Schlieren images of a flow field evolution showing re-ignition behind the Mach shock following jet entrainment potentially due to forward jetting of the slipline. The initial pressure and temperature was 10.5 kPa and 300K. All frames were obtained from the same experiment using the high speed video camera with an inter-frame delay of 6.03 μsec. For a reference, the horizontal length of the tape in the top-left side is 17.5 mm. *Test ID: CH4+O2-08-03-12(1.49psiTEST4)* 153

G.11 Continuation of the flow field evolution shown in Figure G.10 above. *Test ID: CH4+O2-08-03-12(1.49psiTEST4)* 153

G.12 Schlieren images of a flow field evolution showing spontaneous re-ignition behind the Mach shock. The initial pressure and temperature was 10.5 kPa and 300K. All frames were obtained from the same experiment using the high speed video format with an inter-frame delay of 12.97 μsec. *Test ID: CH4+O2-08-03-12(1.49psiTEST2)* 154

G.13 Schlieren images of a flow field evolution showing spontaneous re-initiation of the Mach stem and transverse waves into a detonation wave. The initial pressure and temperature was 16.8 kPa and 300K. All frames were obtained from the same experiment using the high speed video format with an inter-frame delay of 12.91 μsec. *Test ID: CH4+O2-08-01-12(2.4psiTEST4)* 155

G.14 Schlieren images of a flow field evolution for $p_0 = 5.5$ kPa and $T_0 = 300$K with an inter-frame delay of 12.97 μsec. *Test ID: CH4+O2-07-25-12(0.8psiTEST1)* 157

G.15 Schlieren images of a flow field evolution for p_0 = 10.5 kPa and T_0 = 300K with an inter-frame delay of 12.97 μsec. *Test ID: CH4+O2-07-27-12(1.49psiTEST5)* 158

G.16 Schlieren images of a flow field evolution for p_0 = 12.3 kPa and T_0 = 300K with an inter-frame delay of 12.97 μsec. *Test ID: CH4+O2-07-25-12(1.75psiTEST7)* 159

G.17 Schlieren images of a flow field evolution for p_0 = 12.3 kPa and T_0 = 300K with an inter-frame delay of 12.97 μsec. *Test ID: CH4+O2-07-24-12(1.75psiTEST5)* 160

G.18 Schlieren images of a flow field evolution for p_0 = 5.5 kPa and T_0 = 300K using the roughness plate with an inter-frame delay of 10 μsec. *Test ID: CH4+O2-07-13-12(0.8psiTEST3)roughness* 161

G.19 Continuation of the flow field evolution shown in Figure G.18. *Test ID: CH4+O2-07-13-12(0.8psiTEST3)roughness* 162

G.20 Schlieren images of a flow field evolution for p_0 = 5.5 kPa and T_0 = 300K using the roughness plate with an inter-frame delay of 12.34 μsec. *Test ID: CH4+O2-07-13-12(0.8psiTEST4)roughness* 163

G.21 Continuation of the flow field evolution shown in Figure G.20. *Test ID: CH4+O2-07-13-12(0.8psiTEST4)roughness* 164

G.22 Schlieren images of a flow field evolution for p_0 = 10.3 kPa and T_0 = 300K with an inter-frame delay of 12.97 μsec. *Test ID: CH4+O2-07-27-12(1.47psiTEST8)* 165

G.23 Schlieren images of a flow field evolution for p_0 = 12.3 kPa and T_0 = 300K with an inter-frame delay of 12.97 μsec. *Test ID: CH4+O2-07-24-12(1.75psiTEST7)* 166

G.24 Continuation of the flow field evolution shown in Figure G.23. *Test ID: CH4+O2-07-24-12(1.75psiTEST7)* 167

G.25 Schlieren images of a flow field evolution for p_0 = 10.5 kPa and T_0 = 300K with an inter-frame delay of 12.97 μsec. *Test ID: CH4+O2-07-24-12(1.49psiTEST6)* 168

G.26 Schlieren images of a flow field evolution for p_0 = 10.5 kPa and T_0 = 300K with an inter-frame delay of 12.97 μsec. *Test ID: CH4+O2-07-27-12(1.49psiTEST6)* 169

G.27 Schlieren images of a flow field evolution for p_0 = 12.3 kPa and T_0 = 300K with an inter-frame delay of 12.97 μsec. *Test ID: CH4+O2-07-23-12(1.75psiTEST4)* 170

G.28 Schlieren images of a flow field evolution for p_0 = 12.3 kPa and T_0 = 300K with an inter-frame delay of 12.97 μsec. *Test ID: CH4+O2-07-24-12(1.75psiTEST3)* 171

G.29 Schlieren images of a flow field evolution for p_0 = 12.3 kPa and T_0 = 300K with an inter-frame delay of 12.97 μsec. *Test ID: CH4+O2-07-25-12(1.75psiTEST8)* 172

G.30 Schlieren images of a flow field evolution for p_0 = 11.9 kPa and T_0 = 300K with an inter-frame delay of 12.97 μsec. *Test ID: CH4+O2-07-27-12(1.7psiTEST1)* 173

G.31 Schlieren images of a flow field evolution for p_0 = 3.5 kPa and T_0 = 300K with an inter-frame delay of 11.53 μsec. *Test ID: CH4+O2-08-20-12(0.5psiTEST4)* 174

G.32 Continuation of the flow field evolution shown in Figure G.31. *Test ID: CH4+O2-08-20-12(0.5psiTEST4)* 175

G.33 Schlieren images of a flow field evolution for p_0 = 9.8 kPa and T_0 = 300K with an inter-frame delay of 12.97 μsec. *Test ID: CH4+O2-08-01-12(1.4psiTEST1)* 176

G.34 Continuation of the flow field evolution shown in Figure G.33. *Test ID: CH4+O2-08-01-12(1.4psiTEST1)* 177

G.35 Schlieren images of a flow field evolution for $p_0 = 5.5$ kPa and $T_0 = 300$K with an inter-frame delay of 12.91 μsec. *Test ID: CH4+O2-08-14-12(0.8psiTEST3)* 178

G.36 Continuation of the flow field evolution shown in Figure G.35. *Test ID: CH4+O2-08-14-12(0.8psiTEST3)* 179

G.37 Schlieren images of a flow field evolution for $p_0 = 10.5$ kPa and $T_0 = 300$K with an inter-frame delay of 6.03 μsec. *Test ID: CH4+O2-08-01-12(1.5psiTEST6)* 179

G.38 Continuation of the flow field evolution shown in Figure G.37. *Test ID: CH4+O2-08-01-12(1.5psiTEST6)* 180

G.39 Schlieren images of a flow field evolution for $p_0 = 10.5$ kPa and $T_0 = 300$K with an inter-frame delay of 6.03 μsec. *Test ID: CH4+O2-08-01-12(1.5psiTEST8)* 180

G.40 Continuation of the flow field evolution shown in Figure G.39. *Test ID: CH4+O2-08-01-12(1.5psiTEST8)* 180

G.41 Schlieren images of a flow field evolution for $p_0 = 9.8$ kPa and $T_0 = 300$K with an inter-frame delay of 12.97 μsec. *Test ID: CH4+O2-08-03-12(1.4psiTEST1)* 181

G.42 Schlieren images of a flow field evolution for $p_0 = 7$ kPa and $T_0 = 300$K with an inter-frame delay of 12.91 μsec. *Test ID: CH4+O2-08-14-12(1.0psiTEST2)* 182

G.43 Continuation of the flow field evolution shown in Figure G.42. *Test ID: CH4+O2-08-14-12(1.0psiTEST2)* 183

G.44 Schlieren images of a flow field evolution for $p_0 = 14.0$ kPa and $T_0 = 300$K with an inter-frame delay of 12.97 μsec. *Test ID: CH4+O2-08-01-12(2.0psiTEST3)* 184

G.45 Schlieren images of a flow field evolution for p_0 = 16.8 kPa and T_0 = 300K with an inter-frame delay of 6.03 μsec. *Test ID: CH4+O2-08-01-12(2.4psiTEST9)* 185

G.46 Schlieren images for p_0 = 5.5 kPa and T_0 = 300K. *(a)Test ID: CH4+O2 - 08-4-11(0.85psi)5*; *(b)Test ID:CH4+O2 - 08-4-11(0.85psi)6*; *(c)Test ID: CH4+O2 - 08-4-11(0.85psi)8*; *(d)Test ID:CH4+O2 - 08-12-11(0.85psi)1* 186

G.47 Schlieren images for p_0 = 5.5 kPa and T_0 = 300K. *(a)Test ID: CH4+O2 - 07-27-11(0.85psi)2*; *(b)Test ID: CH4+O2 - 07-27-11(0.85psi)3*; *(c)Test ID: CH4+O2 - 07-27-11(0.85psi)5*; *(d)Test ID: CH4+O2 - 07-31-11(0.85psi)5* 187

G.48 Schlieren images for p_0 = 5.5 kPa and T_0 = 300K. *(a)Test ID: CH4+O2 - 08-24-11(0.85psi)11*; *(b)Test ID: CH4+O2 - 08-24-11(0.85psi)12*; *(c)Test ID: CH4+O2 - 07-31-11(0.85psi)4* 188

G.49 Schlieren images for p_0 = 10.5 kPa and T_0 = 300K. *(a)Test ID: CH4+O2 - 08-24-11(1.49psi)2*; *(b)Test ID: CH4+O2 - 08-4-11(1.49psi)2*; *(c)Test ID: CH4+O2 - 08-4-11(1.49psi)4*; *(d)Test ID: CH4+O2 - 08-3-11(1.49psi)2* 189

G.50 Schlieren images for p_0 = 10.5 kPa and T_0 = 300K. *(a)Test ID: CH4+O2 - 05-10-11(1.49psi4)*; *(b)Test ID: CH4+O2 - 08-2-11(1.49psi)5* 190

G.51 Schlieren images for p_0 = 10.5 kPa and T_0 = 300K. *(a)Test ID: CH4+O2 - 08-26-11(1.49psi)3*; *(b)Test ID: CH4+O2 - 05-10-11(1.49psi3)* 190

G.52 Schlieren images for p_0 = 12.0 kPa and T_0 = 300K. *(a)Test ID: CH4+O2 - 03-13-11(1.72psi)5*; *(b)Test ID: CH4+O2 - 03-14-11(1.72psi)1*; *(c)Test ID:CH4+O2 - 03-12-11(1.71psi)2 (top frame)*; *(d)Test ID: CH4+O2 - 03-12-11(1.71psi)2 (bottom frame)* 191

G.53 Schlieren images for p_0 = 12.0 kPa and T_0 = 300K. *(a)Test ID: CH4+O2 - 03-12-11(1.72psi)7*; *(b)Test ID: CH4+O2 - 03-13-11(1.72psi)4*; *(c)Test ID: CH4+O2 - 03-13-11(1.72psi)3*; *(d)Test ID: CH4+O2 - 03-13-11(1.72psi)1* 192

Nomenclature

Roman Symbols

T	Static temperature
p	Static pressure
d	Gap size
ht	Height
V_0	Voltage
u	Absolute velocity
c	Sound speed
v	Relative velocity
x	Distance from center of cylinder
D	Cylinder diameter

Greek Symbols

ρ	Static density
$\Delta_{1/2}$	Half reaction length
λ	Cell width
τ_{ig}	Ignition delay
γ	Specific heat ratio

Non-Dimensional Numbers

M	Mach number
$S = x/D$	Distance (number of diameters, D) from center of obstacle

Subscripts

bw	Bottom Wall
tr	Triple point phase velocity
cl	Centerline
HC	Half-cylinder
FC	Full-cylinder
0	State 0 (initial state)
th	Theoretical (predicted)
exp	Experimental
I	Incident wave
F	Flame

Abbreviations

C-J - Chapman-Jouguet

Z-N-D - Zel'dovich - von Neuman - Doering

K-H - Kelvin-Helmholtz

R-M - Richtmyer-Meshkov

SWACER - Shock wave Amplification Coherence Energy Release

TSG - Triggered Spark Gap

ICP - Integrated Circuit Piezoeletric (registered trademark of PCB Piezotronics Inc.)

HVI - High Volate Ignitor

TM - Trigger Module

BNC - Berkeley Nucleonics Corporation

CEA - Chemical Equilibrium Application

GRI - Gas Research Institute

PCC - Phantom Camera Control (application)

Chapter 1

Introduction

1.1 The ideal detonation wave

A detonation wave is a supersonic combustion wave that propagates through a reactive gaseous mixture of fuel and oxidizer, converting reactants into products [1]. Current research devoted to detonation waves is motivated by applications of detonations to propulsion, such as the pulse detonation engine, and to industrial safety.

The overpressures generated by detonation waves can be estimated accurately with the Chapman-Jouguet (C-J) theory. The C-J theory applies a control volume around a detonation wave and uses the governing equations of mass, momentum and energy to determine the outflow conditions based on the given initial conditions [1]. Using the C-J theory one can accurately predict various detonation parameters, including its steady averaged velocity called the C-J velocity. However, the control volume approach gives no insight into the structure of a detonation wave. This limits our understanding of the underlying gas dynamics that influence how a detonation wave fails, is re-initiated and propagates. The classical Zel'dovich-von Neumann-Doering (Z-N-D) theory provides a model for the reaction zone structure and treats a detonation as an one dimensional, steady, inviscid combustion wave. According to the Z-N-D theory, a supersonic detonation combustion wave comprises a planar shock front followed by an induction zone, which is followed by a reaction zone [1]; Fig. 1.1 shows a schematic diagram of this

simplified model along with the temperature, pressure and density profiles across the detonation wave.

The internal structure and propagation mechanism of an ideal detonation wave was formally established by the Z-N-D theory [1]. From Fig. 1.1, the induction zone is a thermally nearly inactive region, where shocked gas molecules dissociate to form active radicals. Here, the temperature and pressure of the shocked reactants remain relatively constant. When a sufficient concentration of these active radicals are produced, rapid exothermic reactions are initiated converting reactants to final products. The exothermic reactions in the reaction zone cause the temperature to rise while the pressure and density decrease as the gas expands. Using the Z-N-D model, the propagation mechanism for an ideal detonation wave can be described as follows. Gas particles, first shocked by the shock front, begin to react in the reaction zone after some induction delay. During these exothermic reactions, the gas is heated and expands. The expansion of the products provides amplification to forward-facing compression waves that support the shock front. In turn the shock front continues to process more reactants downstream, thus forming a positive feedback loop.

1.2 The detonation cellular structure

The Z-N-D model was instrumental in providing a fundamental understanding of the internal structure and propagation mechanism of a detonation wave. However, detonation waves in nature, as shown in Fig. 1.2(a), are vastly different from the idealized Z-N-D model; their structure is three dimensional, highly unsteady and have a "multi-front" shock structure [1]. It is now well known that there are pressure, temperature and velocity fluctuations with respect to the shock front caused by instabilities [2]. These instabilities in real detonation waves are caused, in part, by the exponential temperature dependence of the chemical reaction rates, as well as the hydrodynamic instabilities of the reaction front [2]. The instabilities manifest themselves as the ubiquitous cellular structure along with the transversely propagating shock waves, which occur in pairs and propagate in opposite directions. Figure 1.2(a) clearly shows a transverse shock wave trailing behind the detonation front like "whiskers", while Fig. 1.2(b) shows a typical detonation cellular pattern etched on to an aluminium foil covered by soot, after the

detonation has passed over it. The cellular dynamics of a self-propagating detonation wave have been well observed and studied by past researchers both experimentally and numerically [3, 4, 5, 6, 7, 8, 9]. To help the reader understand this cellular behaviour, Fig. 1.3 shows a schematic diagram that explains a typical sequence of events during a single cell cycle in a self-propagating detonation wave.

Figures 1.3 (A) to (B) shows an incident wave propagating from left to right with its strength weakening and the reaction zone de-coupled from the front (a de-coupled shock-flame complex) as the triple points approach each other. In Fig. 1.3 (C) the converging triple points are about to collide as the de-coupled shock-flame complex continues to propagate towards the right. Following this collision, Fig. 1.3 (D) shows the de-coupled incident wave has re-initiated into an overdriven Mach detonation wave (velocity greater than the ideal Chapman-Jouguet velocity). From Figs. 1.3 (D) to (E) the triple points diverge from each other while the overdriven Mach stem continues to expand rapidly. From the above description it is clear that as a cellular detonation wave propagates, a de-coupled shock-flame complex periodically re-initiates into an overdriven Mach detonation at the start of each cell cycle following the triple point collision.

1.3 Present state of knowledge

1.3.1 Reactive shock reflections

To understand the factors that contribute to high combustion rates and cause re-initiation into a detonation at the start of the cell cycle, it is crucial to have an insight of the gas dynamic behaviour near the triple point behind the Mach shock. To elucidate this triple point physics, consider Fig. 1.4 which shows a typical reactive single Mach reflection propagating towards the right. A brief description of a triple point is presented here while additional information can be found in G. Ben-Dor's monograph [10]. As shown in Fig. 1.4, a triple point is a confluence of three shock waves and a shear layer. The shock waves are the incident wave, the Mach shock (or Mach stem) and the transverse wave. The shear layer is called a slip line (or slipstream) and has a velocity gradient across it. The slip line also separates two distinct states - one state behind the Mach shock and the other state behind the transverse wave. While the pressure is kept constant across

the slip line, the velocity, temperature and density vary almost discontinuously across it.

Austin [5] showed that just prior to the triple point collision, the slip line that separates the reacted gas behind Mach stem and the unreacted gas behind the transverse wave is unstable due to the Kelvin-Helmholtz (K-H) instability. She also speculated that the volute like structures produced by the K-H instability may cause mixing of the burned and unburned gases. This presumably forms localized "hot spots" (isolated regions of intense chemical reactivity) that "explode" to release energy in a short duration, eventually contributing to the re-initiation into a detonation.

When a pressure gradient across a transverse shock interacts with a density gradient across a reaction zone, this can produce vorticity through the baroclinic mechanism leading to the formation of the Richtmyer-Meshkov (R-M) instability. Radulescu et al. [7] suggested that mixing of burned and unburned gases by the vorticity present at the reaction zone may give rise to an induction gradient that favours a synchronized deposition of energy via hot spots (SWACER mechanism) and causes amplification of compression waves. This in turn increases combustion rates and eventually leads to re-initiation into a detonation [11]. However, they point out that their experimental resolution was not sufficiently high to determine the origins of the final explosion leading to re-initiation into a detonation.

At high Mach numbers, the slip line curves forward, as shown in Fig. 1.4, because the streamlines in the state behind the transverse wave stagnate, either on a confining wall or a line of symmetry. This stagnation point sets up a static pressure gradient around it thereby deflecting flow away from it. This causes some of the flow to divert downstream, with respect to the stagnation point, and thereby forcing the slip line to curve forward [12, 13]. A mechanism that has been suggested to play a role in shock reflections leading to re-initiation into a detonation is the jet formed in irregular shock reflections [3, 12, 14]. The forward jetting of the shear layer in Mach reflections can potentially re-inject combustion products of the trailing reaction zone into the unreacted shocked gas behind the Mach stem, as proposed by Sorin et al. [15]. Indeed, very recent numerical simulations of cellular detonations performed by Mazaheri et al. [16] have shown that jet formation along shear layers plays a role in increasing the number of hot spots (isolated regions of intense chemical reactivity) in the unburned gases behind the Mach stem.

Oran et al. [17] numerically studied the structure of two-dimensional detonation waves using a reactive Euler model along with a detailed chemical reaction mechanism for hydrogen-oxygen combustion. They showed that re-initiation into a detonation may occur due to rapid release of high energy by: (a) the collision of transverse waves just prior to the triple point collision; (b) the collision of the triple points themselves. However, the mixture used for their model was a heavily diluted, low activation energy mixture and therefore the mechanisms of re-initiation into a detonation may not be applicable to high activation energy mixtures such as a stoichiometric methane-oxygen mixture [7].

Gamezo et al. [4] performed numerical simulations of two-dimensional C-J detonations using reactive Euler equations with the Arrhenius law and showed that large pockets of unreacted gas were observed in unstable detonations, especially for high activation energy mixtures. Evidence of these pockets of unreacted gas suggests that adiabatic shock compression heating alone cannot be responsible for detonation propagation, particularly for high activation energy mixtures, and that a mechanism that promotes mixing between burned-unburned gases potentially plays a significant role [1]. They however point out that the model cannot explain why detonation cells are formed and therefore are not able to elucidate the mechanisms that cause re-initiation into an overdriven detonation wave.

Despite identifying these important mechanisms, the sequence of events that clearly show which mechanism(s) is responsible in increasing combustion rates and subsequently causing re-initiation into a detonation is still lacking. This is because the spatial and temporal scales of cellular detonations are very small to permit a clear visualization of propagation of detonation waves as these waves periodically diffract, quench and are re-initiated in every cell cycle. In addition, cellular detonation waves are highly stochastic, unsteady and hence not very reproducible. This irregularity in cellular pattern was noted by Ng et al. [18] where they numerically showed, using a two-step reaction mechanism governed by the Arrhenius law in a 1D flow, that mixtures with high activation energies, such as stoichiometric oxy-methane, are highly unstable due to the strong sensitivity of the chemical induction time and energy release to initial perturbations. The irregularity was clearly illustrated by Sharpe and Radulescu [19] who showed, using high resolution numerical soot foils with a one-step Arrhenius reaction model in a 2D flow, that the cellular dynamics become rapidly chaotic with an increase in activation energy.

1.3.2 Detonation diffraction around obstacles

To better understand the detonation re-initiation process while addressing the stochasticity and small length scale issues, the technique of allowing a detonation wave to quench behind an obstacle and subsequently form a Mach reflection was adopted. It is now well understood that when a self-propagating C-J detonation wave is allowed to expand through the process of diffraction behind an obstacle or through an abrupt change in area, the positive feedback mechanism between the reaction zone and cellular shock front structure begins to weaken allowing the reaction zone to de-couple from the shock front [20, 21, 22]. To help the reader understand this process of detonation diffraction behind a full cylinder obstacle, Fig. 1.5 shows a schematic diagram that illustrates a typical sequence of events.

Figure 1.5 (A) shows a stable cellular detonation wave propagating from left to right and is about to collide against the full cylinder obstacle. Following this collision, Fig. 1.5 (B) illustrates the detonation wave diffracting around the downstream surface of the obstacle which results in a velocity deficit. If this diffraction is allowed to continue, this may result in a de-coupled shock-flame complex caused by weakening the positive feedback mechanism [21, 22]. Figure 1.5 (C) shows that the detonation wave has now quenched to form two de-coupled shock-flame complexes. Here both incident shock fronts form a regular reflection off of each other. Following this regular reflection of the de-coupled shock-flame complexes along the line of symmetry, a transition occurs which eventually forms a Mach reflection as seen in Fig. 1.5 (D). Here a Mach shock front is formed and it expands while propagating forward as the two triple points diverge from each other. It is therefore evident that if the shock front of a de-coupled shock-flame complex is allowed to reflect off a wall or another shock front along the line of symmetry behind an obstacle, one can recover a Mach reflection similar to what is observed periodically at the start of each cell cycle in a propagating detonation wave. This type of configuration presents results on a larger scale than cellular dynamics with a higher degree of reproducibility and therefore allows us to make detailed observations.

Teodorczyk, Lee and Knystautas [23, 24] studied the wall-reflection of a detonation diffracted around a baffle using high speed Schlieren visualization. From their experiments, they clearly correlated the re-ignition of the gas with the region behind the Mach stem. These authors have also pointed out that mixing of hot reacted gases with colder

unreacted gases along the slip-line emanating from the triple points may also have a strong influence.

Ohyagi et al. [25] and Obara et al. [26] studied the diffraction and re-initiation of detonation waves that take place behind a backward facing step and a slit plate respectively. Their high speed Schlieren images and soot foils clearly indicated that re-initiation into a detonation takes place behind the Mach stem. They provided evidence that the re-initiation event is accompanied by transverse detonations. Such transverse detonations have also been inferred from soot foils and open shutter photographs.

Open shutter photography by Radulescu and Maxwell [27] has shown evidence of intense chemi-luminescence near triple points prior to re-initiation into a detonation. From their analysis, as transverse detonations were ruled out, the evidence pointed towards the possibility of mixing between burned and unburned gas. The experiments, however, could not identify the true mechanism responsible for the intense chemi-luminescence observed.

1.3.3 Summary of current state of knowledge

In summary, past research has played a crucial role in identifying key mechanisms that cause re-ignition following a Mach reflection process. To date, five distinct mechanisms have been proposed:

- high temperature behind the Mach stem leads to a significant reduction of the ignition delays and rapid reaction of the gases;
- Kelvin-Helmholtz (K-H) instability along the slip line emanating from the triple points promotes mixing between reacted and unreacted gases, leading to increased burning rates;
- when transverse shocks interact with the density gradients in the flame interface, the presence of the Richtmyer-Meshkov (R-M) instability can promote mixing and enhance the burning rates;
- rapid energy release behind the transverse shocks lead to transverse detonations, and;

- the forward jetting slip line, formed behind the Mach stem, can enhance mixing between burned-unburned gases and lead to the reaction of a substantial amount of gases.

Whereas the first mechanism is commonly accepted, evidence in support for the other four mechanisms remains inconclusive. This study is an experimental attempt to isolate the key mechanisms that contribute to the acceleration of the reaction rates and cause the re-initiation of a de-coupled shock-flame complex, following a Mach reflection, into an overdriven detonation wave behind a cylindrical obstacle.

1.4 Problem definition and research objective

The objective of this research is to experimentally investigate the important mechanisms controlling the re-initiation of the de-coupled shock-flame complex into an overdriven detonation, following a Mach reflection. To achieve this objective, a self-supported cellular detonation wave is allowed to diffract around cylindrical obstacles and quench to obtain a de-coupled shock-flame complex (see Fig. 1.5). The shock front of this de-coupled shock-flame complex is then allowed to reflect off the wall or along the line of symmetry to eventually form an irregular (Mach) reflection; the focus of this study will be on the events that take place following the Mach reflection by varying the initial pressure and obstacle used. The flow field evolution is visualized by using the Schlieren technique that has a high spatial and temporal resolution.

1.5 Thesis outline

This thesis is organized as follows. Chapter 2 details the experimental setup used as well as the procedure used for the experiments. Chapter 3 presents experimental Schlieren images that illustrate the cellular behaviour of a self-propagating detonation wave without the presence of an obstacle. Chapter 4 focuses mainly on the events following a Mach reflection process of a quenched detonation behind an obstacle. Chapter 5 presents the analyses carried out and discusses the findings. Finally, in Chapter 6 conclusions are

drawn based on the qualitative and quantitative findings of this work followed by some recommendations for future work. The appendices (Section A - G) include uncertainty estimation, a brief description of the different computational tools used and analyses as well as additional Schlieren images.

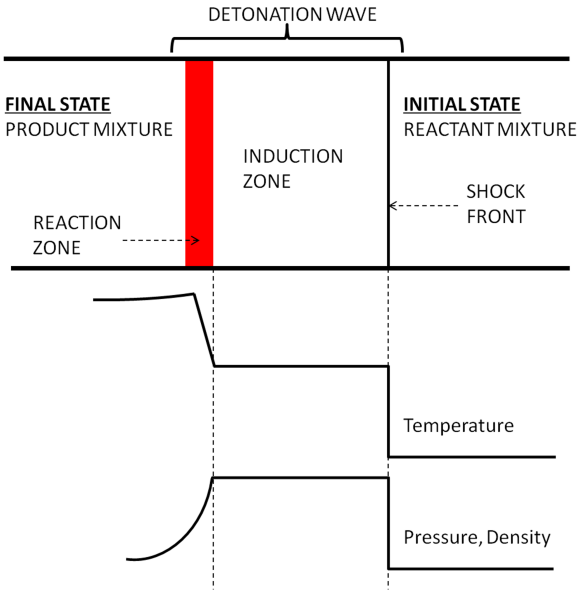

Figure 1.1: A schematic diagram showing a Z-N-D detonation model propagating towards the right and temperature, pressure and density profile across the detonation wave.

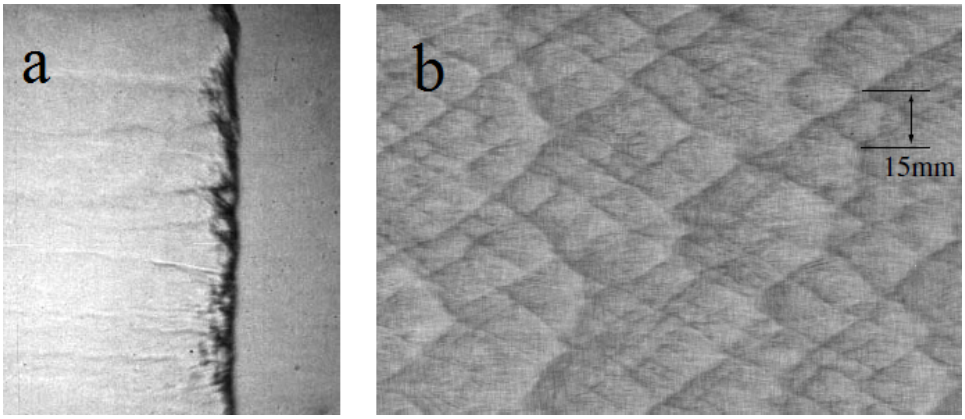

Figure 1.2: Figure (a) shows a shadowgraph of a detonation front propagating from left to right in a channel in C_2H_4+$3O_2$+$6N_2$ at an initial pressure $p_0 = 20$ kPa. Figure (b) shows a soot foil from another experiment showing the irregular cellular pattern in C_2H_4+$3O_2$+$5N_2$ at an initial pressure $p_0 = 20$ kPa indicating that the cell width (λ) is 15 mm. Photographs courtesy of J. M. Austin. See also Ref. [5]

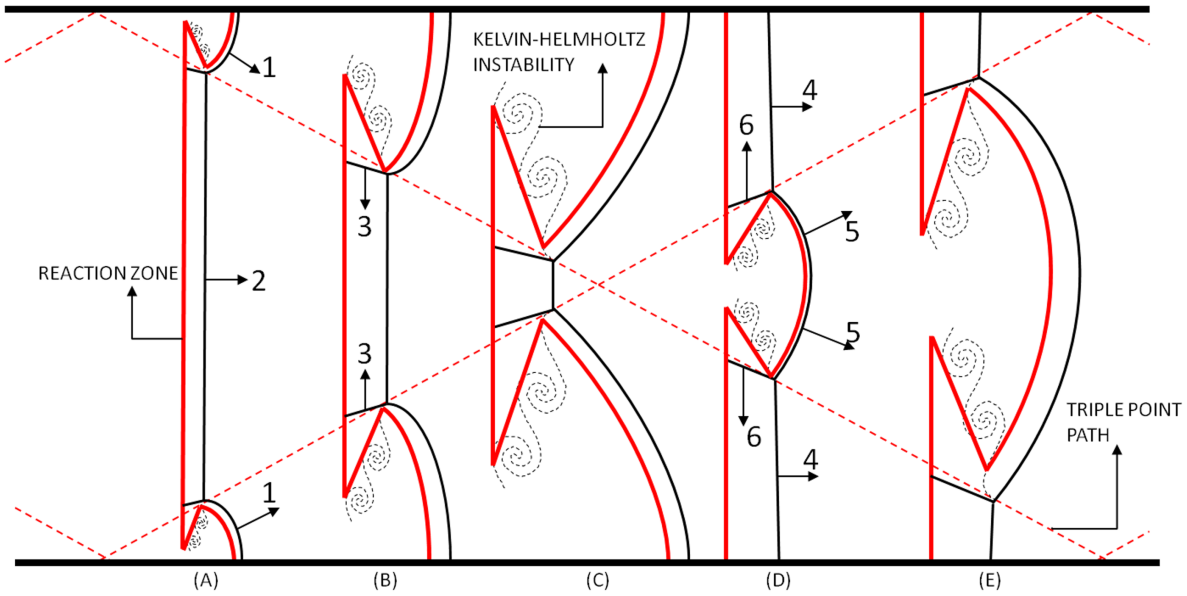

Figure 1.3: A schematic diagram illustrating the sequence of events in a single cell cycle for a propagating cellular detonation wave with the direction of propagation for each shock wave shown: (1) strong Mach stems; (2) weak incident wave; (3) transverse waves traveling towards each other; (4) weak incident waves; (5) overdriven Mach stem; (6) transverse waves traveling away from each other. Also labeled are the Kelvin-Helmholtz (K-H) instability and, the triple point path which is not observed in the Schlieren images

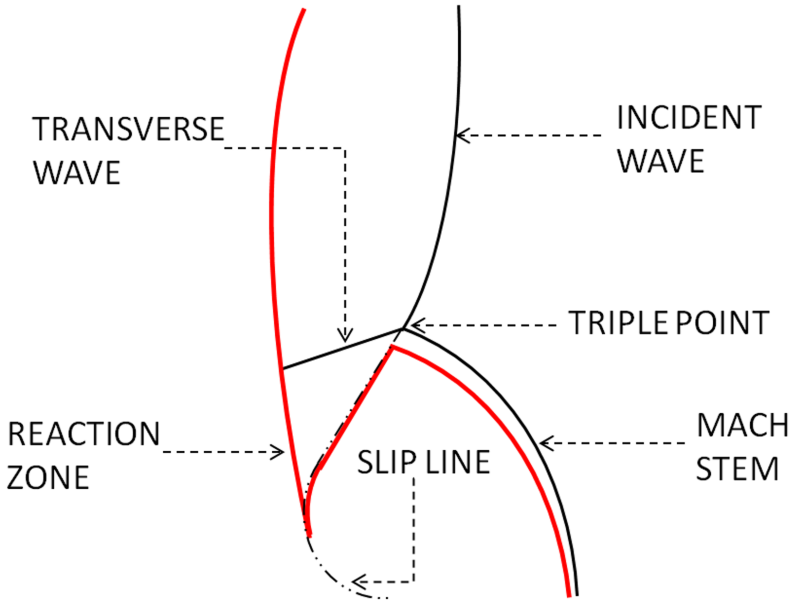

Figure 1.4: A schematic diagram of a reactive single Mach reflection, propagating towards the right, identifying the key features - the Mach stem, the incident wave, the transverse wave, a slip line, a triple point and the reaction zone.

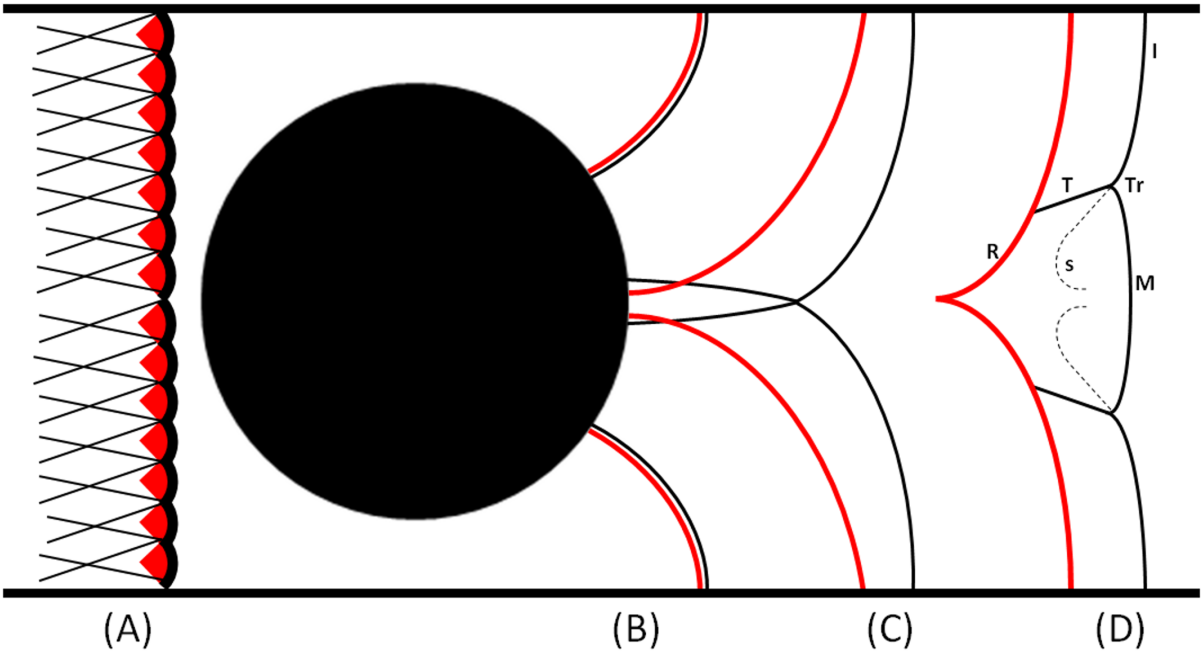

Figure 1.5: A schematic diagram showing the diffraction of a detonation wave behind a full-cylinder obstacle to form two de-coupled shock-flame complexes, which forms a Mach reflection after interacting with each other. Description of the labels are as follows: (I) - Incident wave, (M) - Mach stem, (T) - Transverse wave, (Tr) - Triple point, (s) - slip line, (R) - Reaction zone (or flame interface)

Chapter 2

Experimental Setup

2.1 Flow facility

Figure 2.1 shows a schematic diagram of the 3.4 m long aluminium rectangular channel used, henceforth referred to as the "shock tube", with an internal height and width of 203.2 mm and 19.1 mm respectively. This internal width was found to be the optimum value to suppress the transverse perturbations and thus approximating the flow as 2D; additional details can be found in Drolet's undergraduate thesis [28]. The shock tube has three separate sections of equal length. This modular design allows for increased versatility when initiating a detonation wave. Non-tempered glass panels are installed in the third or "window" section, which permits Schlieren visualization. The obstacle was placed in this "window" section. To ignite the mixture a spark plug is installed in the first section of the shock tube. Dynamic pressure transducers were installed along the top wall to record the arrival of the detonation wave and monitor its strength.

The schematic diagram shown in Fig. 2.2 shows a gas panel, which was designed for multiple purposes - preparing the test mixture, filling and purging of shock tube channel. The Swagelok needle valves on the bottom right corner are connected to different fuels while the oxygen (O_2) line is connected to the needle valve on the bottom left. Additional valves are installed to avoid any accidental mixing, reverse-flow and to protect sensitive instruments. The absolute static pressure in the shock tube is monitored in pound per

square inch (psi units) by two OMEGA DPI32 programmable digital meters, with varying degrees of accuracy. The type of pressure transducer installed is a piezoresistive OMEGA transducer (model nos. PX409-015A5V and PX409-150A5V). The vacuum pressure in the shock tube is measured using an OMEGA DVG-64 vacuum gauge (Pa units). Figure 2.2 shows a schematic diagram of the gas line connections between the gas panel and the shock tube. The test mixture was fed into the shock tube from the mixing tanks, via the gas panel, through Swagelok rubber insulated gas lines. The test mixture was prepared in the mixing tank, by the method of partial pressures, and left to stand for a period of approximately 24 hours. Ball valves connected onto the shock tube are used to seal either a section or isolate the entire shock tube from the gas panel.

Before every test, the shock tube was first evacuated, to approximately 80 Pa, by a Varian DS602 1PH rotary vane pump (model no. 9299335) to purge the shock tube of any residual gas products left behind from the previous experiment.

Three obstacles were used for this study, all having a thickness of 19 mm. Figure 2.3(a) shows a half-cylinder obstacle, 305 mm in diameter, which was machined out of polyoxymethylene thermoplastic (Delrin). Figure 2.3(b) shows a full-cylinder with a diameter of 152.5 mm, which was machined out of aluminium. Figure 2.3(c) shows a roughness plate, which was also machined out of the same thermoplastic, having a length of 428.6 mm and a total height of 10 mm. The dimensions of each tooth on the roughness plate are 3.2 mm by 3.2 mm; the teeth are separated by groves of length 3.2 mm. Additional details of the roughness plate can be found in the reference [29].

2.2 Measuring and data acquisition systems

The dynamic pressure changes during an experiment were monitored using high frequency piezoelectric PCB pressure gauges, which were mounted along the top wall of the shock tube. As Fig. 2.4 shows, the pressure sensors are housed in an aluminum casing while the sensor diaphragm and face of the aluminum casing are placed flush against the internal surface of the tube thereby mitigating any intrusion. Dynamic pressure sensors of two different ratings were used - PCB Piezotronics 113A24 high frequency ICP pressure sensor (measurement range of 1000psi with a sensitivity of 5mV/psi) and PCB Piezotronics

113A27 high frequency ICP pressure sensor (100psi and a sensitivity of 50 mV/psi).

When the pressure sensors experience a dynamic change in pressure (e.g., passage of a shock wave), a raw voltage signal is relayed through a coaxial cable that interfaces with a PCB Piezotronics 482C05 signal conditioner. The improved signal-to-noise ratio voltage signal from the conditioner is then transferred into a National Instrument DAQ BNC-2110 card. Through a NI LabVIEW interface, the voltage signals can be calibrated and converted into final pressure readings; the calibration specifications were provided by the manufacturer. These final pressure readings are saved onto a computer hard drive for future use. In addition, recording by the NI DAQ card begins when it is triggered by a four channel BNC 575-4C digital delay/pulse generator, which also triggers all other instrumentations at user defined interval delays.

2.3 Flow visualization systems

A Z-configuration Schlieren setup was used for visualizing all experiments as illustrated in Fig. 2.5. The light source emits a high intensity flash that reflects off of two Edmund Optics 32277533 optical grade parabolic mirrors, with enhanced aluminum coating, having a diameter of 317.5 mm. The mirrors have an effective focal length of 2540 mm with an aperture (f-stop inverse) of 8.0.

A brief description of our Z-configuration Schlieren setup is provided below and additional details can be found in Settles' book [30]. A bright flash from the light source is incident upon the first mirror, which produces a parallel beam of light towards the window section. The parallel beam of light is then refracted as it passes through the window section, due to changes in the refractive index in the flow caused by density gradients, before falling onto the second mirror. The light reflected from the second mirror then falls onto a vertical knife edge (a razor blade) shown in Fig. 2.6, where a part of the light is allowed to project onto the high speed camera sensor. For all Schlieren visualization, a vertical knife edge was used, which permitted us to visualize horizontal density gradients. Additional details on how to interpret the Schlieren images presented in this work are provided in Section 2.10.

Two different visualization formats were used for two main purposes: a) high speed

Schlieren videos; b) double-frame Schlieren images. The high speed videos allowed for a clearer understanding of the sequence of events with a lower resolution while the double-frame higher resolution permitted a much clearer visualization. Described below are the different instruments used for both formats.

2.3.1 High speed Schlieren videos

A very high speed camera was used to record Schlieren videos of the experiments performed. For most of the videos taken, the frame rate used was 77108 fps with a resolution of 384 by 288 (horizontal by vertical). Figure 2.7 shows the Phantom high speed camera (model no. V1210) manufactured by AMETEK Vision Research. The optical filter used was a Biermann and Weber (B+W) 2x neutral density filter. This filter was chosen to avoid overexposure from the luminous emission of the detonation wave. For velocimetry, the Phantom Camera Control (PCC) application was used to calculate the shock wave velocity after calibrating the video with a known reference length (e.g., height of the channel).

A high intensity LED light source was used which produced a continuous high intensity light for a duration of 2 sec. Figure 2.8 shows a picture of the LED light source (part no. EL-P300W140D3-XT-ww) manufactured by EFFLED.

2.3.2 Double-frame Schlieren photographs

A very high resolution camera was used to capture two Schlieren images having a maximum resolution of 2112 by 2072 (horizontal by vertical) for each image. The inter-frame time for all experiments visualized in this format was set at 11 μsec. Figure 2.9 shows the PCO-TECH Inc. double frame camera (model pco.2000) used to record these high resolution images. The optical filter used was a Biermann and Weber (B+W) 2x neutral density filter. For velocimetry, the ImageJ application was used after calibrating each frame with a known reference length.

A two-in-line-spark high intensity flash system was used which can deliver sub-microsecond duration flashes. To ensure both flashes were spatially stable across the

electrode gap, argon gas was first flooded inside the housing of the system for a few seconds before discharging the capacitors. Figure 2.10 shows a picture of the PalFlash501 system used, manufactured by PCO-TECH Inc. (formerly The Cooke Corporation).

2.4 Methods for gas ignition

Described below are methods used to ignite the test mixture and initiate a detonation wave.

2.4.1 High voltage ignition (HVI) system

The high voltage igniter (HVI) shown in Fig. 2.11 was custom designed and built by Sev Kamenskih from McGill University. The HVI is a compact ignition system that can be charged to a voltage of approximately 30 kV. The main components of the HVI are the two General Atomics 1 μF capacitors, the triggered spark gap (Perkin Elmer GP-41B) and a TM-11A trigger module. The BNC pulse generator sends a voltage signal to the module, which triggers the spark gap and allows the two capacitors to discharge into the mixture (load), as seen in the circuit diagram shown in Fig. 2.12. The unit is capable of storing up to a 1000J (at a charging voltage of V_0=32 kV) of nominal energy and releasing it with a response time of less than 2 μs; additional details can be found in Appendix B. For the majority of the tests, the capacitors were charged to 24 kV.

Following a rapid discharge of the HVI capacitors, a strong blast wave is produced followed by a high speed deflagration wave. The wiremesh installed near the spark plug, as shown in Fig. 2.13, accelerates the deflagration wave by inducing turbulence thereby leading to a detonation initiation; this phenomenon is termed deflagration-to-detonation (DDT) [1]. The overdriven detonation wave eventually stabilizes before reaching the obstacle. To ensure a detonation wave was established before reaching the obstacle, pressure plots recorded by the two transducers, mounted upstream with respect to the obstacle, (see Fig. 2.1) provides the time of arrival. Knowing the distance between these two transducers, the average velocity of the combustion wave can be estimated and compared to the ideal C-J velocity.

2.4.2 Shock tube with a diaphragm method

A different method, using a driver gas mixture, was used when the HVI system could not initiate a detonation wave by itself; this occurred for low initial pressure mixtures typically below 7 kPa. As shown in Fig. 2.14, the "driver" section of the shock tube was filled with a more reactive mixture (e.g., stoichiometric oxy-acetylene). This driver section was separated from the "driven" or test section, filled with the test gas, by a plastic diaphragm having an average thickness of roughly 80 μm.

To initiate ignition, the BNC trigger sends a voltage signal to the HVI, which rapidly discharges energy into the driver gas. The energy deposited from the spark plug initiates a strong blast wave, which can form a detonation wave in the driver section. If a detonation wave is formed, it ruptures the diaphragm and transmits into the driven section as a strong shock wave. This strong shock wave then transitions into a detonation wave and may eventually stabilize before reaching the obstacle.

2.5 Experimental procedure

2.5.1 Shock tube with a diaphragm installed

The shock tube and all gas lines connecting the mixing tanks, gas panel and shock tube were first purged by evacuating them to 80 Pa. After the desired vacuum pressure was achieved, the driven section was sealed and the driver section was first filled with the driver mixture (e.g., $2C_2H_2 + 5O_2$). Care was taken while filling the driver section by avoiding the pressure difference across the diaphragm to exceed approximately 20 kPa as a high pressure difference can rupture the diaphragm. Once the desired driver pressure was reached, the driver section was sealed off by closing the appropriate valves. Before filling the driven section, since the driver gas was usually different from the driven test gas, all gas lines were purged by evacuating them to less than 60 Pa. After this, the driven section was then filled with the test gas CH_4+$2O_2$, which was used in all experiments. After the pressure in driven section had reached its desired value, the shock tube was then completely sealed and isolated from the gas panel and all gas lines were evacuated

to less than 60 Pa. In the final step, the HVI was charged to 24 kV. The charging process usually took less than 3 minutes after which the mixture was immediately ignited.

2.5.2 Shock tube without a diaphragm installed

The shock tube and all gas lines connecting the mixing tanks, gas panel and shock tube were first purged by evacuating it to 80 Pa. Following this, the shock tube was carefully filled with the test mixture (CH_4+$2O_2$) by controlling the flow from the needle valve on the gas panel. Once the desired initial pressure was obtained, the shock tube was then completely sealed and isolated from the gas panel and all gas lines were evacuated to less than 60 Pa. In the final step, the HVI was charged to 24 kV after which the mixture was immediately ignited.

2.6 First experimental series using a 305 mm diameter half-cylinder

In the first series of experiments, a 305 mm diameter half-cylinder was placed in the shock tube as shown in the Fig. 2.15.

The shortest distance between the top wall and the half-cylinder is described in this work as the "gap size" and is denoted by d. For the 305 mm diameter half-cylinder in the shock tube with an internal cross-sectional height of 203 mm, the gap size was d_{HC} = 51 mm.

2.7 Second experimental series using a 305 mm diameter half-cylinder followed by a roughness plate

From Fig. 2.16, a modification to the first experimental series was made by inserting the roughness plate. One end of the roughness plate was placed flushed against the foot of

the half-cylinder obstacle.

The objective of adding a roughness plate was to artificially introduce hot spots (localized regions of chemical reactions), which were formed inside each groove. This type of study can reveal how the energy release from these hot spots can affect the gas dynamic behaviour behind the Mach shock, following an Mach (or irregular) reflection of a de-coupled detonation wave.

2.8 Third experimental series using a 152 mm diameter full-cylinder

Experiments were also performed using a full-cylinder obstacle with a smaller diameter. From Fig. 2.17, the 152 mm diameter full-cylinder was positioned in the middle of the flange separating the viewing section from the middle section. For the 152 mm diameter full-cylinder in the shock tube with an internal cross-sectional height of 203 mm, the gap size was $d_{FC} = 25.5$ mm.

The objective of using a full-cylinder obstacle was to remove the influence, if any, of the boundary layer behind the Mach shock following an Mach reflection of a de-coupled detonation wave. Thus, this setup is more representative of the shock reflection process observed in the cell cycle of a propagating detonation wave.

2.9 Sensitivity of the gas mixture

By keeping the composition and temperature constant of the test mixture (CH_4+$2O_2$), the mixture sensitivity was controlled by changing only its initial pressure. With an increase in pressure (density), the reaction rates in the mixture are faster and the mixture is more sensitive. Previous correlations have shown that the reaction zone thickness and cell size, vary approximately inversely proportional to the initial pressure as shown by

the following relation [27, 31],

$$\Delta_{1/2} \propto \lambda \propto p_0^{-a} \tag{2.1}$$

where, the half-reaction length or $\Delta_{1/2}$ represents the distance behind the shock front to the point where half the energy is released, in a one dimensional Z-N-D model [27].

Figure 2.18 shows a compilation of experimentally measured cell width for stoichiometric oxy-methane mixture, with varying initial pressures (p_0) [32, 33, 34, 35, 36]. Also shown in Fig. 2.18 is the initial pressure range used in this study, represented by the vertical solid lines. The power law curve fit shown in the graph is given by the expression $\lambda = 831.64{p_0}^{-1.215}$ (where λ is expressed in mm and p_0 in kPa).

2.10 Interpretating the Schlieren images

In an inhomogeneous gaseous medium, the density varies with the refractive index as per the Gladstone-Dale equation. When a parallel beam of light is allowed to pass through this inhomogeneous test section, it causes the light to refract at different angles. Before the refracted light is incident upon the recording plane, it first passes through a cut-off plane where a knife edge blocks a part of the refracted light. The light that is allowed to pass through the cut-off plane forms a bright region (white lines) while the darker regions (black lines) are formed because part of the light is incident upon the knife edge. Since the Schlieren technique responds to the first spatial derivative of density, a sharp or sudden change in density is represented by a thin line. Alternatively, a gradual change is represented by a thicker line or region. As described in Section 2.3 we use a vertical knife edge which allows one to visualize density gradients in the horizontal axis. To help the reader understand how to interpret Schlieren images presented in this study, consider Fig. 2.19 which shows a typical Schlieren image with its corresponding schematic diagram on the right. The Schlieren image shows a failed detonation wave as it diffracts around the half-cylinder obstacle while propagating towards the right.

When traveling from point 1 to 2, a sharp black line is observed which represents a sudden increase in density. A shock wave is a naturally occurring supersonic phenomenon capable of causing a step increase in temperature, pressure and density. Therefore, the

thin black line represents a shock wave traveling towards the right. If we consider the X-axis positive towards the right, then the a shock wave traveling towards the right represents a negative density gradient. Conversely, a shock wave traveling towards the left represents a positive density gradient and will appear as a white line.

If a dark line traveling towards the right represents a negative density gradient, then conversely a white line or region propagating in the same direction will represent a positive density gradient. When traveling from point 2 to 3, a gradual decrease in density is observed represented by the thick white region. A reaction zone represents an interface that separates the heavier unburned gas (state 2) from the lighter burned products (state 3). Therefore, the thick white region represents the reaction zone traveling towards the right. Conversely, a reaction zone traveling towards the left will appear as a dark region.

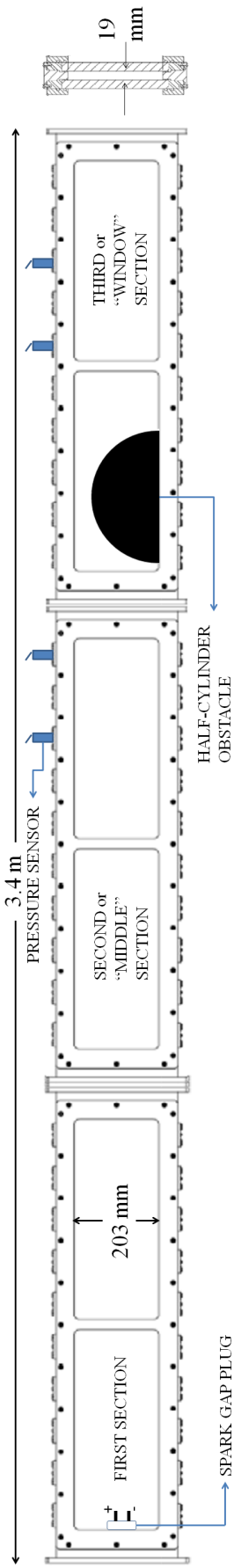

Figure 2.1: A schematic diagram of the shock tube showing the pertinent dimensions and identifying the different sections. Also shown is the half-cylinder obstacle placed in the window section.

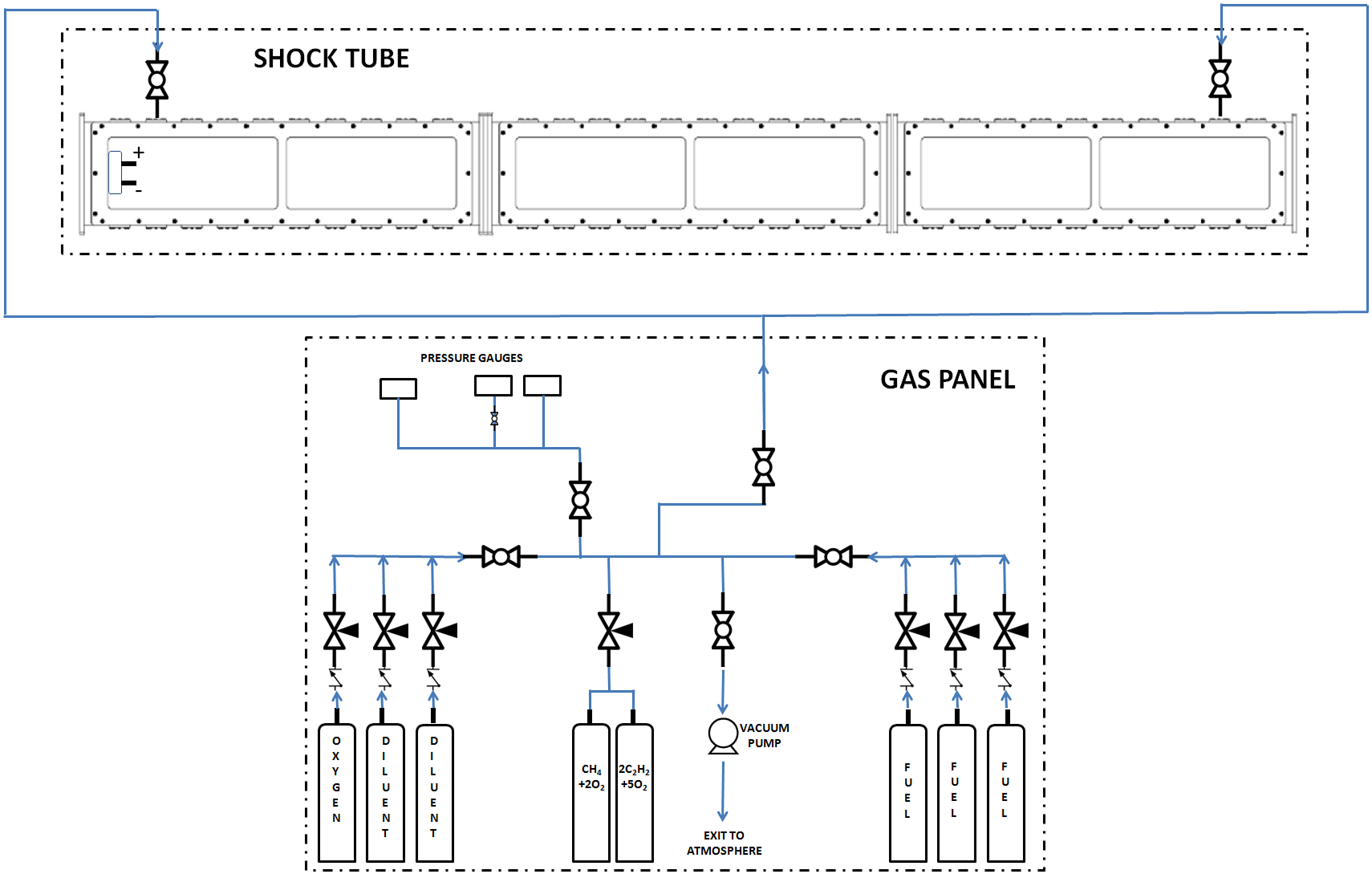

Figure 2.2: A schematic diagram showing the direction of the gas flow between the gas panel and the shock tube.

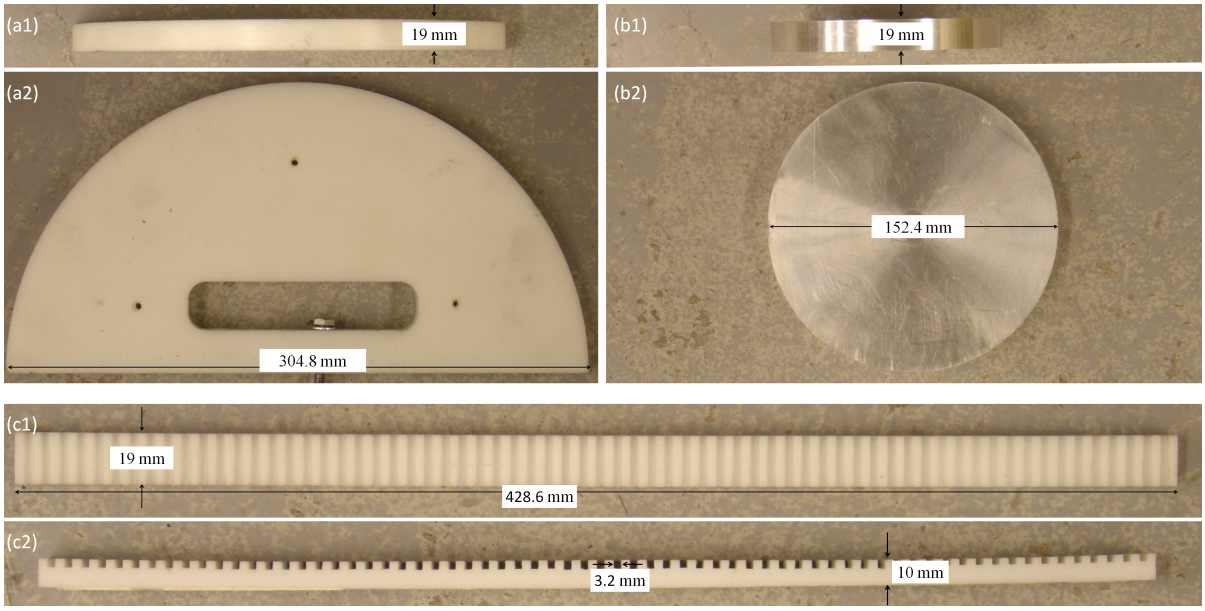

Figure 2.3: Photographs of different obstacles used for all experiments, shown with dimensions: top view (a1) and front view (a2) of the half-cylinder obstacle; top view (b1) and front view (b2) of the full-cylinder obstacle; top view (c1) and front view (c2) of the roughness plate.

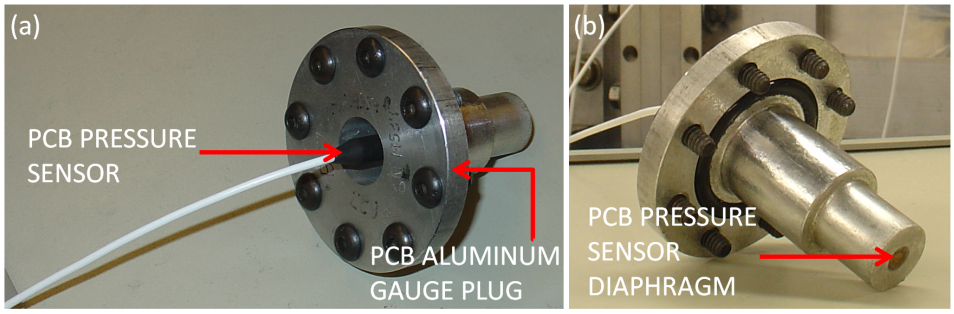

Figure 2.4: Photographs of the PCB pressure sensor aluminum plug. Figure (a) shows the back view of the PCB pressure sensor housed inside the aluminum gauge plug. Figure (b) shows the front view of the PCB pressure sensor with its diaphragm placed flush against the surface of the aluminum gauge plug.

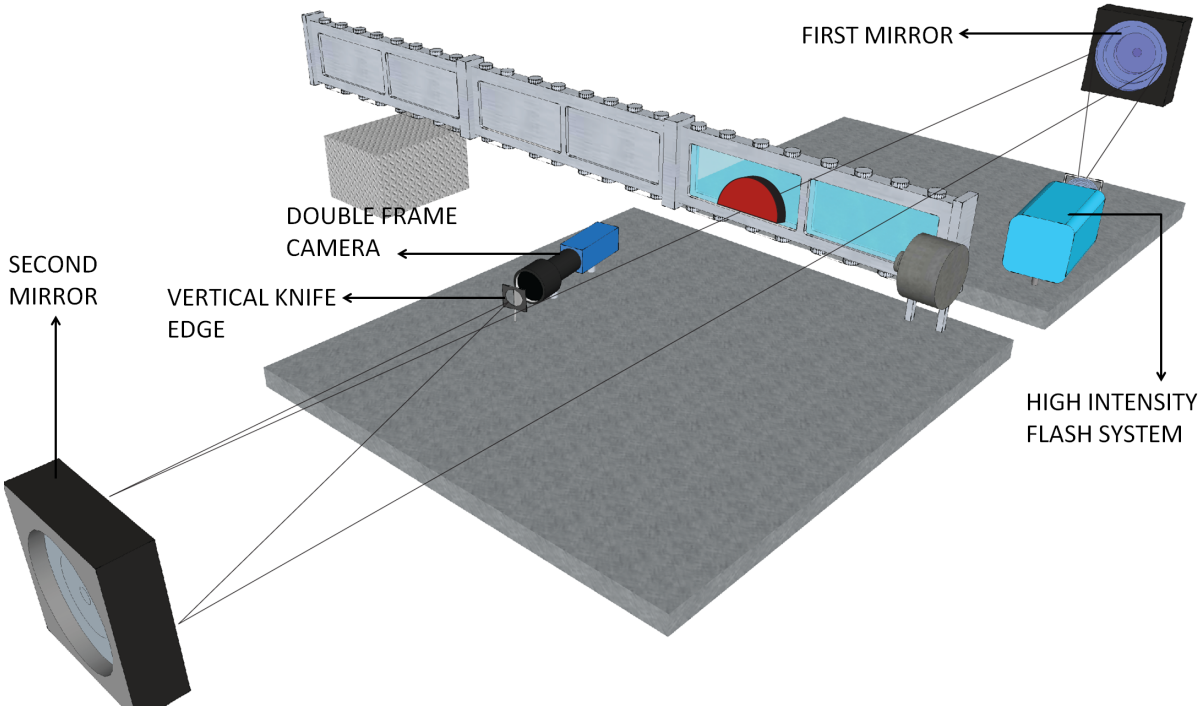

Figure 2.5: A schematic diagram showing the Z-configuration Schlieren setup used for experimental visualization. The high speed camera shown is the pco.2000 double frame camera and the high intensity light source shown is the two-spark PalFlash 501 light source.

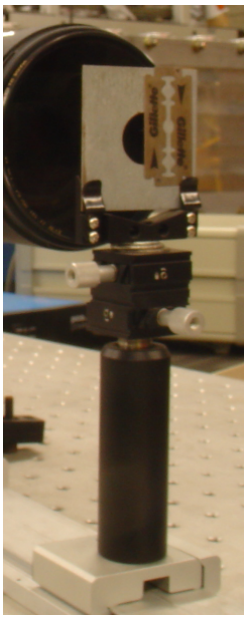

Figure 2.6: A photograph of the vertical knife edge, which resolves the horizontal density gradients in the all Schlieren results obtained.

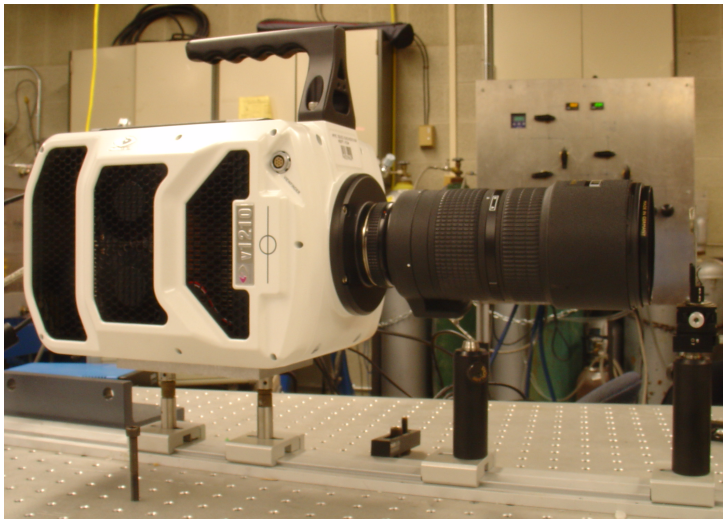

Figure 2.7: A photograph of the side view of the Phantom V1210 high speed camera.

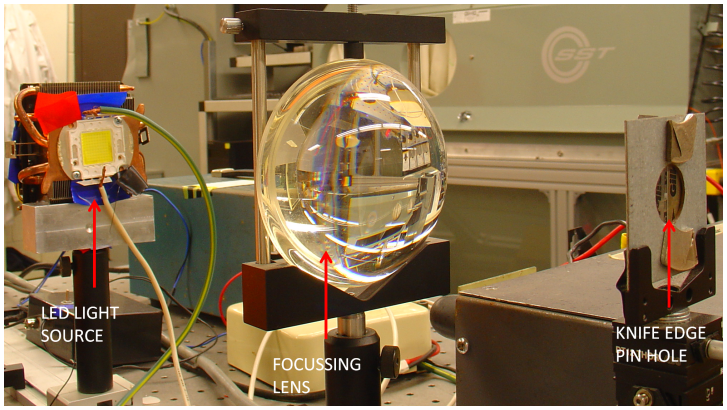

Figure 2.8: A photograph of the high intensity LED light source, the focusing lens and the knife edge pin hole.

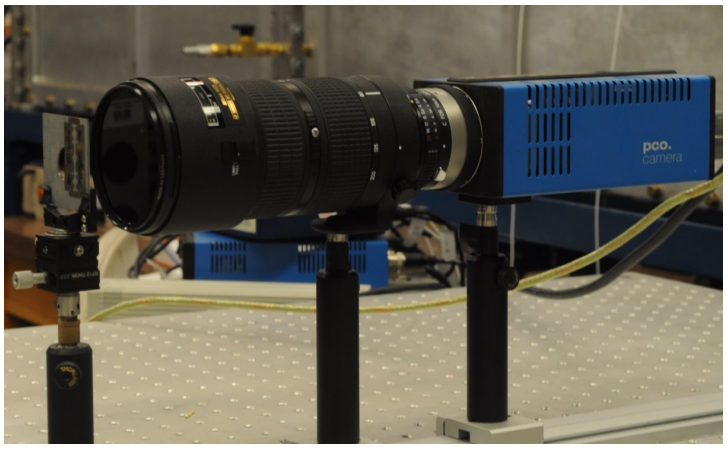

Figure 2.9: A photograph of the side view of the pco.2000 double frame high speed camera. Photograph courtesy of L. Maley.

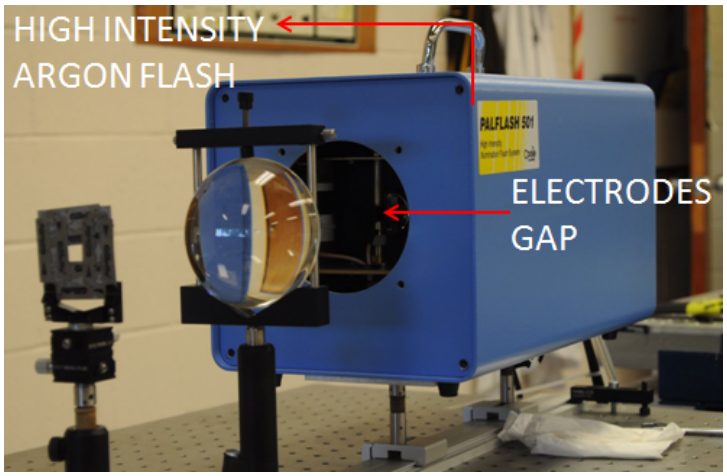

Figure 2.10: A photograph of the two-spark PalFlash 501 high intensity light source, which uses argon gas, the focusing lens and the knife edge pin hole. Photograph courtesy of L. Maley.

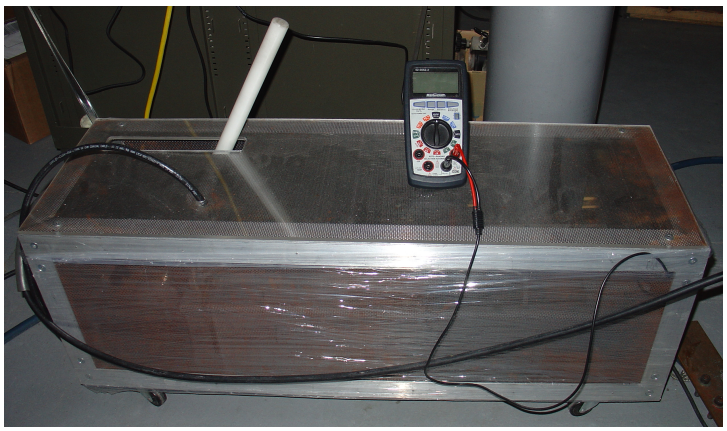

Figure 2.11: A photograph of the High Voltage Igniter (HVI) system.

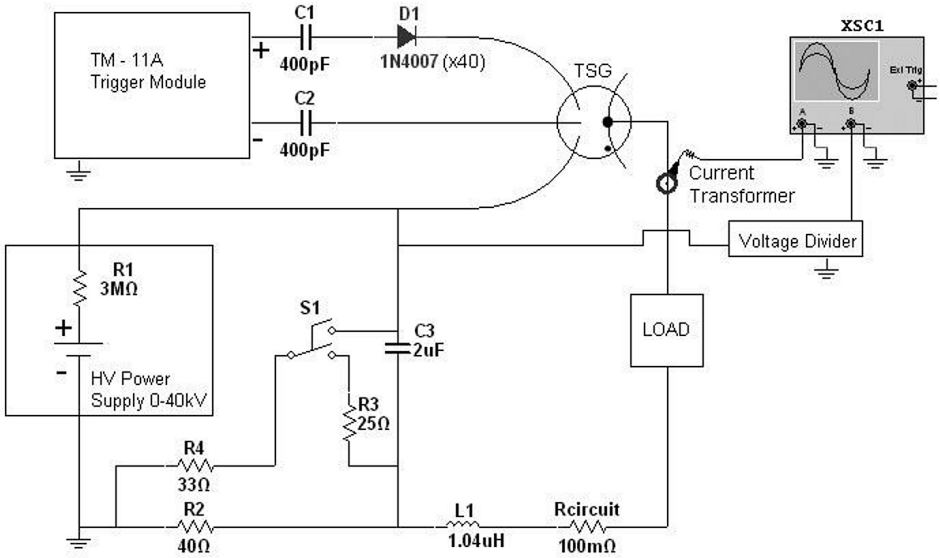

Figure 2.12: An electrical circuit diagram of the HVI system.

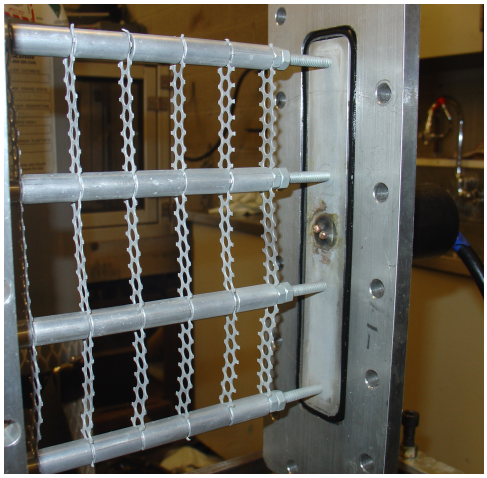

Figure 2.13: A photograph of a wiremesh installed to accelerate the flame in the driver section and cause rapid initiation of a detonation wave.

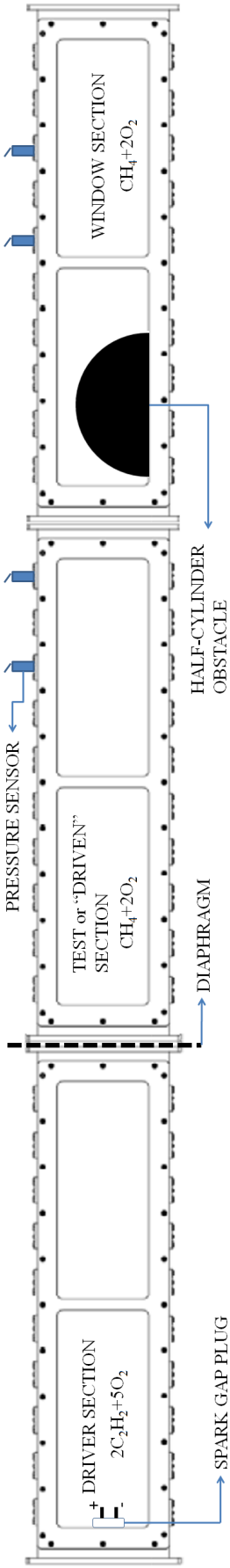

Figure 2.14: A schematic diagram of the shock tube shown with the diaphragm placed between the driver and driven sections.



Figure 2.15: A photograph showing the position of the half-cylinder obstacle in the shock tube for the first series of experiments.

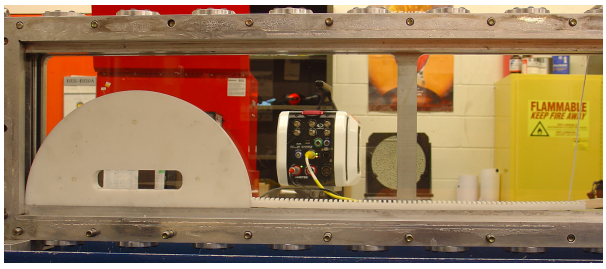

Figure 2.16: A photograph showing the position of the half-cylinder and the roughness plate in the shock tube for the second series of experiments.

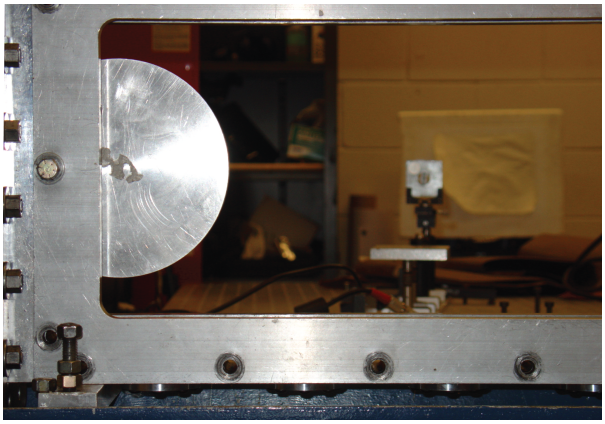

Figure 2.17: A photograph showing the position of the full-cylinder obstacle in the shock tube for the third series of experiments.

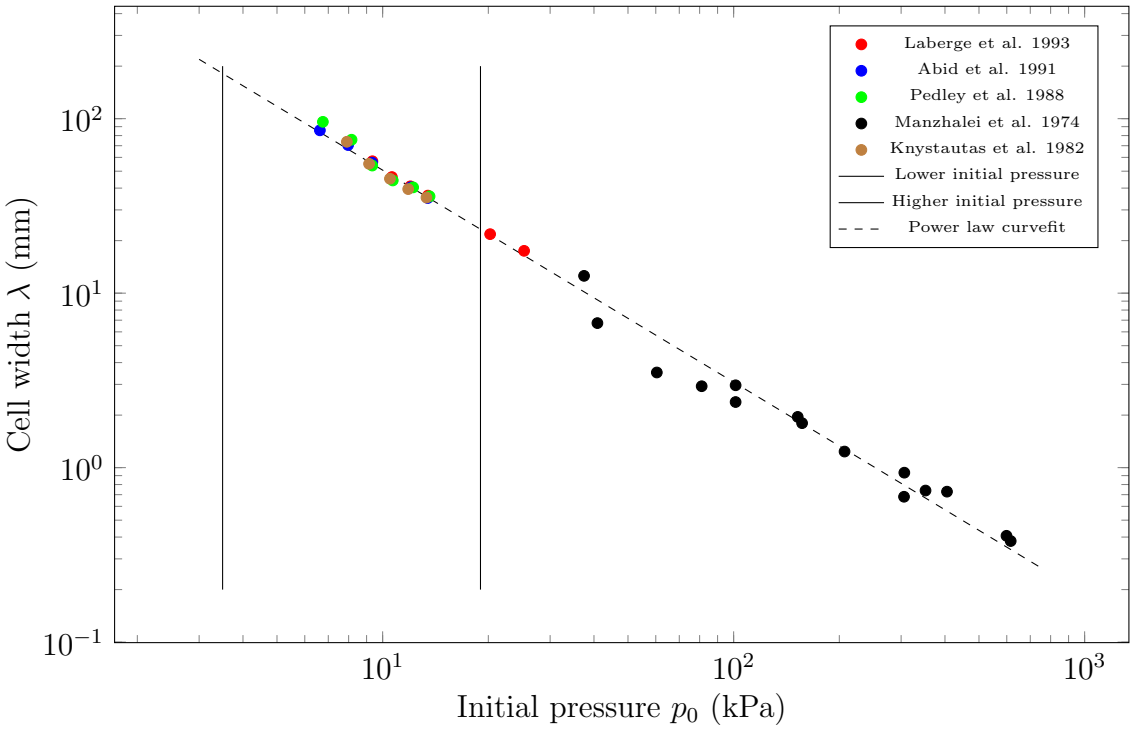

Figure 2.18: Variation of detonation cell width with initial pressure in CH_4+2O_2. The black vertical lines represent the range of initial pressures used for this work while the dashed line is a fitted trendline given by $\lambda = 831.64{p_0}^{-1.215}$. As expected, by increasing the initial pressure of the test mixture, the detonability (sensitivity of the mixture to detonation) increases, which is quantified by a decreasing cell width λ.

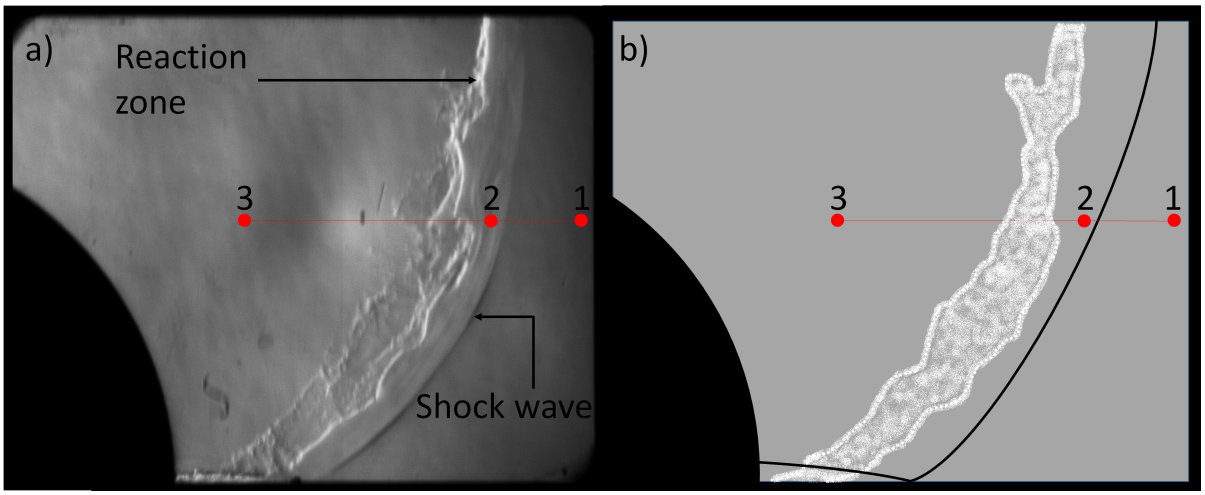

Figure 2.19: Figure a) shows a typical Schlieren image of a quenched detonation wave after it has diffracted behind the half-cylinder obstacle to form a de-coupled shock-flame complex. Figure b) shows a simple schematic diagram of the Schlieren image shown in Fig. a).

Chapter 3

Cellular Detonation Waves

3.1 The detonation cellular structure

As described at the end of Section 1.2, the process that allows a de-coupled shock-flame complex to re-initiate into an overdriven Mach detonation occurs periodically at the start of each cell cycle following a triple point collision; this essentially allows the detonation wave to be self-propagating. While the cellular behaviour of a self-propagating detonation wave has been well documented by past researchers, shown here is a particular example taken from one of our experiments at an initial pressure of $p_0 = 3.5$ kPa. This sequence of Schlieren images clearly illustrates the cellular cycle in the detonation wave.

Figures 3.1 (a) to (d) depict an incident wave propagating towards the right with its strength weakening and the reaction zone de-coupled from the front (a de-coupled shock-flame complex) as the triple points approach each other. Also observed are the shock fronts of the neighbouring (half) cells, which are stronger Mach stems with their respective reaction zones closely coupled to the Mach shock. In Fig. 3.1 (e), the de-coupled shock-flame complex continues to propagate forward with a velocity less than the CJ velocity ($\sim$70% CJ velocity) while the triple points are just about to collide against each other. In Fig. 3.1 (f), immediately following this collision, a Mach reflection with an overdriven detonation wave ($\sim$110% CJ velocity) is observed. Notice that the de-coupled incident wave has now re-initiated into an overdriven Mach detonation wave. Following

this collision, Figs. 3.2 (g) to (l) show the triple points moving away from each other while the overdriven Mach stem starts to expand rapidly. In addition, the shock fronts of its neighbouring (half) cells have transformed from strong Mach stems to weak incidents waves with thicker induction zones.

It is interesting to note from Figs. 3.2 (j) to (l) that the slip lines jet forward to form "hook" like structures that point towards the Mach shock front. The slip lines appear as a dark line moving towards the right because it separates the lighter burned gas behind the Mach shock from the heavier unburned tongue of gas behind the transverse shock. It is also interesting to note that large pockets of unburned gas are formed following the collision, as seen in Figs. 3.2 (g) to (i), which lag behind the detonation wave. These have been observed in the past [3]. In Figs. 3.2 (j) to (l), the trailing unburned gas pockets eventually disappears, potentially due to heat and mass diffusion or due to interaction through vortices [1, 4]. Finally, Figs. 3.1 (e) and 3.2 (l) show the volute-like structures of the Kelvin-Helmholtz (K-H) instability along the slip lines.

3.2 The stochastic behaviour of a cellular detonation wave

While the sequence of images above clearly illustrates the cell cycle process, what was also clear from Figs. 3.1 (e) to (f) was that the length and time scales were too small to discern which mechanism(s) was responsible for causing re-initiation into a detonation. In addition, cellular detonation waves are highly stochastic, unsteady and hence not very reproducible as discussed in Section 1.3.1. To help the reader better visualize this stochastic behaviour of self-propagating detonation waves, consider Figs. 3.3 (a1) to (c1) and Figs. 3.3 (a2) to (c2), which were obtained from two of our experiments using the same initial conditions. Furthermore, both tests were recorded for the same distance from the end of the shock tube. The comparison clearly demonstrates that the cellular structure is considerably different, as there appears to be more cells in the second test, i.e. Figs. 3.3 (a2) to (b2), than in Figs. 3.3 (a1) to (b1) and therefore a direct comparison cannot be made.

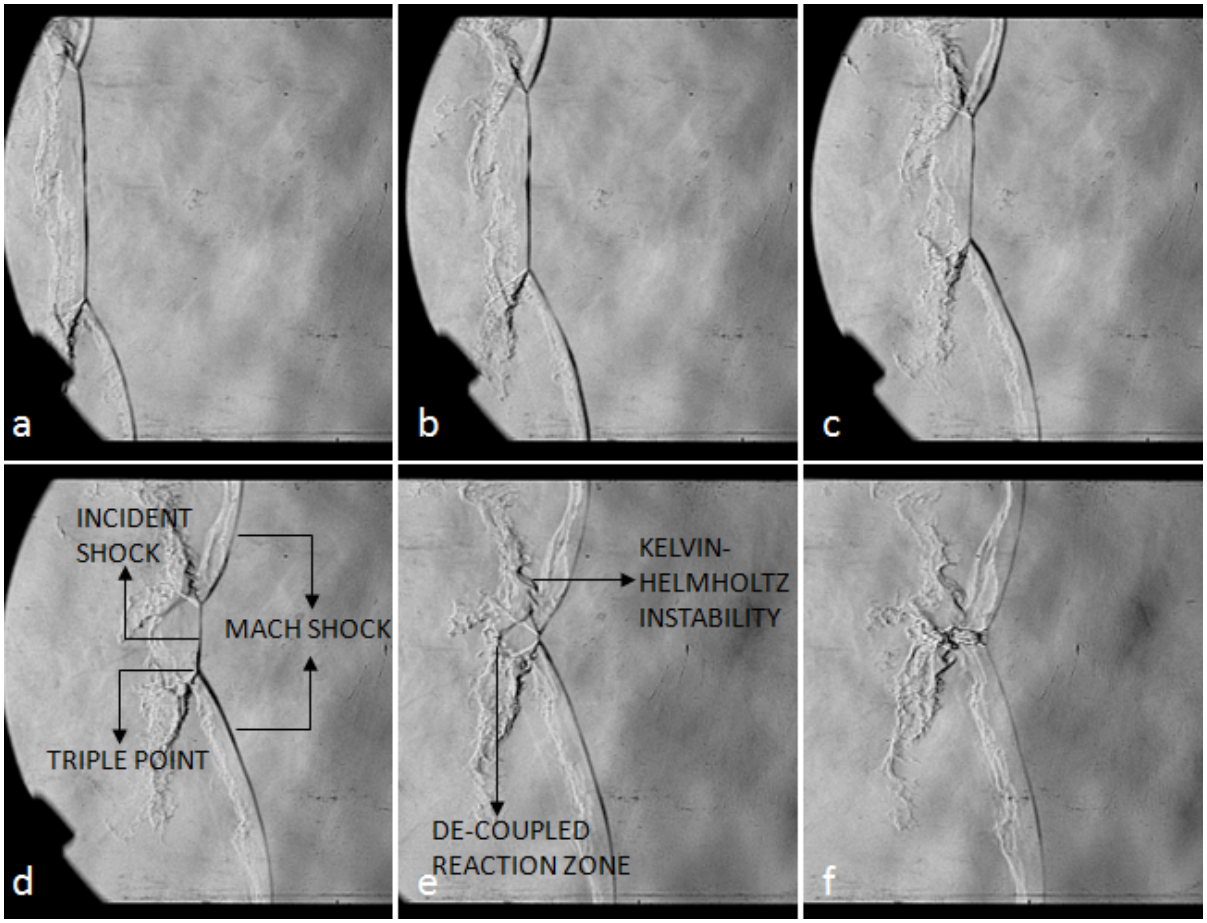

Figure 3.1: Schlieren images of a self-propagating detonation wave in stoichimetric oxy-methane mixture, at an initial pressure and temperature of $p_0 = 3.5$ kPa and $T_0 = 300$K respectively, showing: (a) - (c) a weakening incident wave with the reaction zone de-coupled from it and the two triple points approaching each other. Shown also are the stronger Mach stems, in the adjoining (half) cells, with the reaction zone closely coupled to their respective shock fronts; (d) - (f) the triple points are about to collide and then form an irregular (Mach) reflection immediately after collision while the failed incident wave has re-initiated into an overdriven Mach stem. The channel height is 203.2 mm and the inter-frame delay is 11.53 μsec. *Test ID: CH4+O2-08-24-12(0.5psiTEST1)*

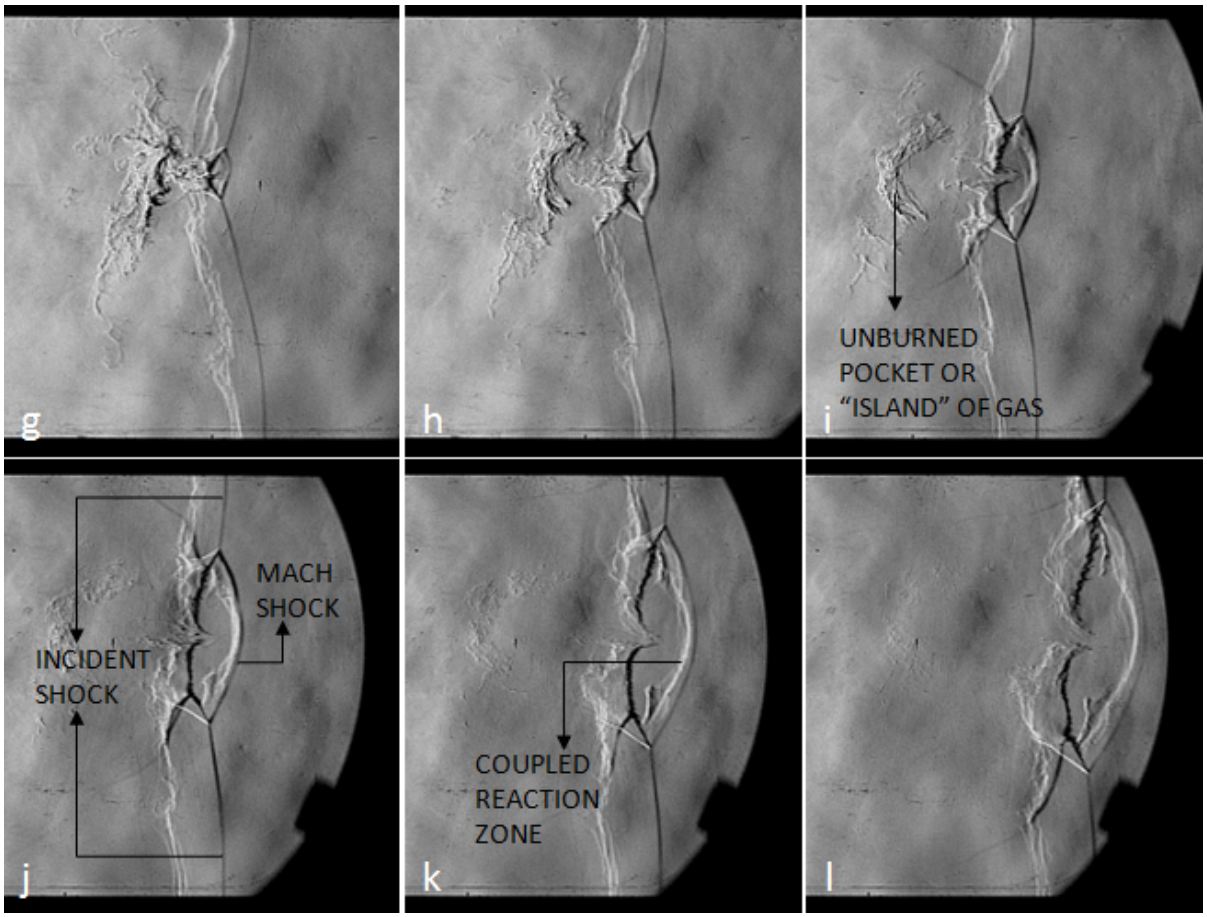

Figure 3.2: A continuation of the evolution of the flow field from Fig. 3.1 now showing: (g) - (i) an overdriven Mach shock with the reaction zone closely coupled to it and the two triple points moving away from each other. Note the neighbouring cells are now weaker incident waves with their reaction zones de-coupled from the front; (j) - (l) the Mach stem rapidly expanding as the triple points move away from each other. The inter-frame delay is 11.53 μsec.

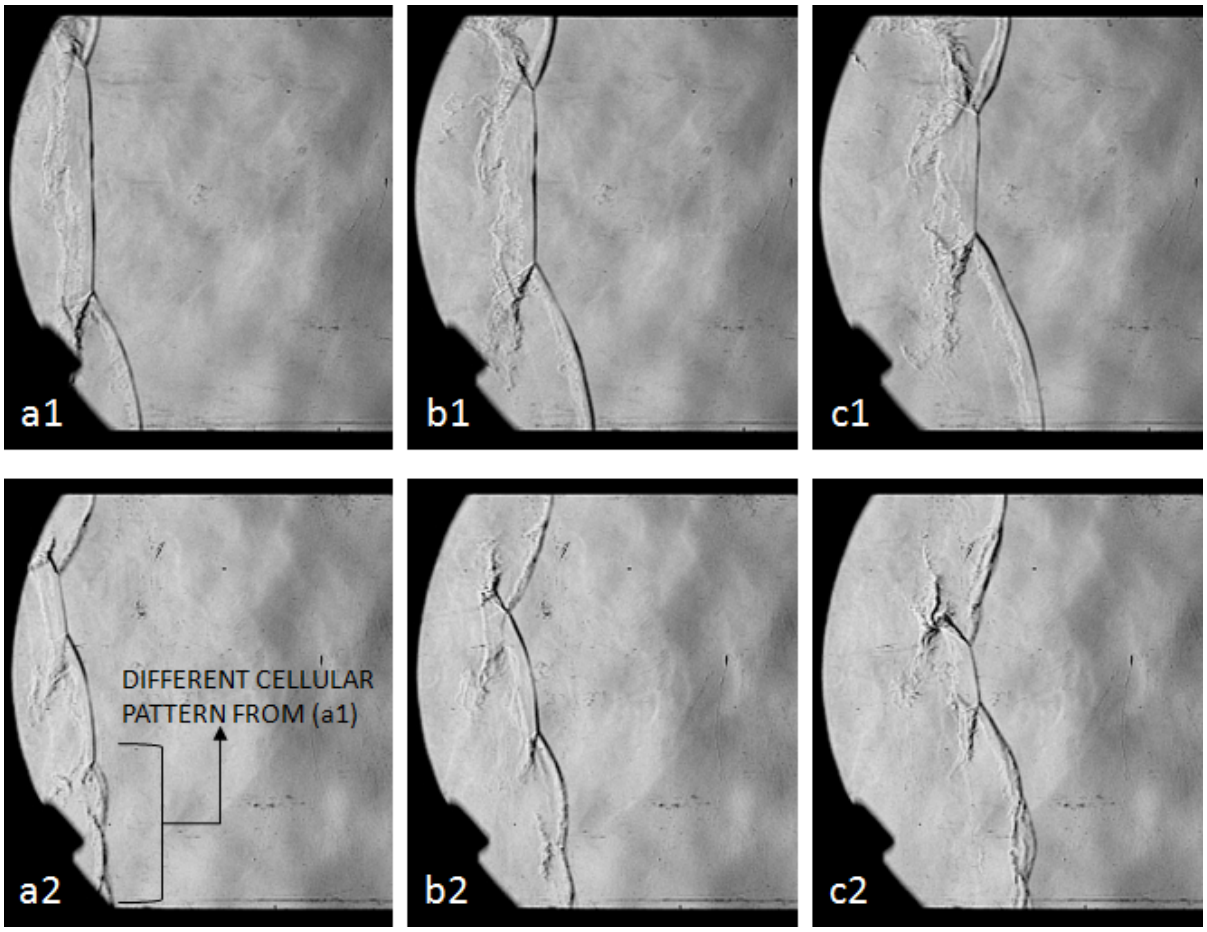

Figure 3.3: Figures (a1)-(c1) were obtained from a test using stoichiometric mixture of methane-oxygen with an initial pressure of 3.5 kPa and an initial temperature of 300K. Figs. (a2)-(c2) was taken from a separate test using the same conditions but shows a very different cellular pattern thus shedding light on the stochasticity of self-propagating cellular detonations waves

Chapter 4

Mach Reflection Process Behind An Obstacle - Results

The experimental results presented here describes the behaviour of a self-sustaining detonation wave with the presence of a cylindrical obstacle, in contrast to Chapter 3. First, the well understood process of detonation diffraction and quenching behind a cylindrical obstacle is briefly discussed. This is then followed by experimental results that describe the behaviour of a de-coupled shock-flame complex following a transient Mach reflection process, which is the focus of this study.

4.1 Detonation diffraction around obstacles

It is very evident from Chapter 3 and from previous studies that self-sustaining detonation waves exhibit a stochastic behaviour and that the length and time scales are very small following the triple point collision. Thus, it is very challenging to distinguish between the mechanisms that contribute to the re-initiation into a detonation. Therefore, as described in Section 1.3.2, the technique of using an obstacle to first quench a detonation wave and subsequently allowing it form a Mach reflection was adopted. To clearly illustrate this diffraction process, consider the Schlieren images shown Fig. 4.1 that was recorded during one of our experiments having an initial pressure of $p_0 = 8.4$ kPa.

Fig. 4.1(a) shows a planar cellular detonation wave approaching the full-cylinder obstacle. In Fig. 4.1 (b) the detonation wave reflects off the upstream face of the full-cylinder obstacle, which sends a leftward moving shock wave, represented as a white line. The detonation wave continues to propagate through a converging area along the surface of the obstacle, on both sides, until it just passes the throat section, which is shown in Fig. 4.1(c). Following this, Fig. 4.1(d) shows the detonation wave now begins to propagate through an expanding area, on either side of the full-cylinder obstacle. As the detonation wave diffracts around the downstream surface of the obstacle, its curvature and velocity decreases. If diffraction is allowed to continue, this may result in a de-coupled shock-flame complex due to weakening of the positive feedback mechanism [20, 21, 22] and this is precisely observed in Figs. 4.1(e) to (f).

The following sections shall now primarily focus on the behaviour of this de-coupled shock-flame complex, following a Mach reflection behind different obstacles (see Section 2.1). The behaviour of this de-coupled shock-flame complex can vary depending on the initial pressure of the gas mixture (see Section 2.9).

4.2 Detonation failure

At sufficiently low initial pressures, the detonation interaction with the half-cylinder resulted in a de-coupled shock-flame complex. A typical example is shown in Fig. 4.2 which shows an evolution of the flow field at an initial pressure of $p_0 = 5.5$ kPa. Note that each image was recorded from separate experiments at different times-of-arrival for the same initial conditions.

Figure 4.2 (a) shows the detonation wave, propagating towards the right, attenuating as the reaction zone separates from the shock front. Figure 4.2 (b) shows a fully de-coupled, or "quenched", detonation wave where the reaction zone has clearly separated from the shock front with a relatively longer distance. We also observe a regular reflection on the bottom wall where the incident and reflected shocks are clearly identifiable. Figure 4.2 (c) shows, at a later time, that the regular reflection has transitioned into an irregular or Mach reflection. Here we can clearly discern the Mach shock, incident wave and transverse wave along with the reflected wave which has refracted at the flame interface.

After some time interval, Fig. 4.2 (d) shows that the triple point has moved up and to the right with the Mach shock expanding. We can now clearly see the forward jetting of the slip line along the bottom wall. Also, the reflected wave travels faster in the burned gas, owing to the higher sound speed, and eventually forms a Mach reflection off the top wall. It should also be pointed out that no noticeable flame corrugation is observed when the reflected wave refracts at the flame interface. In Fig. 4.2 (e), this reflected wave moves further to meet with the original triple point and to form a quasi-steady "quadruple point". This "quadruple point" structure appears to be a confluence of four shock waves and a shear layer - Mach shock, incident wave, transverse wave, the reflected wave and the slip line. However, due to the transient nature of this "quadruple point" no analyses were carried out. Figure 4.2 (e) also clearly shows the K-H instability along the slip line. As the "quadruple point" continues to move upward and to the right, Fig. 4.2 (f) shows that the new triple point, formed due to the collision of the reflected wave with the top wall and progressing downward and right, approaches the "quadruple point". We also continue to observe the volutes of the K-H instability along the slip line as well as the forward jetting of the slip line near the bottom wall. We, thus, see that there is no localized re-ignition immediately behind the Mach shock and thus characterize this behaviour as a "detonation failure".

For all velocity graphs presented in this work, the Y-axis represents the velocity of the shock front. The shock front strength is given in terms of its Mach number (M) by dividing the absolute shock velocity (U_s) with the sound speed (c) in the undisturbed medium predicted by the NASA CEA equilibrium code. The absolute shock velocity (U_s) was measured from the sequential Schlieren images by knowing the inter-frame delay and the distance traveled; the softwares used for velocimetry are mentioned in Section 2.3. The X-axis represents the distance from the center of the obstacle (x), which is non-dimensionalized with respect to the cylinder diameter (D) and is denoted by S.

Figure 4.3 shows a general trend of the incident and Mach shock velocities, measured along the top and bottom walls respectively. Note that the shock speeds shown in Fig. 4.3 were measured between two successive frames for a given experiment, captured by the double framing camera as described in Section 2.3.2. Figure 4.3 clearly shows that both the incident and Mach shock decay with increasing distance from the half-cylinder obstacle, with the Mach shock stronger that the incident wave. Figure 4.3 also shows that when the detonation wave has failed, or quenched, the Mach shock strength is

approximately half of the C-J detonation velocity, which is characteristic of complete shock-flame de-coupling. Indeed streak photographs taken by Radulescu and Lee [37], who experimentally studied the failure mechanisms of a detonation wave over a porous wall, have also observed that a quenched detonation wave propagates at roughly $0.4M_{CJ}$.

A similar sequence of events leading to detonation failure was also observed in the experiments using the full-cylinder (smaller diameter), albeit at lower initial pressures - see Section 4.6 for scaling. Figures 4.4 and 4.5 shows an example of the detonation failure behaviour using the full-cylinder at $p_0 = 3.5$ kPa; only the main frames of interest are shown here while Appendix G shows the remaining frames. Figure 4.4 (a) shows that the front separates into a leading shock, which appears very smooth, and a de-coupled reaction zone. The shock fronts then reflect, along the line of symmetry, to form a regular reflection shown in Fig. 4.4 (b). This regular reflection eventually transitions into an irregular or Mach reflection shown in Fig. 4.4 (c). Figures 4.4 (d) to (f) shows that, owing to the low initial pressure, the sensitivity of the shocked reactants to ignition was not sufficient to cause any re-ignition behind the Mach stem. The Mach shock front expands as the two triple points move away from each other towards the top and bottom walls. Figures 4.5 (g) to (i) shows evidence of the forward jetting of the slip line, the K-H instability and islands of unburned gas can be seen trailing behind.

Figure 4.6 shows the velocity measurements of the shock front, for the experiment shown in Figs. 4.4 and 4.5. The velocity of the Mach shock, measured along the center-line, shows it is decreasing gradually as it diffracts. Similarly, the incident shock waves, along the top and bottom walls, also decreases with increasing distance from the full-cylinder. The error bars shown represent a maximum uncertainty of 21% of the measured shock velocity (see Appendix A).

4.2.1 A comparison of the events following a Mach reflection with and without an obstacle

Here some parallels are drawn by comparing the events following a Mach reflection process between: a) a self-sustaining detonation wave following a triple point collision; b) a de-coupled shock-flame complex formed behind an obstacle. For this consider Figs. 4.5(g) and 3.2(i). Firstly, the familiar triple point configuration, which is a characteristic

feature of the Mach reflection process, is very obvious - the Mach shock, incident wave, transverse wave and the slip line are all attached to the main triple point. Secondly, pockets of unburned gas are observed in both cases that trail behind. Thirdly, the presence of the K-H instability is clearly observed along the body of the slip line and is more prominent in Fig. 3.2(l). Fourth, the forward jetting slip lines are also observed. Finally, the fifth comparison that may be drawn is the refraction of the reflected wave at the flame interface which extends into burned products; this is clearly illustrated between Figs. 4.4(e) and 3.2(i).

For a quantitative comparison consider the strength of the Mach shock. For the self-propagating detonation wave case, the strength of the Mach shock was measured approximately along the centerline between Figs. 3.1 (f) and 3.2 (g). The velocity of the Mach shock, in terms of its Mach number, was measured to be 7.2. For the given initial conditions, the ideal C-J Mach number was predicted to be 6.3 which implies the Mach shock front is clearly overdriven by at least 10%. For the case following a Mach reflection behind an obstacle, the velocity graph in Fig. 4.6 indicates that the strength of the Mach shock front never reaches the ideal C-J velocity. Thus, it is evident that the strength of the Mach shock front is much lower than that measured in a self-propagating detonation wave. This is precisely the reason why the sensitivity of the gas shocked behind the weaker Mach shock is much lower than that found in a self-sustaining detonation wave and hence the reaction occurs after a much longer ignition delay. This permits us to visualize the flow field evolution behind the Mach shock before any hot spot re-ignition occurs.

4.3 Experiments using the half-cylinder and roughness plate

Experiments were also performed at similar conditions as the detonation failure regime by lining the bottom wall with a roughness plate, the details of which can be found in Section 2.1. The plate permitted us to trigger ignition in the plate grooves, and use the burned gas layer near the wall as a Lagrangian marker for the flow field in the failure regime described above.

Figures 4.7 and 4.8 shows an evolution of the flow field when a roughness plate is added with the half-cylinder, for an initial pressure of $p_0 = 7$ kPa. Figures 4.7 (a) to (c) shows that following a Mach reflection of the de-coupled shock-flame complex behind the half-cylinder obstacle, "hot spots", which are localized regions of combustion, are produced inside the grooves of the roughness plate. These hot spots burn and expand the gas behind the foot of the Mach shock as it propagates towards the right. We also observe shocklets generated due to the collision of the Mach shock against the edge of each tooth. Figure 4.7(d) to Fig. 4.8(f) shows that as the hot combusted gas expands, the forward jetting slip line appears to entrain the burned gas into unburned gas and cause mixing. Also seen is a "backward propagating" shock wave and Figs. 4.8(g) to (h) clearly shows this shock propagating into the tongue of unburned gas, behind the inert transverse wave. Also clearly discernible is the corrugation of the tongue of unburned gas, with active hot spot formation, possibly indicating an increase in chemical reaction rates. A more thorough analysis of the forward jet is conducted in Chapter 5.

Figure 4.9 shows the velocity measurement of the incident and Mach shocks for the roughness plate experiment shown in Figs. 4.7 and 4.8. Figure 4.9 shows that the strength of the Mach shock stays relatively constant with an average Mach number of $M_{bw} = 4.5$. This indicates that following jet entrainment and re-ignition behind the Mach shock, the energy release from the coupled flame continues to support the Mach shock as it diffracts, with increasing distance from the half-cylinder. This is in contrast to Fig. 4.3 where there was no energy release to sustain the Mach shock thereby resulting in a steady decline in its strength. However, from Fig. 4.9, the energy release was not sufficient to increase the strength of the Mach shock beyond the C-J detonation velocity. Additionally, the strength of the incident wave is lower than that of the Mach shock and appears to decrease very gradually.

4.4 Hot spot re-ignition behind the Mach stem

For more sensitive mixtures at a higher initial pressure, localized re-ignition hot spots were observed behind the Mach shock. Figures 4.10 and 4.11 shows an example obtained at $p_0 = 10.3$ kPa using the half-cylinder. Figures 4.10 (a) to (c) shows that following a Mach reflection of a de-coupled shock-flame complex, the triple point travels right and

up while the Mach shock propagates towards the right with an expanding curved front. Figures 4.10 (d) to (e) show that re-ignition just occurs near the foot of the Mach stem, close to the slip line, and appears to be entrained behind the Mach shock. Figure 4.10 (f) shows corrugation of the gas behind the Mach shock, following localized re-ignition. Figures 4.11 (g) to (i) shows that following localized re-ignition, the flame couples behind the Mach shock. Trailing pockets of unburned gas are also observed along the bottom wall. Figures 4.11 (g) to (i) also shows, along the slip line, the volutes of the K-H instability separating the burned gas, behind the reactive Mach stem, and the unburned gas, behind the non-reactive transverse wave.

Figure 4.12 shows the velocity of the shock front measured from the localized re-ignition experiment, using the half-cylinder, shown in Figs. 4.10 and 4.11. Figure 4.12 shows that the strength of the de-coupled incident shock, from the reaction zone, weakens very gradually with increasing distance from the half-cylinder obstacle. Localized combustion was observed behind the foot of the Mach shock, as shown in Figs. 4.10(d) to (e), and the energy release appears to have lead to an increase in strength of the Mach shock along the bottom wall. This is indicated by the sudden increase in velocity to $M_{bw} \approx 6$ at $S \approx 1.5$ - 1.6. The increase in strength, however, was not sufficient to overdrive the strength the Mach shock beyond the ideal C-J detonation velocity. Finally, similar trends were observed in the numerical simulations performed by Lau-Chapdelaine [38], using a one-step chemistry model at $p_0 = 10.3$ kPa.

Figure 4.13 illustrates two sequential images obtained using the double frame camera, that were recorded from another experiment having the same initial pressure of $p_0 = 10.5$ kPa. Figures 4.13 (a) to (b) now clearly illustrates the corrugation of the tongue of unburned gas with rapid growth of hot spot activity. An example of a growing hot spot can be seen, in Fig. 4.13 (a), near the main triple point where, after a 11 μsec delay, in Fig. 4.13 (b) the hot spot grows to consume the unburned shocked gas around it. Qualitatively, Fig. 4.13 (a) also clearly shows how the volutes of the K-H instability, along the slip line, can entrain burned gas into unburned gas and potentially increase combustion rates. This is evident in Fig. 4.13 (b) where we observe rapid thinning of the vortex. These images look very similar to the photographs taken by Radulescu et al. [9].

Figure 4.14 shows another example of hot spot re-ignition behaviour behind the Mach

stem. Re-ignition is indicated by: a) the presence of the reaction zone structure immediately behind the Mach shock; b) the sharp density gradients along the slip line, indicative of a burned-unburned gas interface. In this example, however, the camera resolution was not sufficient to resolve the cause of re-ignition. Figure 4.14 (a) shows that a Mach reflection has just formed on the bottom wall following an irregular reflection of a quenched detonation wave behind the half-cylinder obstacle. Figure 4.14 (b) shows the newly formed triple point evolving in time and we can clearly discern the three shock waves that confluence at the triple point. Figure 4.14 (c) now clearly shows that the Mach shock has re-ignited to form a reactive wave with the flame coupled to the shock front; due to the chosen sampling rate, no frames were captured between Figs. 4.14(b) to (c). Finally in Fig. 4.14 (d), we see the the reactive Mach shock traveling towards the right, along the bottom wall, and expands while a tongue of unburned gas trails behind the non-reactive transverse wave.

Figure 4.15 shows the velocity profile for the half-cylinder spontaneous re-ignition experiment, shown in Fig. 4.14. Here we find that the velocity of the Mach shock, as measured along the bottom wall, remains relatively constant, close to the predicted C-J detonation Mach number. This suggests that the Mach shock may have re-ignited even before entering the field of view because it has a velocity of $M_{bw} \approx 6$, which is comparable to the velocity profile described in Fig. 4.12.

Some degree of stochasticity was encountered such that hot spot re-ignition was also observed at higher initial pressures of $p_0 \approx 12$ kPa. To illustrate this, the experiment shown in Figs. 4.16 and 4.17 is one example that shows Mach stem re-ignition, which does not proceed to re-initiation into a detonation at these higher initial pressures. Figure 4.16 (a) shows Mach reflection has just formed following the reflection of a de-coupled shock-flame complex. Figures 4.16 (b) to (c) shows the triple point moving up and to the right with the Mach shock, incident wave and transverse wave clearly visible. We also see the reflected wave refracting at the flame interface. As the Mach shock expands and propagates towards the right with the triple point evolving in time, Figs. 4.16 (d) to 4.17 (g) now clearly shows localized re-ignition has occurred along the bottom wall behind the foot of the Mach shock, where localized coupling between the flame and the shock front takes place. In Fig. 4.17 (h) we begin to see that the forward jetting slip line appears to entrain the flame. Figure 4.17 (i) now clearly shows the flame being entrained by the forward jetting of the slip line behind the Mach stem. We can observe a "kink" along

the Mach shock, which maybe indicative of initiation of the bifurcation process. Finally at later times, we observe in Fig. 4.17 (j) a shock wave that propagates backwards into the tongue of unburned gas behind the non-reactive transverse wave. Behind this shock wave, we can also clearly observe corrugation in this unburned gas region caused due to hot spot formation, which qualitatively suggests an increase in chemical reaction rates. Figures 4.17 (k) to (l) shows a development of the corrugated unburned gas, particularly closer to the bottom wall.

The velocimetry for Figs. 4.16 and 4.17 is shown in Fig. 4.18. Re-ignition behind the Mach shock, along the bottom wall, may have occurred between Figs. 4.16(c) to (d) as suggested by an increase in velocity to $M_{bw} = 5.4$ at $S \approx 1.5$. Following re-ignition the Mach shock, supported by the energy release from the coupled flame, propagates without much loss in strength but does not exceed the ideal C-J detonation velocity.

Using the double frame camera, it was challenging to obtain high resolution images that showed the sequence of events leading up to localized hot spot re-ignition (or re-initiation into a detonation) behind the Mach shock. Figure 4.19 shows two images recorded from separate experiments at $p_0 = 10.4$ kPa, which were recorded just prior to full re-ignition of the Mach stem. Note that Figs. 4.19 (a) to (b) were not observed very reproducibly. Fig. 4.19(a) shows localized combustion along the bottom wall behind the Mach shock and the flame appears to couple near the foot of the Mach shock. We also observe the slip line curved forward. Fig 4.19(b) now appears to show that hot burned products are entrained behind the Mach shock in the vicinity of the forward jetting slip line. Also, clearly visible from both frames are the compression waves present between the propagating flame and the incident shock wave.

The hot spot re-ignition tests conducted with the smaller full-cylinder showed a very similar sequence of events. Figures 4.20 and 4.21 shows one example of localized re-ignition behind the Mach shock for an initial pressure of $p_0 = 8.4$ kPa. Figures 4.20(a) to (c) shows that following diffraction and quenching behind the full-cylinder obstacle, a de-coupled shock-flame complex is formed, which reflects to eventually form a Mach reflection. Figures 4.20 (d) to 4.21 (g) shows that the Mach shock expands as the two triple points move away from each other and towards the top and bottom walls of the channel. During this Mach shock expansion, we observe the flame front of the receding reaction zone approaching the Mach shock front along the line of symmetry, where the

two forward jetting slip lines meet. From Figs. 4.21(h) to (i) a kernel of reacted gas is evident immediately behind the Mach shock. A system of shocks is clearly evident as originating from the explosion of this kernel. While a backwards facing shock interacts with the tongue of unburned gas, localized bifurcations are also evident on the leading Mach shock; a higher resolution image of a strong Mach stem bifurcation is shown in Fig. G.48(c) recorded behind the half-cylinder obstacle.

Figure 4.22 shows the measured velocity of the Mach and incident shocks obtained from the localized re-ignition experiment, using the full-cylinder, shown in Figs. 4.20 and 4.21. From the velocity profile, it is clear that the strength of the Mach shock remains approximately constant due to the energy release behind it to compensate for the diffraction process. However, this is not the case for the incident shock strength measured along the top and bottom walls as there was no hot spot re-ignition in its vicinity.

For a clearer visualization, the resolution was reduced and frame rate was increased to focus on the events that take place along the line of symmetry local to the region where the slip lines meet, which is illustrated in Figs. 4.23 and 4.24. Figures 4.23 (a) to (b) shows the formation of a Mach reflection of a de-coupled shock-flame complex following detonation quenching behind the full-cylinder obstacle. The two triple points formed travel in opposite directions while the Mach shock expands as it progresses towards the right. Figures 4.23 (c) to (d) shows the shocked region between the Mach shock front and the slip lines having noticeable density gradients, particularly along the line of symmetry. Figures 4.24 (e) to (f) shows the flame propagating along the line of symmetry, where the two forward jetting slip lines meet, and "jets" into the shocked region behind the Mach shock; this is very similar to what was observed in Figs. 4.20(e) to 4.21(g). Figures 4.24 (g) to (h) shows the flame continues to propagate forward until it couples with the Mach shock front.

Figure 4.25 shows the Mach shock strength, measured approximately along the centerline, for the experiment shown in Figs. 4.23 and 4.24. Similar to the Mach shock velocity profile in Fig. 4.22, the Mach shock velocity in this Fig. 4.25 does not show any noticeable increase in strength. Again, the strength of the Mach shock stays below the ideal C-J detonation $M_{CJ} = 6.4$.

Another example of hot spot re-ignition behind the Mach shock is illustrated in

Fig. 4.26 at $p_0 = 10.5$. As a reminder, re-ignition is indicated by: a) the presence of the reaction zone structure immediately behind the Mach shock; b) the large density gradients along the slip line, indicative of a burned-unburned gas interface. Similar to Fig. 4.14, however, the camera resolution was not sufficient to resolve the cause of re-ignition. In Figs. 4.26 (a) to (b), we observe a Mach reflection of a quenched detonation wave, following which in Fig. 4.26 (c) shows a spontaneous ignition event that takes place near the Mach shock front, which results in a fully coupled shock - flame wave as seen in Fig. 4.26 (d). Due to the sampling rate selected, no frames were captured between Fig. 4.26(b) to (c) while the low resolution could not resolve the event behind the Mach shock. Figures 4.26 (e) to (f) shows that this reactive Mach shock continues to expand and travel towards the right as the two triple points shown propagate away from each other.

Figure 4.27 shows the velocity profile of the shock front for the experiment shown in Fig. 4.26. The centerline velocity, which approximately represents the Mach shock strength, is shown in Fig. 4.27 and it appears that the strength continues to increase until we observe re-ignition between Figs. 4.26(c) to (d), which is supported by the increase in velocity to $M_{cl} = 5.5$ at $S \approx 1.5$. The re-ignited Mach shock strength eventually decreases due to diffraction as it expands, similar to what is observed in the cell cycle process in a self-propagating detonation wave.

4.5 Re-initiation into a detonation along the Mach shock and transverse shock

At still higher pressures than that described above, both the transverse and Mach waves became self-supported detonation waves. Figures 4.28 and 4.29 are an example that illustrates re-initiation into a detonation, using the half-cylinder obstacle, for $p_0 = 12.3$ kPa. Figure 4.28 (a) shows that after the detonation quenches behind the half-cylinder obstacle, the de-coupled shock-flame complex reflects to just form a Mach reflection. Figures 4.28 (b) to (c) show the characteristic physical features of the Mach reflection which grows, as time evolves, and the triple point moves towards the right and up. In Figure 4.28 (d) we can see the forward wall jet effect of the slip line behind the Mach stem. In Fig. 4.28 (e) re-ignition behind the Mach stem, near its foot, is clearly observed.

Figure 4.28 (f) now shows localized combustion, following re-ignition, along with a re-initiated detonation wave formed at the foot of the Mach stem. This qualitatively appears to be a re-initiation into a detonation because of the very fine cellular structure. Figure 4.29 (g) now shows that following re-initiation into a detonation along the entire body of the Mach stem, a highly exothermic chemical reaction takes places close the triple point, characterized by the intense luminosity. Following this rapid chemical energy release Fig. 4.29 (h) now shows other areas of the tongue of unburned gas around the transverse wave ignites violently, again illustrated by the bright regions. This rapid ignition of the tongue of unburned gas near the transverse wave is what leads to the re-initiation into a transverse detonation wave as seen in Figs. 4.29 (h) to (i). Following this very violent re-ignition of this tongue of unburned gas, Figs. 4.29 (h) to (i) show a strong shock wave that propagates in all direction.

Figure 4.30 shows the velocity measurements of the incident and Mach shock, as well as the triple point phase velocity, obtained from the re-initiation into a detonation experiment shown in Figs. 4.28 and 4.29 with the half-cylinder. Between Figs. 4.28(d) to (e) re-ignition may have occurred behind the Mach shock at its foot and this is indicated in Fig. 4.30 by an increase in velocity to $M_{bw} = 6$ at $S \approx 1.6$. This is immediately followed by re-initiation into a detonation, as seen in Figs. 4.28(e) to (f) and quantitatively supported by another the increase in velocity to $M_{bw} = 7$ at $S \approx 1.7$. For the given initial conditions, the C-J Mach number was found to be $M_{CJ} = 6.44$ and the re-initiated Mach shock was estimated to be overdriven at 109%C-J. One can approximate the transverse detonation velocity by measuring the triple point phase velocity. The triple point phase velocity measured between Figs. 4.29 (h) to (i) was estimated to be $M_{tr} = 4.6$ at $S \approx 2.0$. For the state behind the incident wave, the calculated C-J Mach number was $M_{CJ} = 4.1$. This implies the transverse detonation wave was also overdriven.

Figure 4.31 shows high resolution pictures of re-initiation into a detonation, which were captured for $p_0 = 10.4$ kPa. Figures 4.31 (a) to (b) were taken from different experiments for the same initial pressure; note that the sequence of events illustrated in Fig. 4.31 were not observed very reproducibly. Figure 4.31 (a) shows that after re-initiation into a detonation takes place along the Mach shock, a backward propagating shock wave is observed. From a qualitative perspective, the detonation wave that re-initiates on the Mach stem has a cellular structure and very thin induction zone. Furthermore, we also

observe that the transverse wave is inert with a thick tongue of unburned gas behind it. This configuration of an inert transverse wave and a re-initiated Mach shock was also observed in numerical simulations by Radulescu et al. [9], Lau-Chapdelaine [38] and Kessler et al. [39]. Figure 4.31(b) shows spontaneous ignition of the tongue of unburned gas near the transverse wave, due to rapid combustion after the Mach shock had re-initiated, leading to re-initiation into a detonation along the transverse wave and a shock wave propagating away from the explosion site.

Very high resolution images, obtained from the double frame camera, showing full re-initiation into a detonation along the Mach stem and transverse wave are shown in Fig. 4.32. The structures of the detonation waves formed along the Mach stem and transverse waves are clearly seen. Figures 4.32 (a) to (b), clearly shows the Mach stem and transverse wave have re-initiated because of the: distinct "whisker" pattern trailing behind both waves; new triple points formation; no tongue of unburned gases behind the Mach and transverse front. Also noticeable is the marked difference in appearance between the Mach stem and the incident shock front (along top wall), which clearly appears to be de-coupled from its reaction zone. The transverse wave has also re-initiated into a detonation wave, or "super detonation wave", propagating into the shocked unburned gases trapped between the incident shock front and the trailing reaction zone. Upon careful observation in the vicinity of the triple point, the re-initiated transverse wave appears to be separated from the detonation Mach stem and incident shock wave. This triple point configuration was seen numerically by Kessler et al. [39] and Gamezo et al. [40].

A certain degree of stochasticity was observed such that re-initiation into a detonation was also observed at relatively lower initial pressures i.e. $p_0 \approx 10$ kPa. This is illustrated in Fig. 4.33, where we observe full re-initiation into a detonation behind the Mach shock and transverse wave for an initial pressure of $p_0 = 10.5$ kPa. Figure 4.33 (a) shows rapid combustion behind the Mach shock, which appears to transition into a re-initiated detonation wave at the foot of the Mach shock in Fig. 4.33 (b). Also noteworthy is what appears to be a backward propagating shock wave observed in Fig. 4.33 (b). Following this, Fig. 4.33 (c) shows intense chemical luminosity in the tongue of unburned gas near the non-reactive transverse wave. This is indicative of rapid combustion rates, which eventually lead to the transverse wave being re-initiated, as shown in Fig. 4.33 (d). In Figs. 4.33 (e) to (f), the re-initiated Mach and transverse wave propagate rightwards

and up respectively.

Figure 4.34 shows the velocity measured from experiment shown in Fig. 4.33. Re-initiation into a detonation at the foot of the Mach shock was first noted in Fig. 4.33(b) and this is quantified by the increase in velocity to roughly $M_{bw} = 7.5$ at $S \approx 1.4$ - 1.5. For the given initial conditions, the theoretical C-J detonation velocity is $M_{CJ} = 6.4$ which implies that the re-initiated Mach shock is overdriven by approximately 17%. The strength of the transverse wave can be approximated by determining the phase velocity of the triple point. For the propagating transverse detonation wave observed in Fig. 4.33, the triple point phase velocity was measured to be $M_{tr} = 5.2$ at $S \approx 1.9$. The measured speed was then compared to the ideal C-J detonation velocity in the state behind the incident shock, which was calculated to be $M_{CJ} = 4.4$. This indicates that the transverse detonation wave was also overdriven.

Similar sequence of events of prompt initiation into a detonation were also observed in the full-cylinder tests. Figures 4.35 and 4.36 shows the re-initiation into a detonation using a full-cylinder obstacle for an initial pressure of $p_0 = 16.8$ kPa. Figures 4.35 (a) to (c) shows that following diffraction around a full-cylinder obstacle, the detonation wave partially quenches as this is evident with the presence of a triple point and a locally coupled flame to the incident shock front running along the bottom wall of the shock tube. Figures 4.35 (d) to (f) shows that immediately after a Mach reflection, the Mach stem and transverse waves have re-initiated into a detonation. This is evident from the fine cellular structure of the Mach shock front and the intense chemical luminous regions near the transverse waves. These re-initiated transverse waves propagate through the shocked unburned gas behind the incident waves thus forming super detonations. Figures 4.36 (g) to (i) shows that the re-initiated Mach stem expands and weakens such that the fine cellular structure is now coarser. The re-initiated transverse waves propagate away from each other until they collide against the top and bottom walls. After this collision, two non-reactive shock waves travel towards each other, in the burned gas region, and transversely with respect to the detonation front.

Figure 4.37 shows the velocity measurements of the incident and Mach shock, as well as the triple point phase velocity, obtained from the experiment shown in Figs. 4.35 and 4.36 with the full-cylinder. The re-initiation into a detonation is clearly indicated by the sudden jump in velocity to $M_{cl} = 6.8$ at $S \approx 1.3$. The re-initiated Mach shock was

estimated to be overdriven with a strength of 105%C-J for a C-J velocity of $M_{CJ} = 6.44$. Following re-initiation into a detonation of the Mach shock, the graph shows that the wavefront velocity along the centerline (approximately) continues to stay overdriven as the re-initiated Mach shock diffracts while moving rightwards. For the lower transverse wave, re-initiation into a detonation was observed simultaneously with the Mach shock. This is indicated by the increase in the triple point phase velocity to $M_{trans} = 4$. For a C-J Mach number of $M_{CJ} = 4.3$ in the state behind the incident shock, the re-initiated lower transverse wave is approximately 92%C-J, which suggests it is a detonation wave.

Figures 4.38 and 4.39 shows an unusual case where one of the transverse wave had re-initiated while the other transverse wave remained inert. Figures 4.38 (a) to (c) shows a Mach reflection of a quenched detonation wave, following which Fig. 4.38 (d) to Fig. 4.39 (e) shows a spontaneous event that takes place behind the Mach shock, which results in a fully coupled shock - flame reaction wave as seen in Fig. 4.39 (f). Figure 4.39 (g) shows that re-initiation into a detonation of the Mach stem and a transverse wave occurs after a violent explosion takes place behind the transverse wave that is attached to the lower triple point. The transverse wave on the opposite triple point remains non-reactive. Figure 4.39(h) shows that after re-initiation into a detonation of one transverse wave and the Mach shock occurs, the Mach detonation continues to propagate towards the right and expand while the re-initiated transverse wave and non-reactive transverse wave propagate away from each other towards the bottom and top wall respectively.

4.6 Summary

Figure 4.40 summarizes the different detonation regimes observed for the range of initial pressures used in this study, for both the half-cylinder ($d_{HC} = 51$ mm) and full-cylinder ($d_{FC} = 25.5$ mm) obstacles. To determine the gap size to cell width ratio (d/λ), the cell width predicted by the power law curve fit is used (see Fig. 2.18).

From Fig. 4.40, the **detonation failure** regime (e.g., Fig. 4.2) was observed when $p_0 \approx 6$ kPa and 3 kPa for the half and full cylinders respectively. Using the power law curve fit, this implies a cell width of roughly $\lambda \approx 95$ mm and 220 mm respectively or a gap size to cell width ratio of $(d_{HC}/\lambda)_{fail} \approx 0.5$ and $(d_{FC}/\lambda)_{fail} \approx 0.1$, respectively.

Since few experiments were performed between $p_0 \approx 6$ - 10 kPa, Fig. 4.40 shows no clear transition from failure to **hot spot re-ignition** (e.g., Fig. 4.10). Furthermore, due to the stochastic behaviour noted earlier around $p_0 \approx 10$ kPa, Fig. 4.40 shows overlapping of all three regimes; this is especially true for the half-cylinder due to the higher volume of experiments performed. Therefore, the hot spot re-ignition regime was moderately observed for $p_0 \approx 10$ kPa. This implies $\lambda \approx 51$ mm or $(d_{HC}/\lambda)_{reig} \approx 1.0$ and $(d_{FC}/\lambda)_{reig} \approx 0.5$.

From Fig. 4.40, the **detonation re-initiation** regime (e.g., Fig. 4.28) was observed when $p_0 \approx 12$ kPa (half-cylinder) and $p_0 \approx 16$ kPa (full-cylinder) with a cell width of $\lambda \approx 41$ and 29 mm respectively. Therefore, detonation re-initiation was observed when $(d_{HC}/\lambda)_{rein} \approx 1.2$ and $(d_{FC}/\lambda)_{rein} \approx 0.9$. This suggests that by keeping the $(d/\lambda)_{rein} \approx$ constant, both the gap size (d) and cell width (λ) have to be scaled appropriately in order to observe the same detonation re-initiation behaviour. Radulescu and Maxwell [27] studied detonation attenuation through a porous bed media using an equimolar mixture of oxy-acetylene. They found, from their experiments, detonation re-initiation to occur for a gap size to cell width ratio between 1.3 to 2.5. The lower end of their range appears to compare well with the findings here.

Figure 4.41 and Fig. 4.42 illustrates the propensity for observing a particular regime when (d/λ) is varied, for both obstacles. It was mentioned earlier that to observe the re-initiation phenomenon, both the gap size and cell width have to be scaled appropriately when using obstacles of different diameters. This is further shown when comparing Fig. 4.41 and Fig. 4.42. Thus, under different operating conditions if the gap size is fixed, the $(d/\lambda) \approx 1.0$ ratio may be used as a guideline to vary the initial pressure (and hence cell width) when investigating the re-initiation regime. But it should be remembered that this ratio is conservative at best due to - a) stochasticity, and b) fewer experiments performed using the full-cylinder obstacle (about one-fifth of the half-cylinder).

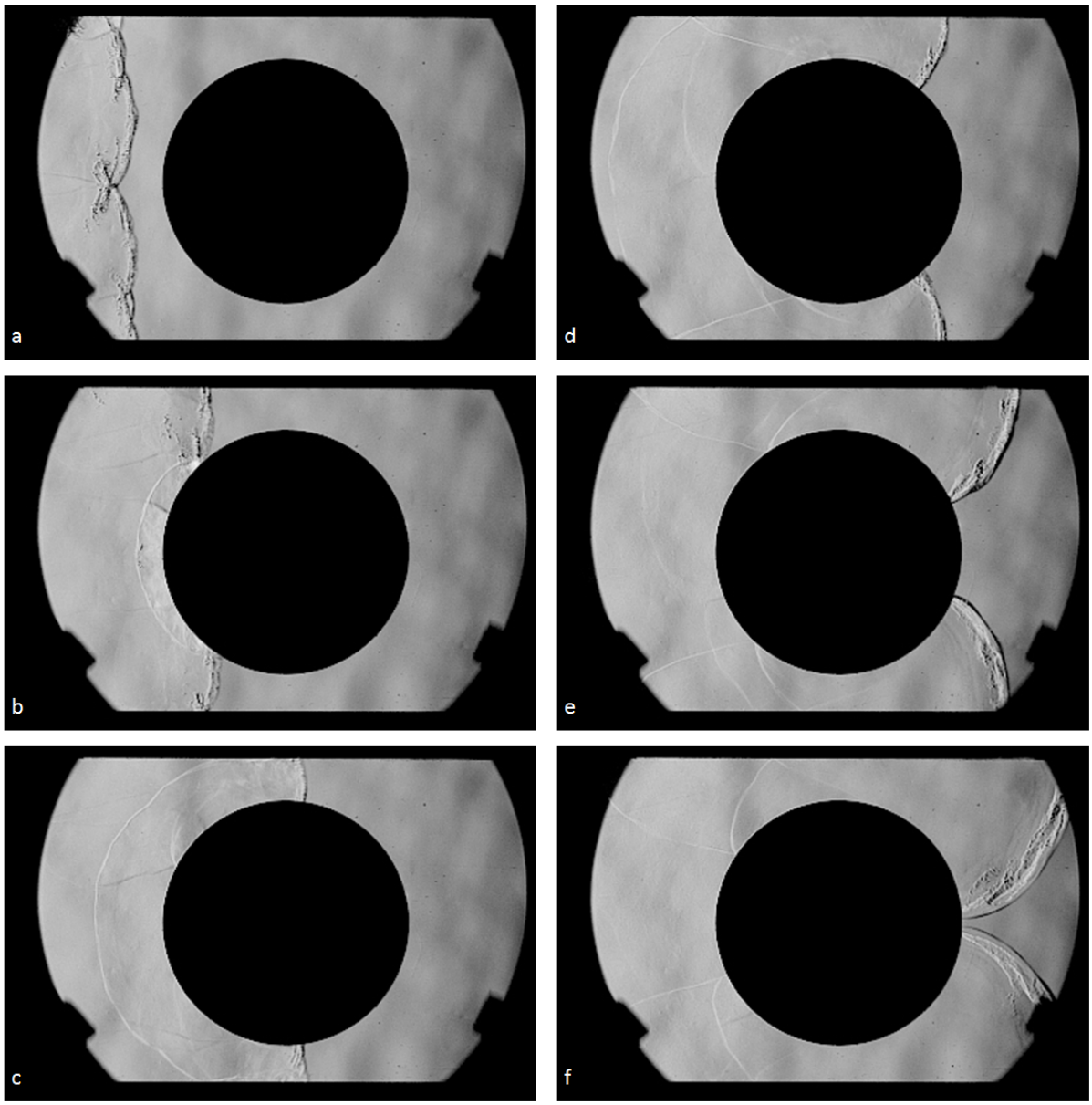

Figure 4.1: A sequence of Schlieren images of a self-propagating cellular detonation in stoichiometric methane-oxygen mixture, at an initial pressure and temperature of 8.4 kPa and 300K, respectively, showing how it diffracts around a 152.4 mm diameter full-cylinder obstacle to form a de-coupled shock-flame complex devoid any triple point structure across its front. Also observed are shock structures (white lines) that reflect off the full-cylinder and the confining wall and propagate back. The channel height is 203.2 mm with an inter-frame delay of 23.06 μsec. *Test ID: CH4+O2-08-22-12(1.2psiTEST3)*

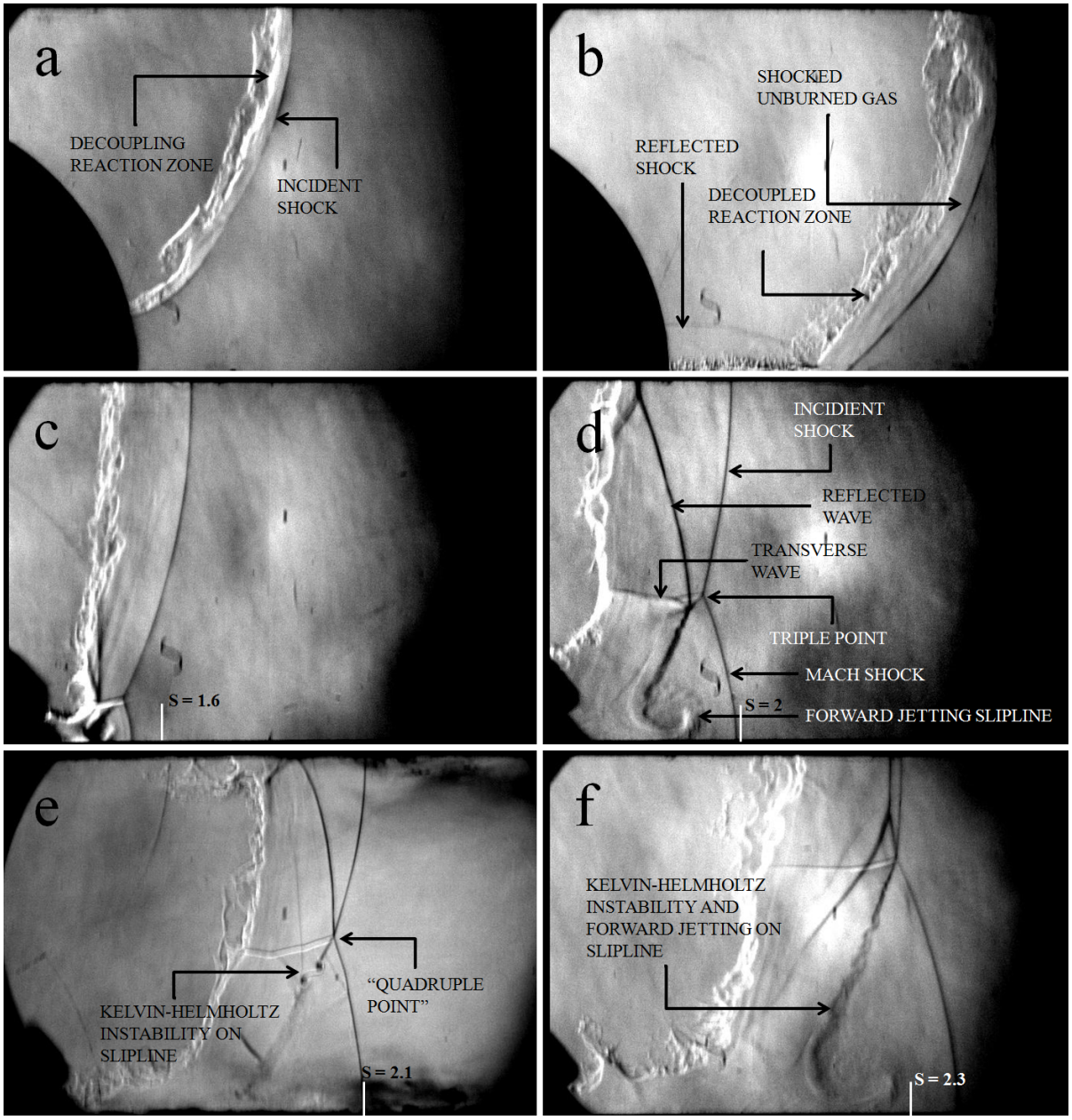

Figure 4.2: Schlieren images showing the evolution of a flow field of inert shock reflections of a quenched detonation wave behind the half-cylinder obstacle. The initial pressure and temperature was 5.5 kPa and 300K. Each image represents a different experiment at the same initial conditions using the dual-frame camera. *(a)Test ID: CH4+O2 - 08-4-11(0.85psi)6; (b)Test ID: CH4+O2 - 08-12-11(0.85psi)1; (c)Test ID: CH4+O2 - 08-28-11(0.85psi)3; (d)Test ID: CH4+O2 - 07-31-11(0.85psi)1; (e)Test ID: CH4+O2 - 01-15-11(0.8psi)1a; (f)Test ID: CH4+O2 - 07-31-11(0.85psi)3*

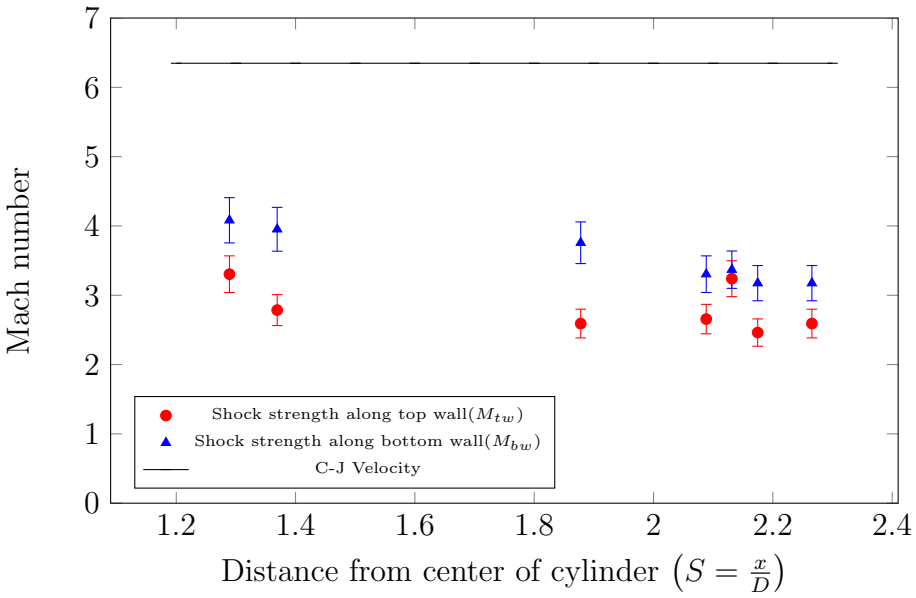

Figure 4.3: General velocity trend of the incident and Mach shock for the detonation failure case with the half-cylinder; the solid line shows the CEA calculated C-J Velocity for $p_0 = 5.5$ kPa, $T_0 = 300$K. Note that each data point was obtained from different experiments.

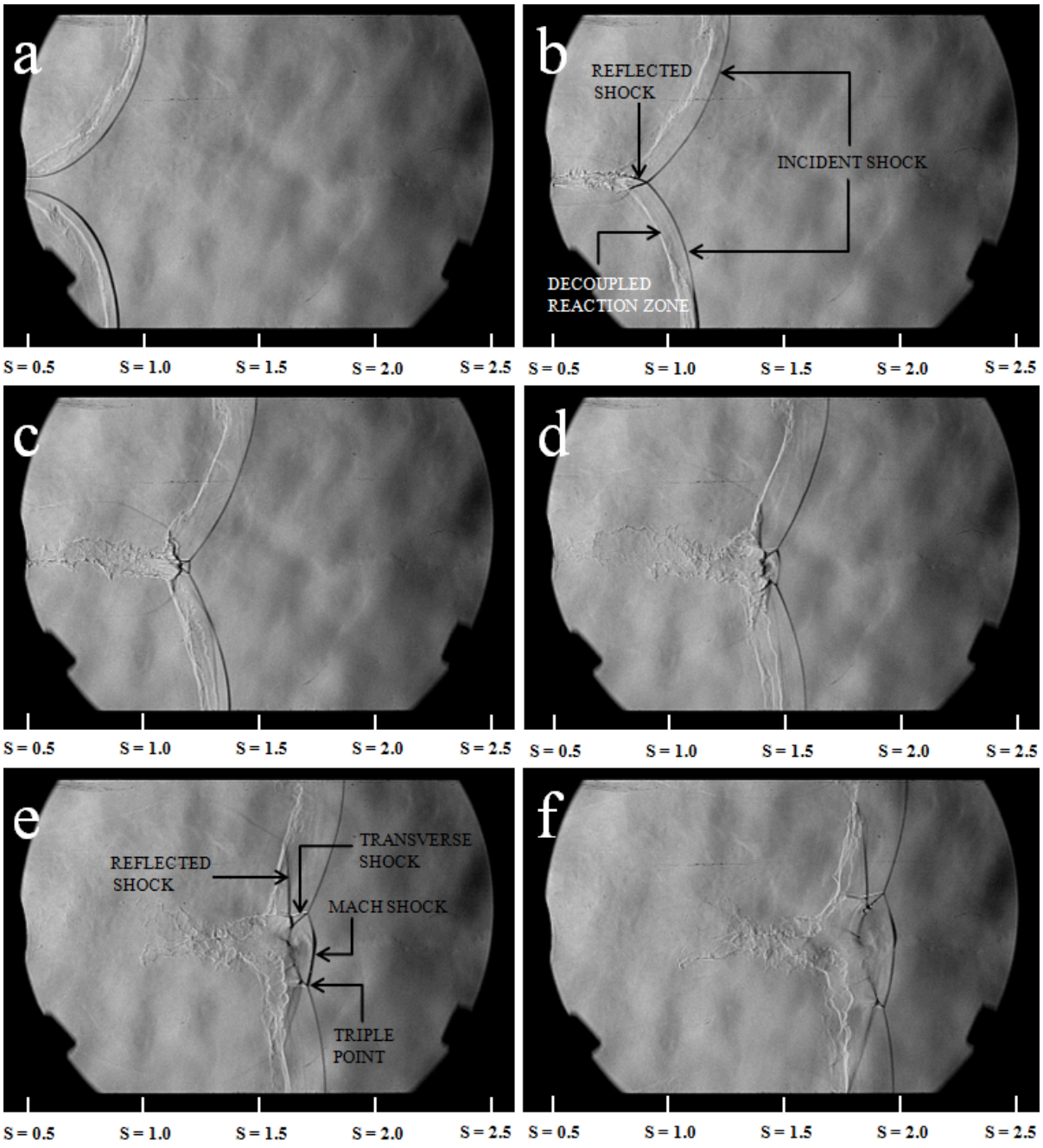

Figure 4.4: A flow field evolution showing a quenched detonation wave failing behind the full-cylinder obstacle. Since the detonation structure has quenched, there is no energy release in the vicinity of the shock front. Shown clearly is the transition of this shock-flame complex from a regular reflection to a Mach reflection with the important features identified. The initial pressure and temperature was 3.5 kPa and 300K. See Fig. G.8 for remaining frames. *Test ID: CH4+O2-08-20-12(0.5psiTEST1)*

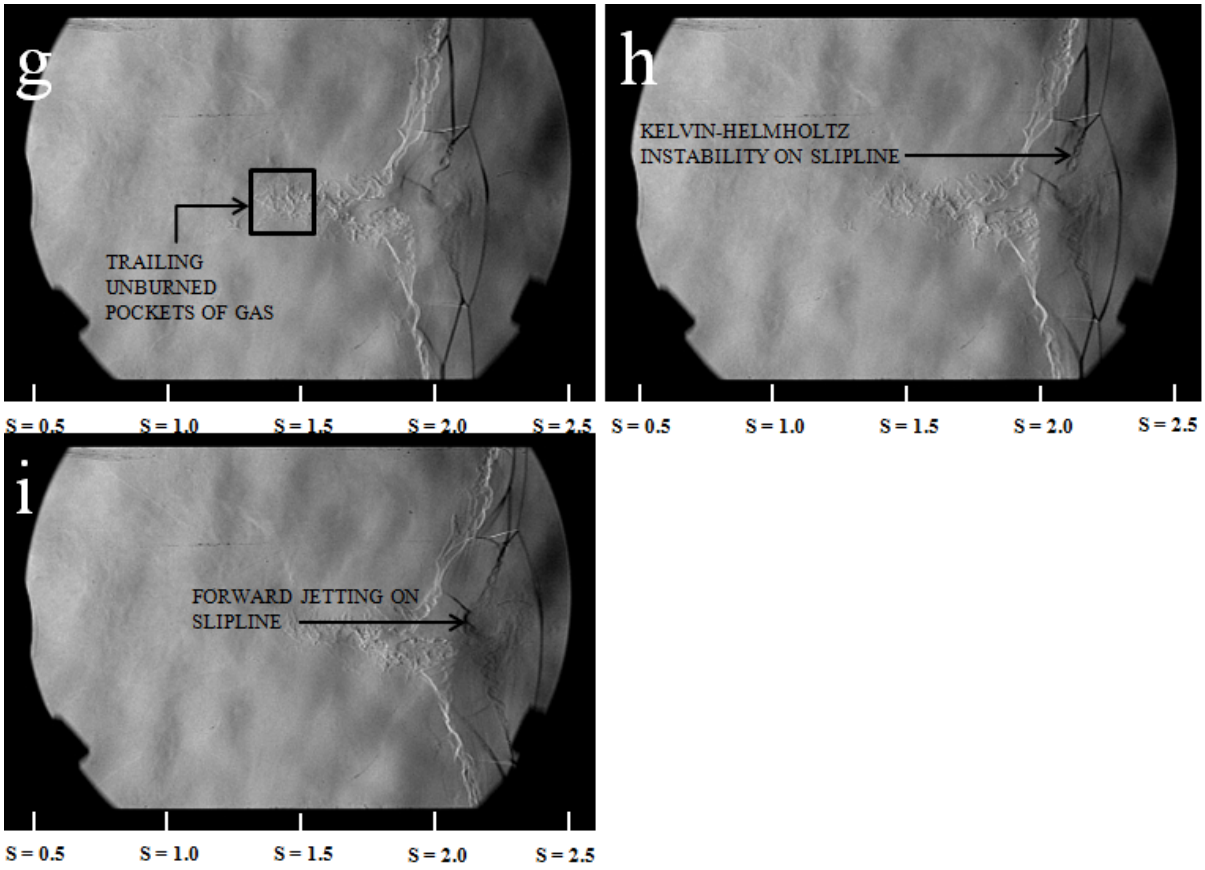

Figure 4.5: Continuation of the flow field evolution shown in Fig. 4.4. The images show trailing pockets of unburned gas as well as the K-H instability and forward jet along the slip line. The initial pressure and temperature was 3.5 kPa and 300K. *Test ID: CH4+O2-08-20-12(0.5psiTEST1)*

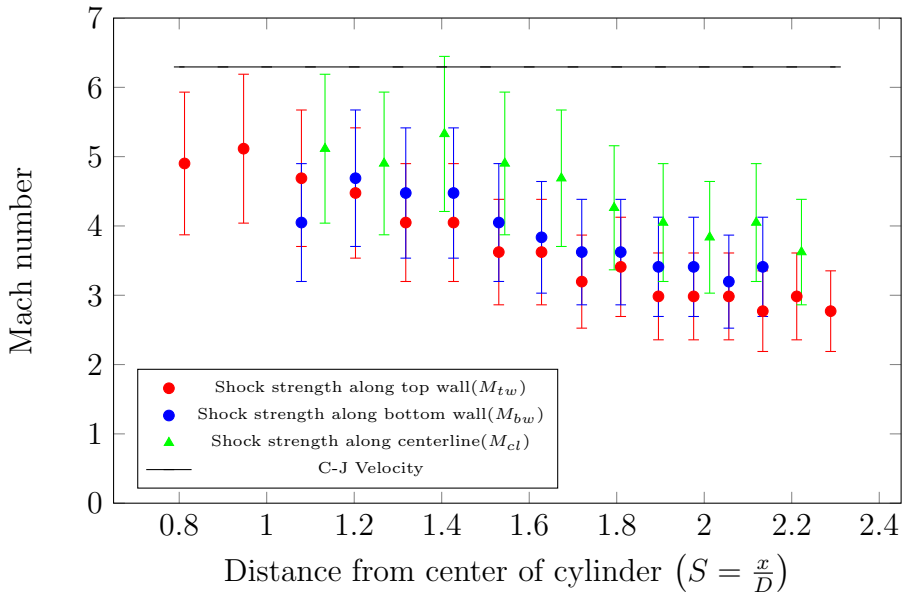

Figure 4.6: Velocimetry of the incident shock (top and bottom walls) and Mach shock (centerline) of a flow field showing inert shock reflections behind the full-cylinder obstacle. These values were obtained from the experiment shown in Figs. 4.4 and 4.5.

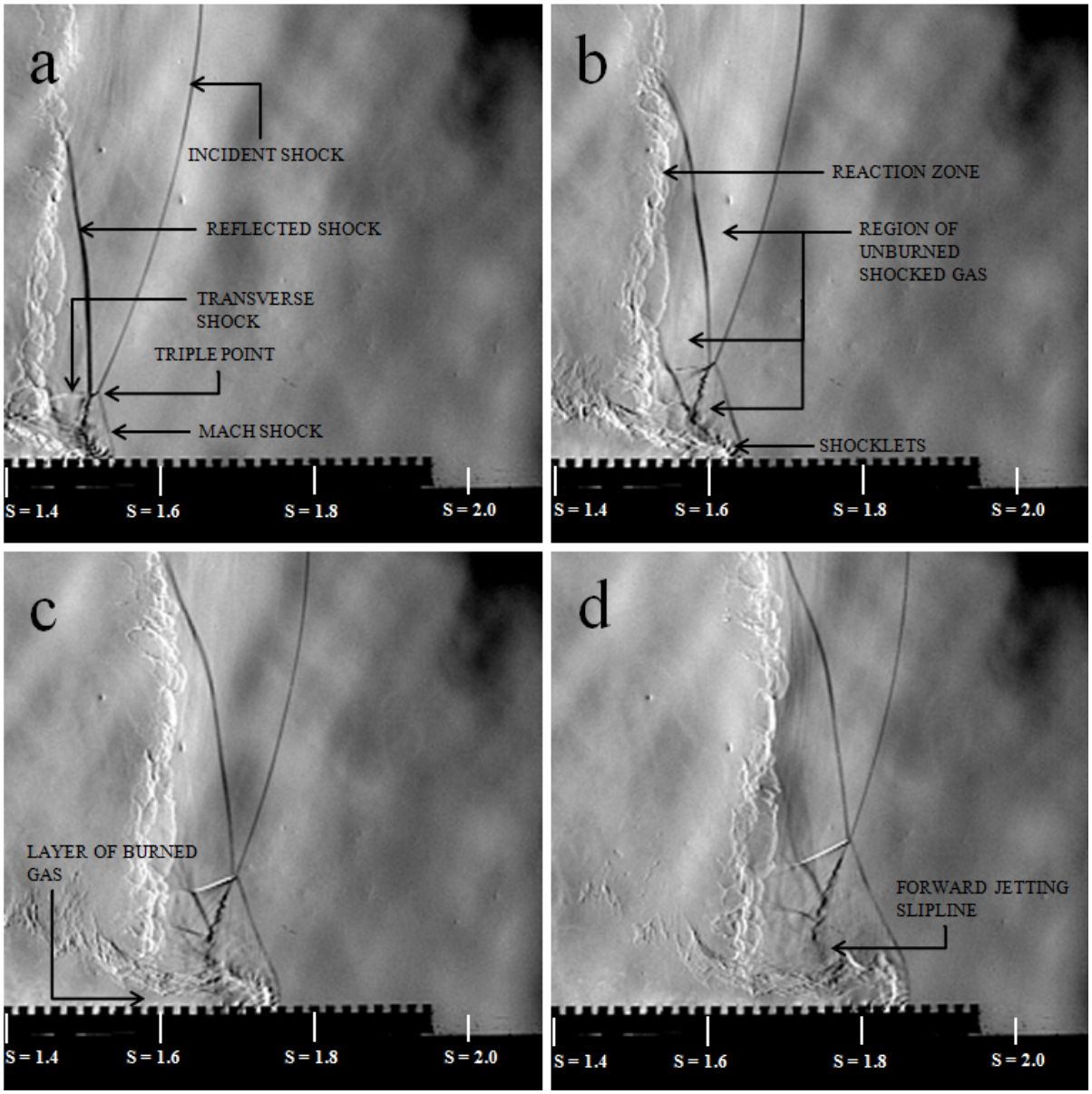

Figure 4.7: Flow field evolution showing re-ignition behind the Mach shock where a layer of burned gas is formed over the roughness plate obstacle (Images courtesy of L. Maley and K. Dennis). As the burned gas expands we also observe the slip line jetting forward. The initial pressure was 7 kPa. All frames were obtained from the same experiment using the high speed video camera and the remaining frames are shown in Figures G.6 and G.7. *Test ID: CH4+O2-07-13-12(1.0psi)roughness*

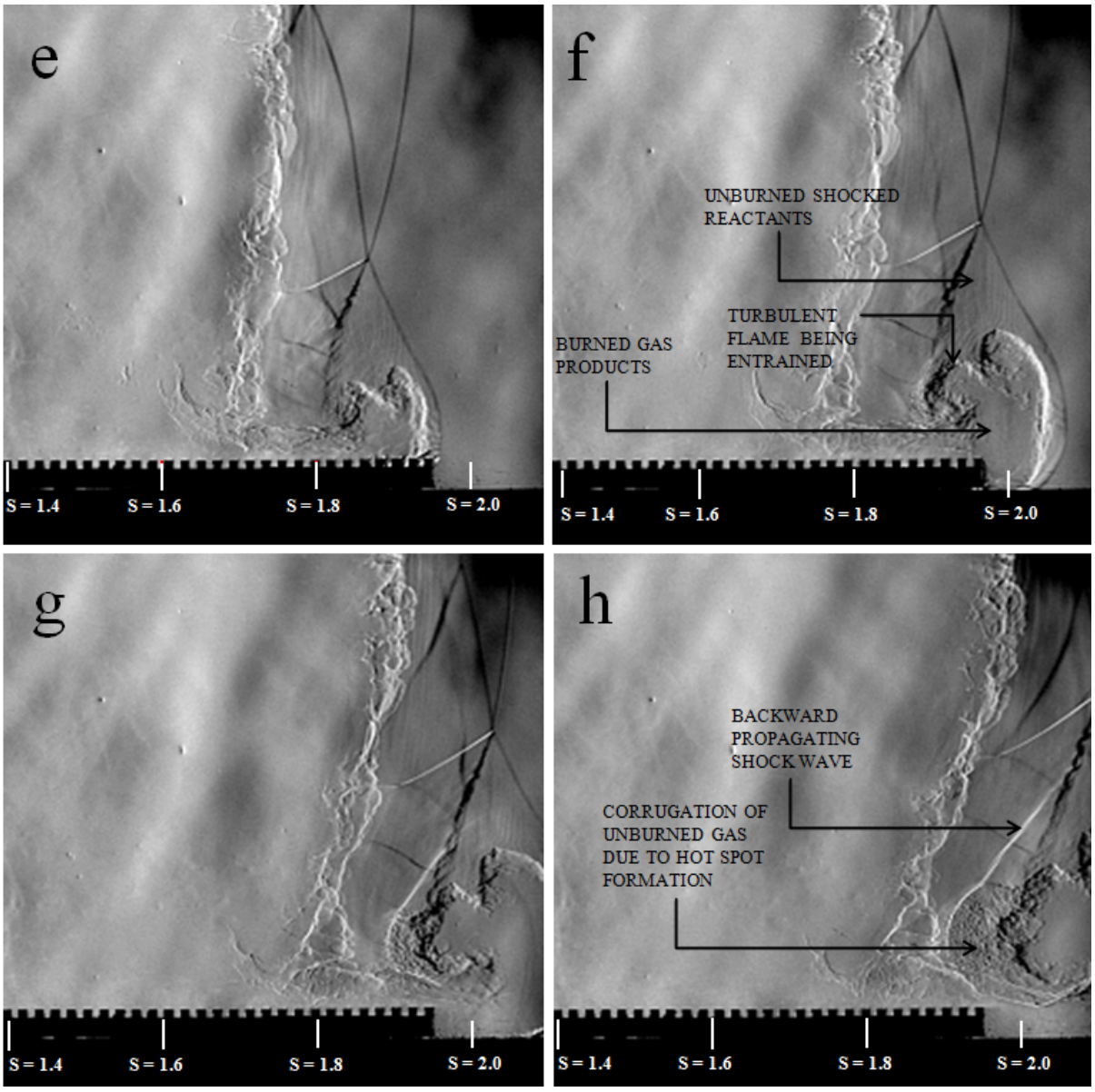

Figure 4.8: Continuation of the flow field evolution shown in Fig. 4.7. Shown here is the burned gas being entrained with cooler reactants to form a vortex behind the Mach shock. Also shown is a back propagating shock wave, which propagates through unburned gas behind the transverse wave. In addition corrugation of the unburned gas, punctuated by hot spot formation, behind this shock wave is clearly seen. The initial pressure was 7 kPa. *Test ID: CH4+O2-07-13-12(1.0psi)roughness*

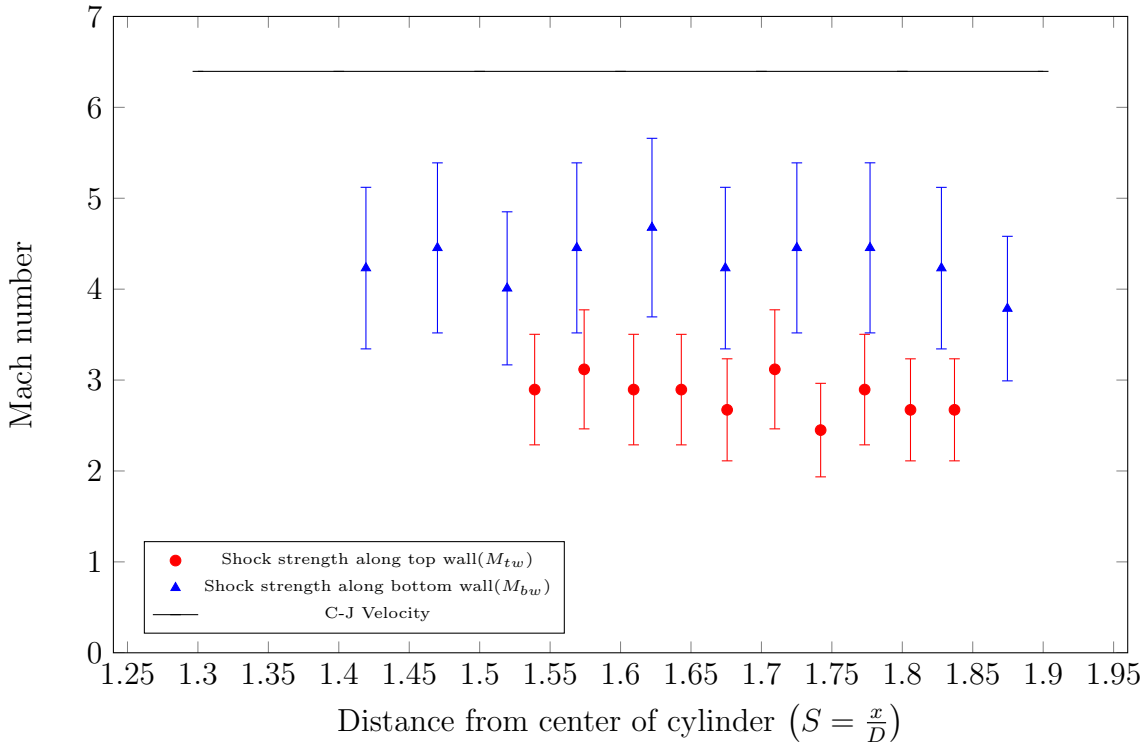

Figure 4.9: Velocity profile of the incident shock (top wall) and Mach shock (bottom wall) for the roughness test, where localized ignition events were observed behind the Mach shock. These values were obtained from the experiment shown in Figs. 4.7 and 4.8.

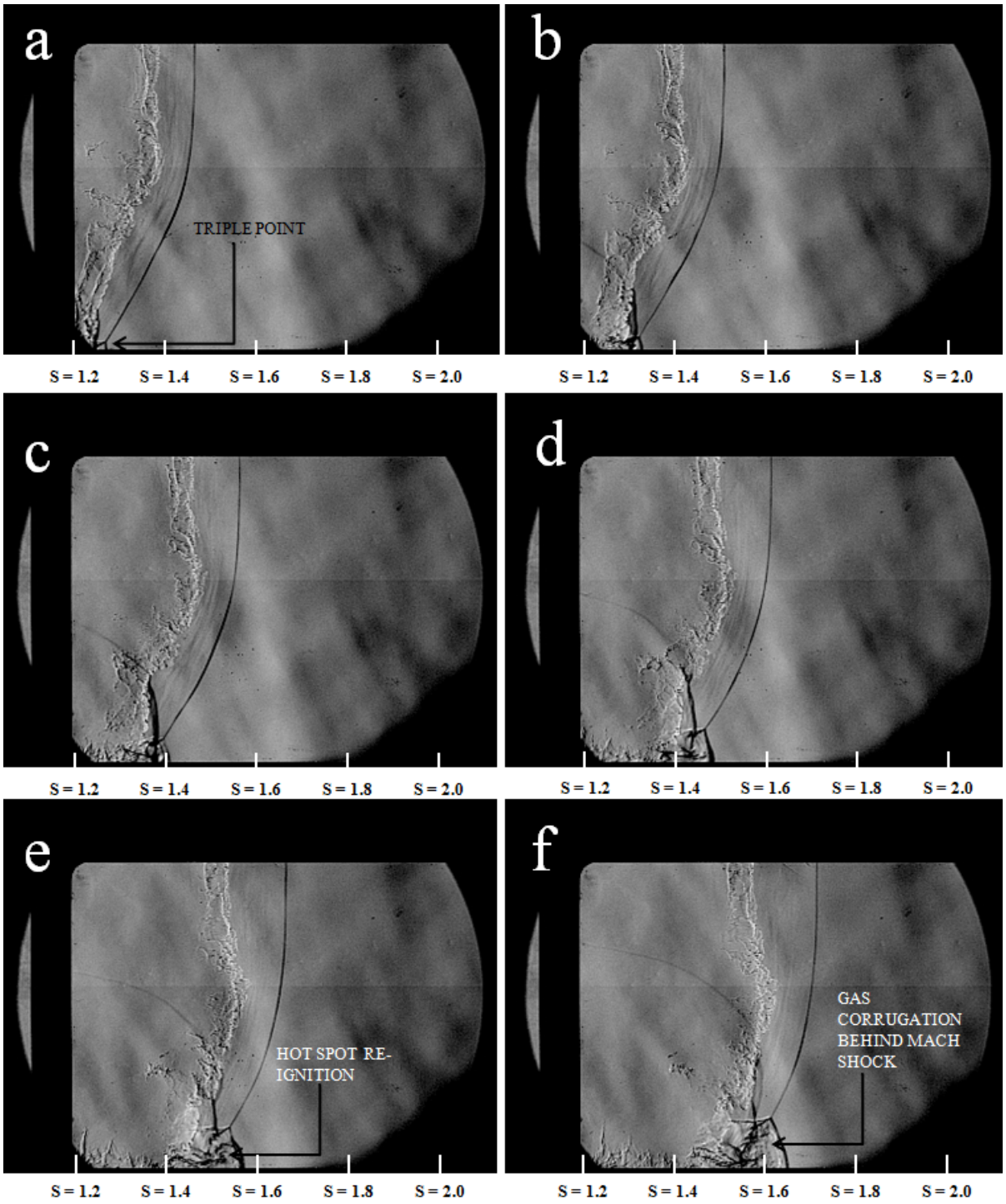

Figure 4.10: An evolution of a flow field showing re-ignition first at the foot of the Mach shock for a smooth wall test using the half-cylinder obstacle. The initial pressure was 10.3 kPa. All frames were obtained from the same experiment using the high speed video camera and the remaining frames are shown in Fig. G.1. *Test ID: CH4+O2-07-27-12(1.47psiTEST7)*

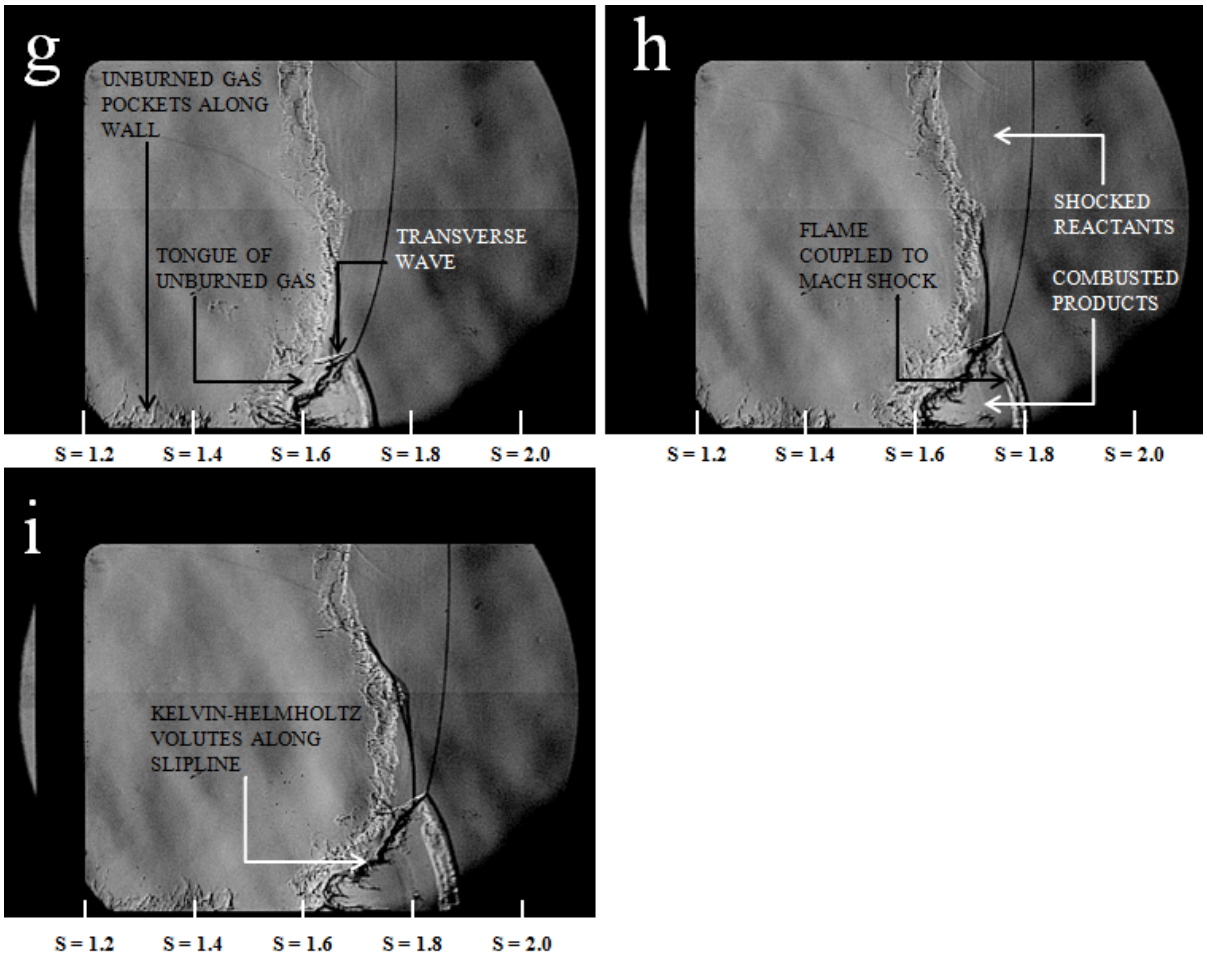

Figure 4.11: A continuation of the flow field evolution shown in Fig. 4.10. The flame formed behind the Mach shock eventually evolves in time to couple with the entire Mach shock front. Also observable are the unburned gas pockets along the bottom wall and the K-H instability along the slip line. The initial pressure was 10.3 kPa. *Test ID: CH4+O2-07-27-12(1.47psiTEST7)*

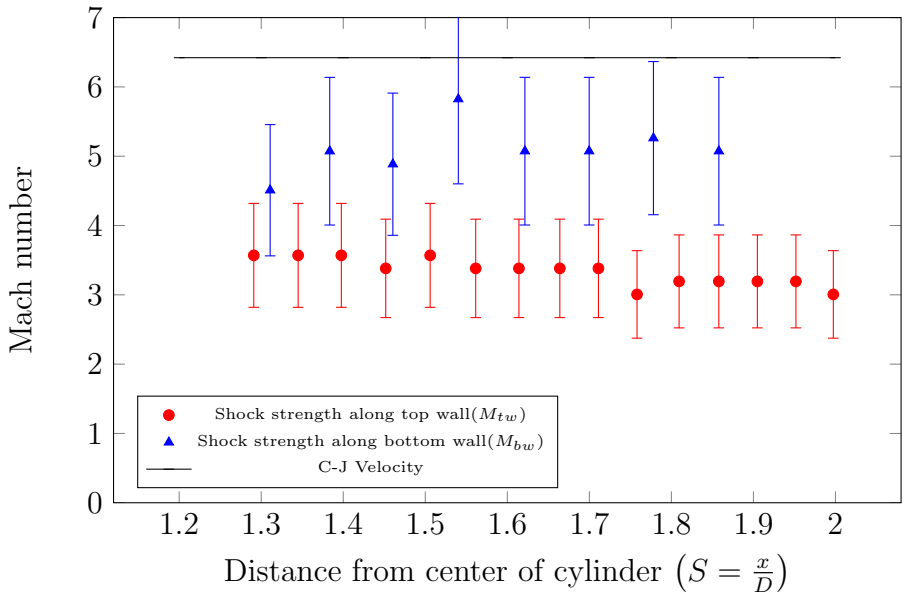

Figure 4.12: Velocimetry of the incident shock (top wall) and Mach shock (bottom wall) obtained from the experiment shown in Figs. 4.10 and 4.11. The solid line shows the CEA calculated C-J velocity for $p_0 = 10.3$ kPa.

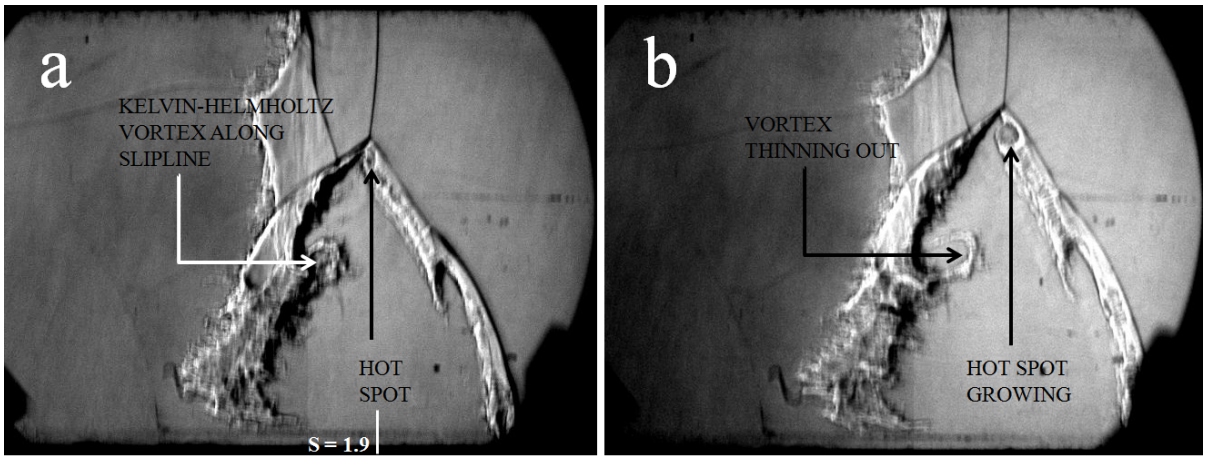

Figure 4.13: Two sequential frames showing corrugation of the tongue of unburned gas due to hot spot formation as well as thinning out of the volute of the K-H instability along the slip line for $p_0 = 10.5$ kPa. Both frames were obtained from the same experiment using the dual-frame camera. *Test ID: CH4+O2 - 05-11-11(1.49psi3)*

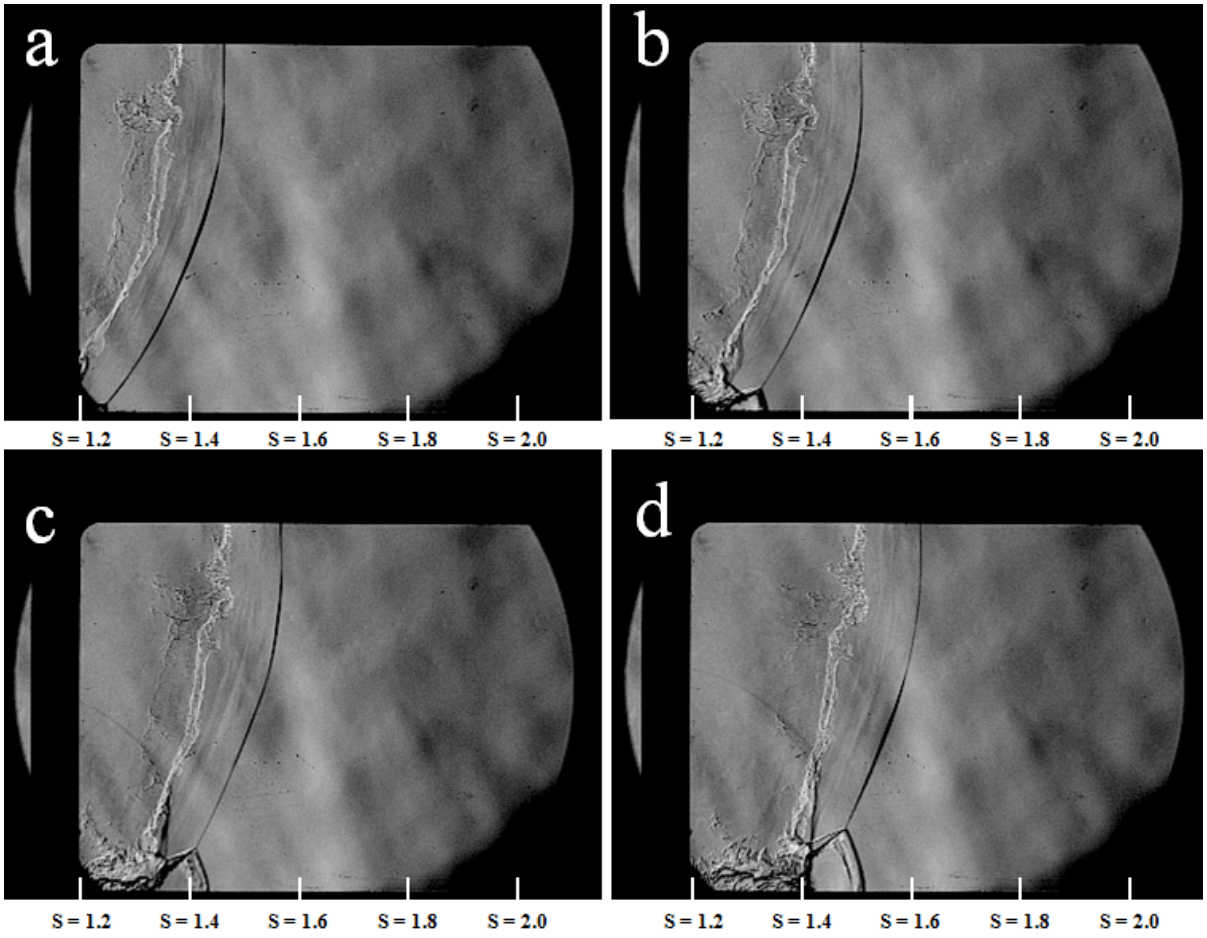

Figure 4.14: Flow field evolution showing an spontaneous re-ignition event behind the Mach shock, rather that a gradual sequence as seen in Fig. 4.10 for $p_0 = 9.8$ kPa. All frames shown were obtained from the same experiment using the high speed video camera and the remaining frames are shown in Fig. G.2. *Test ID: CH4+O2-07-27-12(1.4psiTEST3)*

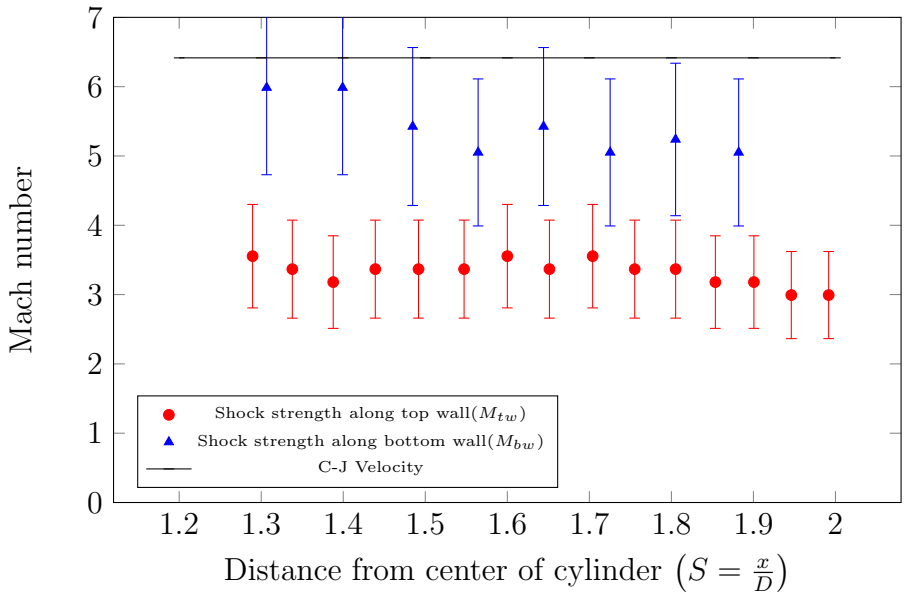

Figure 4.15: Velocimetry of the incident shock (top wall) and Mach shock (bottom wall) of a flow field showing spontaneous ignition following a Mach reflection; the solid line shows the CEA calculated C-J velocity for $p_0 = 9.8$ kPa. These values were obtained from the experiment shown in Fig. 4.14.

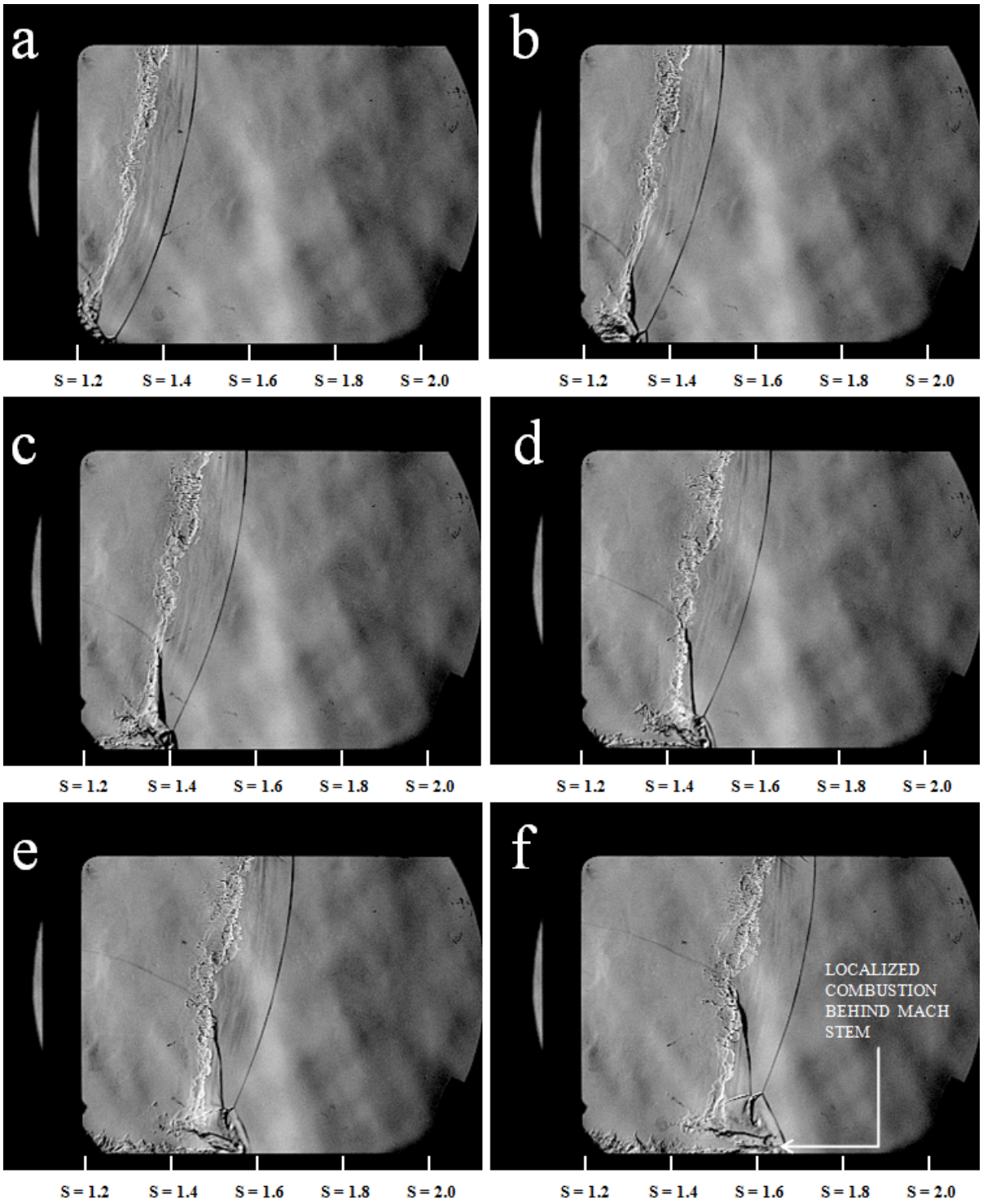

Figure 4.16: Sequence of images showing localized hot spot re-ignition behind the foot of the Mach shock for a smooth wall test using the half-cylinder obstacle. The initial pressure was 12.3 kPa. All frames were obtained from the same experiment using the high speed video camera and the remaining frames are shown in Fig. G.5. *Test ID: CH4+O2-07-24-12(1.75psiTEST4)*

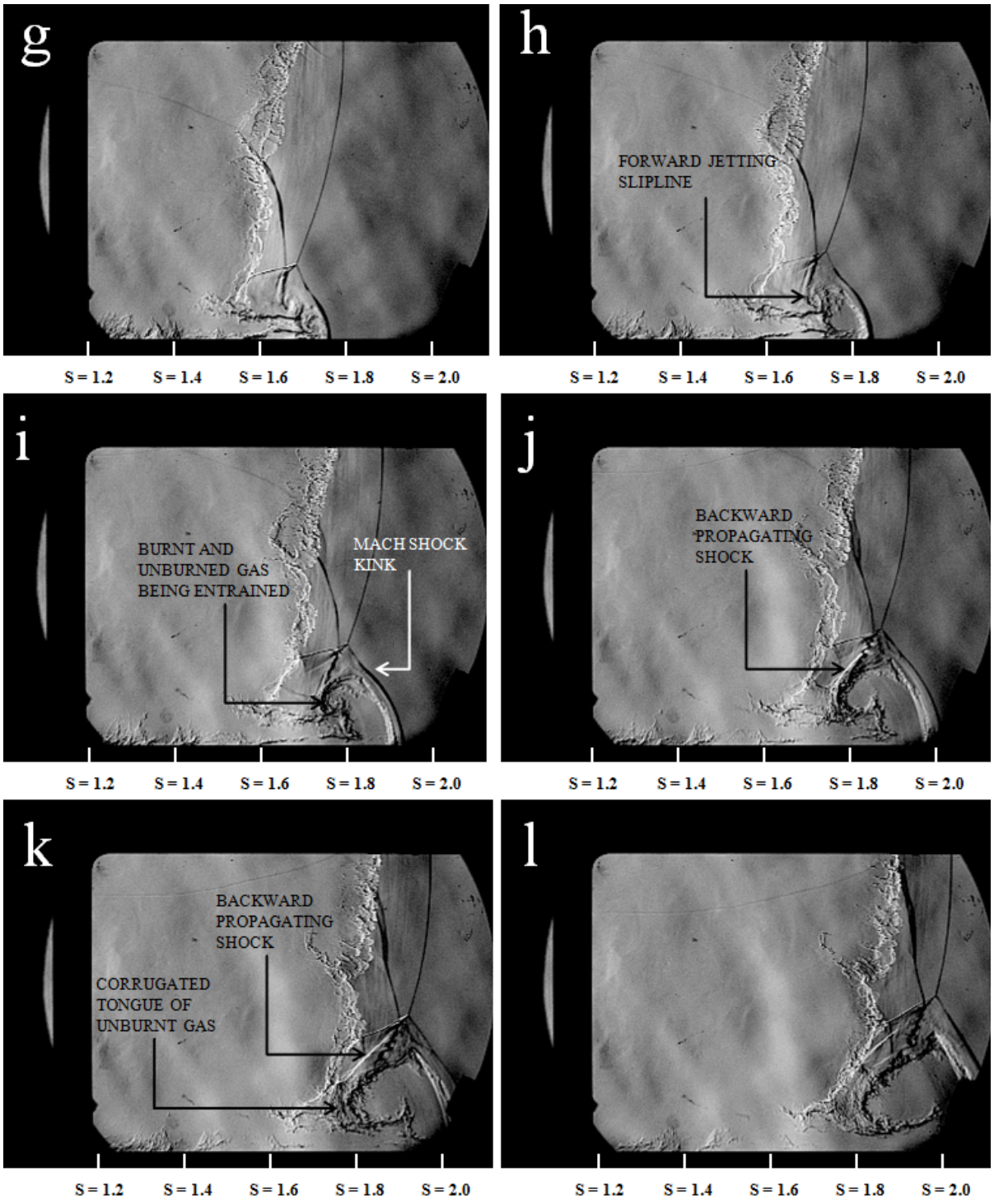

Figure 4.17: A continuation of the flow field evolution immediately after Fig. 4.16(f). Following re-ignition behind the Mach shock, the hot gas products appear to be entrained by the forward jetting slip line. Also observable is a backward propagating shock wave. The initial pressure was 12.3 kPa. *Test ID: CH4+O2-07-24-12(1.75psiTEST4)*

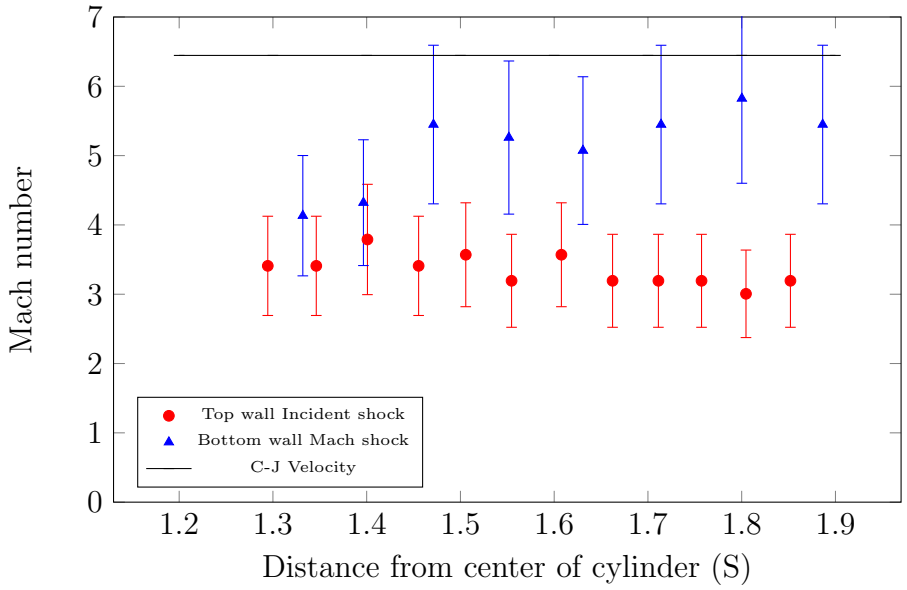

Figure 4.18: Velocimetry of the incident shock (top wall) and Mach shock (bottom wall) of a flow field showing re-ignition following a Mach reflection. These values were obtained from the experiment shown in Figs. 4.16 and 4.17.

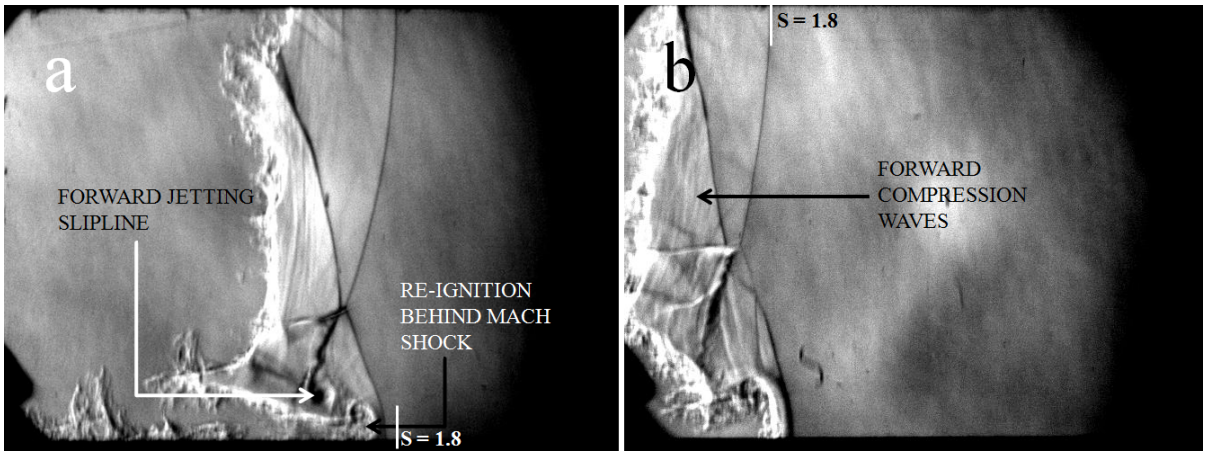

Figure 4.19: A general evolution of a flow field showing re-ignition of the Mach shock following jet entrainment of hot burned gas with unburned gas behind the Mach stem, for $p_0 = 10.4$ kPa. Each image represents a different experiment at the same initial conditions using the dual-frame camera. *(a)Test ID: CH4+O2 - 08-3-11(1.49psi)3; (b)Test ID: CH4+O2 - 08-2-11(1.49psi)2*

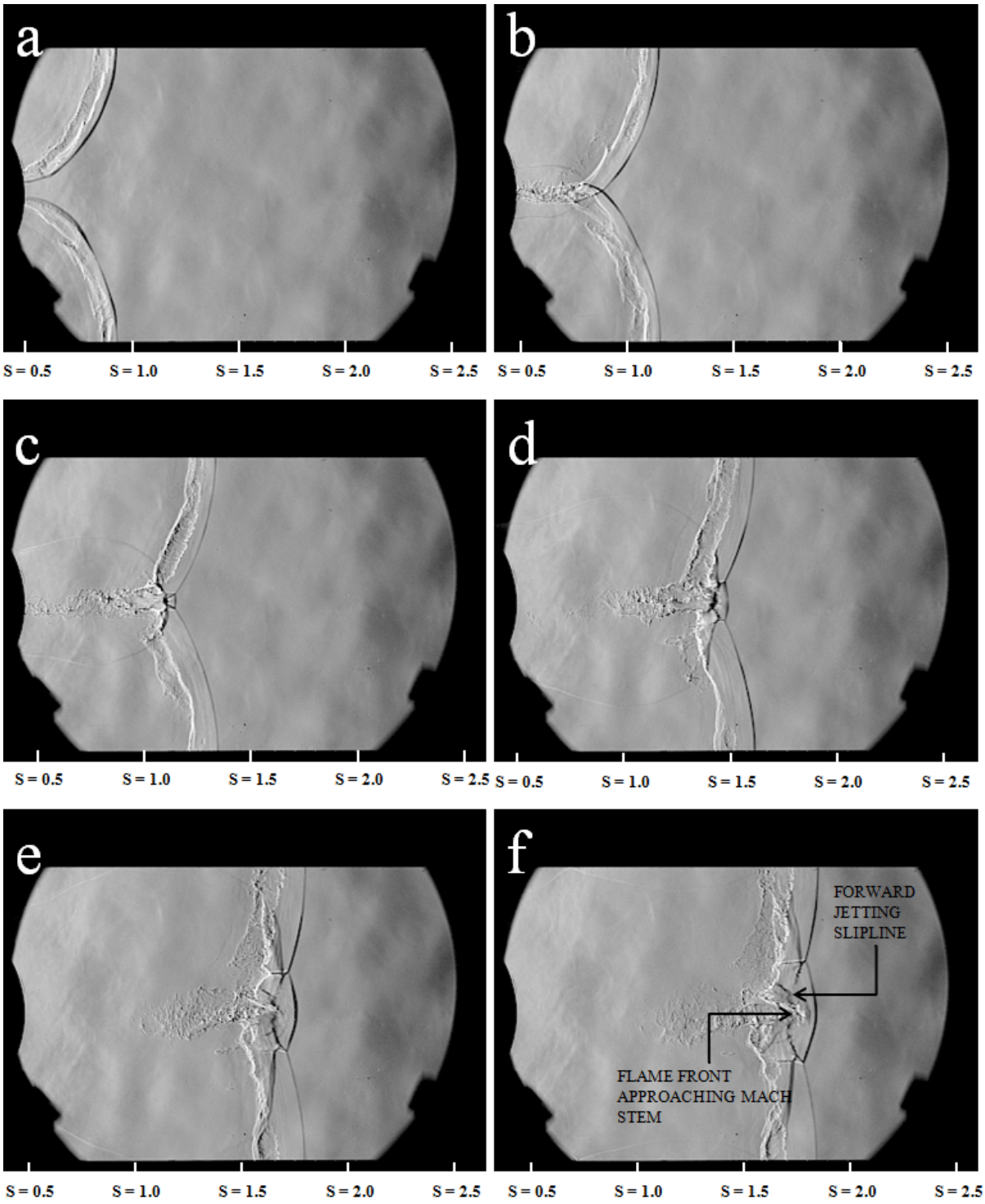

Figure 4.20: A flow field evolving in time showing re-ignition behind the Mach shock. The sequence of images indicate the development of the forward jetting slip line as the flame front approaches the Mach shock front. The initial pressure was 8.4 kPa. All frames were obtained from the same experiment using the high speed video camera and the remaining frames are shown in Fig. G.9. *Test ID: CH4+O2-08-14-12(1.2psiTEST1)*

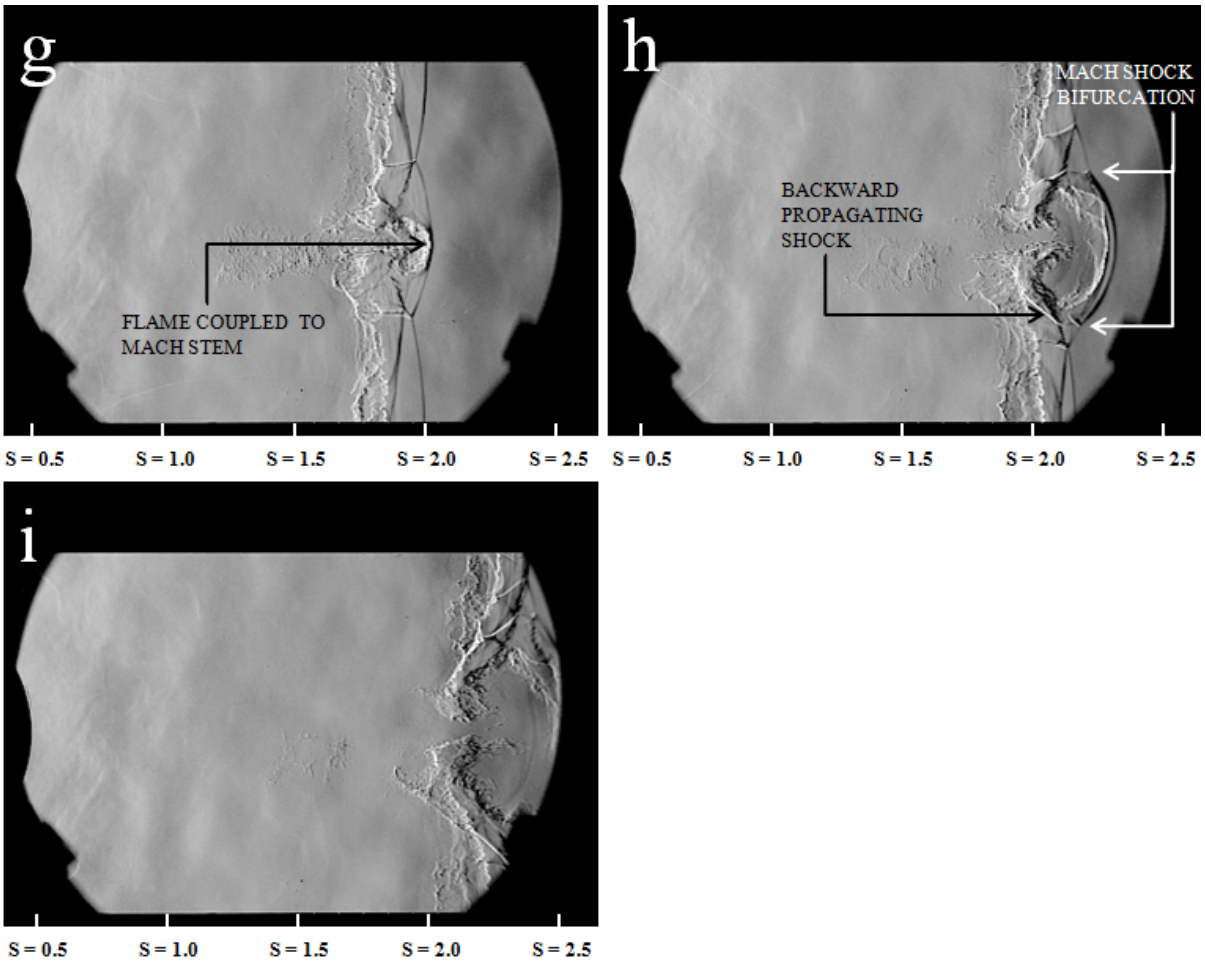

Figure 4.21: A continuation of the flow field evolution shown in Fig. 4.20. Following the earlier sequence of events, a strong coupling of the flame with the Mach shock front is observed. Also shown is a strong bifurcation of the Mach shock to form two new triple points that are moving away from each other. The initial pressure was 8.4 kPa. *Test ID: CH4+O2-08-14-12(1.2psiTEST1)*

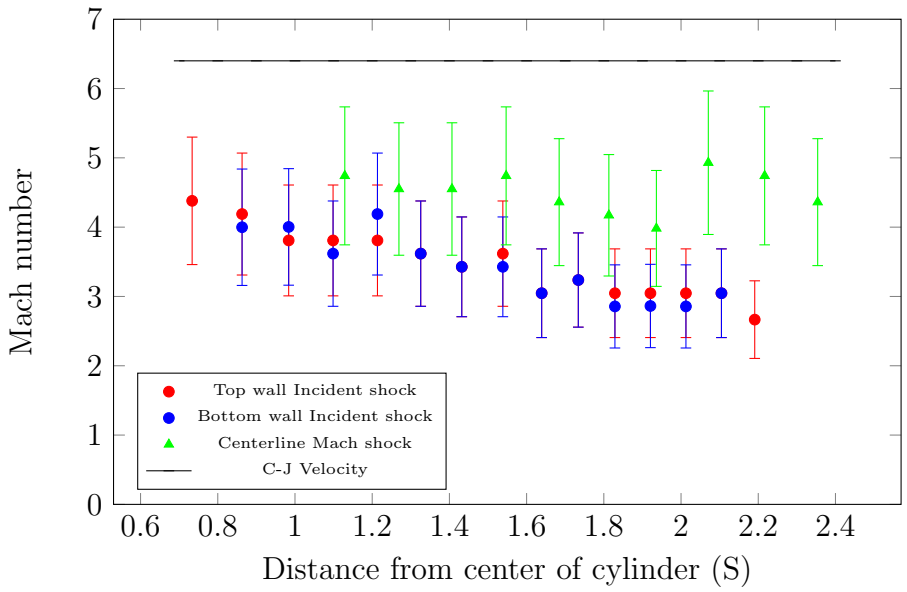

Figure 4.22: Velocimetry of the incident shock (top and bottom walls) and Mach shock (centerline) of a flow field showing re-ignition events following a Mach reflection behind the full-cylinder obstacle. These values were obtained from the experiment shown in Fig. 4.20 and 4.21.

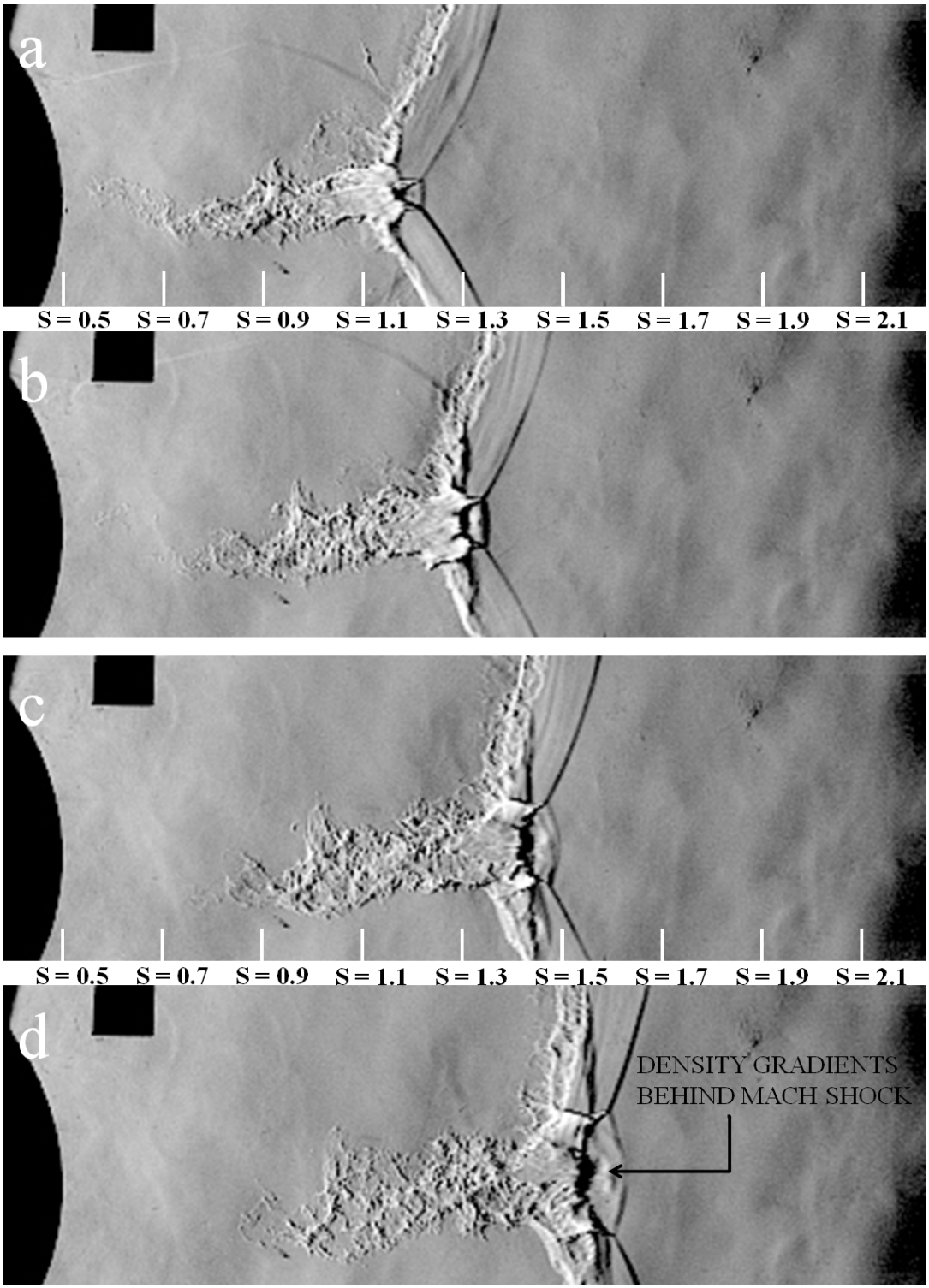

Figure 4.23: A sequence of Schlieren images showing that following a Mach reflection, distinct density gradients are observed behind the Mach shock. Also the flame interface, near the lower slip line, begins to approach the Mach shock front. The initial pressure was 10.5 kPa. See Figs. G.10 and G.11 for remaining frames. *Test ID: CH4+O2-08-03-12(1.49psiTEST4)*

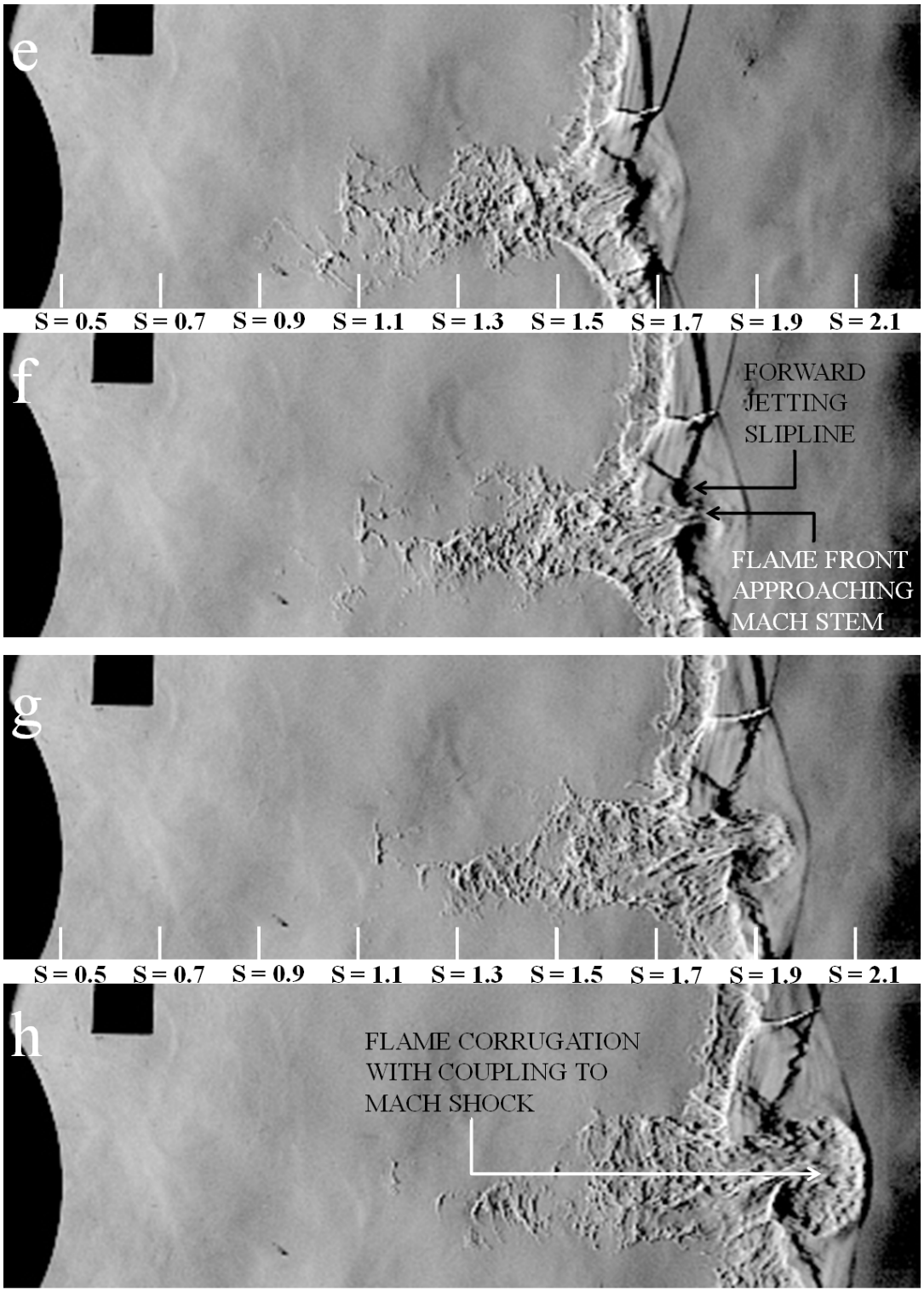

Figure 4.24: A continuation of the flow field shown in Fig. 4.23 where we observe re-ignition behind the Mach shock. Here the familiar forward jet effect of the slip line is seen along with the flame front until it couples with the Mach shock. The initial pressure 10.5 kPa. *Test ID: CH4+O2-08-03-12(1.49psiTEST4)*

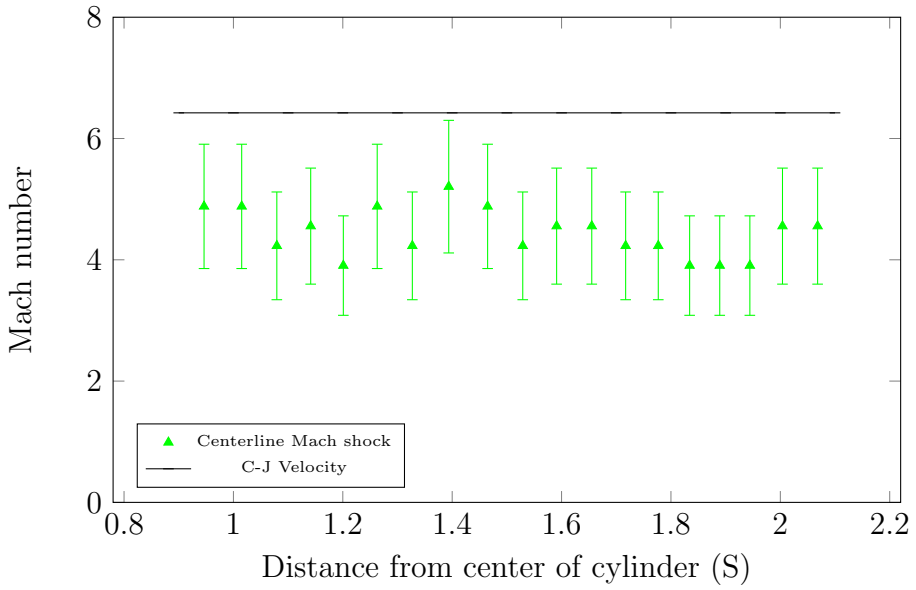

Figure 4.25: Velocimetry of the incident shock (top and bottom walls) and Mach shock (centerline) of a flow field showing re-ignition events following a Mach reflection behind the full-cylinder obstacle. These values were obtained from the experiment shown in Figs. 4.23 and 4.24.

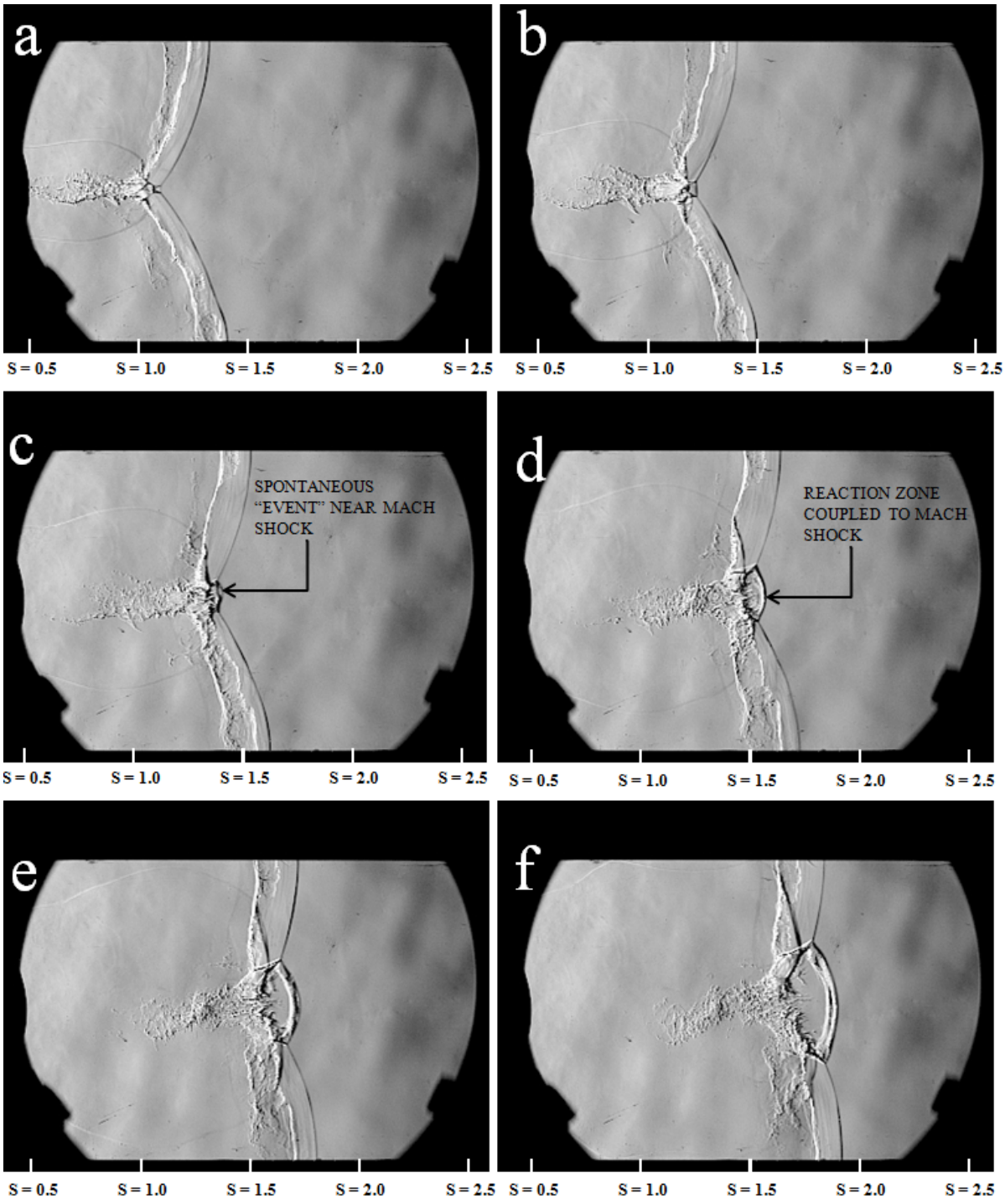

Figure 4.26: An evolution of a flow field showing spontaneous re-ignition behind the Mach shock, instead of a gradual process as observed in Fig. 4.23 for the same initial conditions. The initial pressure was 10.5 kPa. All frames were obtained from the same experiment using the high speed video camera and the remaining frames are shown in Fig. G.12. *Test ID: CH4+O2-08-03-12(1.49psiTEST2)*

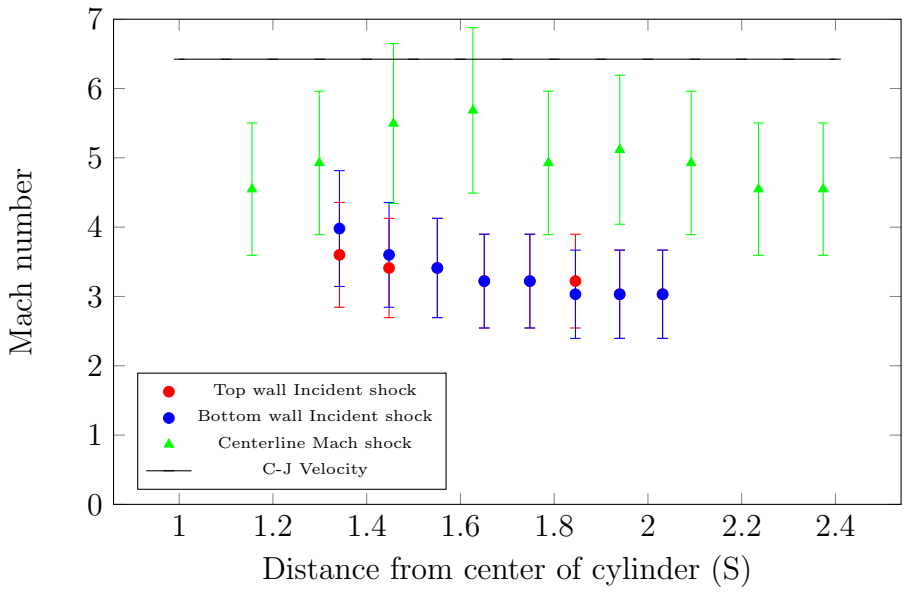

Figure 4.27: Velocimetry of the incident shock (top and bottom walls) and Mach shock (centerline) of a flow field showing spontaneous re-ignition events following a Mach reflection behind the full-cylinder obstacle. These values were obtained from the experiment shown in Figure 4.26.

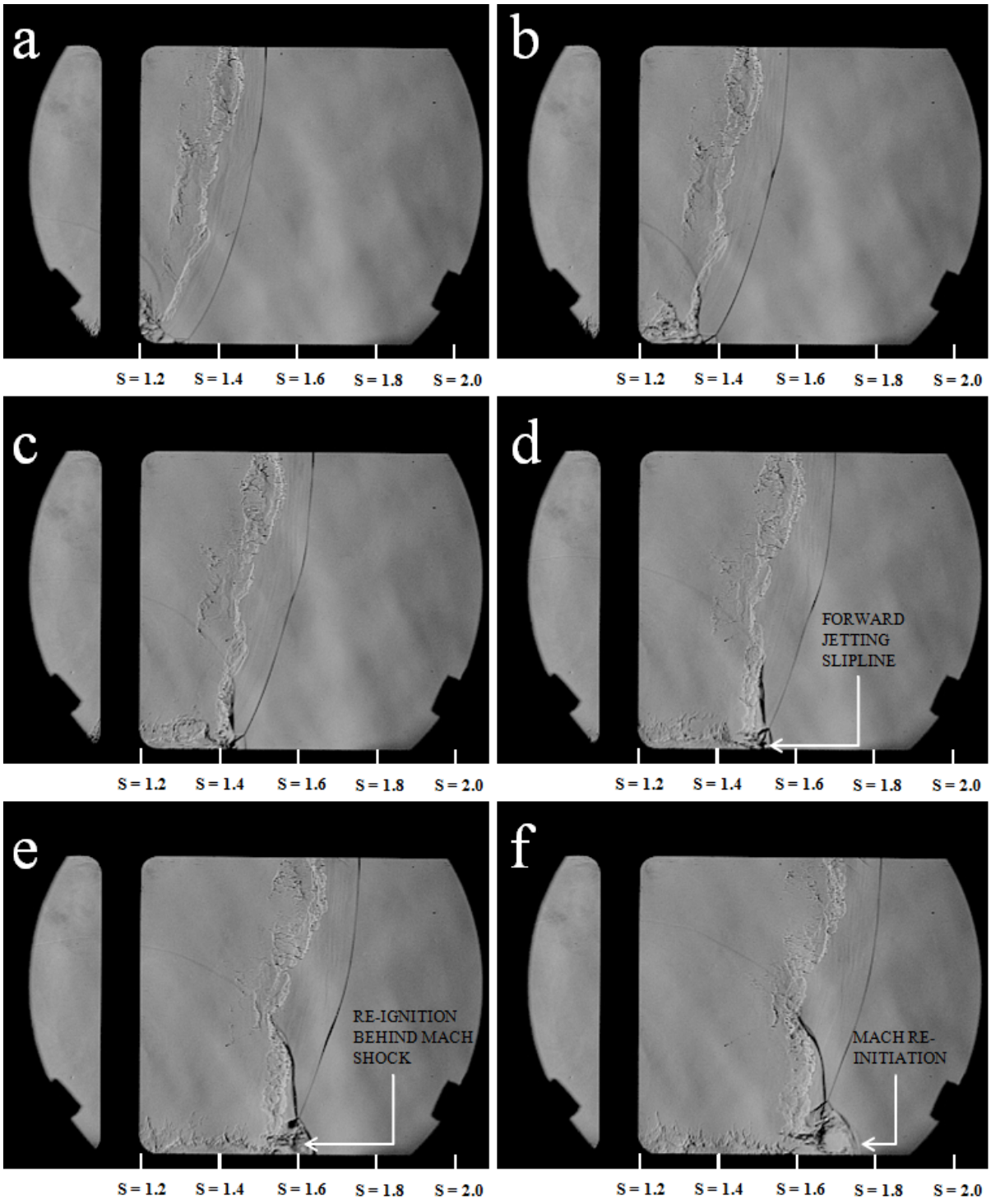

Figure 4.28: Sequence of images showing detonation re-initiation of the Mach shock at its foot for $p_0 = 12.3$ kPa. All frames were obtained from the same experiment using the high speed video camera and the remaining frames are shown in Fig. G.4. *Test ID: CH4+O2-07-25-12(1.75psiTEST6)*

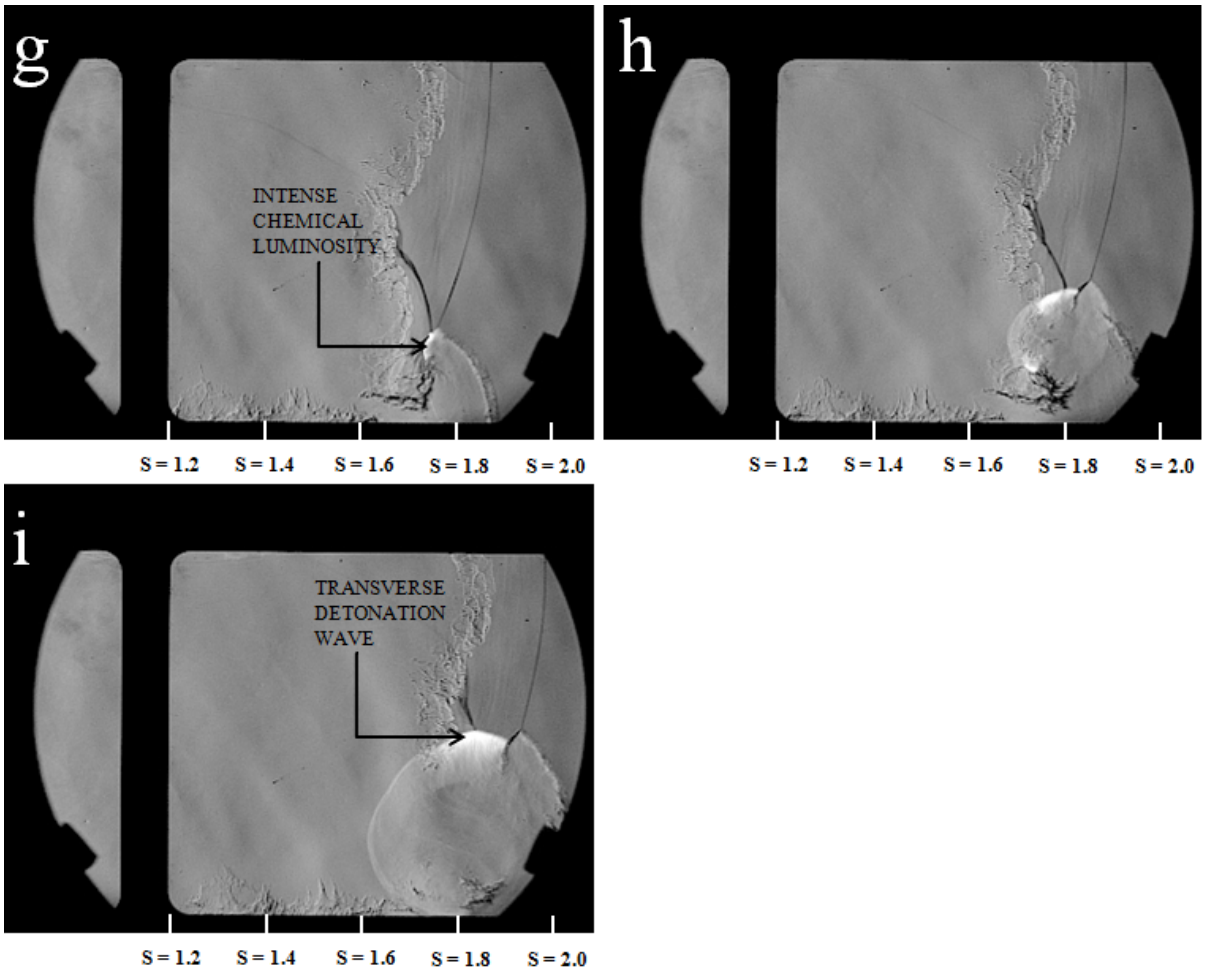

Figure 4.29: A continuation of the sequence of images shown in Fig. 4.28. Following detonation re-initiation of the Mach shock rapid exothermic reactions near the transverse shock is observed. This is followed by a transverse detonation wave. The initial pressure is $p_0 = 12.3$ kPa. *Test ID: CH4+O2-07-25-12(1.75psiTEST6)*

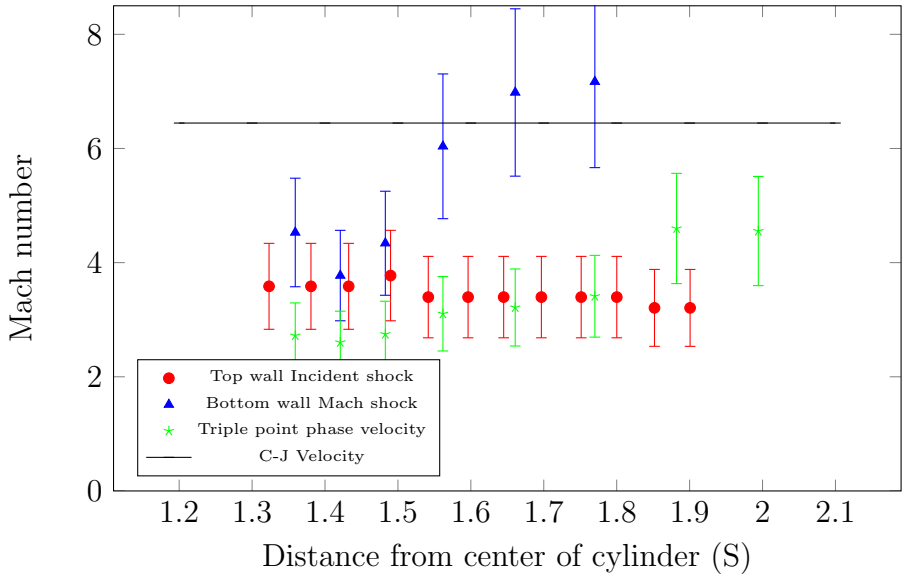

Figure 4.30: Velocimetry of the incident shock (top wall), Mach shock (bottom wall) and triple point phase velocity of a flow field showing re-initiation following a Mach reflection. These values were obtained from the experiment shown in Figs. 4.28 and 4.29.

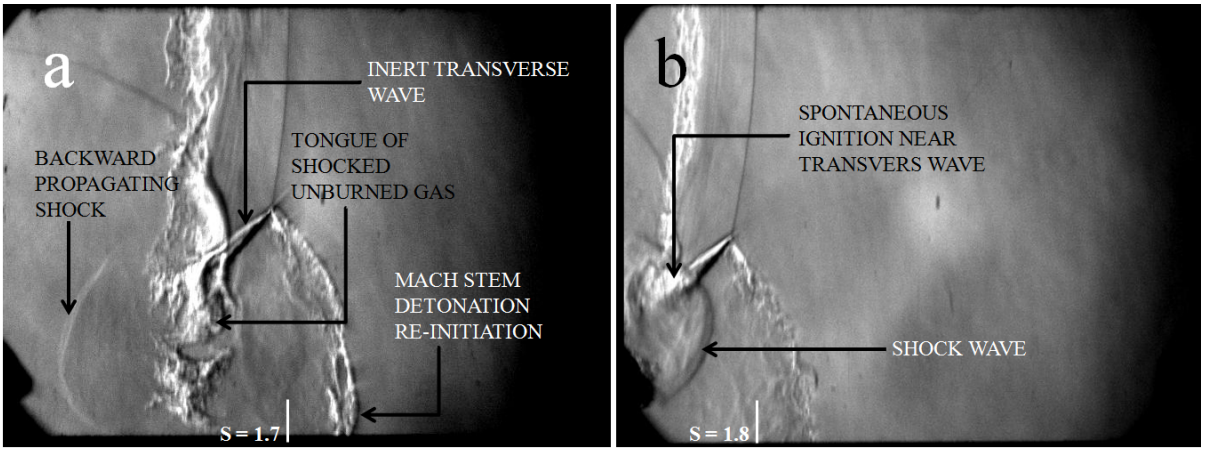

Figure 4.31: A general evolution of a flow field showing re-initiation of the Mach shock followed by re-initiation of the transverse wave. Also clearly observable are strong inert shock waves formed after detonation re-initiation on the Mach and transverse shock, indicative of rapid chemical reaction rates. The initial pressure was 10.4 kPa. Each image represents a different experiment at the same initial conditions using the double frame camera. *(a)Test ID: CH4+O2 - 08-3-11(1.49psi)1; (b)Test ID: CH4+O2 - 08-2-11(1.49psi)1*

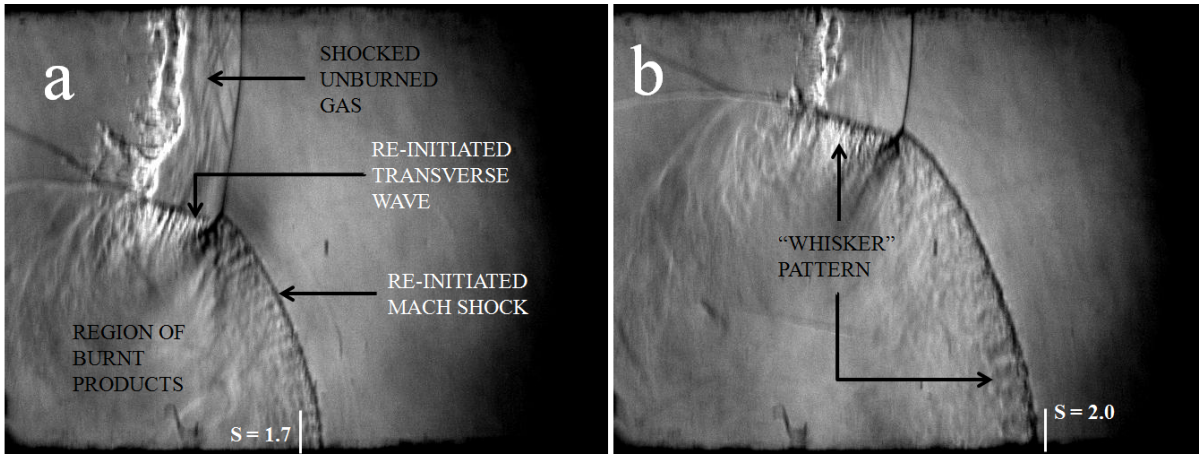

Figure 4.32: A reproducible flow field evolution showing a re-initiated Mach shock and transverse wave propagating towards the right and up. The initial pressure was 12.0 kPa. Each image represents a different experiment at the same initial conditions using the dual-frame camera. *(a) Test ID: CH4+O2 - 03-12-11(1.72psi)4; (b)Test ID: CH4+O2 - 03-12-11(1.72psi)6*

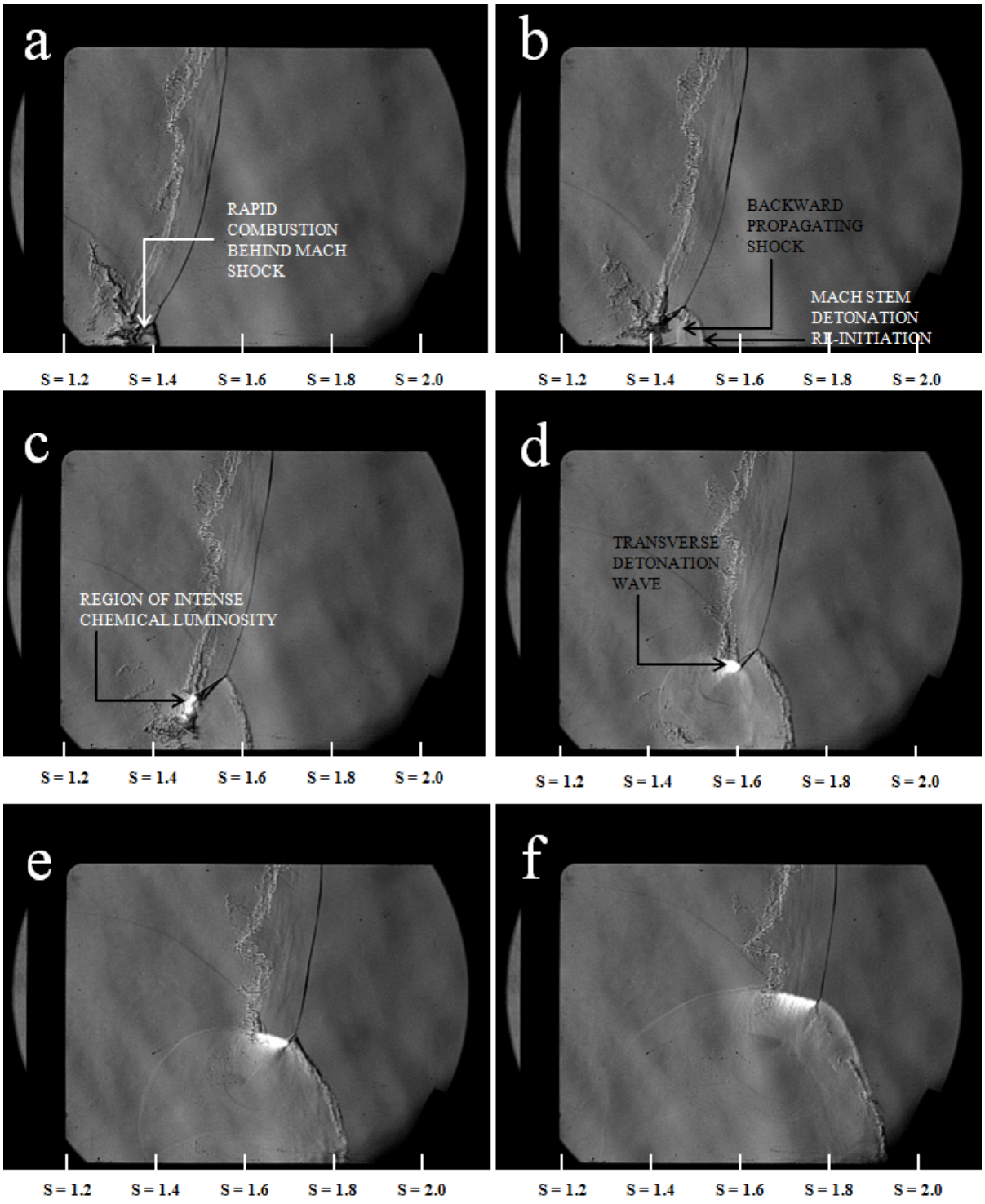

Figure 4.33: Flow field evolution showing rapid re-initiation first at the foot of the Mach shock. This is followed by a violent detonation re-initiation event on the transverse shock. The initial pressure was $p_0 = 10.5$ kPa. All frames were obtained from the same experiment using the high speed video camera and the remaining frames are shown in Fig. G.3. *Test ID: CH4+O2-07-27-12(1.5psiTEST2)*

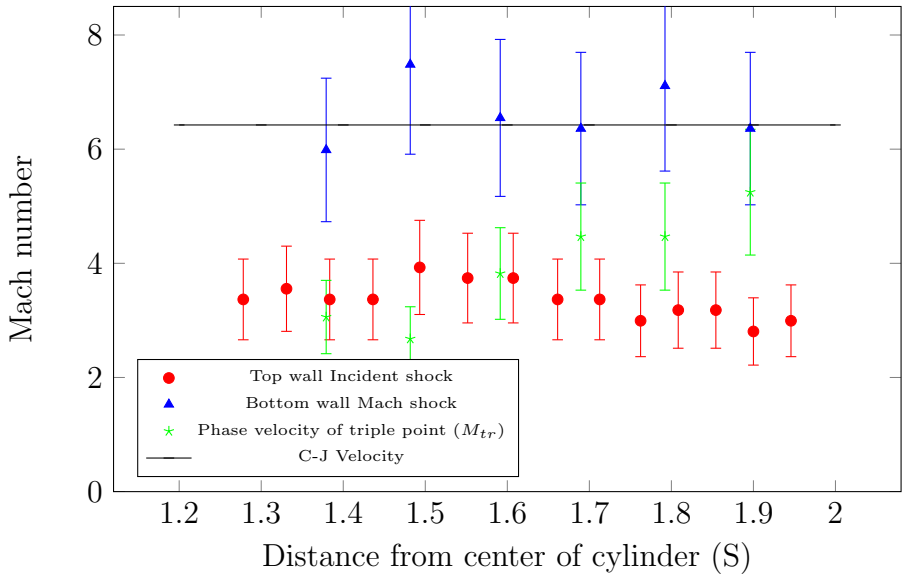

Figure 4.34: Velocimetry of the incident shock (top wall), Mach shock (bottom wall) and phase velocity of the triple point for a flow field evolution showing re-initiation following a Mach reflection; the solid line shows the CEA calculated C-J velocity for $p_0 = 10.5$ kPa, $T_0 = 300$K. These values were obtained from the experiment shown in Fig. 4.33.

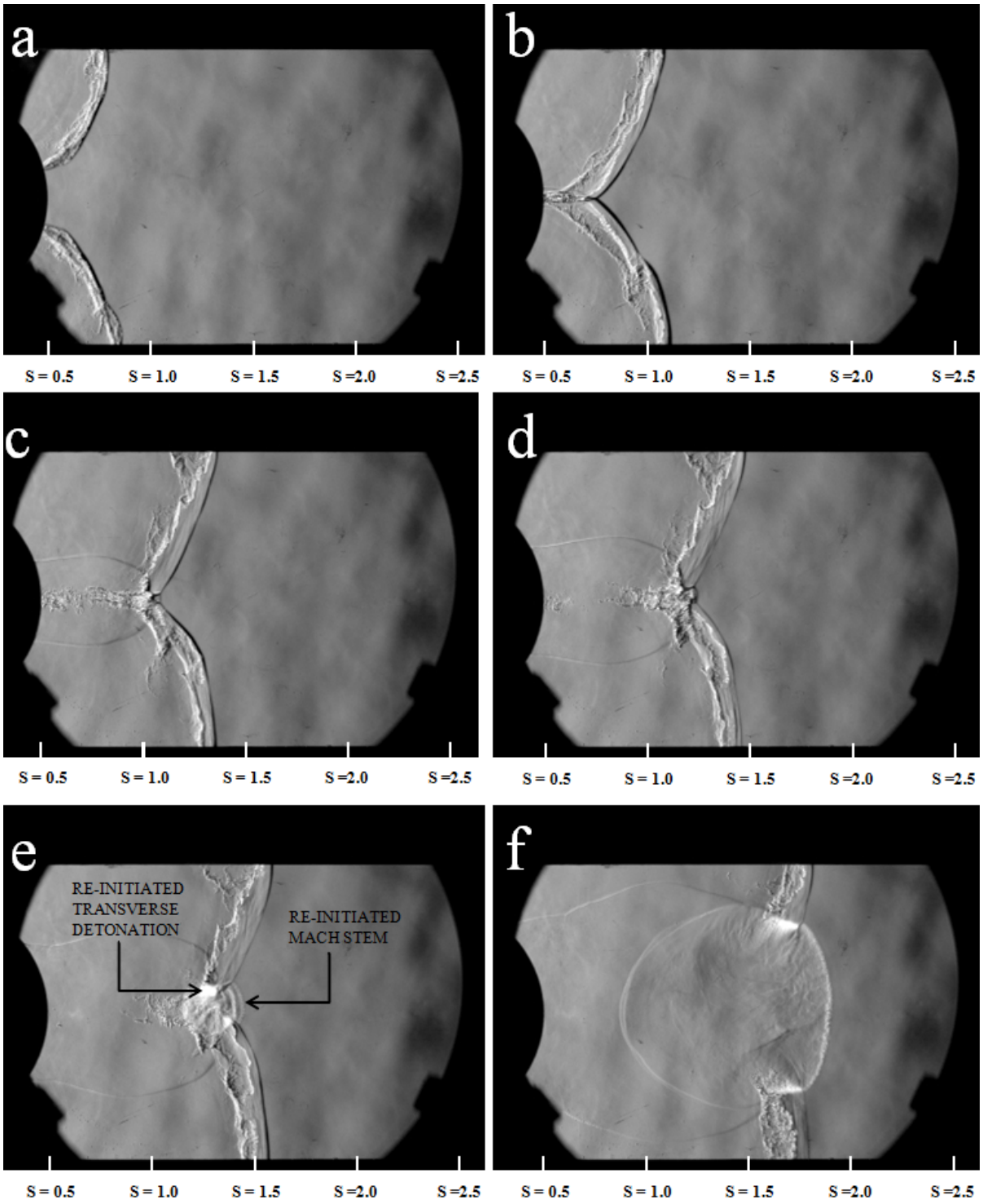

Figure 4.35: A flow field evolution showing simultaneous detonation re-initiation of the Mach shock and transverse wave for $p_0 = 16.8$ kPa. All frames were obtained from the same experiment using the high speed video camera and the remaining frames are shown in Fig. G.13. *Test ID: CH4+O2-08-01-12(2.4psiTEST4)*

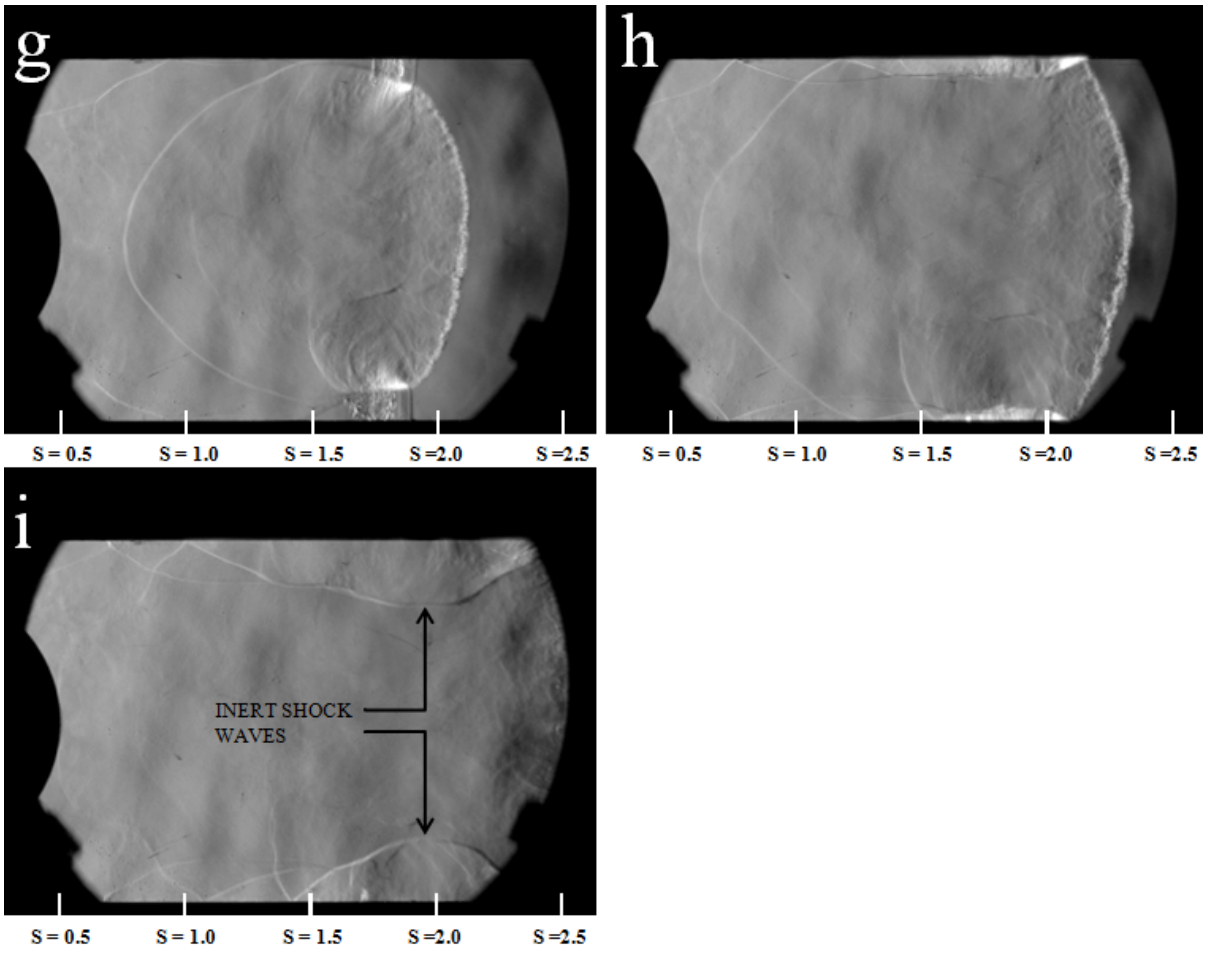

Figure 4.36: A continuation of the flow field evolution shown in Fig. 4.35 for $p_0 = 16.8$ kPa. *Test ID: CH4+O2-08-01-12(2.4psiTEST4)*

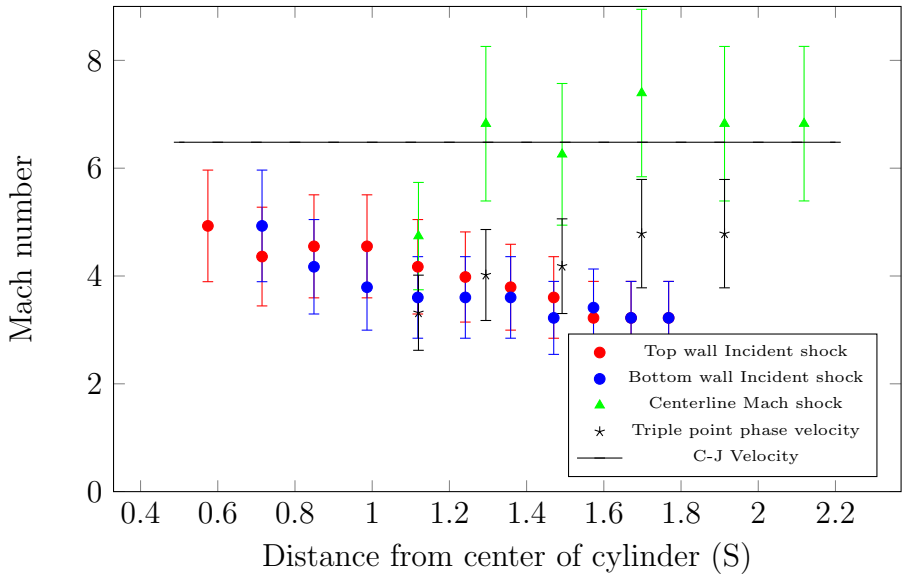

Figure 4.37: Velocimetry of the incident shock (top and bottom walls), Mach shock (centerline) and triple point phase velocity of a flow field showing re-initiation following a Mach reflection behind the full-cylinder obstacle. These values were obtained from the experiment shown in Figs. 4.35 and 4.36. The initial pressure and temperature is 16.8 kPa and 300K.

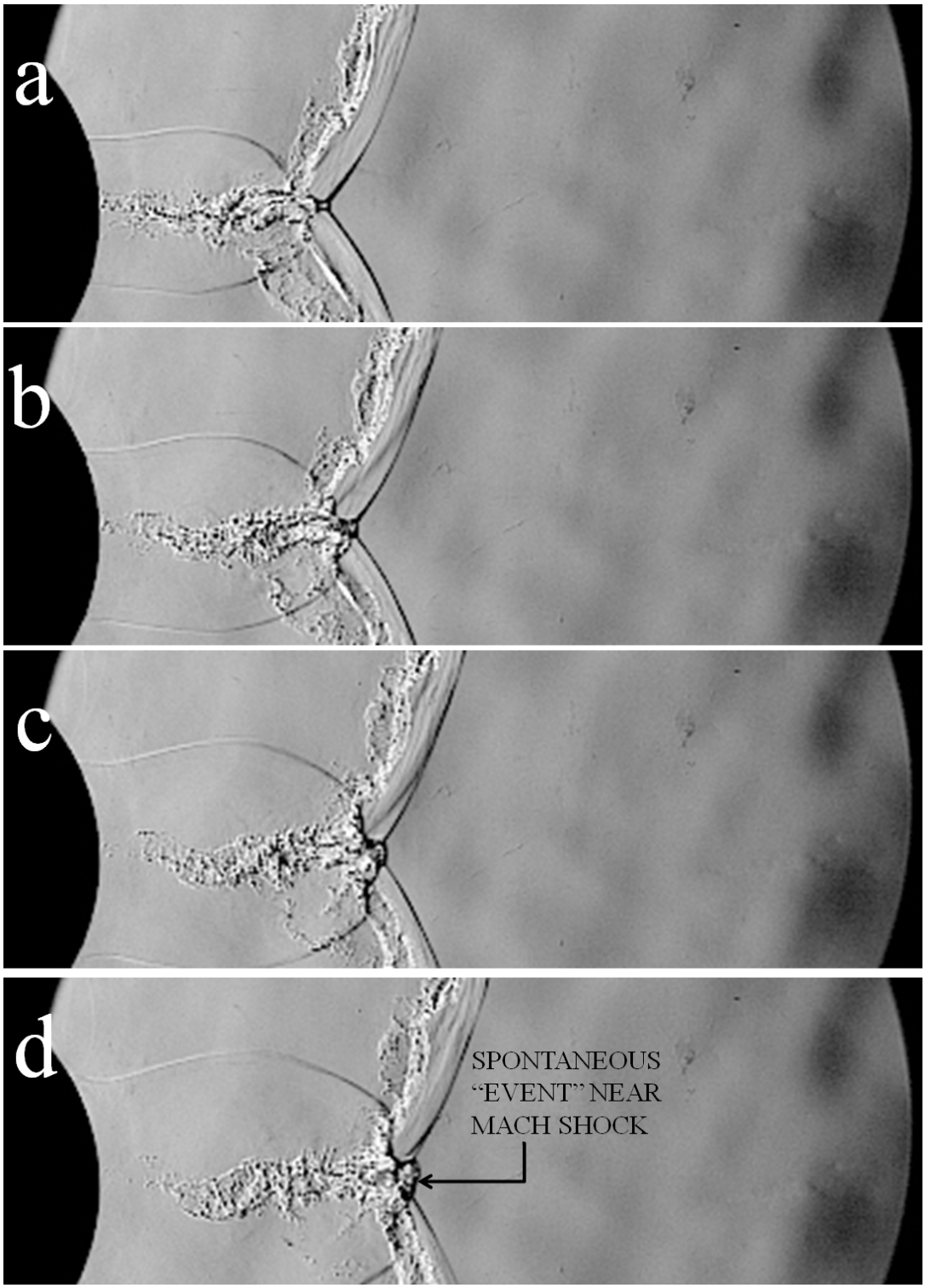

Figure 4.38: A flow field showing first a Mach reflection of a de-coupled shock-flame complex. A spontaneous event occurs near the Mach shock, which cannot be well resolved. The initial pressure and temperature was 16.8 kPa and 300K. All frames were obtained from the same experiment using the high speed video camera. *Test ID: CH4+O2-08-01-12(2.4psiTEST5)*

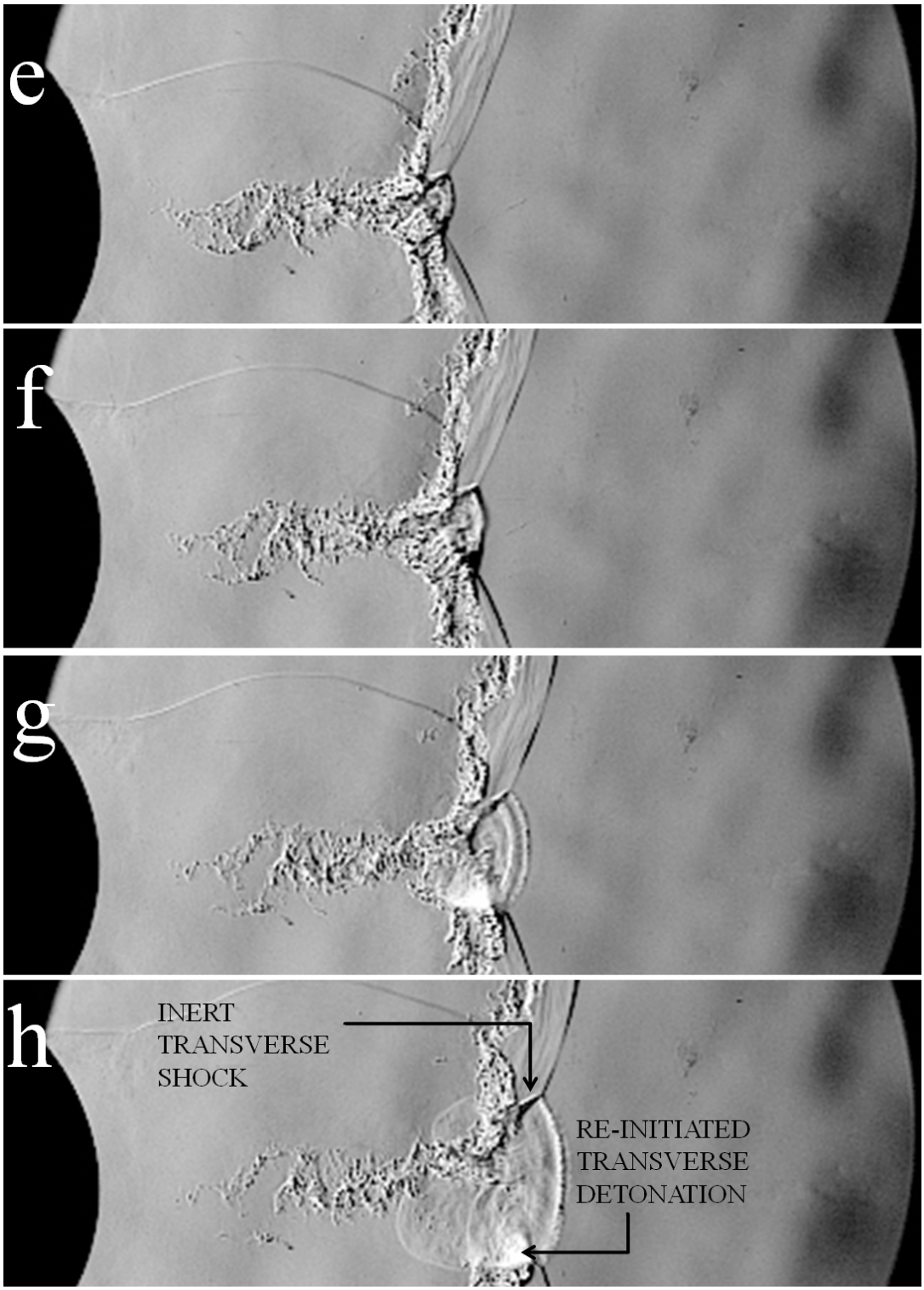

Figure 4.39: A continuation of the flow field immediately following the event shown in Fig. 4.38(d). At a later time detonation re-initiation occurs at the Mach shock. However an unusual case is observed where detonation re-initiation only occurs along the lower transverse wave while the upper transverse shock remains non-reactive. This is indicated by the long trailing unburned pockets of gas. The initial pressure and temperature was 16.8 kPa and 300K. *Test ID: CH4+O2-08-01-12(2.4psiTEST5)*

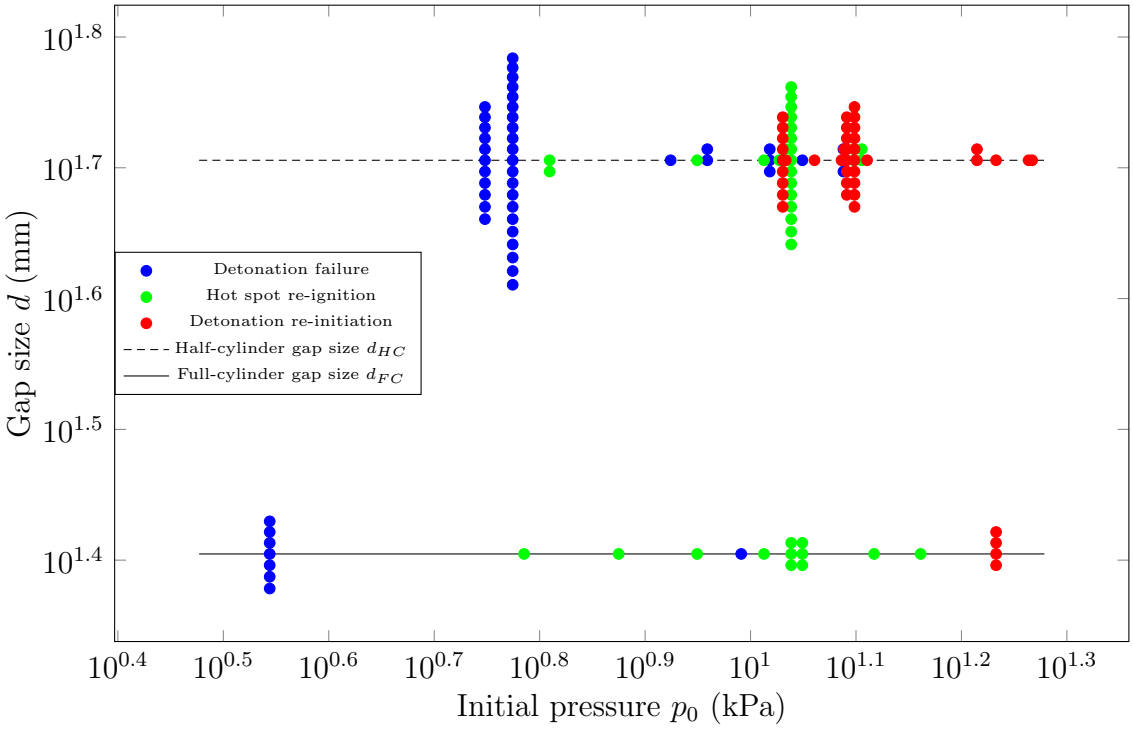

Figure 4.40: A summary of all experiments showing the different gas dynamic behaviours observed for different initial pressures.

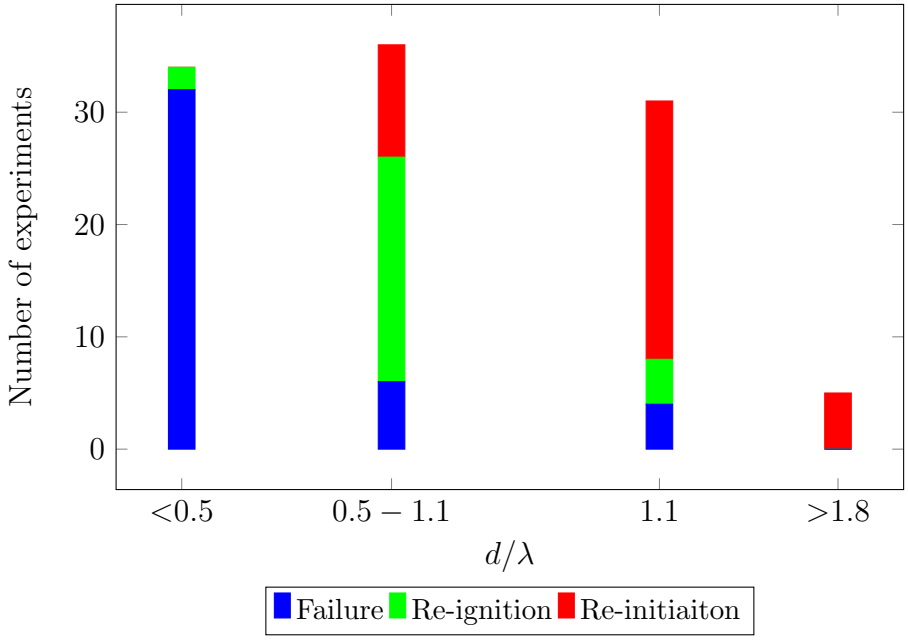

Figure 4.41: A histogram summary of all experiments illustrating the different detonation regimes observed using only the half-cylinder obstacle. Note that experiments using the roughness plate have been excluded.

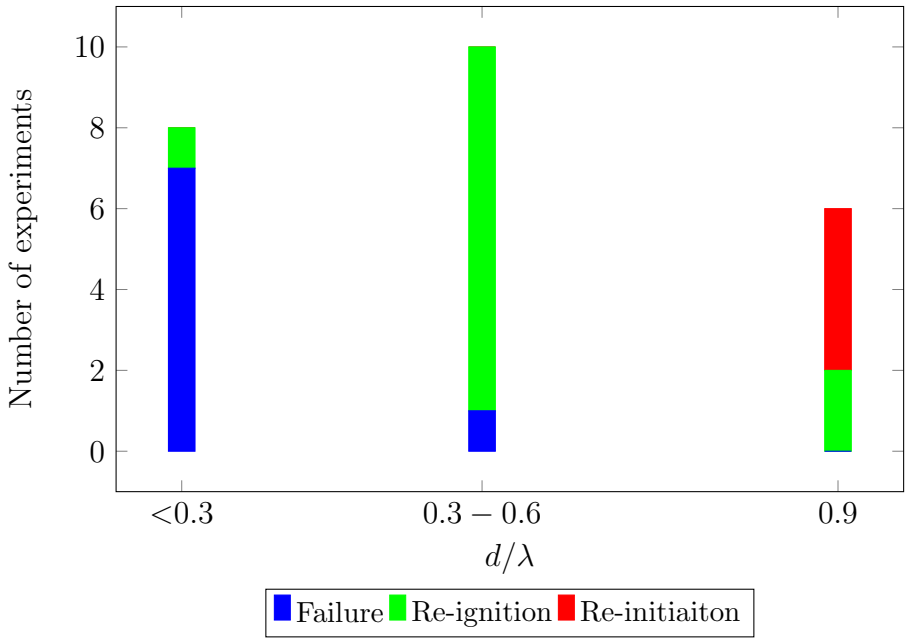

Figure 4.42: A histogram summary of all experiments illustrating the different detonation regimes observed using only the full-cylinder obstacle.

Chapter 5

Analyses and Discussions

5.1 Sequence of the re-initiation process into a detonation wave

This section summarizes the phenomenological observations made in Chapter 4. Here a sequence of events is provided, shown in Figs. 5.1 to 5.2, that illustrates a possible process of re-initiation into a detonation following the Mach reflection of a quenched detonation wave behind a cylinder. In doing so, we aim to identify specific events that are unclear.

Firstly, from Figs. 5.1(A) to (B), the relative distance between the flame interface and the Mach shock front decreases, following a Mach reflection of a de-coupled shock-flame complex (see Fig. 4.24); for simplicity the reflected shock wave is not shown. Figure 5.1(C) shows that the burned gas is then entrained by a forward jetting slip line, behind the Mach shock, to form a vortex of burned and unburned shocked gases (see Fig. 4.8). In some cases a kink was formed along the Mach shock following this entrainment (see Fig. 4.17). Next, after hot spot re-ignition occurs behind the Mach shock, Fig. 5.2(D) shows the flame appears coupled to the Mach stem and in some cases even causes a bifurcation of the Mach stem to create new triple points (see Fig. 4.21). However, for more reactive cases, Fig. 5.2(E) illustrates that the Mach shock re-initiates into a cellular detonation wave (see Figs. 4.31 and 4.28) and velocimetry confirms that it is an

overdriven detonation wave (see Fig. 4.30).

After the Mach shock has re-initiated into a detonation, Fig. 5.2(E) shows that in *some* cases a back propagating shock wave was observed (see Fig. 4.31(a)). This shock wave can interact with the tongue of unburned gas, behind a non-reactive transverse wave, and may increase combustion rates. This was supported by the observations of hot spot formation as shown in Figs. 4.8 (g) to (h), where a back propagating shock wave corrugates the unburned gas in the region close to the roughness plate, and also in Fig. 4.17 (j) to (l). Also observed were the vortical structures of the K-H instability along the slip line, as shown in Fig. 4.13, which may cause mixing locally. Figures 4.29(h) and 4.33(c) strongly suggest that the origins of the re-initiation of the transverse wave into a detonation was due to rapid combustion of the tongue of unburned gas behind it. Finally, from Fig. 5.2(F) both the transverse and Mach shock propagate as re-initiated detonation waves (see Fig. 4.32).

From the above description of the sequence of events, three main questions arises:

1. *Can we attribute the accelerating burning rates that lead to hot spot re-ignition, behind the Mach shock, to adiabatic shock compression alone?*

2. *Following hot spot re-ignition behind the Mach shock, was the flame observed laminar or not?*

3. *From the previous two questions what role, if any, do the mechanisms that lead to mixing between burned and unburned gas (forward jetting slip line, R-M and K-H instabilities) play in hot spot re-ignition that may lead re-initiation into a detonation?*

5.2 Predicting ignition delay in smooth wall tests

As mentioned earlier, it is unclear what mechanisms are responsible for accelerating the combustion rates and causing re-ignition to occur behind the Mach shock. To ascertain if shock compression alone is responsible for the re-ignition event behind the Mach shock, one can compare the presence of chemical reactions with predictions of ignition delay

times. Since such predictions assume negligible mixing, i.e. heat and mass transfer, such comparisons can be used to gauge the importance of mixing; a similar approach was used by Radulescu et al. [9] and Kiyanda and Higgins [8].

The general definition of ignition delay times, denoted henceforth as τ_{ig}, is the time delay from when a combustible mixture is brought to critical ignition conditions (e.g., by adiabatic shock compression), until a flame is "observed" [41]; Gardner [42] gives an excellent review of several techniques that are used to quantify when a flame is observed. In this work, the predicted ignition delay time $\left(\tau_{ig_{th}}\right)$ was calculated by first estimating the temperature and pressure behind the Mach stem of known strength, using NASA's CEA program (Appendix C) with frozen chemistry. Next, using the GRI mechanism (GRI-Mech) version 3.0 and a Cantera package (see Appendix D), $\tau_{ig_{th}}$ was predicted, for a constant volume, by tracking changes in the CH radical concentration.

From Chapter 4 it was observed that typically around $p_0 \approx 10$ kPa in the smooth wall tests, the hot spot re-ignition regime was characterized by localized regions of ignition kernels that occurred behind the Mach shock without artificially introducing them. Therefore, starting with these smooth walled experiments it is of interest to know if shock compression alone is a primary mechanism for causing ignition behind the Mach shock without artificially promoting chemical reactions.

As an example for the hot spot re-ignition case using the half-cylinder obstacle, consider the experiment shown in Figs. 4.10 and 4.11. Table 5.1 lists the predicted ignition delay times for varying Mach shock strengths as it propagates from left to right until ignition was observed in Fig. 4.10(e).

Table 5.1: Theoretical $\tau_{ig_{th}}$ values for Fig. 4.10 prior to and following localized ignition behind the Mach shock using the half-cylinder obstacle.

Mach no.	vN Temperature (K)	vN Pressure (kPa)	$\tau_{ig_{th}}$ (μsec)
4.5	1100	250	1.3×10^4
5.1	1300	320	9.2×10^2
4.9	1200	290	2.1×10^3
5.8	1600	420	5.1×10^1

From Table 5.1, typically the ignition delay time was greater than 900 μsec until ignition occurs leading to a stronger Mach shock strength or a smaller ignition delay of $\tau_{ig_{th}} = 51$ μsec. To get an upper-bound limit of the ignition delay from the experiments $\tau_{ig_{exp}}$, the inter-frame delay was added until hot spot re-ignition was observed behind the Mach shock, as shown in Fig. 4.10(e). This was done because the ignition observed may have occurred when particles, shocked at earlier times, propagated in the same direction as the Mach shock and auto-ignited after some delay. Thus, from experiments we have typically $\tau_{ig_{exp}} < 100$ μsec which implies $\tau_{ig_{exp}} < \tau_{ig_{th}}$.

Similarly, for the full-cylinder obstacle, consider the experiment shown in Figs. 4.20 and 4.21. Table 5.2 lists the predicted ignition delay times for varying Mach shock strengths as it propagates from left to right until ignition was observed in Fig. 4.21(g).

Table 5.2: Theoretical $\tau_{ig_{th}}$ values for Fig. 4.20 prior to and following localized ignition behind the Mach shock using the full-cylinder obstacle.

Mach no.	vN Temperature (K)	vN Pressure (kPa)	$\tau_{ig_{th}}$ (μsec)
4.7	1200	220	5.1×10^3
4.6	1100	210	1.3×10^4
4.6	1100	210	1.3×10^4
4.7	1200	220	5.1×10^3
4.4	1100	190	3.6×10^4
4.2	1000	170	1.0×10^5
4.0	960	160	3.1×10^5

Table 5.2 indicates that the ignition delay is at least of the orders of milliseconds. From the experiments, to obtain an upper-bound limit of the auto-ignition delay time, the inter-frame delay was added until Fig. 4.20(g) to yield $\tau_{ig_{exp}} < 200$ μsec. Therefore, the ignition delay parameter estimated from both experiments indicates that adiabatic shock compression alone may not be responsible for the flame formed behind the Mach shock.

Past researchers [42, 43] have noted that the ideal ignition delays predicted by the GRI-Mech 3.0 database deviate from experimentally measured ignition delays for very sensitive mixtures at low temperatures, particularly below 1300K. To account for these

discrepancies Gardner [42], in her Ph.D. study of auto-ignition delay times for methane mixtures, numerically modified a chemical kinetics tool (SENKIN), which uses the GRI-Mech 3.0 thermochemical database to predict ignition delays, by adding a volume oscillation parameter. Variation of this parameter resulted in changes in volume of an element, which was used to simulate periodic density (or temperature) fluctuations. These fluctuations in densities would simulate the inhomogeneities commonly observed in the hot spot re-ignition regime, where localized regions of intense chemical reactions can be found. It was found that for a specific range of this parameter, the changes in temperature with respect to constant volume estimations, were enough to recreate the experimentally measured ignition delay times for her study. She concluded that the non-ideal ignition behaviour (formation of hot spot ignition kernels) for methane mixtures at low temperatures can be attributed to the inhomogeneities in the flow field behind the reflected shock. In addition, turbulence also plays an important role by accelerating the diffusive processes thereby allowing the ignition kernels to grow.

5.3 Predicting ignition delay in the roughness tests

The auto-ignition delay calculations in smooth wall tests above showed that adiabatic shock compression may not be solely responsible for forming the flame behind the Mach shock. However, inhomogeneities in the flow field behind the Mach shock can spontaneously form localized hot spots owing to the strong sensitivity of the reaction rates to temperature. Such erratic behaviour can cause significant stochasticity in the flow field evolution and therefore throws some doubt on any predictive calculations. Indeed, it was noted that irreproducibility was observed in the hot spot re-ignition regime for the smooth walled tests. This served as a motivation to conduct experiments using the roughness plate at lower initial pressures (detonation failure regime). The roughness plate grooves can artificially introduce localized combustion behind the Mach shock and the effect the energy release has on the flow field evolution can be studied with relatively better reproducibility.

An experiment using the roughness plate and the half-cylinder obstacle is shown in Figs. 4.7 and 4.8. Table 5.3 lists the $\tau_{ig_{th}}$ parameter behind the Mach shock, as it propagates towards the right. The strength of the Mach shock was measured from the

time it enters the field of view until re-ignition was observed in Fig. 4.7(c).

Table 5.3: Theoretical $\tau_{ig_{th}}$ values for Fig. 4.7 prior to and following localized ignition behind the Mach shock using the half-cylinder and roughness plate.

Mach no.	vN Temperature (K)	vN Pressure (kPa)	$\tau_{ig_{th}}$ (μsec)
4.2	1000	150	8.7 $\times 10^4$
4.5	1100	160	2.6 $\times 10^4$
4.0	1000	130	3.2 $\times 10^5$
4.5	1100	160	2.6 $\times 10^4$
4.7	1200	180	8.3 $\times 10^3$
4.2	1000	150	8.7 $\times 10^4$

From Table 5.3, it is clear that typically the predicted ignition delay is approximately larger than 8 milliseconds behind the Mach shock. As a reminder, to get an upper-bound limit of the ignition delay from the experiments, the inter-frame delay was added until re-ignition was observed behind the Mach shock, as shown in Fig. 4.7(c). This was done, because, the ignition observed may have occurred when particles, shocked at earlier times, propagated in the same direction as the Mach shock and auto-ignited after some delay. Thus, from experiments we have typically $\tau_{ig_{exp}}$<100 μsec, which implies $\tau_{ig_{exp}} \ll \tau_{ig_{th}}$. This miss-match in time scales by two orders of magnitude suggests that the flame observed behind the Mach shock may not have formed due to simple adiabatic shock compression.

If shock compression alone was not responsible for hot spot re-ignition, then where did the flame come from? To determine the origins of the flame behind the Mach shock, the following calculations were carried out, as a first approximation attempt. Using Fig. 4.7(b), the measured strength of the Mach shock is $M_{bw} \approx 4.5$. From the known initial conditions of the mixture $p_0 = 7$ kPa and $T_0 = 300$K, the post shock conditions with frozen composition were computed as shown in Table 5.4.

Table 5.4: Temperature, pressure and density behind the Mach shock of known strength.

Mach no.	vN Temperature (K)	vN Pressure (kPa)	Density ρ_1 (kg/m^3)
4.5	1100	160	0.5

Next using the Python script shown in Appendix E, the equilibrated temperature and density were calculated by assuming that a gas pocket, inside a groove, equilibrates to the same post Mach stem pressure and maintains a constant enthalpy, as shown in Table 5.5.

Table 5.5: Conditions behind Mach shock after equilibrating at constant pressure-enthalpy.

Temperature (K)	Pressure (kPa)	Density ρ_2 (kg/m^3)
3200	160	0.1

From this, the expansion ratio was estimated to be approximately $\frac{v_2}{v_1} = 3.8$. Using the dimensions of the each groove, which has an approximate height, width and depth of 3.2 mm, 3.2 mm and 19.1 mm respectively, the final volume of the gas pocket, after it has equilibrated at constant pressure-enthalpy, is shown in Table 5.6

Table 5.6: Final volume of the gas pocket after equilibrating at constant pressure-enthalpy.

Expansion ratio, $\frac{v_2}{v_1}$	v_1 (mm^3)	v_2(mm^3)
3.8	200	740

It was assumed that the burned gas pocket expands from the groove such that only the height increases. An increase in this predicted height, measured from the bottom surface of the groove, was estimated to be $h_{th} = 12$ mm. From Fig. 5.3, the distance measured from the groove surface to the flame interface gives $h_{exp} \approx 8$ mm, which is comparable with the predicted value.

This first approximation analysis suggest that the flame was first formed due to localized combustion inside the groves of the roughness plate. Following expansion, the

hot burned products was then entrained by the forward jetting slip line to form the vortex, which is clearly visible in the Fig. 4.8.

5.4 Flame speed calculations

The ignition delay analysis suggests that adiabatic shock compression alone may not be responsible for combustion. Observations made in this work and by past researchers [3, 5, 7, 8, 16] indicate that mixing of hot burned products with cooler shocked reactants might increase reaction rates and lead to hot spot re-ignition behind the Mach shock. The objective here is to quantify if the flame observed was laminar or not. A non-laminar flame can accelerate to high velocities and, in extreme cases, spontaneously transition into an overdriven detonation wave (deflagration to detonation transition or DDT) [1, 44]. Therefore, to determine how non-laminar the flame observed was, one first-approximation approach is experimentally measuring the speed of the flame behind the Mach shock and comparing it with the predicted laminar flame speed (see Appendices F and D for additional details).

5.4.1 Absolute flame speed measurements

First, Fig. 5.4 shows the two frames that were used for the flame speed calculations. To estimate the absolute velocity of the flame tip points 1 and 2, as indicated in the Fig. 5.4, were selected. After calibrating the image, using the gap or tooth thickness of the roughness plate as a reference length, the absolute velocity of the flame tip was measured several times using Phantom's PCC application. From this the average absolute flame speed was estimated to be $u_{flame} \approx 1600$ m/s with the direction of the flame tip acting at an approximate angle of 30°.

Knowing the magnitude and direction of the flame tip speed, the vertical and horizontal components of the velocity vector, as shown in Fig. 5.5, were estimated. The component of the absolute flame velocity acting vertically was estimated to be approximately $u_{flame_Y} \approx 780$ m/s. This value will subsequently be used to determine to relative

velocity of the flame tip (see Section 5.4.3) in the vertical axis by using the formula,

$$v_{flame_Y} = u_{flame_Y} - u_{particle_Y} \tag{5.1}$$

5.4.2 Post Mach shock estimations

Figure 5.6 shows both images taken from Fig. 5.4 that were superimposed and modified to obtain an image where only the dark density gradients were retained. Also shown is point 1 on the Mach stem, close to the flame tip, in order to measure the velocity vector of the Mach stem.

Figure 5.7 shows a tangent was first drawn, at point 1, followed by a perpendicular until it met the second Mach shock front, at point 2. This distance was then measured between the two frames. With an inter-frame delay of 10 μsec, the velocity of the Mach stem was estimated. Using NASA's CEA program (see Appendix C), the post shock conditions were computed; the average post-shock temperature, pressure and particle velocity were estimated to be $T \approx 970$K, $p \approx 130$ kPa, $u_{particle} \approx 1200$ m/s acting at an angle 25° measured counterclockwise from the horizontal. The absolute particle velocity will be used to first calculate its vertical component and then determine the relative velocity of the flame tip in the vertical axis. The averaged post Mach shock conditions will be used as initial input conditions to predict the laminar flame speed in a 1D domain (see Section 5.4.3) using a Cantera package.

5.4.3 Burning flame velocity

Equation 5.1 was used to determine the burning velocity of the flame tip acting in the Y-axis denoted by v_{flame_Y}. Using the post-shock particle velocity and it's orientation, one can estimate the particle velocity component in the Y-axis, denoted by $u_{particle_Y}$. Thus, the average burning velocity of the flame tip acting in the vertical direction was estimated from the experiment to be $v_{flame_Y} \approx 280$ m/s.

The theoretical laminar burning velocity in a 1D domain was determined using the GRI-Mech 3.0 database and Cantera object-oriented package (Appendix D) using the

averaged post shock conditions of $T = 970$K and $p = 130$ kPa. The laminar flame velocity was predicted to be $v_{flame_{th}} \approx 14.0$ m/s.

Comparing $v_{flame_{th}} \approx 14$ m/s with $v_{flame_Y} \approx 280$ m/s, it is clear that the experimentally measured flame tip speed is greater than the predicted laminar burning velocity by a factor of 20. This first approximation analysis shows that the flame is indeed non-laminar behind the Mach stem, which can also be seen from the pictures. From the experimental results shown, this departure from a laminar flame structure could potentially be due to the jet entrainment of burned gas with unburned gas by the forward jetting slip line.

5.5 Mechanisms that cause mixing between burned and unburned gases

5.5.1 Forward jetting slip line

Figures 4.8, 4.19, 4.21, 4.24, 4.17 qualitatively show the forward jetting slip line(s) mixing products with reactants prior to hot spot re-ignition behind the Mach shock. While this study attempted to quantify that:

1. shock compression alone may not be a dominant mechanism;
2. the vortex formed is non-laminar following the forward jet effect,

no direct justification was provided if indeed the flame interface was being jetted forward behind the Mach shock by a strong forward jet effect. Past researchers [12, 13] have shown that when the jet effect of the slip line is severe it can reach the Mach shock and cause it to form a "bulge". This in turn can give rise to a "kink" in the Mach stem, which eventually forms a triple point and hence bifurcating the Mach stem (Fig. 5.8).

Mach [12] investigated the bifurcation mechanism of a Mach shock reflection, over a compressive ramp, for both inert shocks (see Fig. 5.9) and for irregular detonations. He used an Euler model (reactive for detonations) with a perfect gas and constant specific

heats and molecular weight. For his numerical study, three parameters were varied, as shown in Fig. 5.9 - the strength of the incident shock (M_I), the ramp angle (θ_w) and the post shock specific heat ratio (γ_1). Overall, he noted that the propensity for the Mach shock to bifurcate (hence strong jet effect) increased when the shock strength and ramp angle were increased while decreasing the specific heat ratio.

Now consider Fig. 5.10, which shows a typical Mach shock reflection that follows after a detonation wave diffracts behind the full-cylinder obstacle, as discussed several times in Chapter 4; the Schlieren image was specifically selected from the experiment shown in Fig. 4.20, which showed a strong Mach stem bifurcation.

Since the shock reflection process is almost symmetric about the reflective surface, Fig. 5.11(a) shows only the upper half with the pertinent parameters labeled with the reaction zone and reflected shock wave omitted for simplicity. The pertinent parameters labeled are - the incident shock strength (M_I), the angle between the tangent to the incident wave and the vertical axis (θ_I) and the specific heat ratio in state 1 (γ_1). It was assumed that the shock wave has negligible curvature near the triple point.

By rotating Fig. 5.11 (a) counter-clockwise by angle θ_I, the incident shock wave is now vertical while the reflective surface makes the same angle θ_I with the horizontal. Thus, comparing Fig. 5.11(b) with Fig. 5.9 (b) it is clear that angles θ_I and θ_w are equivalent. For the stated initial conditions of $p_0 = 8.4$ kPa, $T_0 = 300$K, from Fig. 5.10 the following measurements were obtained:

- Incident shock strength (M_I) ≈ 3.5
- Incident shock angle (θ_I) $\approx 30^\circ$
- CEA post shock specific heat ratio (γ_1) ≈ 1.2

It should be noted that the measured shock strength and angle were approximated and can vary (recall uncertainty of 21% for shock velocity). Figures 5.12 and 5.13 shows the numerical simulation results of a non-reactive Mach shock reflection for incident shock strengths of $M_I = 3$ and $M_I = 4$, respectively, with $\theta_I = 30^\circ$ and $\gamma_I = 1.2$.

As per Mach's findings, by increasing the strength of the incident shock wave from $M_I = 3$ to $M_I = 4$, the forward jet effect of the slip line is more prominent in the latter case. In regards to the severity of the jet effect, $M_I = 3$ case does not bifurcate the Mach stem. The $M_I = 4$ case, however, appears to develop a distinct bulge on the foot of the Mach stem but it does not cause a strong bifurcation, as shown in Fig. 4.21(h). While no bifurcation is predicted for the given input velocity range, the bifurcating limit for the non-reactive shock reflections appears to be close to the conditions that cause re-initiation. However, this requires further investigation. In conclusion, this numerical simulation confirms the existence of a strong forward jet effect of the slip line that can develop a kink, as the foot of the Mach stem bulges, but not severe enough to bifurcate it for the given input parameters.

5.5.2 Hydrodynamic instabilities

This work strongly confirmed the findings by past researchers (see Section 1.3.1) that both the K-H instability and forward jetting slip line are present along the slip line behind the Mach shock. While the findings of this study suggest that the forward jet effect of the slip line behind the Mach shock appears to be an important mechanism in causing hot spot re-ignition, it is unclear if both the K-H instability and forward jetting slip line act simultaneously in causing detonation re-initiation. Figures 4.8 and 4.17 clearly showed the corrugation of the tongue of unburned gas behind the transverse shock, punctuated by hot spot formation. This, presumably, was indicative of an increase in combustion rate behind the transverse shock as a back propagating shock wave processed it. However, the presence of the R-M instability behind the transverse wave was not observed from the experimental results. Therefore, without any quantitative analysis, it is unclear if the R-M and K-H instabilities play a simultaneous role in causing rapid ignition that can lead to re-initiation into a detonation.

5.6 Summary

The phenomenological observations made in Chapter 4 gave detailed insight into the flow field evolution. This provided a possible sequence of events that clarified the process of

re-initiation into a detonation. From these qualitative findings, three main questions were posed that required quantitative clarification: a) *Does adiabatic shock compression alone lead to increased combustion rates?*; b) *How non-laminar is the flame observed behind the Mach shock, following re-ignition?*; c) *How important are the mixing mechanisms in increasing combustion rates that can lead to re-initiation into a detonation?*

Using Cantera and the GRI-Mech 3.0 thermo-chemical database, the auto-ignition time delay behind the Mach shock was predicted and compared to experimentally measured values. Results revealed that for both smooth and rough walled experiments the ideal ignition delay time was orders of magnitude greater than the experiments indicated. This strongly suggested that adiabatic shock compression alone may not be responsible for the re-ignition observed behind the Mach shock.

From the roughness tests, following hot spot re-ignition and flame entrainment by the forward jet behind the Mach shock, the flame morphology appeared to be non-laminar. To quantify that this flame structure was indeed non-laminar, the measured burning velocity of the flame tip was compared to the predicted laminar flame speed calculated using Cantera and GRI-Mech 3.0 database. Results showed the measured burning velocity was greater that the predicted laminar flame speed by a factor of 20 indicating the flame was non-laminar.

Earlier analyses showed that adiabatic shock compression may not be solely responsible for causing ignition behind the Mach shock. Furthermore, the flame observed was highly non-laminar following entrainment of burned gas with unburned gas by the forward jetting slip line. However, there was no justification if a strong forward jet effect is indeed causing the flame interface to jet forward. A strong forward jet can cause the Mach shock to bulge and eventually bifurcate. To address this, a numerical simulation of the Mach reflection process on a compressive ramp using a non-reactive Euler model was reported, courtesy of Lau-Chapdelaine. The input parameters were the incident shock strength, the ramp angle and the post incident shock specific heat ratio, which were experimentally measured. Numerical results agreed with experiments by predicting a strong forward jet effect that caused the Mach shock to bulge and form a kink. However, it was not severe enough to bifurcate the Mach shock. Finally, since no quantitative analyses were performed to study the effect K-H and R-M instabilities have on the mechanisms that lead to re-initiation into a detonation, no conclusions were drawn.

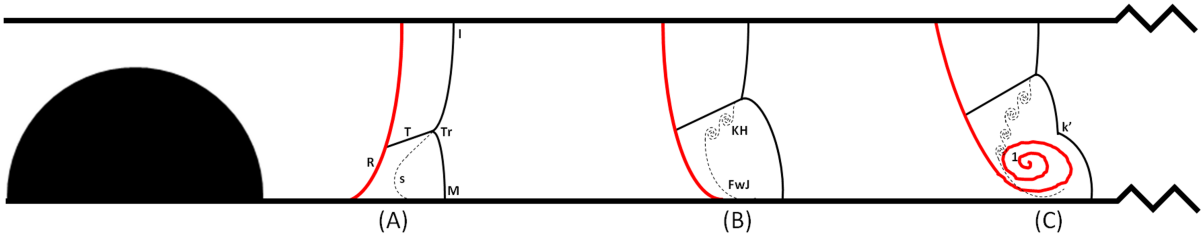

Figure 5.1: A schematic diagram illustrating a possible sequence of events leading to re-initiation of the Mach stem and transverse shock into a detonation. Note for simplicity the reflected shock wave has been omitted. Label descriptions: incident shock (I); Mach stem (M); transverse shock (T); triple point (Tr); slip line (s); reaction zone or flame interface (R); Kelvin Helmholtz (K-H) instability; forward jet (FwJ); kink (k'); entrained products and reactants (1).

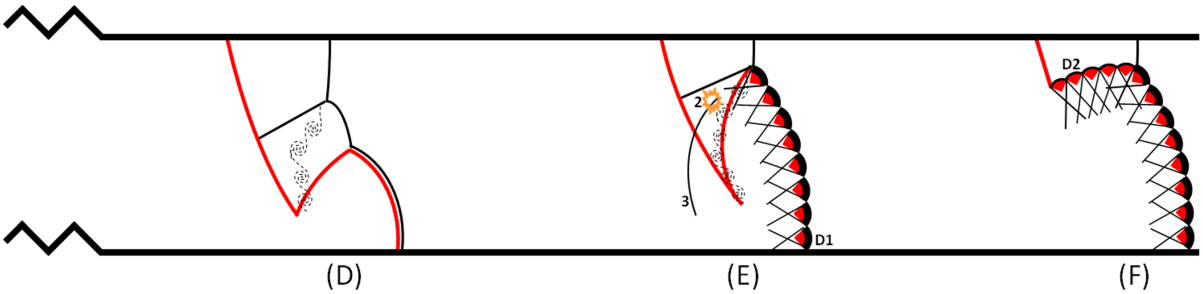

Figure 5.2: A continuation from Fig. 5.1. Label descriptions: Mach detonation (D1); transverse detonation (D2); rapid exothermic reaction (2); back propagating shock (3).

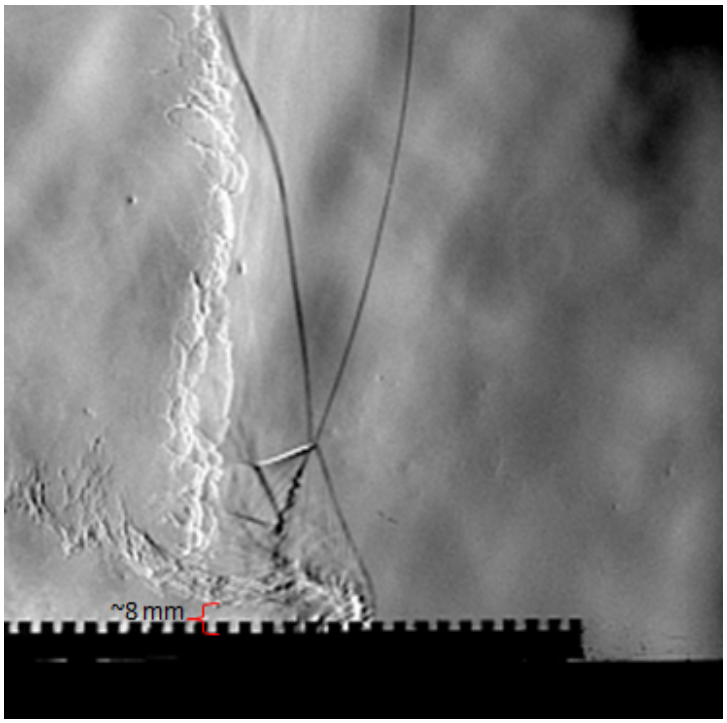

Figure 5.3: Figure showing the height of a layer of burned gas, measured from the bottom surface of the groove, after it has expanded.

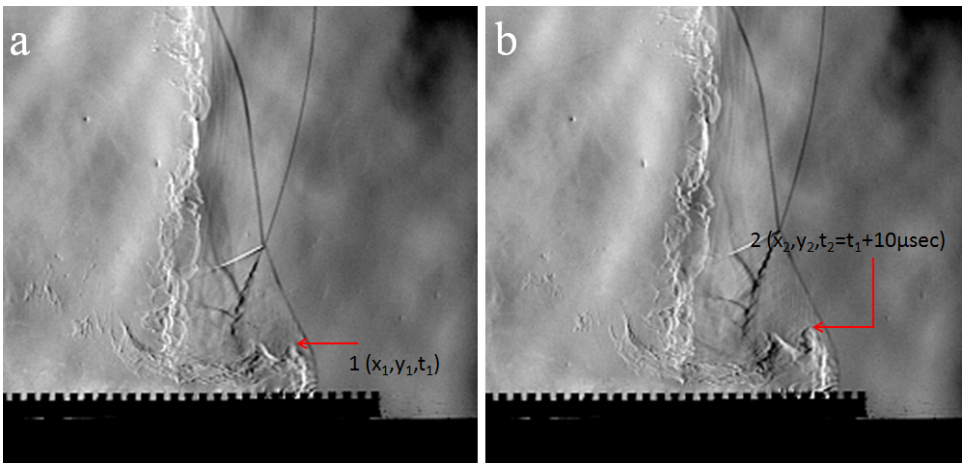

Figure 5.4: Two sequential Schlieren images showing a flame growth behind the Mach shock over the roughness plate behind the half-cylinder obstacle. The initial pressure and temperature was 7 kPa and 300K. Both successive images are 10μsec apart and were recorded using the high speed video camera.

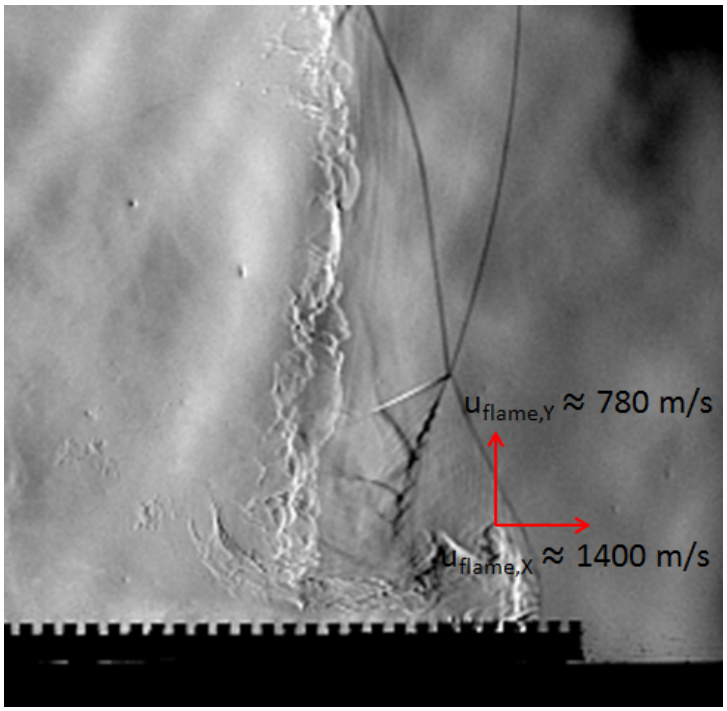

Figure 5.5: A Schlieren image showing the measured velocity component vectors of the flame tip along the vertical and horizontal directions.

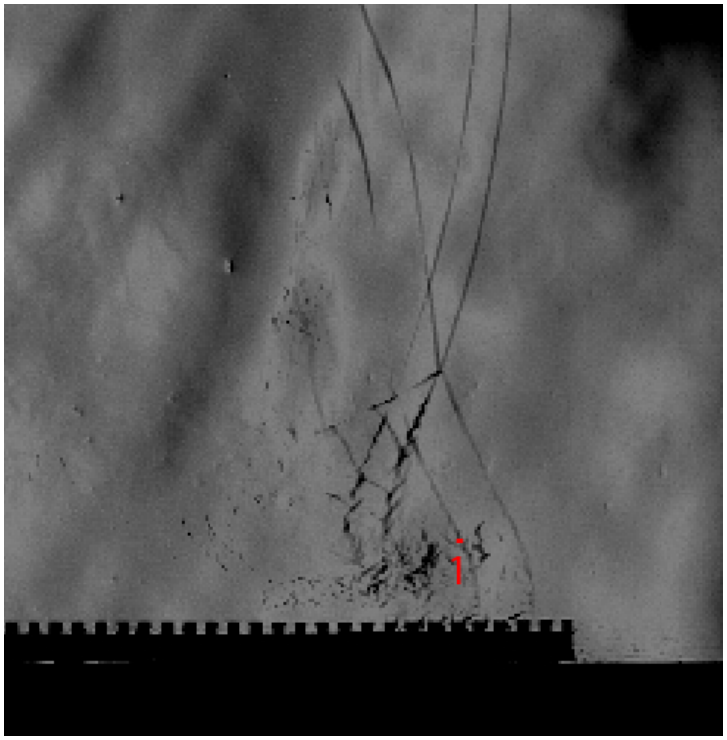

Figure 5.6: A modified Schlieren image wherein two sequential frames (Fig. 5.4) are superimposed with the lighter density gradients subtracted. Also shown is the selected point on the Mach shock front that is approximately close to the flame tip.

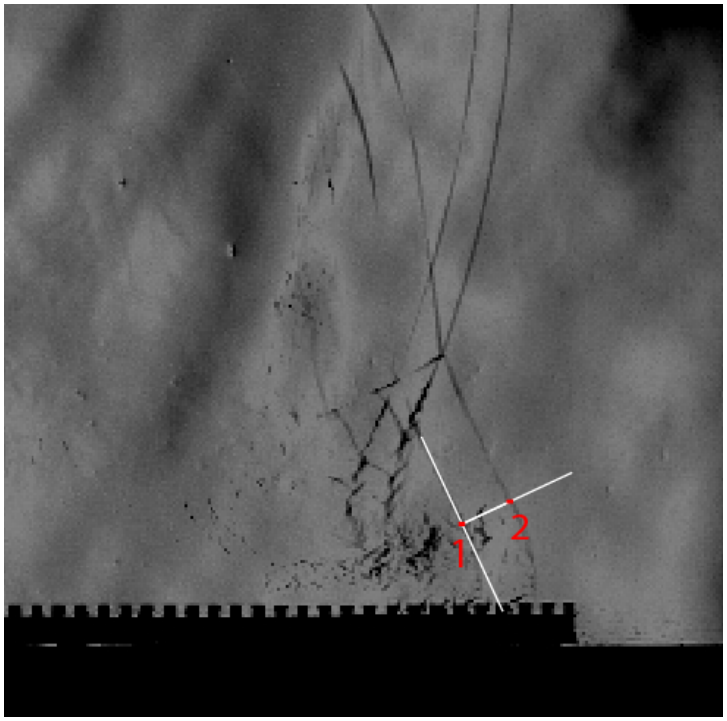

Figure 5.7: The modified Schlieren image now showing the perpendicular drawn to the tangent on the first point that meets the second Mach shock front. These two points were used to measure the displacement and hence calculate the local velocity of the Mach shock in the vicinity of the flame tip.

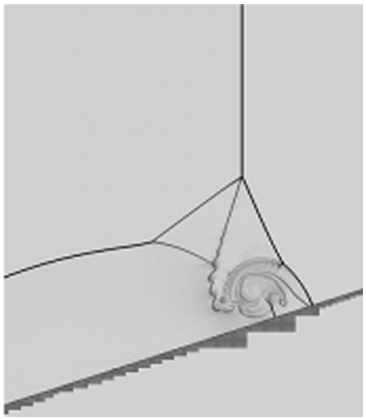

Figure 5.8: A Schlieren numerical image showing the bifurcation of the Mach stem. Image courtesy of P. Mach [12].

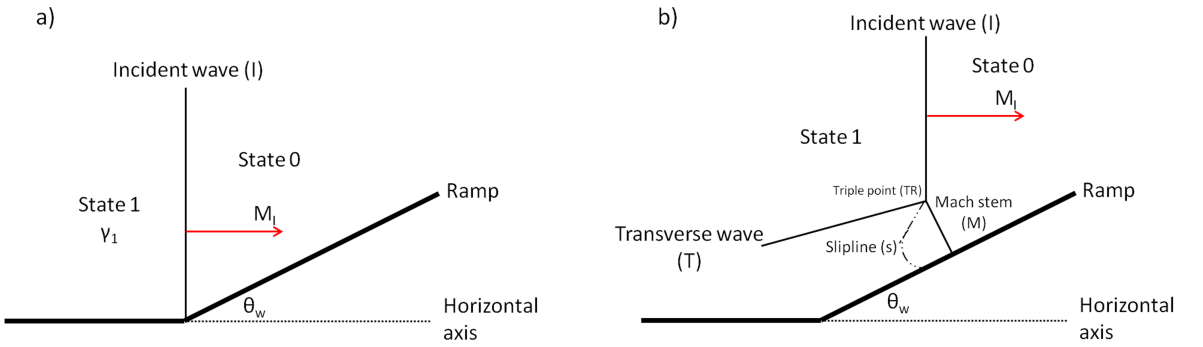

Figure 5.9: A schematic diagram showing a Mach reflection of an inert shock over a compressive ramp used in the bifurcating Mach shock study by P. Mach [12].

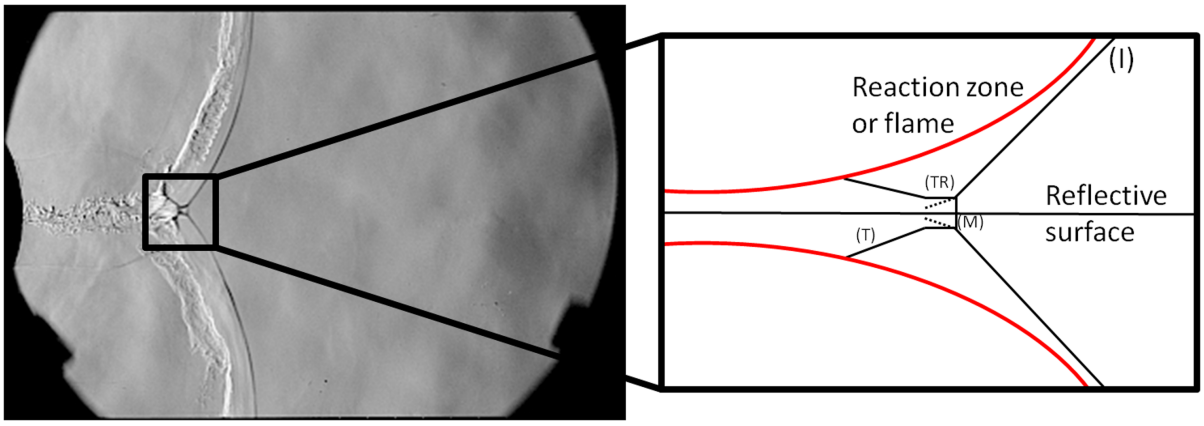

Figure 5.10: The Schlieren image on the left was taken from Fig. 4.20. The schematic diagram on the right shows typical features of a reactive Mach reflection of a de-coupled shock-flame complex. Labels shown are as follows: incident wave (I), triple point (TR), Mach stem (M), transverse wave (T) and the de-coupled reaction zone or flame trailing behind.

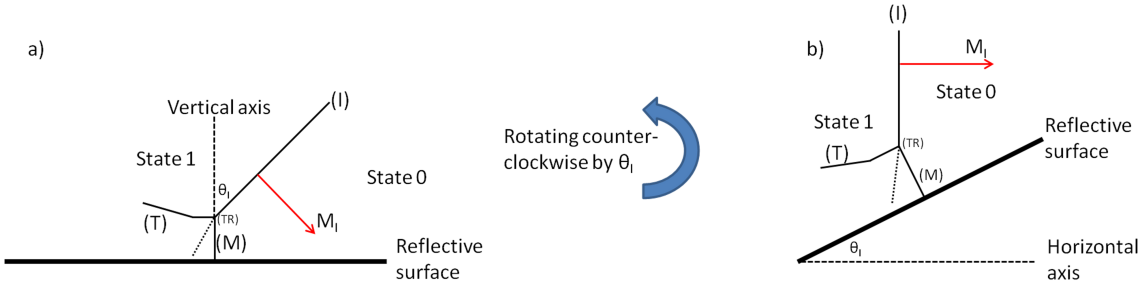

Figure 5.11: Figure (a) shows a schematic diagram that illustrates the Mach reflection process with pertinent parameters labeled. Figure (b) shows a schematic diagram that illustrates the same Mach reflection as Fig. (a) after rotating counter-clockwise by angle θ_I. For simplicity the reflected shock wave has been omitted from the schematic diagram.

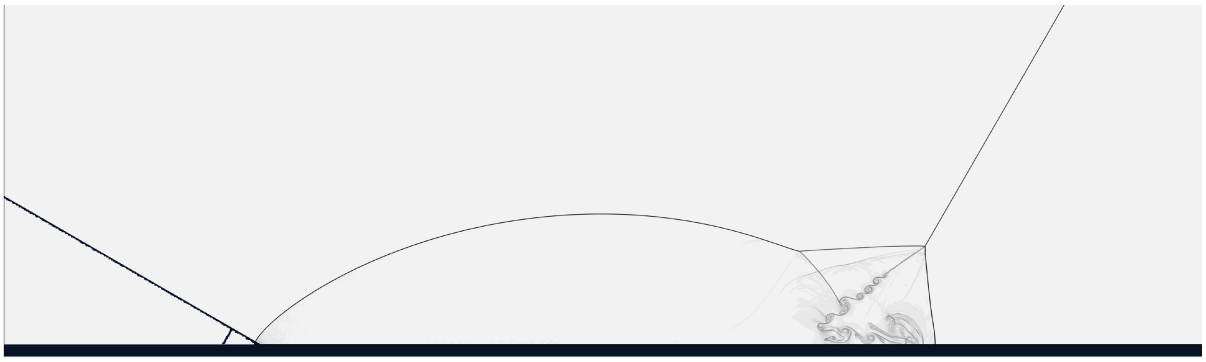

Figure 5.12: A Schlieren numerical simulation showing the forward jet effect of the slip line behind the Mach shock. The input parameters are: $M_I = 3$, $\theta_w = 30^\circ$ and $\gamma = 1.2$. Here, the forward jet is not strong enough to cause a distinct Mach shock bifurcation. Image courtesy of S. S. Lau-Chapdelaine.



Figure 5.13: A Schlieren numerical simulation showing the forward jet effect of the slip line behind the Mach shock. The input parameters are: $M_I = 4$, $\theta_w = 30^\circ$ and $\gamma = 1.2$. Here, the forward jet appears strong enough to cause a kink in the Mach shock. Image courtesy of S. S. Lau-Chapdelaine.

Chapter 6

Conclusions and Recommendations

6.1 Conclusions

During the propagation of a cellular detonation wave, a periodic process occurs at the start of each cell cycle wherein a Mach reflection of a de-coupled shock-flame complex is followed by an overdriven detonation wave. This study addressed this process of re-initiation into a detonation by elucidating key mechanisms, identified by past researchers, that can increase combustion rates and potentially lead to re-initiation of a quenched detonation. For this experimental study, cylindrical obstacles of varying diameters were used to quench the detonation wave into a shock-flame complex, which have been used by past researchers to study the process of re-initiation into a detonation with better reproducibility and higher spatial resolutions. The gas mixture used was stoichiometric oxy-methane.

Re-initiation into a detonation was first observed along the foot of the Mach shock, provided the initial pressure was sufficiently high. It was observed that the forward jet effect of the slip line, behind Mach shock, appeared to play an important role by entraining hot products into cooler reactants, potentially increasing reaction rates. This observation was supported by qualitative findings using high resolution Schlieren images from both smooth and rough walled experiments, where a roughness plate was placed along the wall. In addition the measured ignition delay times differed from the predicted

auto-ignition delay time, by orders of magnitude. This strongly indicated that adiabatic shock compression alone cannot account for the local ignition kernels present behind the Mach shock, which past researchers have also found. Furthermore, comparison of the measured flame speed, formed behind the Mach shock, to the predicted laminar flame speed was found to be greater by a factor of 20 thus suggesting that the flame was indeed very non-laminar.

When the Mach stem first re-initiated into an overdriven detonation, it had a very fine cellular structure while the transverse shock wave remained non-reactive. Behind the non-reactive transverse wave, a tongue of unburned gas was observed whose corrugated structure appeared to be punctuated by hot spot formation. The Kelvin-Helmholtz instability along the slip line was clearly evident. In addition, following rapid re-initiation of the Mach shock into a detonation, in some cases, a back propagating shock wave was observed which propagated through the density gradients of the unburned tongue of gas. Such interactions may cause significant vorticity due to the baroclinic mechanism to yield the Richtmyer-Meshkov instability. However, the findings of this work cannot confirm the presence of the R-M instability. While past researchers have suggested that such hydrodynamic instabilities can play a role in causing mixing between burned and unburned gases, the findings of this study remain inconclusive regarding the true impact these instabilities have on the process that cause re-initiation into a detonation. Nevertheless, the rapid reaction of this gas may be at the origin of the transverse detonations observed in most experiments.

6.2 Recommendations for future work

The work presented here is exclusively based on a stoichiometric oxy-methane mixture. This mixture is known for its high effective activation energy, irregular detonation cellular pattern, unstable behaviour characterized by spontaneous transverse wave formation and large fluctuations in the velocity amplitude during a single cell cycle [1, 2]. In contrast, a mixture such as hydrogen-oxygen diluted with argon has a smaller activation energy, a more regular cellular pattern, weaker acoustic transverse waves and little indication of formation of large islands of unburned gas that is often found in irregular mixtures during detonation propagation. Thus, it is believed that the propagation mechanism

for a regular mixture might very well be different from that of an irregular mixture [7]. Hence, it is suggested that the series of experiments described here be performed on a regular mixture to see if the forward jetting effect is found; Radulescu [31] lists different gaseous mixtures along with their cellular regularity. It is further recommended to start with a lower initial pressure ($p_0 \lesssim 7$ kPa) to first obtain the failure regime such that the flow field evolution without the complexity of any energy release may be studied.

Since all calculations originate from velocimetry of the shock front, it is of paramount importance to develop more accurate methods of measuring the velocity at different points along the body of the shock wave. This is especially important if the post-shock flow field parameters are needed for a curved shock wave; the Mach shock formed following an irregular reflection is always found to be curved. The issues with the technique presented in Section 5.4.2 is that it is a highly approximated manual approach which is susceptible to human error. Thus, it is recommended that an algorithm be developed that can automate the task as well as accurately measure the shock strength, at different points along the body of the shock front, by utilizing edge detection methods. It should be noted that background subtraction should be carried out first before using such algorithms to minimize edge detection errors.

Radulescu [31] experimentally studied the failure mechanisms of a detonation wave in porous walled tubes and rectangular channels. He noted that for a heavily diluted hydrocarbon mixture, if the internal width (w) of the channel was slightly smaller than the cell width (λ), the transverse waves oscillated primarily along the channel height. If, however, the internal width was much smaller than the cell width $\left(w \ll \frac{1}{3}\lambda\right)$, the effect of boundary layers begin to play a role in the propagation mechanism of the detonation wave. For an internal width of 19 mm, this implies a cell width typically greater than 60 mm or an initial pressure typically lower than 10 kPa (see Fig. 2.18), which represents the detonation failure regime in this work. While the shock tube was designed to suppress the transverse perturbations to yield a 2D flow (see Chapter 2), the inevitable presence of boundary layers along the channel walls add more non-idealities to the flow thus making it 3D. In addition, when the reflected shock interacts with the density gradients in the boundary layer, the vorticity generated by the R-M instability can cause mixing thereby introducing more inhomogeneities to the flow field. It is therefore recommended to investigate the 3D effects (boundary layers) might have on the process that leads to re-initiation into a detonation.

Appendix A

Uncertainty Estimation

By knowing the inter-frame delay, the velocity of a moving shock wave can be determined simply by measuring the distance traveled. Measuring this distance, however, was carried out manually and this approach can introduce uncertainty because the shock wave has a finite thickness (or finite number of pixels). This makes it challenging to choose the same point on the shock wave between two frames. The uncertainty is further compounded by poor camera resolution as choosing the same point becomes increasingly difficult if the number of pixels per unit length (pixel/mm) is low. As a reminder, the high speed video camera had a poorer resolution (384 by 288) as compared to the double-framing camera (2112 by 2072). The following approach was used to determine the maximum percentage uncertainty in velocity. To determine the maximum uncertainty, frames from the high speed camera were used.

Firstly, several high speed videos were randomly chosen. Each video was then calibrated, within the PCC application, by manually measuring the height of the channel (203.8 mm) as the known reference length. After calibrating, PCC automatically displays the mm/pixel scaling ratio. Note that since the reference length was measured manually, the scaling ratio can vary. From the randomly selected videos, the maximum scaling ratio was found to be 0.879 mm/pixel.

After determining the maximum scaling ratio to be 0.879 mm/pixel, a few frames from one of the high speed videos was then chosen at random. The thickness of the Mach

shock was determined by counting the number of pixels in the horizontal direction. The number of pixels that contribute to the shock thickness was found to vary between 2 to 5 pixels; with 5 pixels, the deviation from the mean pixel is 2. Thus, one can obtain the deviation in measuring the shock thickness as follows,

$$\begin{aligned} Uncertainty\,in\,thickness &= no.\,of\,pixels \times scaling\,ratio && \text{(A.1)} \\ &= 2 \times 0.879\,\frac{mm}{pixel} && \text{(A.2)} \\ &= 1.758\,mm && \text{(A.3)} \end{aligned}$$

To calculate the uncertainty in shock velocity measured between two frames, consider as an example from *TEST ID: CH4+O2-08-03-12(1.49psiTEST4)*, the inter-frame delay as 6.03 μsec. Using this interval delay the uncertainty in velocity can be estimated as,

$$\begin{aligned} Uncertainty\,in\,velocity &= \frac{Uncertainty\,in\,thickness}{time\,interval} && \text{(A.4)} \\ &= \frac{1.758 \times 10^{-3}\,m}{6.03 \times 10^{-6}\,sec} && \text{(A.5)} \\ &= 291.5\,\frac{m}{sec} && \text{(A.6)} \end{aligned}$$

Finally, the maximum percentage uncertainty in velocity was found by dividing the velocity uncertainty with smallest measured shock velocity. From *TEST ID: CH4+O2-08-03-12(1.49psiTEST4)*, this was found to be 1391 m/s. Hence, our maximum uncertainty percentage was estimated as,

$$\begin{aligned} Percentage\,uncertainty &= \frac{Uncertainty\,in\,velocity}{measured\,velocity} \times 100 && \text{(A.7)} \\ &= \frac{291.5\,\frac{m}{sec}}{1391\,\frac{m}{sec}} \times 100 && \text{(A.8)} \\ &= 20.9\% && \text{(A.9)} \end{aligned}$$

This maximum percentage uncertainty was rounded off to 21% and applied to data points measured from the high speed videos.

Appendix B

High Voltage Igniter (HVI) System

Appended below is the HVI manual prepared by Sev Kamenskih, who designed and built the HVI system.

B.1 Description

The HV Igniter is a compact, versatile high voltage ignition system designed to provide a high current pulse of a fast rise time. The main components of the HV Igniter are the high voltage capacitor bank (consisting of 2 General Atomics capacitors #31158), the spark gap (Perkin Elmer GP-41B) and the TM-11A trigger module for triggering the spark gap. Although HV Igniter was designed for use as an initiation source for detonations/gas dynamics research experiments it can be used in any high current pulsed application such as electromagnetic launcher , pulsed high power laser, railgun and others. The unit is capable of storing of up 1000J of energy and releasing that energy in a form of a high current pulse (up to 35,000A) with a rise time less than 2μs. In order to protect the user from potentially lethal voltage and current levels HV Igniter has two important safety features: the safe discharge grounding switch that safely grounds the terminals of high voltage capacitor bank and the grounded aluminum frame surrounded by a steel cage that houses all the internal components and prevents any charge transfer outside of the system.

B.2 Specifications

Electrical Input:
Voltage 0-32kVDC
Current 0.5-2.5mA
Power 80W

Electrical Output:
Voltage Range 15-32kV (based on use with GP-41B spark gap)
Peak Current 35,000A (@ $V_{\text{initial}} = 30\text{kV}$)
Stored Energy up to 1000J ($0.5CV^2$ @ 32kV)
Pulse width $>3.5\mu$s (@ 1/3 of peak amplitude)
Rise Time $<2\mu$s (measured from 10% to 90% points on leading edge of output pulse)

Mechanical:
Input Cable RG 8/U (for charging), Standard 110/230 VAC, 50/60Hz 3 wire cord (for TM-11A trigger)
Output Cable RG 8/U
External Trigger BNC jack
Remote Trigger Jones plug receptacle
Ground Connection Braided grounding cable 4 gauge with 5/8" lug end.
Controls Off-On Safe Discharge Lever, Off-On trigger push button
Size 12 in. x 36 in. x 14 in.
Weight 70 lb

B.3 Operation

Warning! Do not handle the load or exposed high voltage terminals or attempt to make or remove any connections to HV ignier until the load and/or power supply has been discharged (grounded) . This is done by switching the grounding lever into off position. Make sure there is a firm contact between the lever and the terminals to be grounded. Always make certain that the ground terminal of the HV igniter and the ground terminal of the power

supply are connected to the ground.

B.3.1 Charging the capacitor

1. Switch the grounding lever to the ON (vertical) position.
2. Turn on the power supply and rotate the current control clockwise to the level of <2.5mA . Rotate the voltage control clockwise to the desired level (15-30kV). Wait for charging to complete. (i.e. when current level drops to zero).
3. For repeated firing leave the power supply ON for the next charging cycle to start right after previous one is complete. For single firing turn OFF the power supply to prevent capacitor recharge after firing. Move on to the discharge phase.

B.3.2 Discharging (firing) the capacitor

1. For detonation/gas dynamics experiments: make sure the output electrodes are isolated in your chamber (ie. not in direct contact with any object, except the test mixture).
2. Fire the capacitor by either pushing the trigger button on the TM-11A trigger module or by pushing the remote trigger button.
3. IMPORNANT: After the discharge is complete switch the grounding lever to the OFF (inclined) position by firmly closing it. For safety avoid any personal ground contact during this step.

B.3.3 Guidelines for high voltage work

• Dont work alone - in the event of an emergency another persons presence may be essential.
• Know the emergency procedures to follow in case of an accident (dial 911).
• De-energize the equipment at least twice prior to beginning work. Make sure the capacitor is discharged, or relieved prior to starting work that is the grounding switch is firmly closed (inclined position).
• After you have discharged everything, only touch the circuit with the back of your

hand first. This allows you to let go if you need to.
• Never enter alone into an area containing exposed electrical energy sources.
• Use only the test instruments, and insulated tools rated for the voltage and current specified.
• Always keep one hand in your pocket when anywhere around a powered line-connected or high voltage system.
• Wear rubber bottom shoes or sneakers.
• Dont wear any jewelry or other articles that could accidentally contact circuitry and conduct current, or get caught in moving parts.
• Set up your work area away from possible grounds that you may accidentally contact.
• Know your equipment.
• If you need to probe, solder, or otherwise touch circuits with power off, discharge (across) large power supply filter capacitors (at least 2 times). Monitor while discharging and/or verify that there is no residual charge with a suitable voltmeter.
• If you must probe live, put electrical tape over all but the last 1/16" of the test probes to avoid the possibility of an accidental short, which could cause damage to various components. Clip the reference end if the meter or scope to the appropriate ground return so that you need to only probe with one hand.

`Source: http://euverc.colostate.edu/safetytests/High_Voltage_Safety_Manual.pdf`

B.4 Testing

Testing of the circuit characteristics was performed using the CT-1025 current transformer for current measurement and VD-305A voltage divider for simultaneous measurement of capacitor voltage. The testing circuit diagram is shown in Figure 2.12.

For testing purposes the load was a 4mm spark gap in air at atmospheric pressure. In this case the LOAD can be replaced by the spark resistance of 0.01-0.03Ohm. The Rcircuit is the total circuit resistance resulting from resistance of the connecting wires , triggered spark gap (TSG) and and capacitor plates. The L1 is the parasitic inductance of the circuit.

The voltage and current waveforms were recorded on the oscilloscope for various initial voltages (20kV, 25kV and 30kV). The results are shown below in Figures B.1 to B.6.

Initial Voltage $V_0 = 20$kV

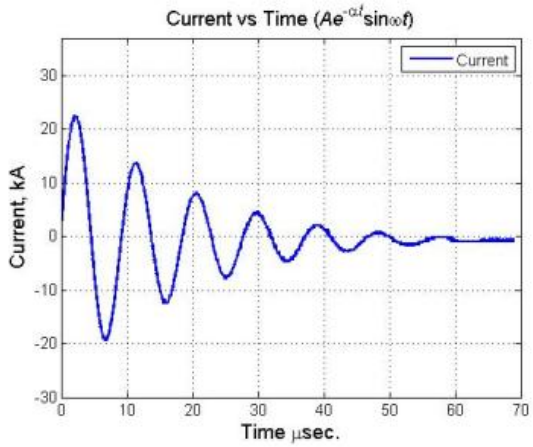

Figure B.1: Current Waveform ($V_0 = 20$kV)

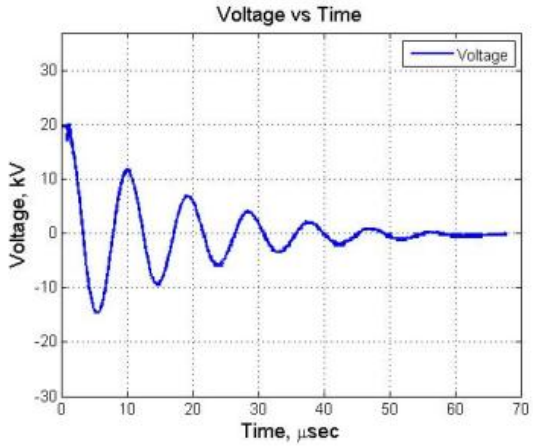

Figure B.2: Voltage Waveform ($V_0 = 20$kV)

Initial Voltage V_0 = 25kV

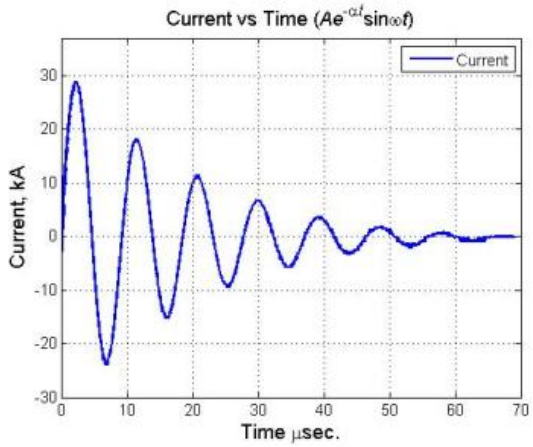

Figure B.3: Current Waveform (V_0 = 25kV)

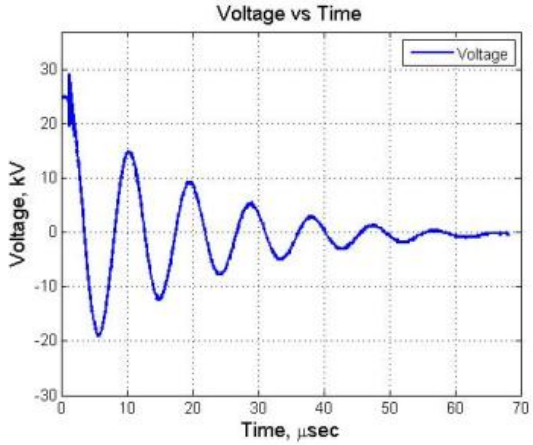

Figure B.4: Voltage Waveform (V_0 = 25kV)

Initial Voltage V_0 = 30kV

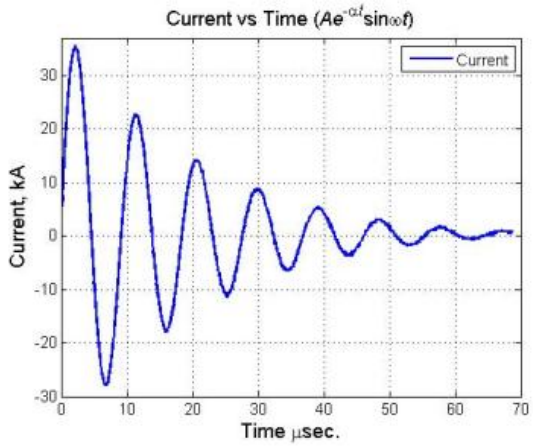

Figure B.5: Current Waveform (V_0 = 30kV)

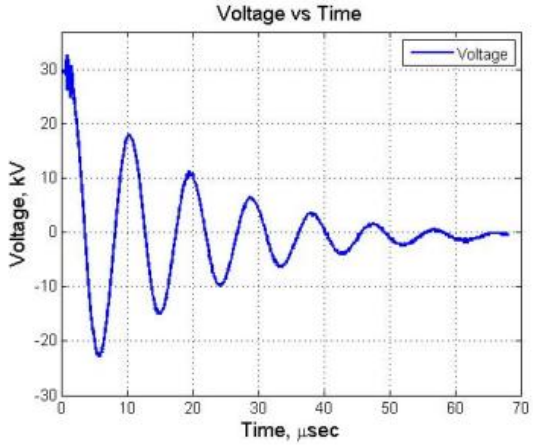

Figure B.6: Voltage Waveform (V_0 = 30kV)

B.5 Spark Energy

As seen in the ignition circuit diagram (Figure 2.12) the energy deposited inside the sphere comes from the discharge of the high voltage capacitor bank. Total energy stored in the capacitors ($E_T = CV^2/2$) could be used to estimate the energy required to detonate a combustible mixture. However this estimate will only give the order of magnitude approximation to the actual energy deposited in the sphere since it does not take into

account energy loss in circuit components and loss via ohmic dissipation. The actual energy deposited inside the mixture is found by integrating the square of current function $i(t)^2$ multiplied by the spark resistance (R_S): $E_S = \int_0^\infty i^2 R_S dt$. The ignition circuit in Figure 2.12 can be simplified to an equivalent RLC circuit shown in Figure B.7(b).

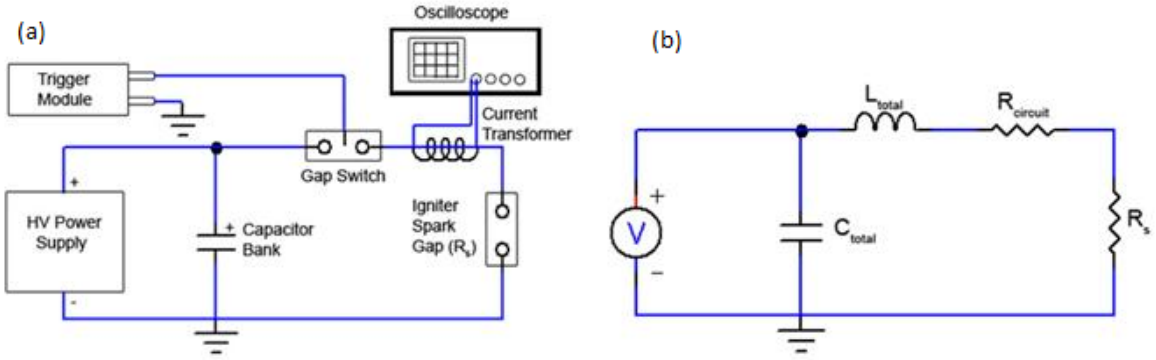

Figure B.7: (a) Ignition Circuit Components Diagram; (b) Equivalent RLC Circuit

Thus for a damped oscillatory discharge the current can be described as: $i(t) = Ae^{-\alpha t}\sin(\omega t)$. Attenuation factor is equal to $\alpha = R_{total}/2L_{total}$ and frequency of the discharge is equal to $\omega = \sqrt{1/(LC)_{total} - (R/2L)_{total}^2} = \omega_n\sqrt{1-\varsigma^2}$, where ω_n is the natural frequency of the undamped discharge and ς is the damping factor. The total circuit resistance ($R_{total} = R_{circuit} + R_s$) is a combination of the resistance of all the circuit components $R_{circuit}$ and igniter spark gap resistance R_s. To estimate the energy E_S deposited into the mixture from a trace of the current function on the oscilloscope, the following procedure is outlined:

1. Natural frequency ω_n is determined using ω and ς found from the current trace.
2. Total circuit inductance is found from $L_{total} = 1/\omega_n^2 C_{total}$
3. Total circuit resistance is found as follows $R_{total} = 2L_{total}\alpha$
4. Spark Resistance Rs is determined by subtracting $R_{total} = R_{circuit}$ when the spark gap is shorted out $R_s \approx 0$ from $R_{total} = R_{circuit} + R_s$ when the spark is not shorted. Current traces of the two cases are shown in Figure B.8 for capacitor initial voltage of 20kV.
5. Total Energy deposited into the mixture is found by numerically integrating the square of the current multiplied by spark resistance $E_S = \int_0^\infty i^2 R_S dt$.

It should be noted that according to Knystautus et al. [45] only the energy deposited in the first 1/4 of the discharge cycle is responsible for detonating the mixture. Thus the test results summarized in Table B.1 include both the total energy and energy deposited

in the first 1/4 cycle.

Table B.1: Discharge characteristics of the HVI system

$E_{total\ 0.5CV^2}$	V_0 (kV)	$C_{circuit}$ (μF)	$L_{circuit}$ (μH)	$R_{circuit}$ (Ω)	R_{spark} (Ω)	$E_{1/4\ cycle}$ (J)	$E_{curve\ fit}$ (J)	E_{total} (J)
400.0	20	2	1.04	0.096	0.011	5.426	5.375	32.2343
625.0	25	2	1.04	0.095	0.0095	8.3326	8.2951	54.1889
900.0	30	2	1.04	0.096	0.0079	11.2182	10.982	61.585

The shorted and open current waveforms are shown below for initial voltages of 20kV, 25kV and 30kV:

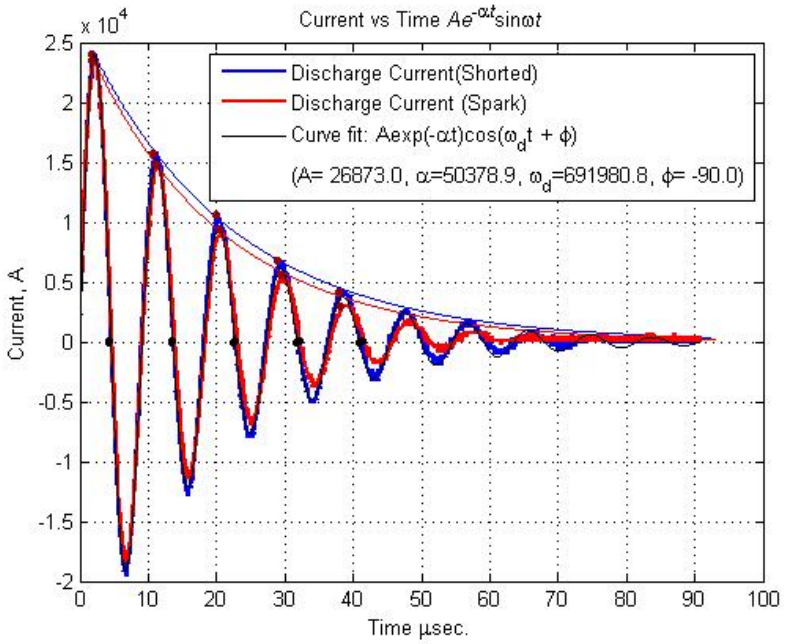

Figure B.8: Current Waveform shorted and open spark gap (V_0 = 20kV)

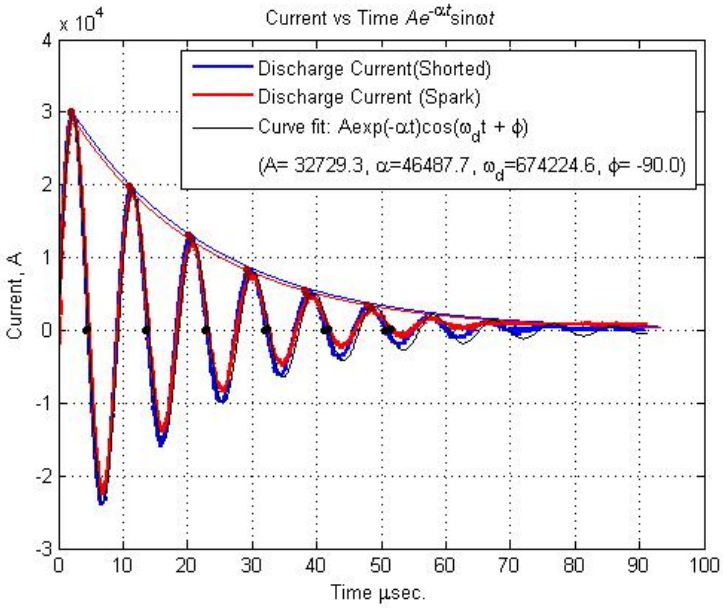

Figure B.9: Current Waveform shorted and open spark gap ($V_0 = 25$kV)

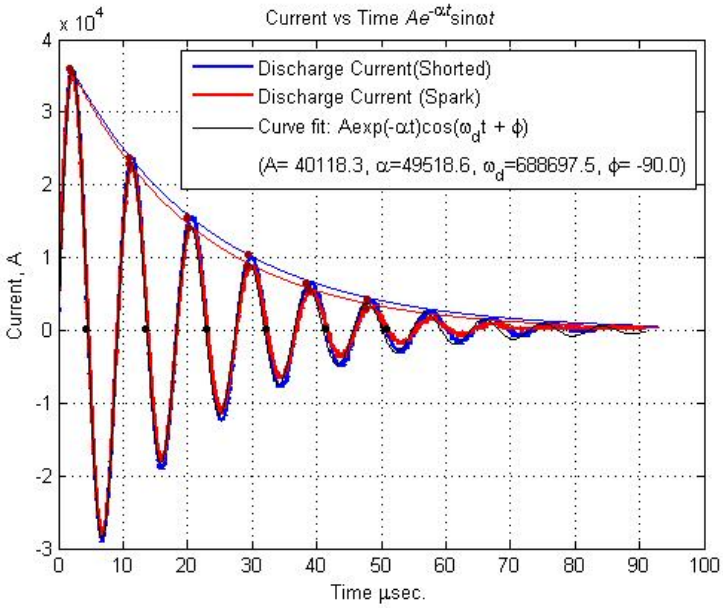

Figure B.10: Current Waveform shorted and open spark gap ($V_0 = 30$kV)

As seen from Table B.1 the spark resistance is small. Increasing the distance between the electrodes or using an exploding wire will increase the resistance of the spark gap and thus increase the energy deposited in the spark gap.

Appendix C

NASA Chemical Equilibrium Application Program (CEA)

The current version of CEA is a product of over 40 years of development and revisions by the NASA Lewis Research Center. CEA is used to calculate complex chemical equilibrium composition and thermodynamic properties of mixtures. Knowing these properties allows one to define the state of a system in equilibrium. Presently, CEA solves the chemical equilibrium problem by the minimization-of-free-energy formulation, such as minimization of Gibbs free energy. CEA finds the theoretical solution to a given problem by iteratively solving equations; for the shock tube and detonation problem, CEA uses the Newton-Raphson method. Additional details can be found in the NASA reference publication by Gordon and McBride 1994 [46].

Consider a shock tube problem to determine the conditions, in a stoichiometric mixture of oxy-methane, behind an incident shock traveling at 1782 m/s (Mach 5). The initial pressure and temperature are 3.5 kPa (0.5 psia) and 300K. Typical input and output .txt files are shown below.

INPUT FILE

```
problem    phi,eq.ratio=1.0,
```

```
    shock  inc  fr  u1=1782.0, t,k=300.0,  p,psia=0.5,
react
  fuel=CH4
  oxid=O2
output
    plot p t rho h u g s m mw cp gam son
end
```

OUTPUT FILE

```
 ******************************************************************************
        NASA-GLENN CHEMICAL EQUILIBRIUM PROGRAM CEA2, MAY 21, 2004
                  BY  BONNIE MCBRIDE AND SANFORD GORDON
     REFS: NASA RP-1311, PART I, 1994 AND NASA RP-1311, PART II, 1996
 ******************************************************************************
 problem    phi,eq.ratio=1.0,
     shock  inc  fr  u1=1782.0, t,k=300.0,  p,psia=0.5,
 react
   fuel=CH4
   oxid=O2
 output
     plot p t rho h u g s m mw cp gam son
 end
 OPTIONS: TP=F  HP=F  SP=F  TV=F  UV=F  SV=F  DETN=F  SHOCK=T  REFL=F  INCD=T
 RKT=F  FROZ=T  EQL=F  IONS=F  SIUNIT=T  DEBUGF=F  SHKDBG=F  DETDBG=F  TRNSPT=F
 T,K =   300.0000
 TRACE= 0.00E+00  S/R= 0.000000E+00  H/R= 0.000000E+00  U/R= 0.000000E+00
 P,BAR =     0.034474
 WARNING!!  AMOUNT MISSING FOR REACTANT  1.
 PROGRAM SETS WEIGHT PERCENT = 100. (REACT)
 WARNING!!  AMOUNT MISSING FOR REACTANT  2.
 PROGRAM SETS WEIGHT PERCENT = 100. (REACT)
    REACTANT          WT.FRAC   (ENERGY/R),K   TEMP,K  DENSITY
        EXPLODED FORMULA
 F: CH4              1.000000   0.000000E+00     0.00  0.0000
```

```
         C  1.00000  H  4.00000
O: O2               1.000000   0.000000E+00     0.00  0.0000
         O  2.00000
 SPECIES BEING CONSIDERED IN THIS SYSTEM
(CONDENSED PHASE MAY HAVE NAME LISTED SEVERAL TIMES)
 LAST thermo.inp UPDATE:    9/09/04
 g 7/97  *C              tpis79  *CH             g 4/02  CH2
 g 4/02  CH3             g11/00  CH2OH           g 7/00  CH3O
 g 8/99  CH4             g 7/00  CH3OH           srd 01  CH3OOH
 tpis79  *CO             g 9/99  *CO2            tpis91  COOH
 tpis91  *C2             g 6/01  C2H            g 1/91  C2H2,acetylene
 g 5/01  C2H2,vinylidene g 4/02  CH2CO,ketene    g 3/02  O(CH)2O
 srd 01  HO(CO)2OH       g 7/01  C2H3,vinyl      g 6/96  CH3CO,acetyl
 g 1/00  C2H4            g 8/88  C2H4O,ethylen-o g 8/88  CH3CHO,ethanal
 g 6/00  CH3COOH         srd 01  OHCH2COOH       g 7/00  C2H5
 g 7/00  C2H6            g 8/88  C2H5OH          g 7/00  CH3OCH3
 srd 01  CH3O2CH3        g 8/00  C2O             tpis79  *C3
 n 4/98  C3H3,1-propynl  n 4/98  C3H3,2-propynl  g 2/00  C3H4,allene
 g 1/00  C3H4,propyne    g 5/90  C3H4,cyclo-     g 3/01  C3H5,allyl
 g 2/00  C3H6,propylene  g 1/00  C3H6,cyclo-     g 6/01  C3H6O,propylox
 g 6/97  C3H6O,acetone   g 1/02  C3H6O,propanal  g 7/01  C3H7,n-propyl
 g 9/85  C3H7,i-propyl   g 2/00  C3H8            g 2/00  C3H8O,1propanol
 g 2/00  C3H8O,2propanol g 7/88  C3O2            g tpis  *C4
 g 7/01  C4H2,butadiyne  g 8/00  C4H4,1,3-cyclo- n10/92  C4H6,butadiene
 n10/93  C4H6,1butyne    n10/93  C4H6,2butyne    g 8/00  C4H6,cyclo-
 n 4/88  C4H8,1-butene   n 4/88  C4H8,cis2-buten n 4/88  C4H8,tr2-butene
 n 4/88  C4H8,isobutene  g 8/00  C4H8,cyclo-     g10/00  (CH3COOH)2
 n10/84  C4H9,n-butyl    n10/84  C4H9,i-butyl    g 1/93  C4H9,s-butyl
 g 1/93  C4H9,t-butyl    g12/00  C4H10,n-butane  g 8/00  C4H10,isobutane
 g 8/00  *C5             g 5/90  C5H6,1,3cyclo-  g 1/93  C5H8,cyclo-
 n 4/87  C5H10,1-pentene g 2/01  C5H10,cyclo-    n10/84  C5H11,pentyl
 g 1/93  C5H11,t-pentyl  n10/85  C5H12,n-pentane n10/85  C5H12,i-pentane
 n10/85  CH3C(CH3)2CH3   g 2/93  C6H2           g11/00  C6H5,phenyl
 g 8/00  C6H5O,phenoxy   g 8/00  C6H6           g 8/00  C6H5OH,phenol
 g 1/93  C6H10,cyclo-    n 4/87  C6H12,1-hexene  g 6/90  C6H12,cyclo-
```

```
 n10/83  C6H13,n-hexyl    g 6/01  C6H14,n-hexane   g 7/01  C7H7,benzyl
 g 1/93  C7H8             g12/00  C7H8O,cresol-mx  n 4/87  C7H14,1-heptene
 n10/83  C7H15,n-heptyl   n10/85  C7H16,n-heptane  n10/85  C7H16,2-methylh
 n 4/89  C8H8,styrene     n10/86  C8H10,ethylbenz  n 4/87  C8H16,1-octene
 n10/83  C8H17,n-octyl    n 4/85  C8H18,n-octane   n 4/85  C8H18,isooctane
 n10/83  C9H19,n-nonyl    g 3/01  C10H8,naphthale  n10/83  C10H21,n-decyl
 g 8/00  C12H9,o-bipheny  g 8/00  C12H10,biphenyl  g 6/97  *H
 g 1/01  HCO              g 6/01  HCCO             g 4/02  HO2
 tpis78  *H2              g 5/01  HCHO,formaldehy  g 6/01  HCOOH
 g 8/89  H2O              g 6/99  H2O2             g 6/01  (HCOOH)2
 g 5/97  *O               g 4/02  *OH              tpis89  *O2
 g 8/01  O3               n 4/83  C(gr)            n 4/83  C(gr)
 n 4/83  C(gr)            g11/99  H2O(cr)          g 8/01  H2O(L)
 g 8/01  H2O(L)
  *** INPUT FOR SHOCK PROBLEMS ***
INCDEQ = F   REFLEQ = F   INCDFZ = T    REFLFZ = F
U1 =    1.782000E+03
MACH1 = 0.000000E+00
O/F =   3.989263
                      EFFECTIVE FUEL     EFFECTIVE OXIDANT        MIXTURE
ENTHALPY                  h(2)/R             h(1)/R                h0/R
(KG-MOL)(K)/KG        0.00000000E+00      0.00000000E+00      0.00000000E+00
KG-FORM.WT./KG             bi(2)              bi(1)                b0i
 *C                   0.62334580E-01      0.00000000E+00      0.12493744E-01
 *H                   0.24933832E+00      0.00000000E+00      0.49974975E-01
 *O                   0.00000000E+00      0.62502344E-01      0.49974975E-01
                        SHOCK WAVE PARAMETERS ASSUMING
                 FROZEN COMPOSITION FOR INCIDENT SHOCKED CONDITI1ONS
CASE =
            REACTANT                     WT FRACTION      ENERGY      TEMP
                                          (SEE NOTE)     KJ/KG-MOL      K
FUEL        CH4                           1.0000000         0.000      0.000
OXIDANT     O2                            1.0000000         0.000      0.000
O/F=    3.98926  %FUEL= 20.043038  R,EQ.RATIO= 1.000000  PHI,EQ.RATIO= 1.000000
INITIAL GAS (1)
```

```
MACH NUMBER1      5.0004
U1, M/SEC        1782.00
P, BAR           0.03447
T, K              300.00
RHO, KG/CU M    3.6874-2
H, KJ/KG          -929.85
U, KJ/KG         -1023.34
G, KJ/KG         -3542.78
S, KJ/(KG)(K)     8.7098
M, (1/n)          26.680
Cp, KJ/(KG)(K)    1.1811
GAMMAs            1.3584
SON VEL,M/SEC      356.4
SHOCKED GAS (2)--INCIDENT--FROZEN
U2, M/SEC         249.99
P, BAR            1.0411
T, K             1271.04
RHO, KG/CU M    2.6284-1
H, KJ/KG          626.67
U, KJ/KG          230.56
G, KJ/KG        -11859.8
S, KJ/(KG)(K)     9.8238
M, (1/n)          26.680
Cp, KJ/(KG)(K)    1.9480
GAMMAs            1.1904
SON VEL,M/SEC      686.7
P2/P1             30.201
T2/T1              4.237
M2/M1             1.0000
RHO2/RHO1         7.1282
V2, M/SEC        1532.01
MOLE FRACTIONS
 CH4             0.33333
 *O2             0.66667
```

Appendix D

Cantera and the GRI mechanism (GRI-Mech) version 3.0

Cantera offers object-oriented tools that solves various problems involving transport processes, chemical kinetics and thermodynamics [47]. When solving these problems for a reactive system, the changes in the thermodynamic properties and chemical composition needs to be accounted for, as the system approaches equilibrium. Therefore, Cantera imports different thermochemical databases, such as the GRI mechanism version 3.0. GRI-Mech 3.0 is essentially a database comprising the thermochemical and transport properties of various species, elemental chemical reactions and their associated rate constants [48]. Finally, using Python allows the user to script a variety of user defined problems. In this study, the following two problems were addressed:

- Ignition delay following adiabatic shock compression, and;
- Adiabatic flame speed

D.1 Ignition delay following adiabatic shock compression

For this problem, it is assumed that the shock wave is planar with a uniform post-shock flow field termed the "von-Neumann" region. The Python script used is given below along with a brief description. After importing the Cantera package and the GRI-Mech 3.0 database, the von-Neumann temperature and pressure are provided as initial inputs along with reactant composition. Then, the program calls a package which simulates the combustion of our system in a constant volume environment; details of this package can be found in Goodwin 2004 "Reactor Networks" [49]. As the simulation marches in time, with a user defined time-step, the code tracks the molar concentration of the CH radical. At every iteration, the time-step is added to the current time to produce an updated time stamp. Once the concentration for the current iteration is lower than the previous iteration, the earlier time is reported as the theoretical ignition delay parameter $\left(\tau_{ig_{th}}\right)$.

```
from Cantera import *
from Cantera.Reactor import *
from Cantera.Func import *
gas = importPhase('GRI30.cti')
T1 = [1232.64000]
P1 = [295.24000]
delT = 1.e-6
for index in range (len(T1)):
    print 'Initial Temp = ', T1[index], 'K'
    print 'Initial Press = ', P1[index], 'kPa'
    gas.set(T = T1[index], P = P1[index]*1000.0, X = 'CH4:1, O2:2')
    r1 = Reactor(gas)  #constant volume
    sim = ReactorNet([r1])
    time=delT
    old=-1
    tig=0.0
    while time < 1:
        sim.advance(time)
        if r1.moleFraction('CH') > old:
```

```
            old=r1.moleFraction('CH')
            tig=time
        else:
            break
        time += delT
    print 'Ignition Delay =', tig*1e6, 'microseconds'
    print '======================================='
```

D.2 Adiabatic flame speed

The Python script, used to determine the laminar flame speed, is given below along with a very brief description. Additional details can be found in a document by Dr. Goodwin [50]. The initial pressure and temperature are specified for a one-dimensional domain. This domain is modeled having a length of 3 cm and is divided spatially into six points. At each point a system of non-linear flow equations are solved iteratively. The iterative method used is a hybrid of the Newton and time-stepping algorithm. After the final solution is reached, the results are stored in a spreadsheet.

```
# ADIABATIC_FLAME - A freely-propagating, premixed methane/air flat
#          flame with multicomponent transport properties
from Cantera import *
from Cantera.OneD import *
from Cantera.OneD.FreeFlame import FreeFlame
#############################################################
#
# parameter values
#
p          =   133530               # unburned gas pressure
tin        =   974.13              # unburned gas temperature
mdot       =   0.04                # kg/m^2/s
comp       =  'CH4:1, O2:2'  # premixed gas composition
initial_grid = [0.0, 0.001, 0.01, 0.02, 0.029, 0.03] # m
tol_ss    = [1.0e-4, 1.0e-6]        # [rtol atol] for steady-state
```

```
                                    # problem
tol_ts    = [1.0e-4, 1.0e-6]        # [rtol atol] for time stepping
loglevel  = 1                       # amount of diagnostic output (0
                                    # to 5)
refine_grid = 1                     # 1 to enable refinement, 0 to
                                    # disable
gas = GRI30('Mix')
#gas = importPhase('gri30.cti')
gas.addTransportModel('Multi')
# set its state to that of the unburned gas
gas.setState_TPX(tin, p, comp)
f = FreeFlame(gas = gas, grid = initial_grid, tfix = 1200)
# set the upstream properties
f.inlet.set(mole_fractions = comp, temperature = tin)
f.set(tol = tol_ss, tol_time = tol_ts)
f.showSolution()
f.set(energy = 'off')
f.setRefineCriteria(ratio = 10.0, slope = 1, curve = 1)
f.setMaxJacAge(50, 50)
f.setTimeStep(1.0e-5, [2, 5, 10, 20, 50])
f.solve(loglevel, refine_grid)
f.save('h2_adiabatic.xml','no_energy',
       'solution with the energy equation disabled')
f.set(energy = 'on')
f.setRefineCriteria(ratio = 3.0, slope = 0.1, curve = 0.2)
f.solve(loglevel, refine_grid)
f.save('h2_adiabatic.xml','energy',
       'solution with the energy equation enabled')
print 'mixture-averaged flamespeed = ',f.u()[0]
gas.switchTransportModel('Multi')
f.flame.setTransportModel(gas)
f.solve(loglevel, refine_grid)
f.save('h2_adiabatic.xml','energy_multi',
       'solution with the energy equation enabled and multicomponent transport')
# write the velocity, temperature, density, and mole fractions to a CSV file
```

```
z = f.flame.grid()
T = f.T()
u = f.u()
V = f.V()
fcsv = open('adiabatic_flame.csv','w')
writeCSV(fcsv, ['z (m)', 'u (m/s)', 'V (1/s)', 'T (K)', 'rho (kg/m3)']
         + list(gas.speciesNames()))
for n in range(f.flame.nPoints()):
    f.setGasState(n)
    writeCSV(fcsv, [z[n], u[n], V[n], T[n], gas.density()]
             +list(gas.moleFractions()))
fcsv.close()
print 'solution saved to adiabatic_flame.csv'
print 'multicomponent flamespeed = ',u[0]
f.showStats()
```

Appendix E

Constant pressure-enthalpy combustion

Python script below was used to estimate the temperature and density of a gas pocket that burns and expands, with a constant pressure-enthalpy process.

```
from Cantera import*
gas = importPhase('gri30.cti');
T1 = [996,1099.51]
P1 = [110.1,164.12]
for index in range(len(T1)):
    gas.set(T = T1[index], P = P1[index]*1000.0, X = 'CH4:1, O2:2')
    print gas
    print 'Initial State - Shocked, unburned gas inside groove'
    print 'rho1', gas.density(), 'kg/cu.m'
    print 'p1', gas.pressure()/1000.0, 'kPa'
    print 'T1', gas.temperature(), 'K'
    gas.equilibrate('HP')
    print 'Equilibrated State - Shocked, burned gas'
    print 'rho2', gas.density(), 'kg/cu.m'
    print 'p2', gas.pressure()/1000.0, 'kPa'
    print 'T2', gas.temperature(), 'K'
```

Appendix F

Flame Speed Calculations

Details of the flame speed calculations, described in Section 5.4, for the roughness experiment is given below.

F.1 Measurements

Table F.1 shows a data set with multiple measurements of the flame speed, in the absolute frame of reference (u_F), and the angle it makes with the horizontal (θ_F). The data set was used to obtain an averaged flame speed, for the selected point shown in Figure 5.4, in the absolute reference.

Table F.1: Estimation of the the averaged absolute flame speed (u_F) and the angle (θ_F) it makes with the horizontal (θ_F), using the PCC application.

No.	Absolute flame velocity, u_F (m/s)	Angle, θ_F (deg)
1	1565.4	30.5
2	1497.6	32.0
3	1565.4	30.5
4	1634.3	29.1
5	1634.3	29.1
6	1634.3	29.1
7	1674.3	31.4
8	1565.4	30.5
9	1565.4	30.5
10	1565.4	30.5
11	1565.4	30.5
12	1565.4	30.5
13	1565.4	30.5
14	1526.7	27.9
15	1597.3	26.6
16	1526.7	27.9
AVERAGE	**1578.1**	**29.8**

From these values, the components of the absolute flame velocity in the X and Y axes can be determined as shown in Table F.2.

Table F.2: The components of the averaged absolute flame speed (u_F) in the Y (vertical) and X (horizontal) axes.

Parameter description	Units	Value
Absolute flame velocity, u_F	m/s	1578.1
Angle, θ_F	deg	29.8
Absolute vertical flame velocity, u_{FY}	m/s	784.1
Absolute horizontal flame velocity, u_{FX}	m/s	1369.5

Next, we calibrate the image by using the tooth thickness on the roughness plates as a reference length. Table F.3 shows the values used for calibration in Adobe Illustrator (AI).

Table F.3: Image calibration in Adobe Illustrator (AI).

AI Units	True Distance (mm)
17.7	28.6
1	1.6

After calibrating the image, Table F.4 shows that the strength of the Mach shock, at the selected point as indicated in Figure 5.6, is calculated for each measurement, by knowing the distance and the inter-frame time of 10 μsec.

Table F.4: Estimation of the Mach shock strength (u_M) and the direction in which it acts (θ_M) for several measurements.

No.	Angle θ_M	AI Units	True distance (mm)	Absolute shock velocity, u_M (m/s)
1	24.9	8.9	14.3	1431.2
2	24.7	8.9	14.4	1440.9
3	24.7	8.8	14.2	1416.6
4	24.4	9.1	14.6	1461.8
5	25.1	8.8	14.2	1421.5
6	24.9	8.9	14.3	1431.2
7	25.5	8.7	14.0	1400.5
8	25.2	9.1	14.7	1471.5
9	25.5	8.7	14.0	1400.5
10	25.8	9.1	14.7	1466.7
11	24.7	8.9	14.4	1440.9
12	25.6	9.0	14.5	1450.5

F.2 Initial state conditions

The initial state of the gas is summarized in Table F.5.

Table F.5: Table summarizing the initial conditions.

Parameter description	Units	Value
Pressure, p_0	psi	1.0
Temperature, T_0	K	300.0
Sound speed, c_0	m/s	356.4

F.3 Post-shock conditions and burning velocity of the flame tip

Using NASA's CEA program (Appendix C), the flow properties behind the Mach shock, local to the chosen point, can be computed as explained in Section 5.4.3. Table F.6 summarizes these results.

Table F.6: A summary of the post shock conditions behind the Mach shock and the final averaged vertical flame speed for each measurement obtained from experiment.

Absolute particle velocity, u_p (m/s)	Temperature (K)	Pressure (kPa)	Vertical particle velocity, u_{pY} (m/s)	Experimental vertical flame speed, V_{FY} (m/s)
1190.4	970.0	132.5	501.8	282.4
1199.9	977.9	134.4	502.2	282.0
1176.2	958.4	129.8	491.7	292.5
1220.4	994.9	138.5	503.6	280.6
1181.0	962.3	130.7	501.5	282.6
1190.4	970.0	132.5	501.8	282.4
1160.4	945.5	126.7	499.9	284.2
1229.9	1002.8	140.4	523.3	260.9
1160.4	945.5	126.7	499.9	284.2
1225.2	998.8	139.4	532.7	251.5
1199.9	977.9	134.4	502.2	282.0
1209.4	985.7	136.3	521.8	262.3
AVERAGE	**974.1**	**133.5**		**277.3**

Appendix G

Additional Schlieren Images

For the readers' interest, the remaining images of the high speed Schlieren videos presented in the report, but not shown, are presented here. All images, obtained from the high speed Schlieren videos, are presented in a sequence that shows the evolution i.e. from left-to-right and top-to-bottom.

G.1 Remaining frames from the high speed Schlieren video results

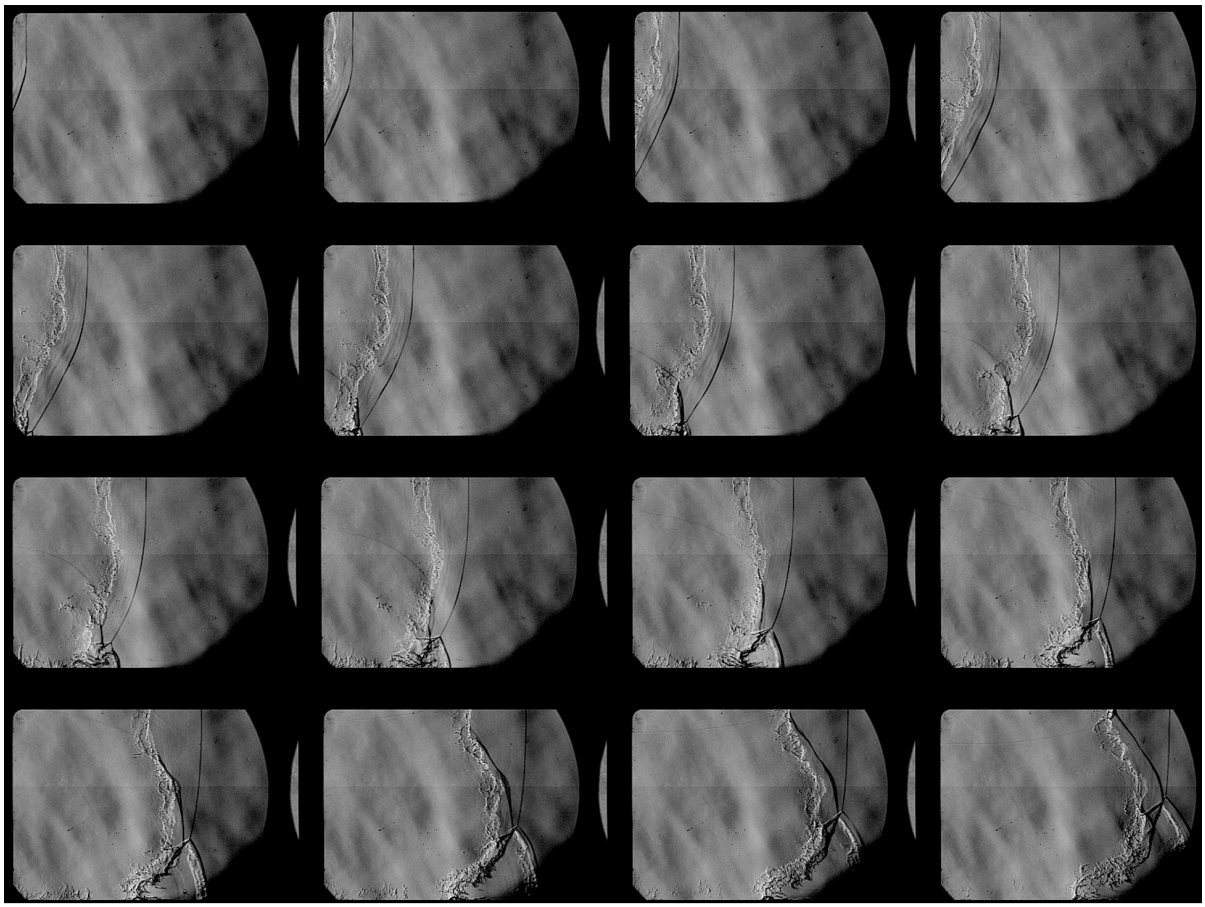

Figure G.1: Schlieren images of a flow field evolution showing re-ignition behind the Mach shock. The initial pressure and temperature was 10.3 kPa and 300K. All frames were obtained from the same experiment using the high speed video format with an inter-frame delay of 12.97 μsec. *Test ID: CH4+O2-07-27-12(1.47psiTEST7)*

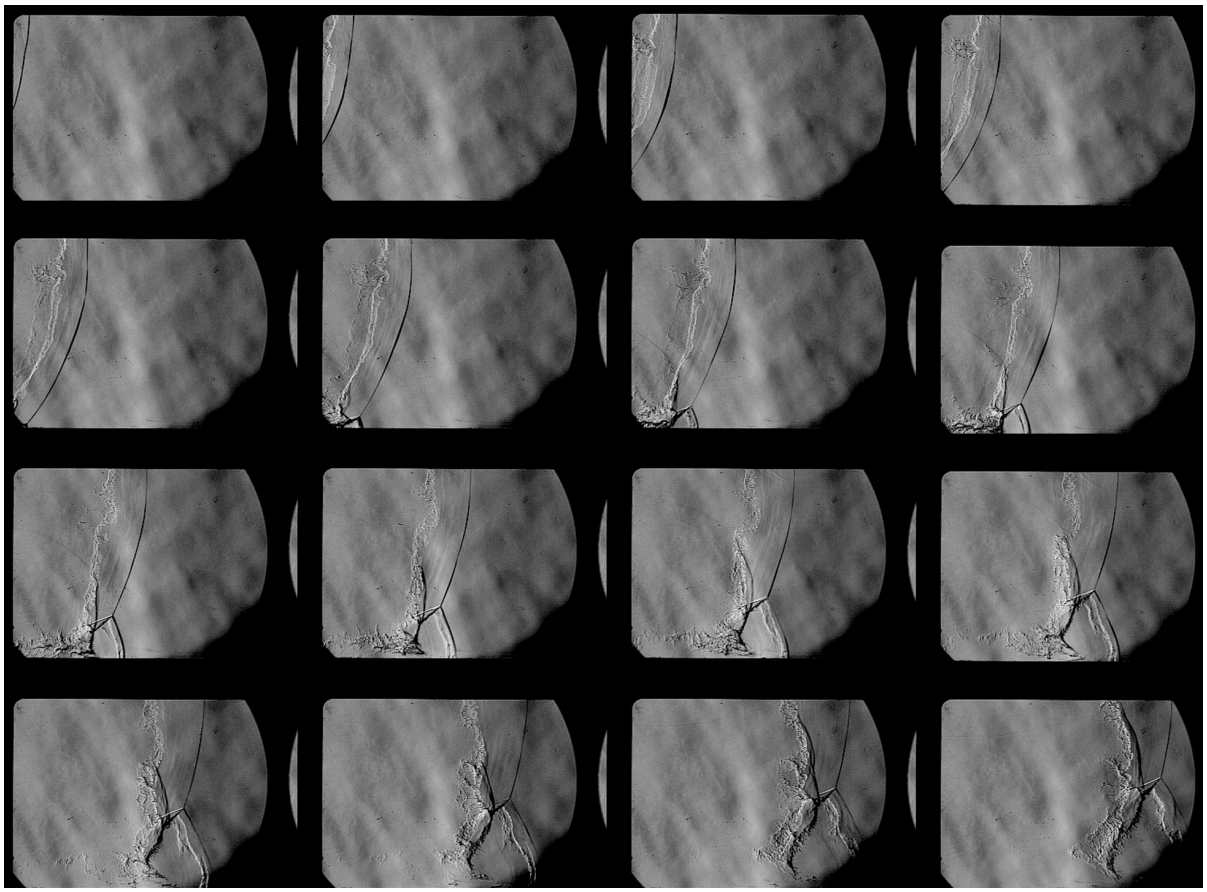

Figure G.2: Schlieren images of a flow field evolution showing re-ignition behind the Mach shock. The initial pressure and temperature was 9.8 kPa and 300K. All frames were obtained from the same experiment using the high speed video format with an inter-frame delay of 12.97 μsec. *Test ID: CH4+O2-07-27-12(1.4psiTEST3)*

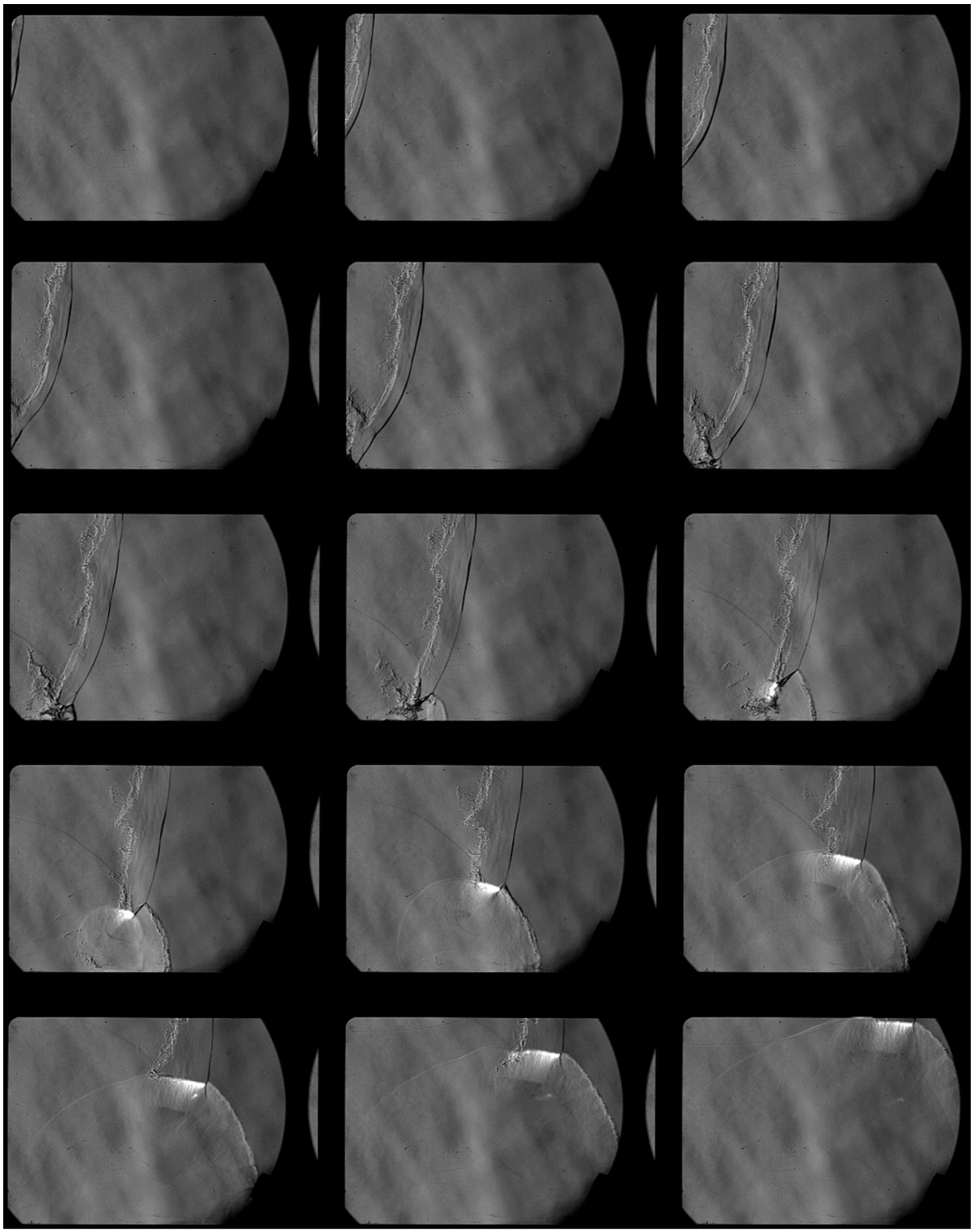

Figure G.3: Schlieren images of a flow field evolution showing re-initiation behind the Mach and transverse shock. The initial pressure and temperature was 10.5 kPa and 300K. All frames were obtained from the same experiment using the high speed video format with an inter-frame delay of 12.97 μsec. *Test ID: CH4+O2-07-27-12(1.5psiTEST2)*

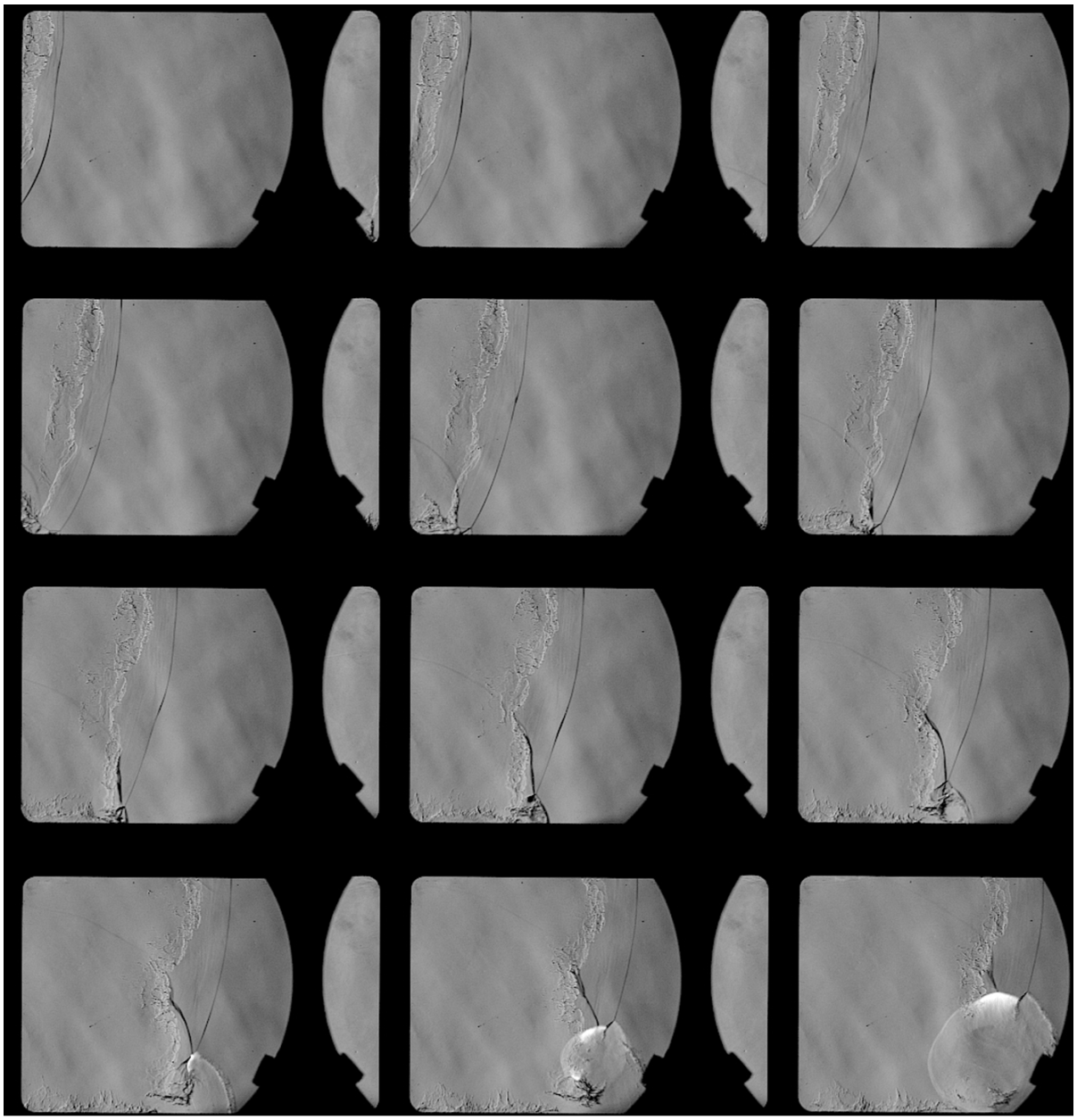

Figure G.4: Schlieren images of a flow field evolution showing detonation re-initiation of the Mach shock and transverse wave, following an increase in chemical reaction rates behind the Mach shock. The initial pressure and temperature was 12.3 kPa and 300K. All frames were obtained from the same experiment using the high speed video format with an inter-frame delay of 12.97 μsec. *Test ID: CH4+O2-07-25-12(1.75psiTEST6)*

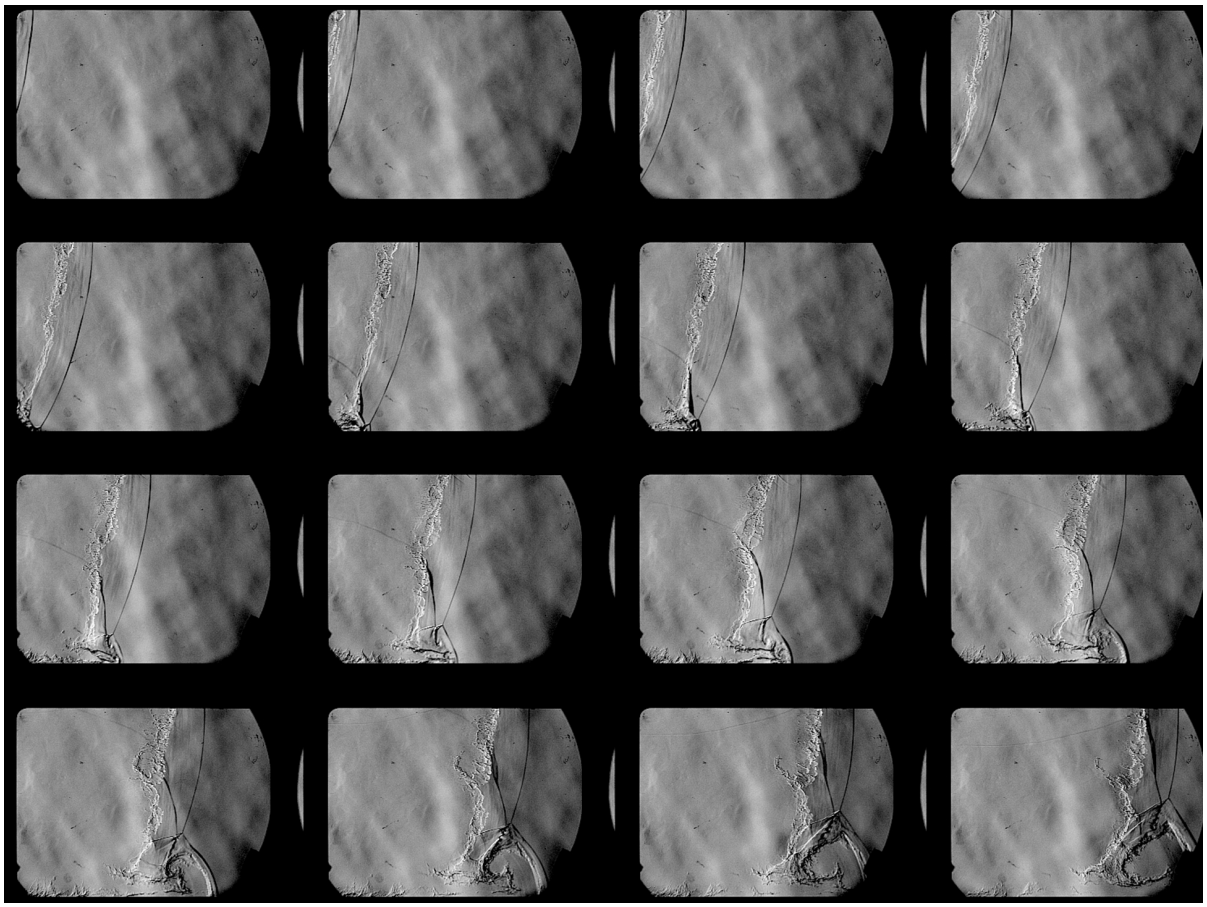

Figure G.5: Schlieren images of a flow field evolution showing re-ignition behind the Mach shock following jet entrainment potentially due to forward jetting of the slipline. The initial pressure and temperature was 12.3 kPa and 300K. All frames were obtained from the same experiment using the high speed video format with an inter-frame delay of 12.97 μsec. *Test ID: CH4+O2-07-24-12(1.75psiTEST4)*

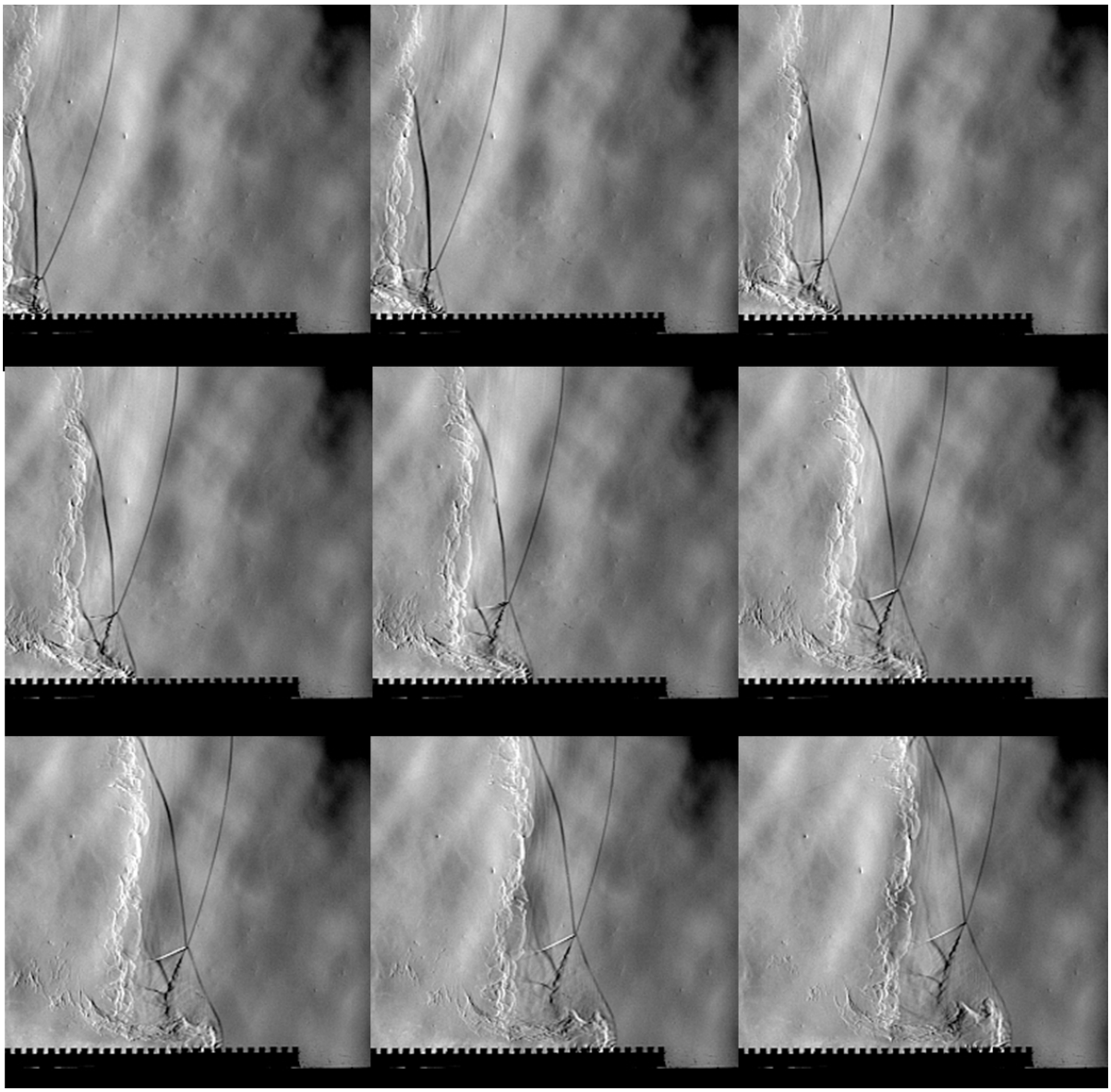

Figure G.6: Schlieren images of a flow field evolution showing re-ignition behind the Mach shock, following jet entrainment of hot burned gas with unburned gas over the roughness plate obstacle. The initial pressure and temperature was 7 kPa and 300K. All frames were obtained from the same experiment using the high speed video format with an inter-frame delay of 10 μsec. *Test ID: CH4+O2-07-13-12(1.0psi)roughness*

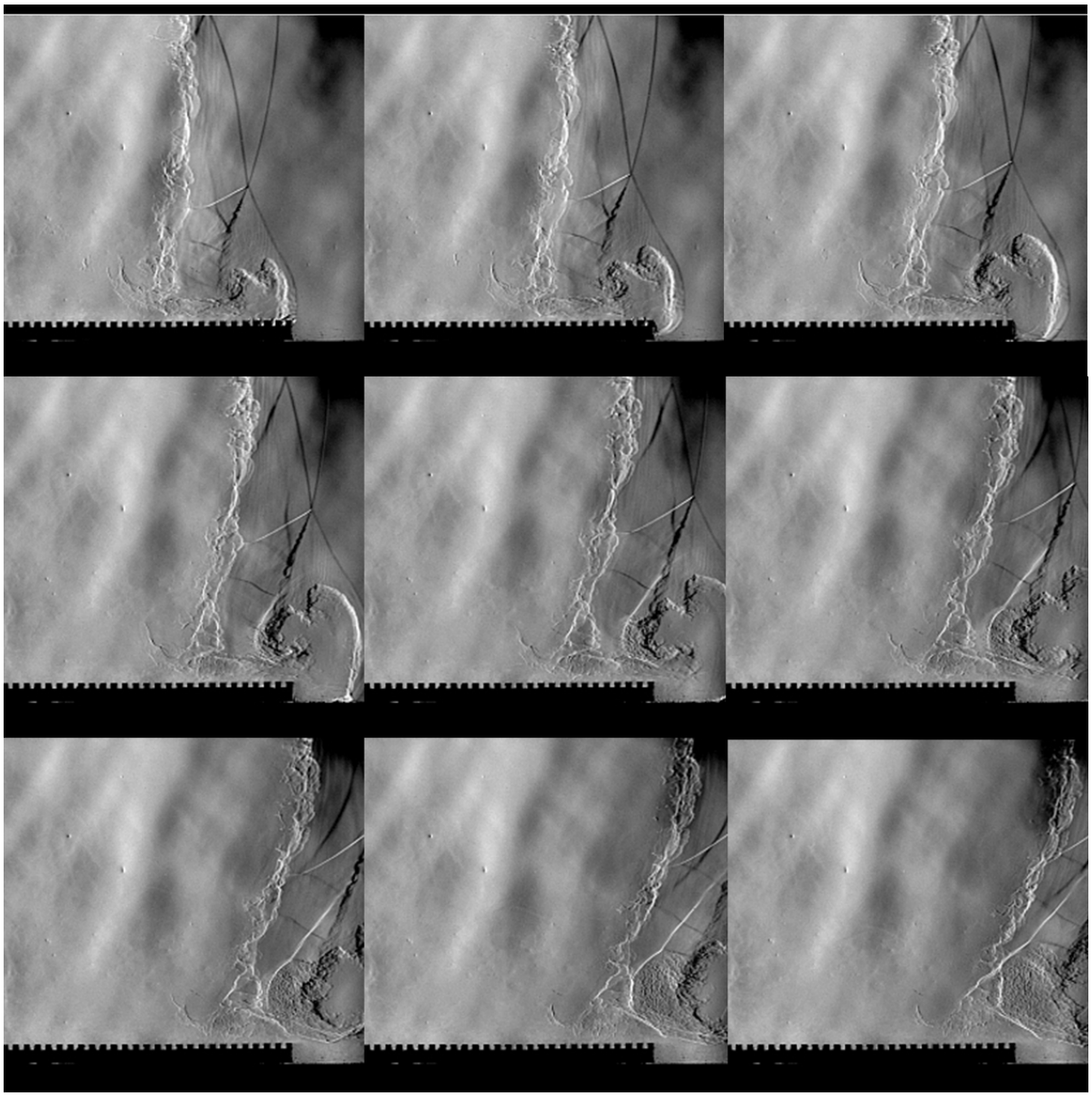

Figure G.7: Continuation of the flow field evolution shown in Figure G.6 above now showing a back propagating shock wave. *Test ID: CH4+O2-07-13-12(1.0psi)roughness*

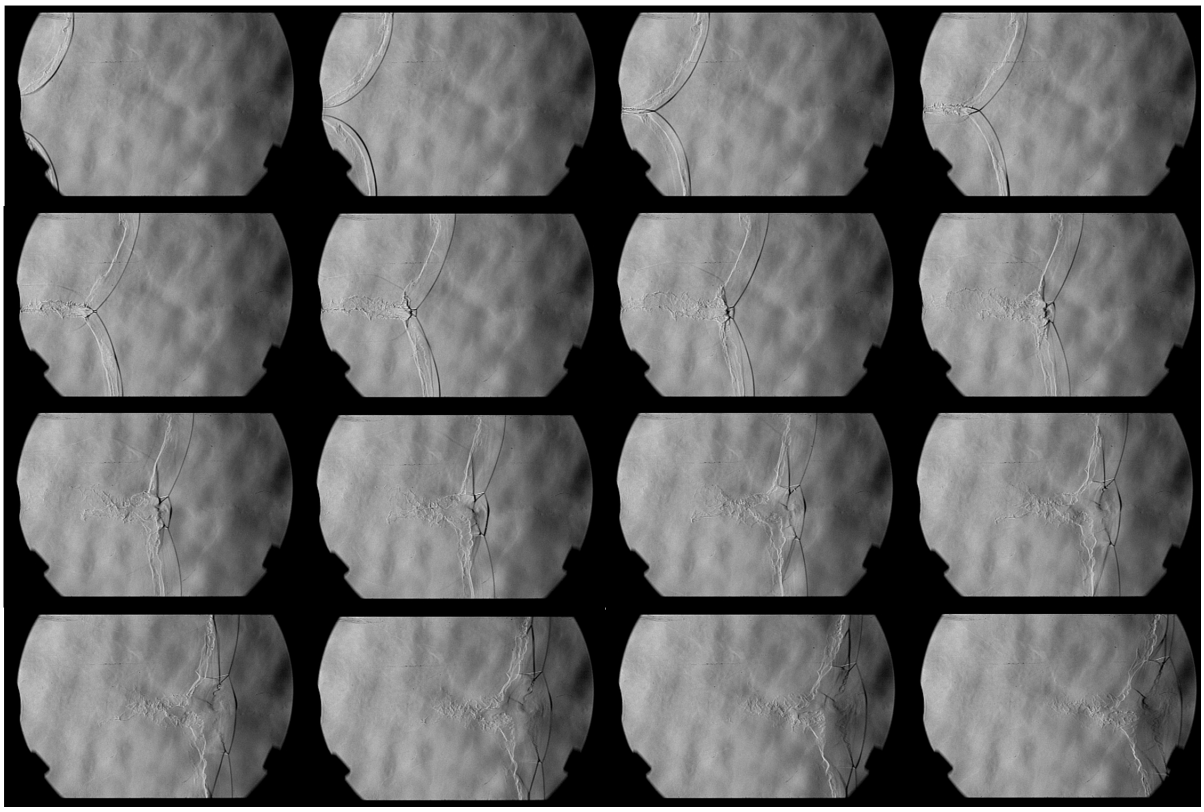

Figure G.8: Schlieren images of a flow field evolution showing inert shock reflections of a quenched detonation wave behind the full-cylinder obstacle. The initial pressure and temperature was 3.5 kPa and 300K. All frames were obtained from the same experiment using the high speed video format with an inter-frame delay of 11.53 μsec. *Test ID: CH4+O2-08-20-12(0.5psiTEST1)*

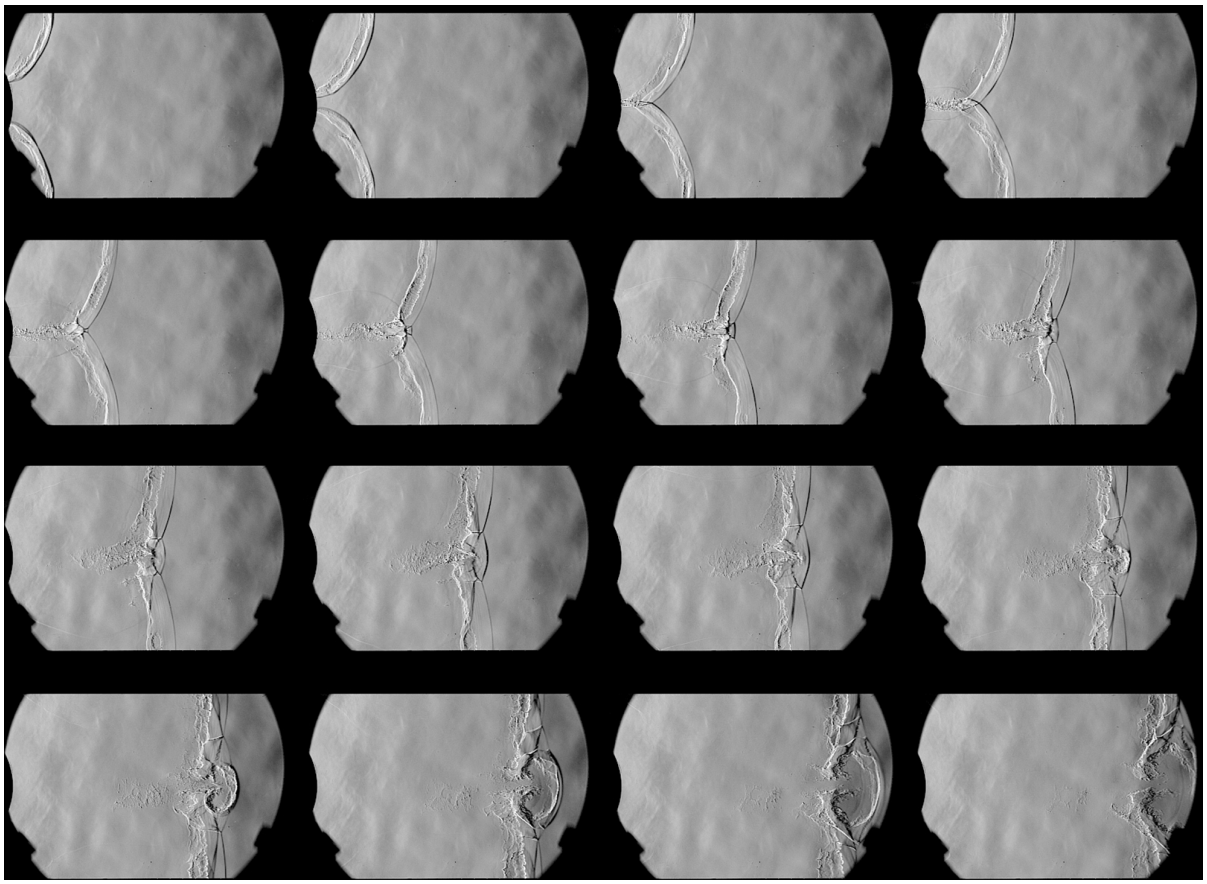

Figure G.9: Schlieren images of a flow field evolution showing re-ignition behind the Mach shock following jet entrainment potentially due to forward jetting of the slipline. The initial pressure and temperature was 8.4 kPa and 300K. All frames were obtained from the same experiment using the high speed video format with an inter-frame delay of 12.91 μsec. *Test ID: CH4+O2-08-14-12(1.2psiTEST1)*

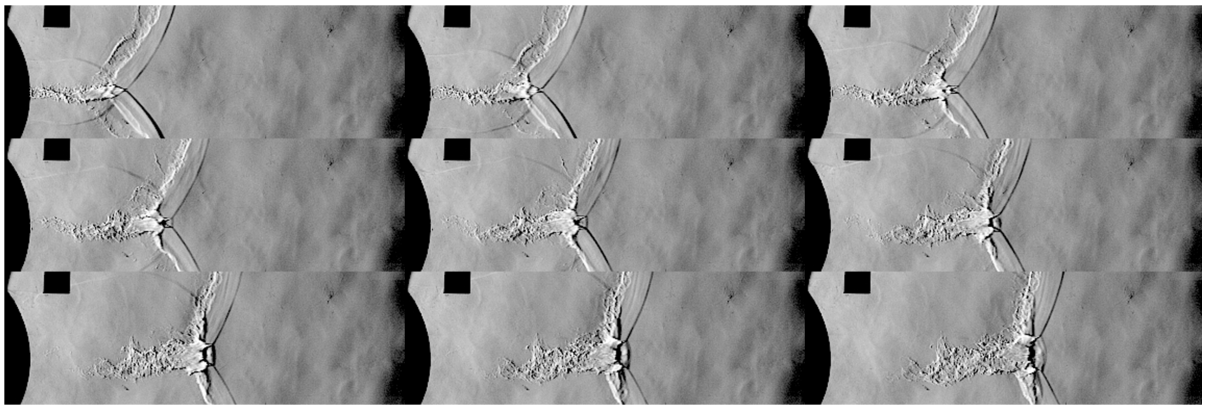

Figure G.10: Schlieren images of a flow field evolution showing re-ignition behind the Mach shock following jet entrainment potentially due to forward jetting of the slipline. The initial pressure and temperature was 10.5 kPa and 300K. All frames were obtained from the same experiment using the high speed video camera with an inter-frame delay of 6.03 μsec. For a reference, the horizontal length of the tape in the top-left side is 17.5 mm. *Test ID: CH4+O2-08-03-12(1.49psiTEST4)*

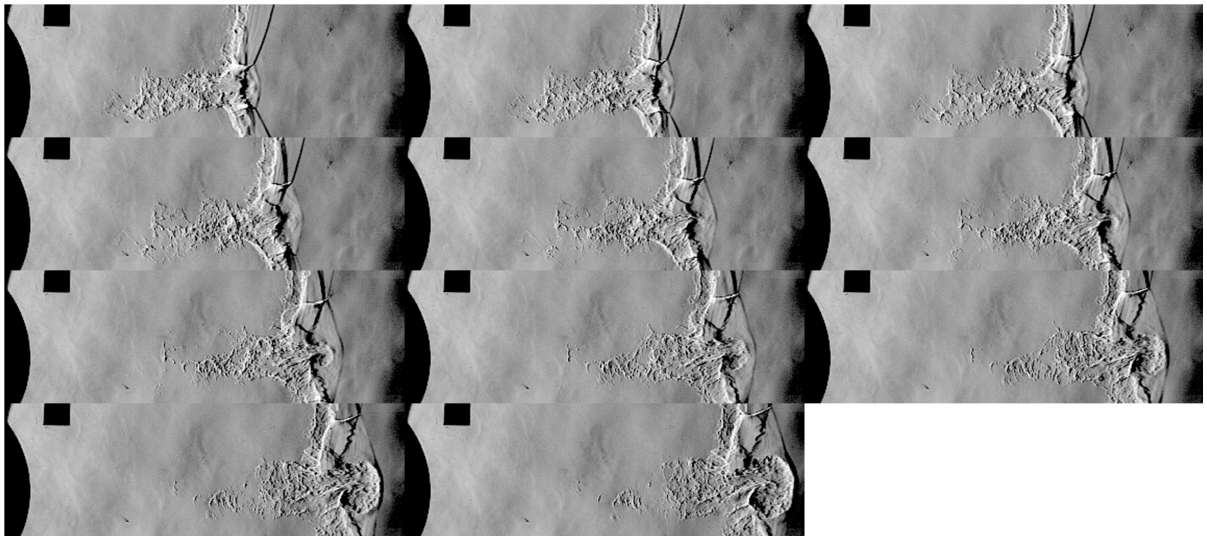

Figure G.11: Continuation of the flow field evolution shown in Figure G.10 above. *Test ID: CH4+O2-08-03-12(1.49psiTEST4)*

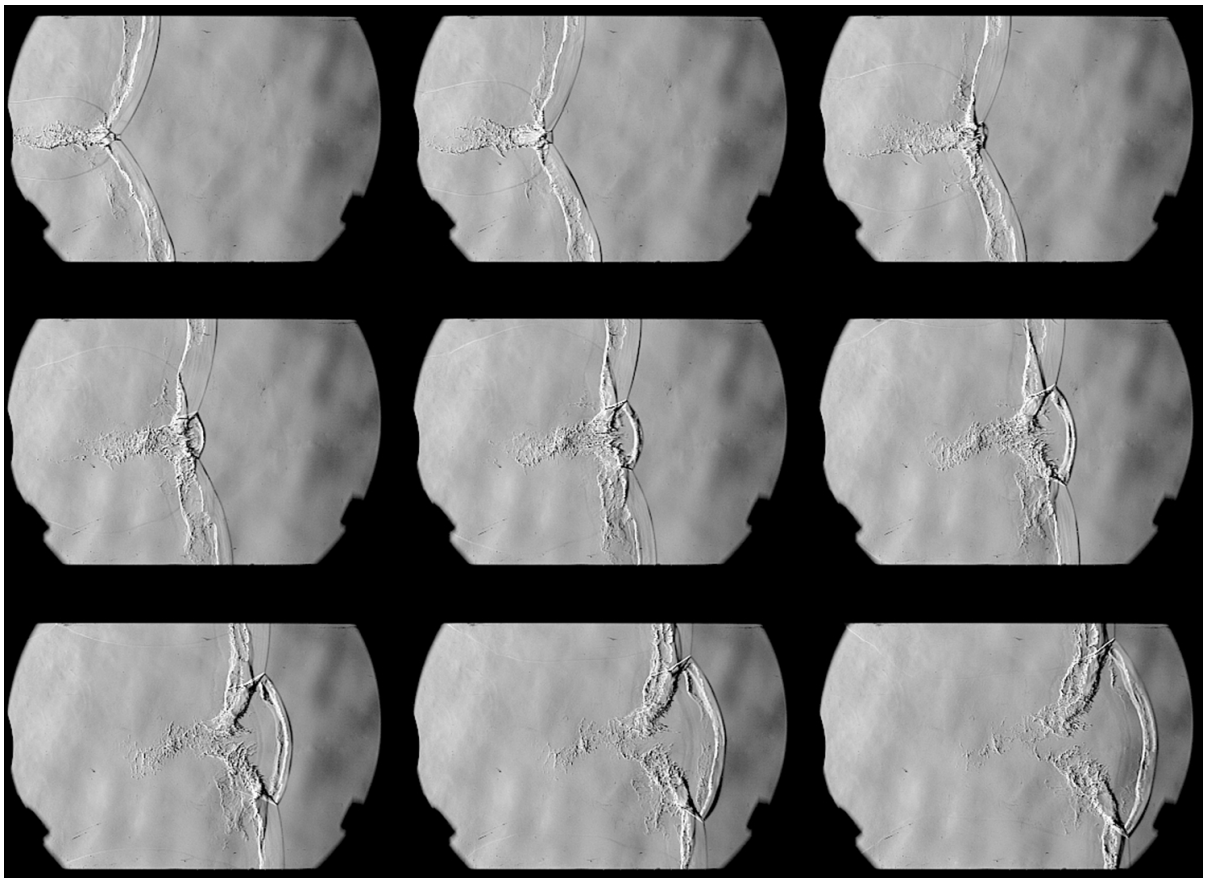

Figure G.12: Schlieren images of a flow field evolution showing spontaneous re-ignition behind the Mach shock. The initial pressure and temperature was 10.5 kPa and 300K. All frames were obtained from the same experiment using the high speed video format with an inter-frame delay of 12.97 μsec. *Test ID: CH4+O2-08-03-12(1.49psiTEST2)*

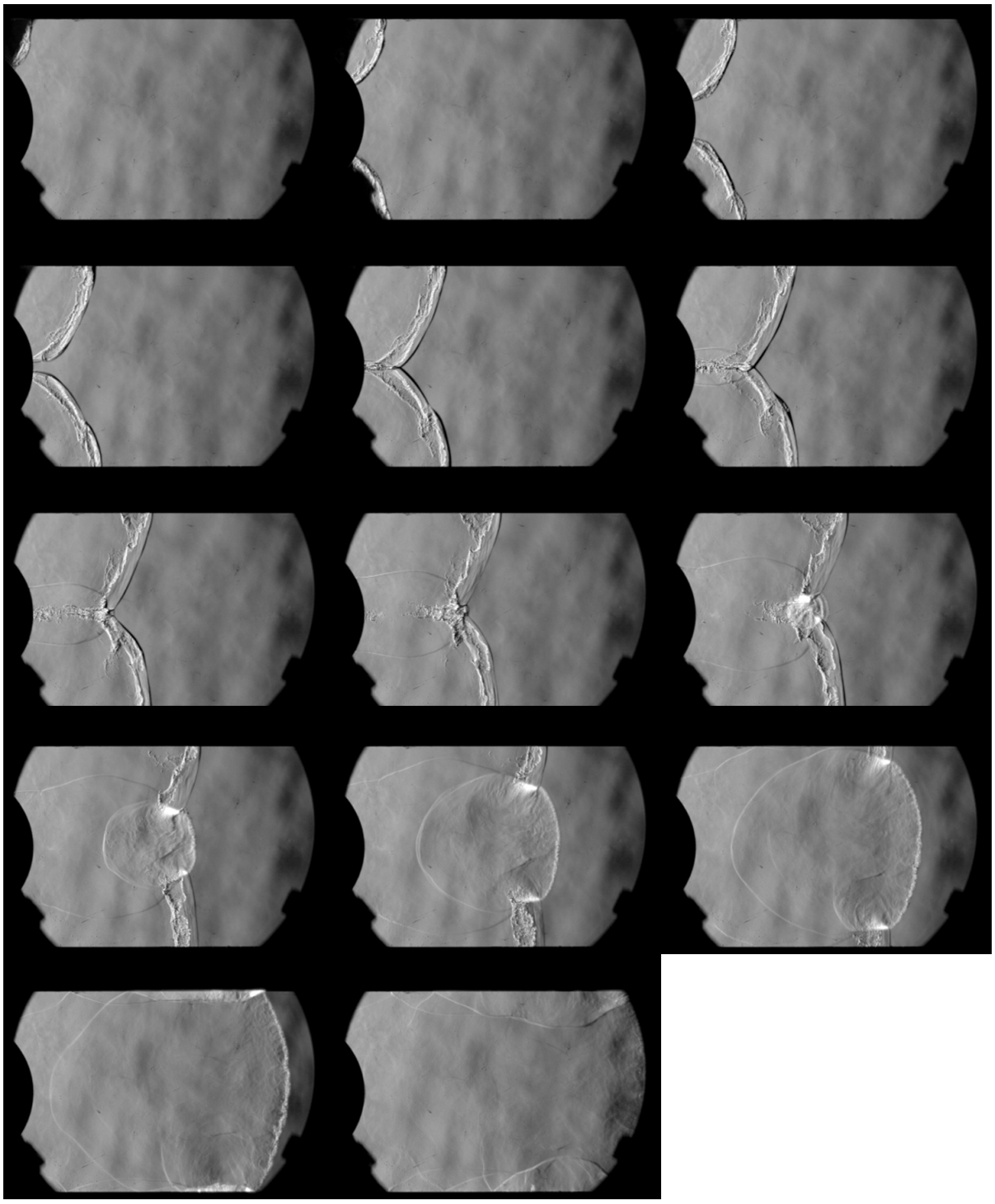

Figure G.13: Schlieren images of a flow field evolution showing spontaneous re-initiation of the Mach stem and transverse waves into a detonation wave. The initial pressure and temperature was 16.8 kPa and 300K. All frames were obtained from the same experiment using the high speed video format with an inter-frame delay of 12.91 μsec. *Test ID: CH4+O2-08-01-12(2.4psiTEST4)*

G.2 High speed Schlieren videos obtained from other experiments

For the readers' interest, shown here are images obtained from high speed Schlieren videos that were recorded from other experiments which were not shown in the body of the report. Images for all obstacles and regimes are shown below.

G.2.1 Detonation failure regime using the half-cylinder obstacle

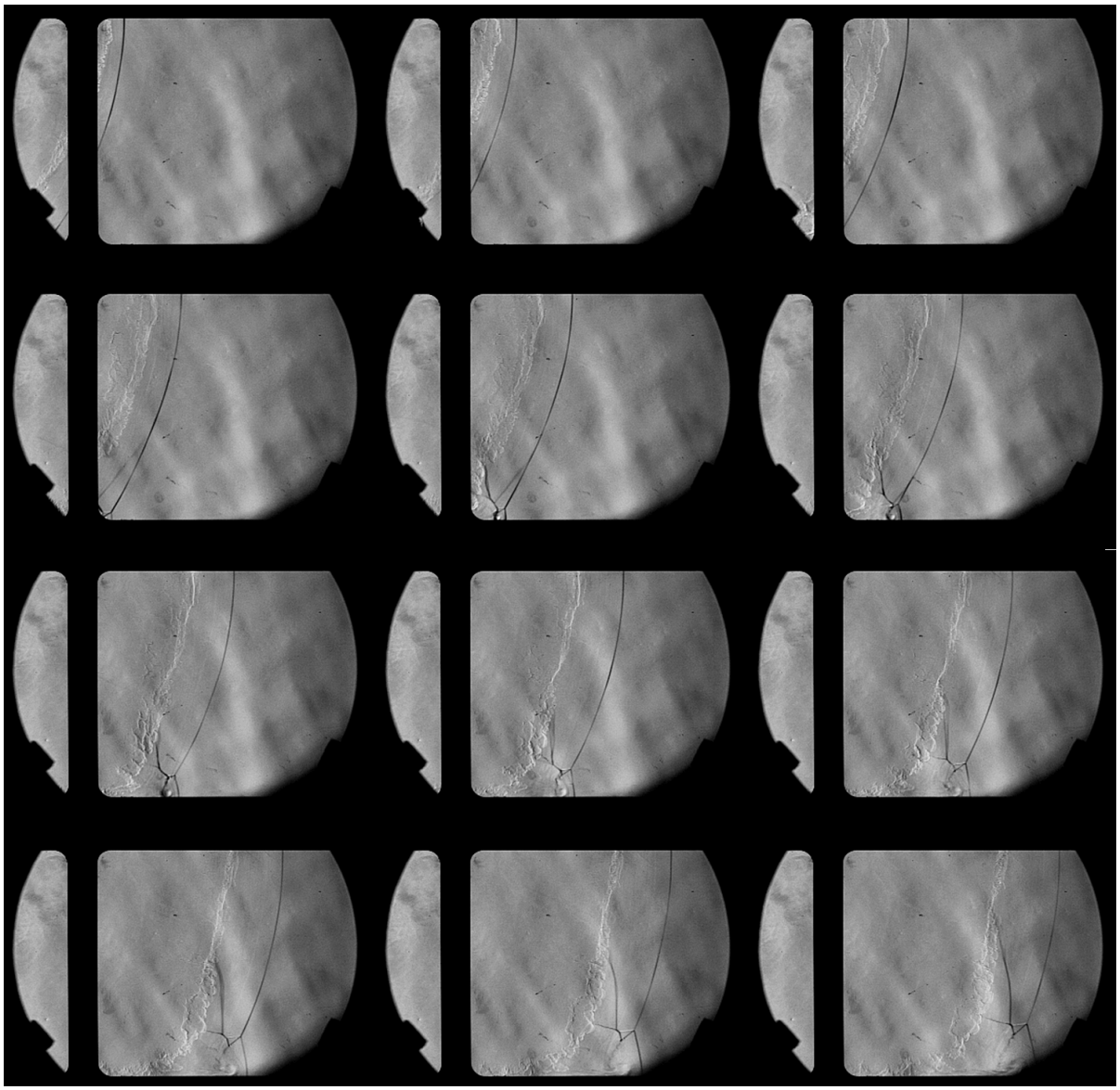

Figure G.14: Schlieren images of a flow field evolution for $p_0 = 5.5$ kPa and $T_0 = 300$K with an inter-frame delay of 12.97 μsec. *Test ID: CH4+O2-07-25-12(0.8psiTEST1)*

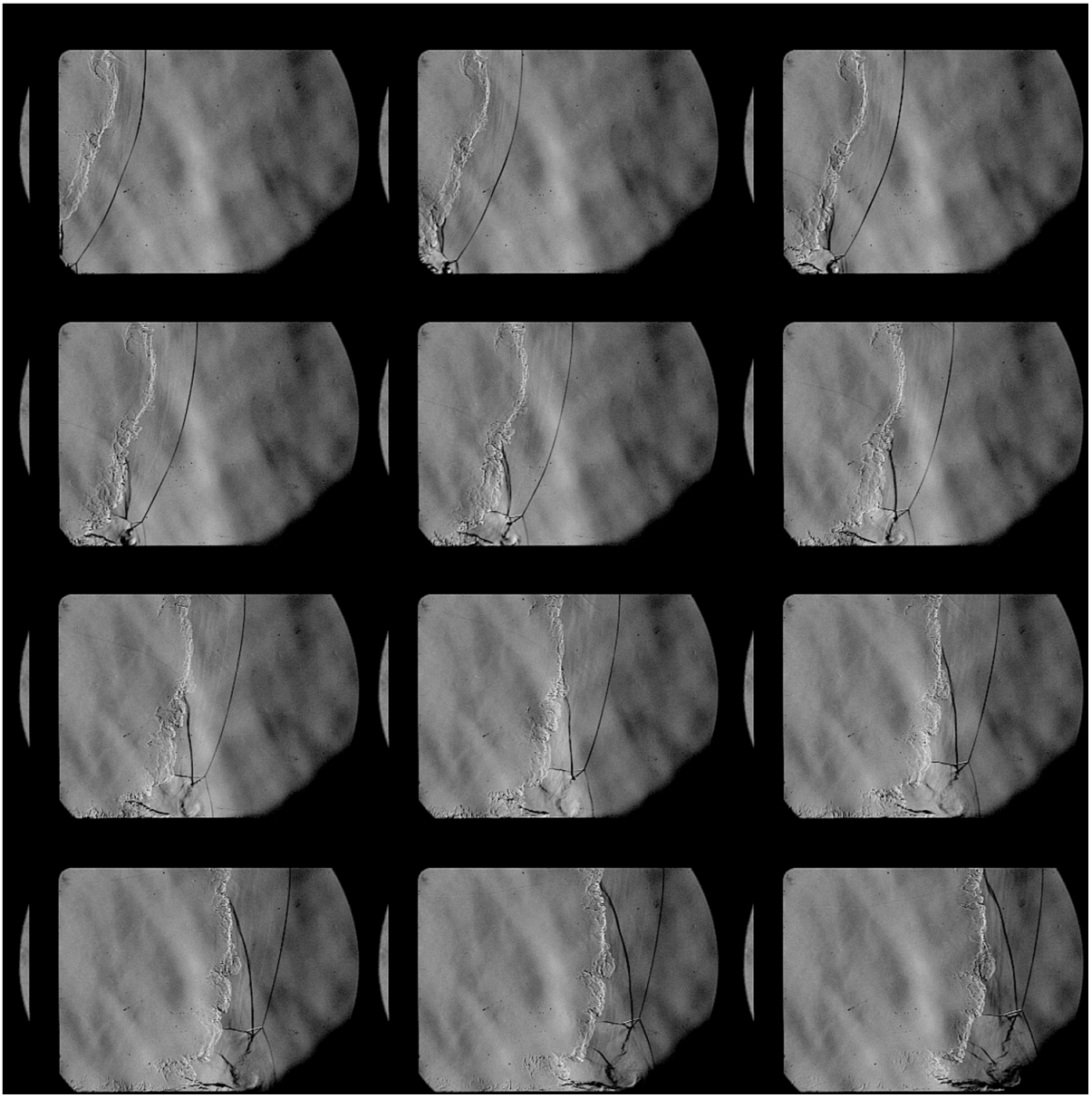

Figure G.15: Schlieren images of a flow field evolution for $p_0 = 10.5$ kPa and $T_0 = 300$K with an inter-frame delay of 12.97 μsec. *Test ID: CH4+O2-07-27-12(1.49psiTEST5)*

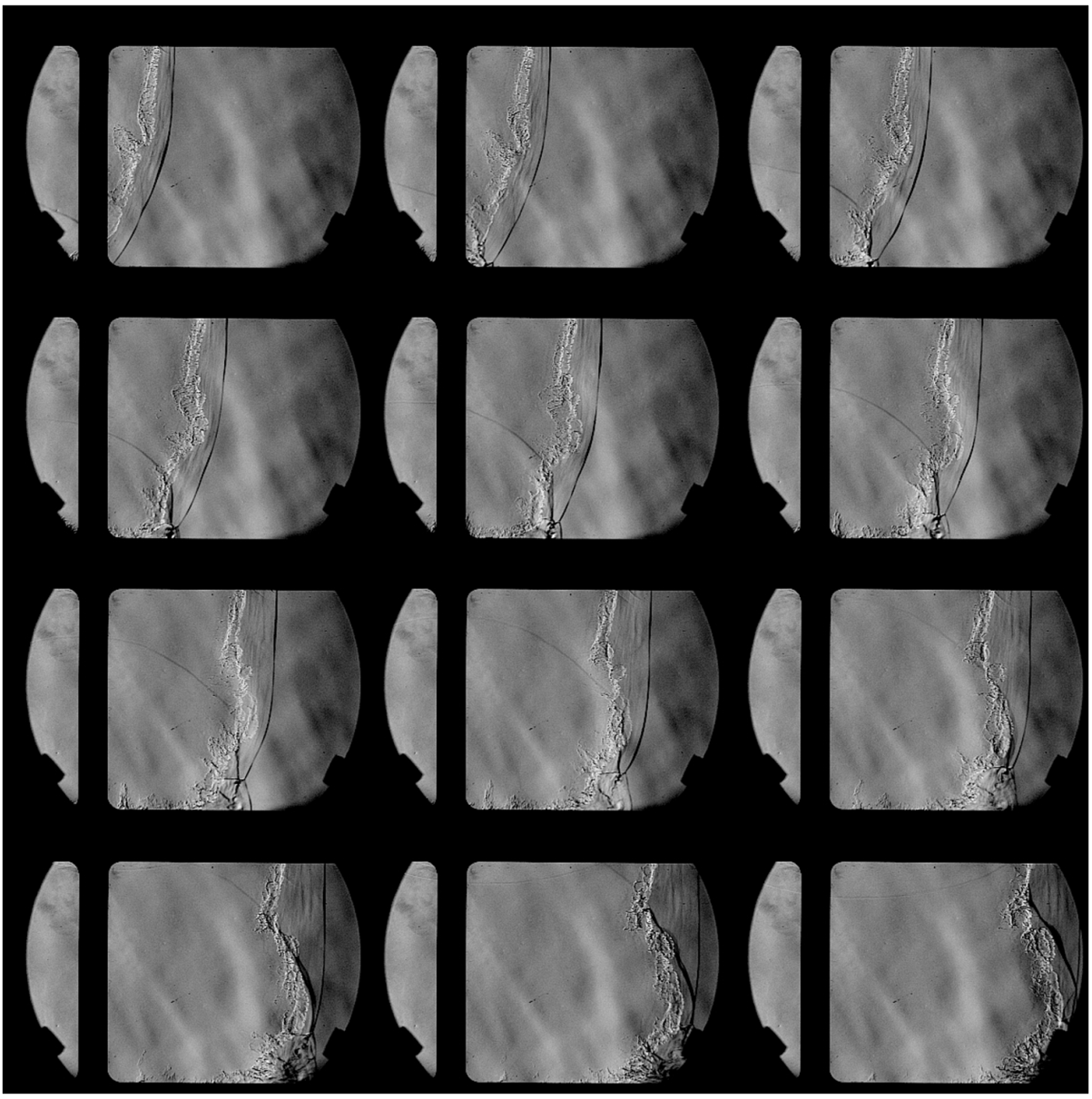

Figure G.16: Schlieren images of a flow field evolution for $p_0 = 12.3$ kPa and $T_0 = 300$K with an inter-frame delay of 12.97 μsec. *Test ID: CH4+O2-07-25-12(1.75psiTEST7)*

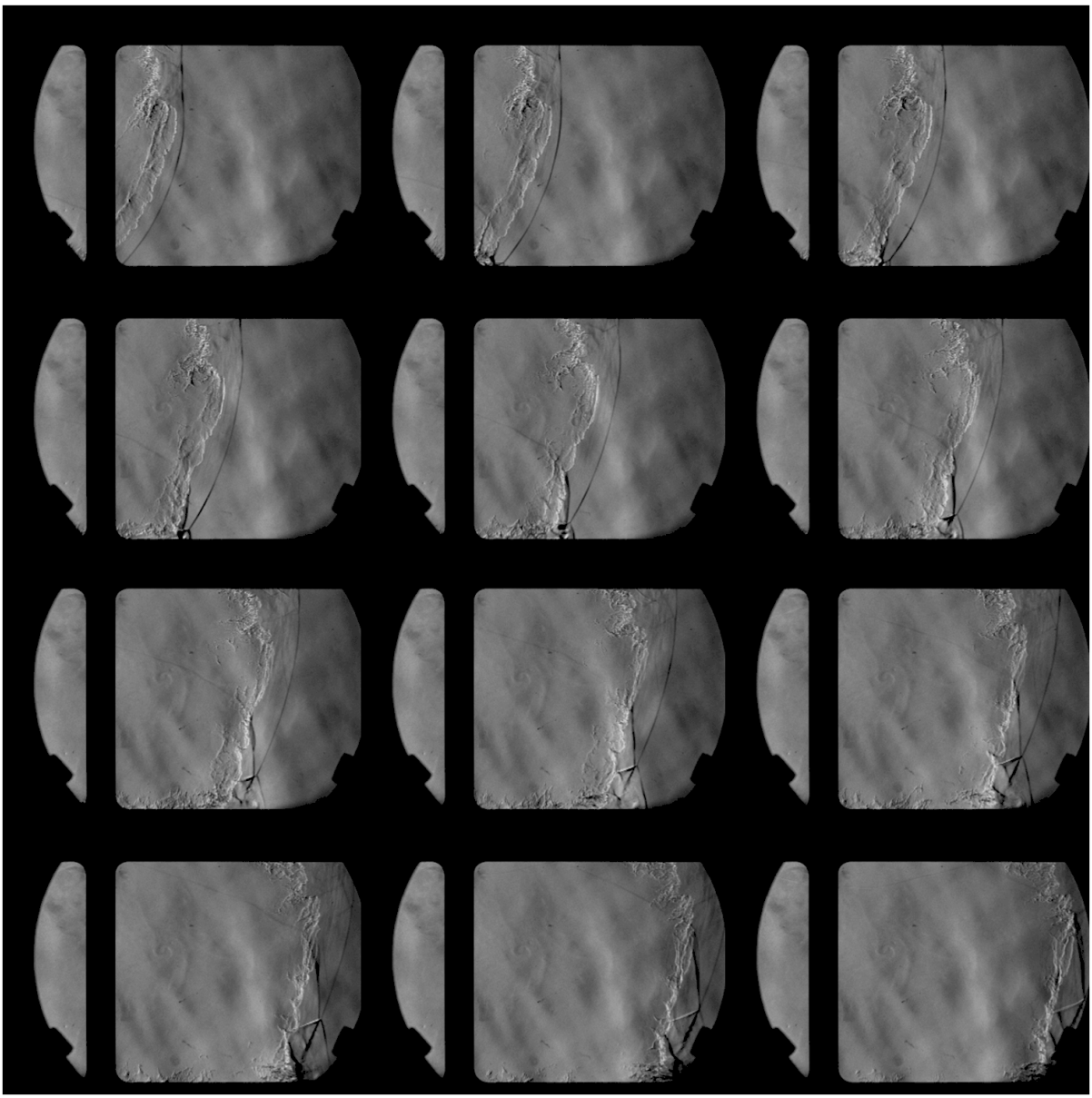

Figure G.17: Schlieren images of a flow field evolution for $p_0 = 12.3$ kPa and $T_0 = 300$K with an inter-frame delay of 12.97 μsec. *Test ID: CH4+O2-07-24-12(1.75psiTEST5)*

G.2.2 Experiments using the half-cylinder with the roughness plate

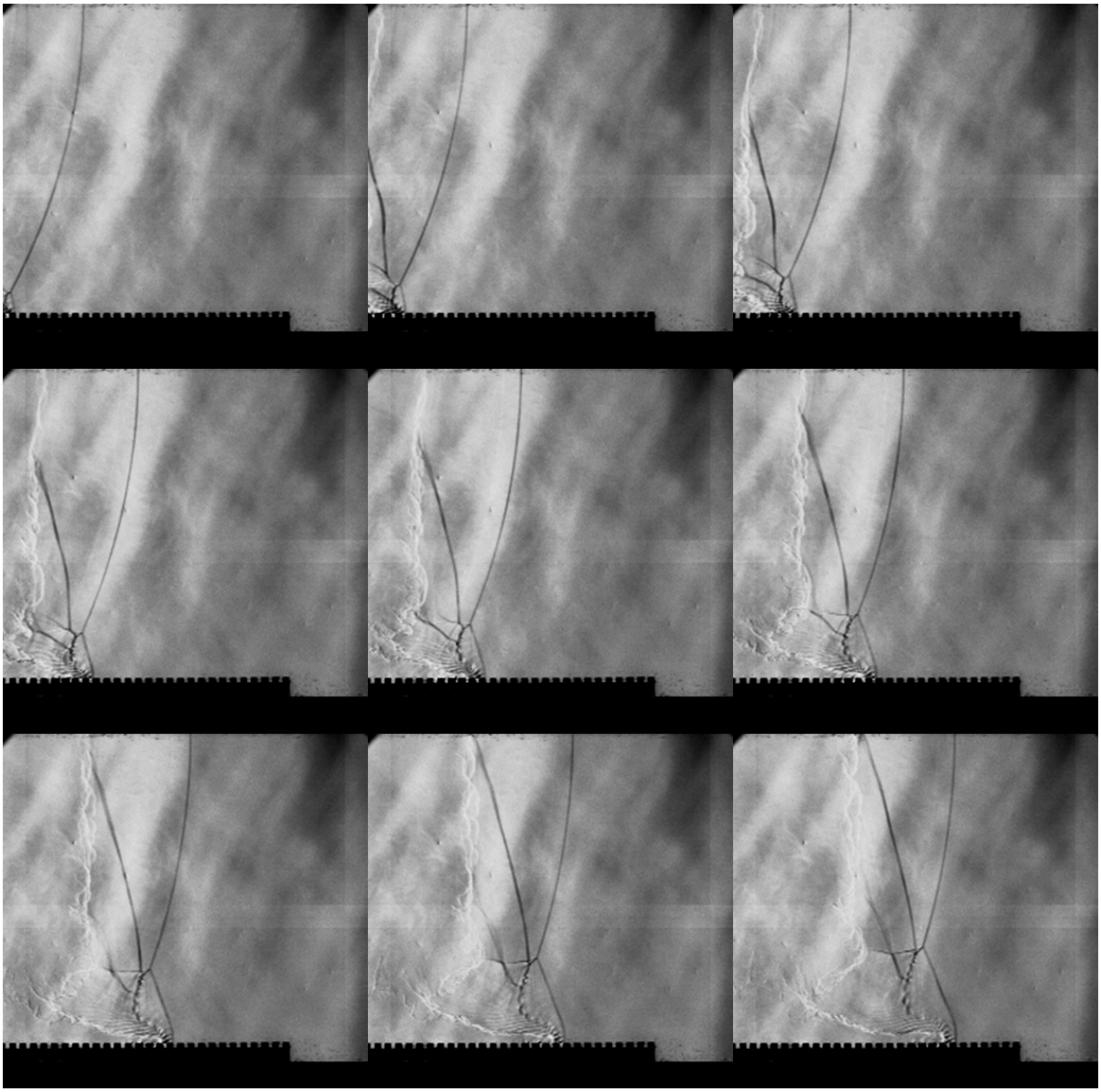

Figure G.18: Schlieren images of a flow field evolution for $p_0 = 5.5$ kPa and $T_0 = 300$K using the roughness plate with an inter-frame delay of 10 μsec. *Test ID: CH4+O2-07-13-12(0.8psiTEST3)roughness*

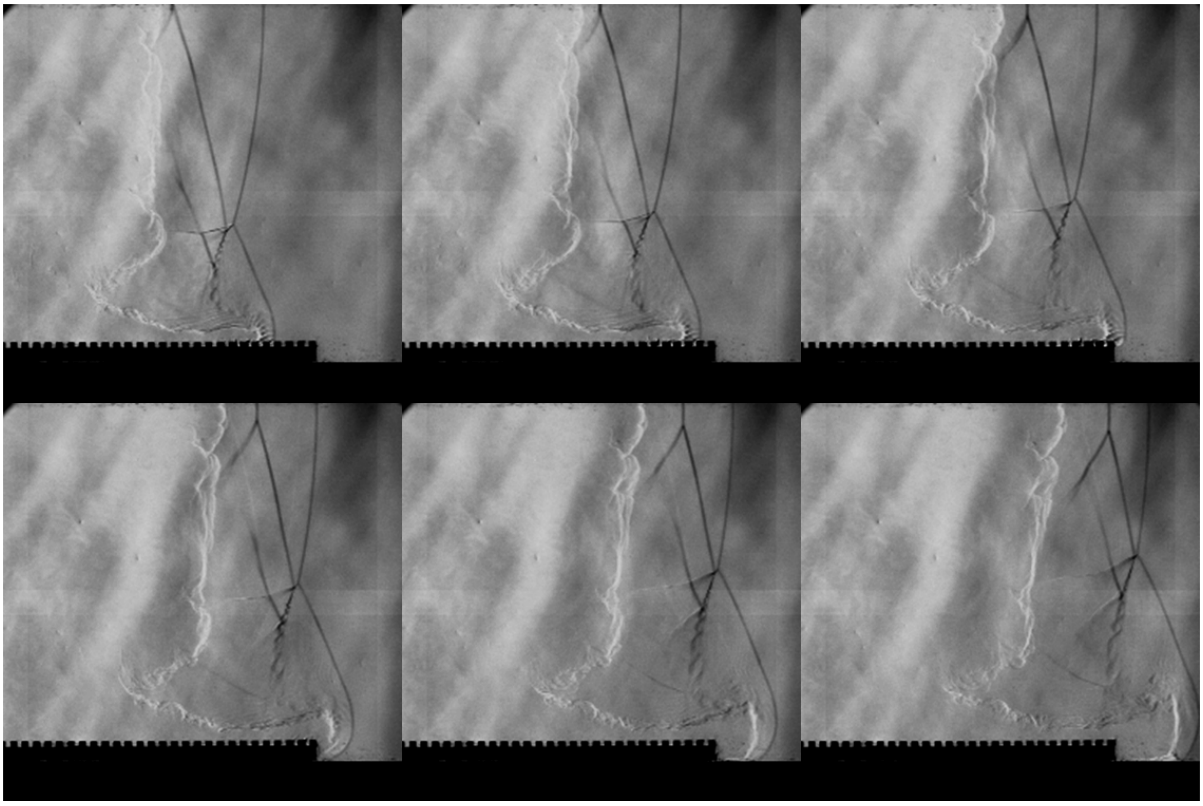

Figure G.19: Continuation of the flow field evolution shown in Figure G.18. *Test ID: CH4+O2-07-13-12(0.8psiTEST3)roughness*

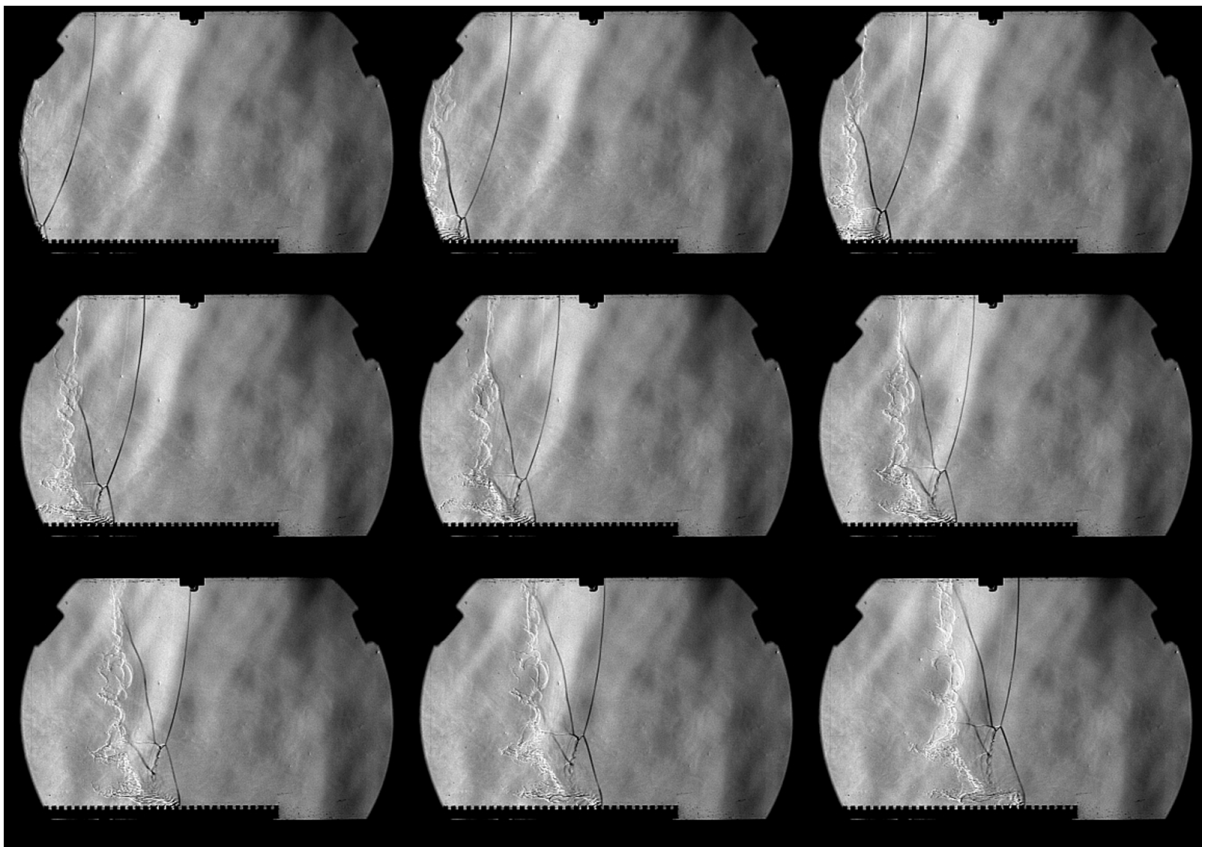

Figure G.20: Schlieren images of a flow field evolution for $p_0 = 5.5$ kPa and $T_0 = 300$K using the roughness plate with an inter-frame delay of 12.34 μsec. *Test ID: CH4+O2-07-13-12(0.8psiTEST4)roughness*

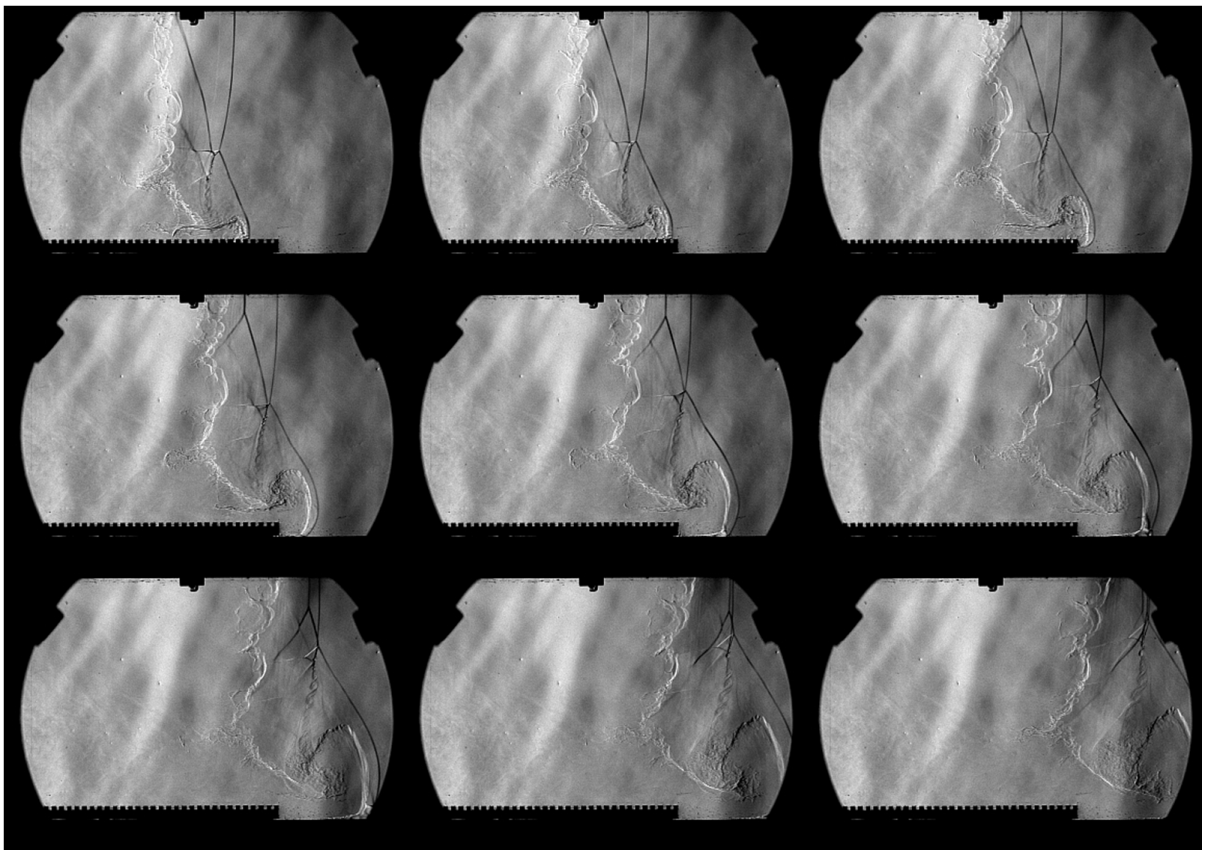

Figure G.21: Continuation of the flow field evolution shown in Figure G.20. *Test ID: CH4+O2-07-13-12(0.8psiTEST4)roughness*

G.2.3 Hot spot re-ignition regime using the half-cylinder obstacle

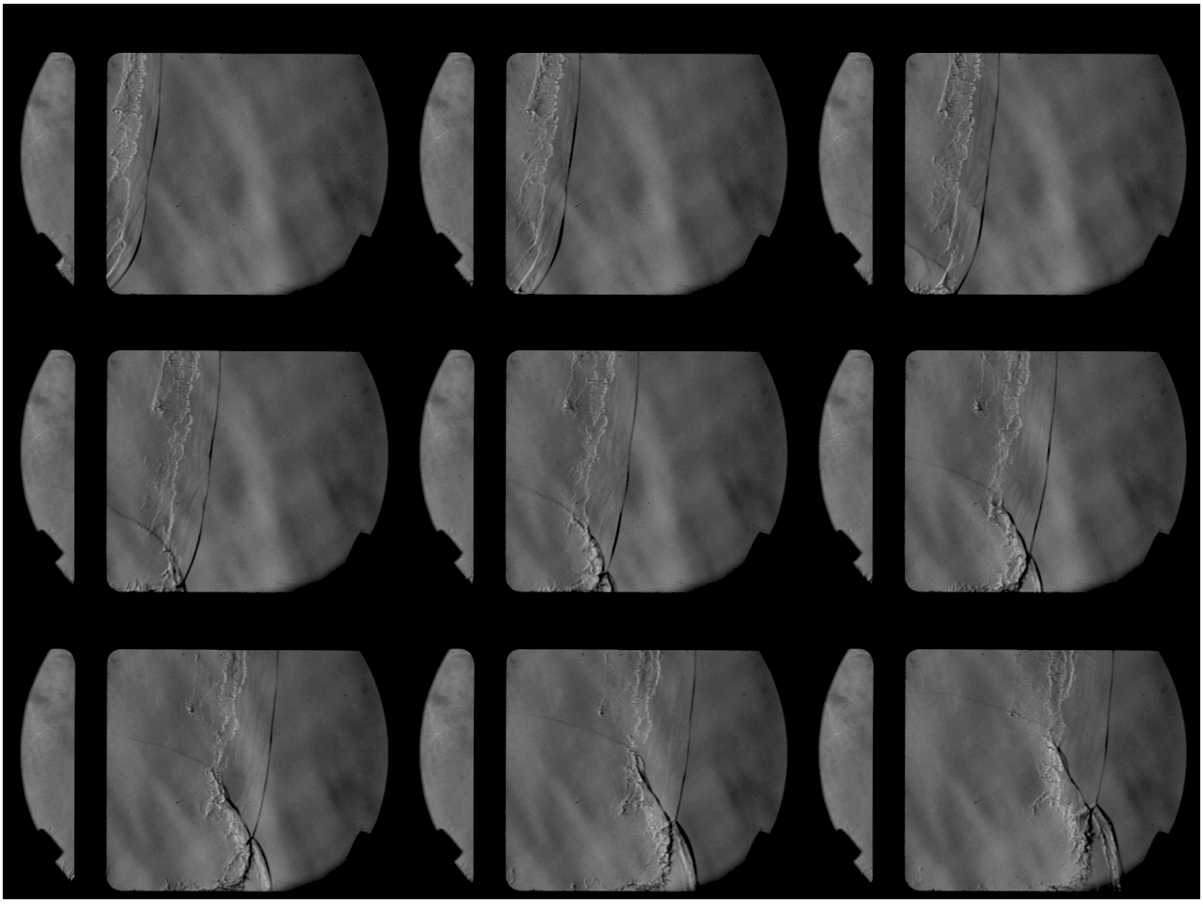

Figure G.22: Schlieren images of a flow field evolution for $p_0 = 10.3$ kPa and $T_0 = 300$K with an inter-frame delay of 12.97 μsec. *Test ID: CH4+O2-07-27-12(1.47psiTEST8)*

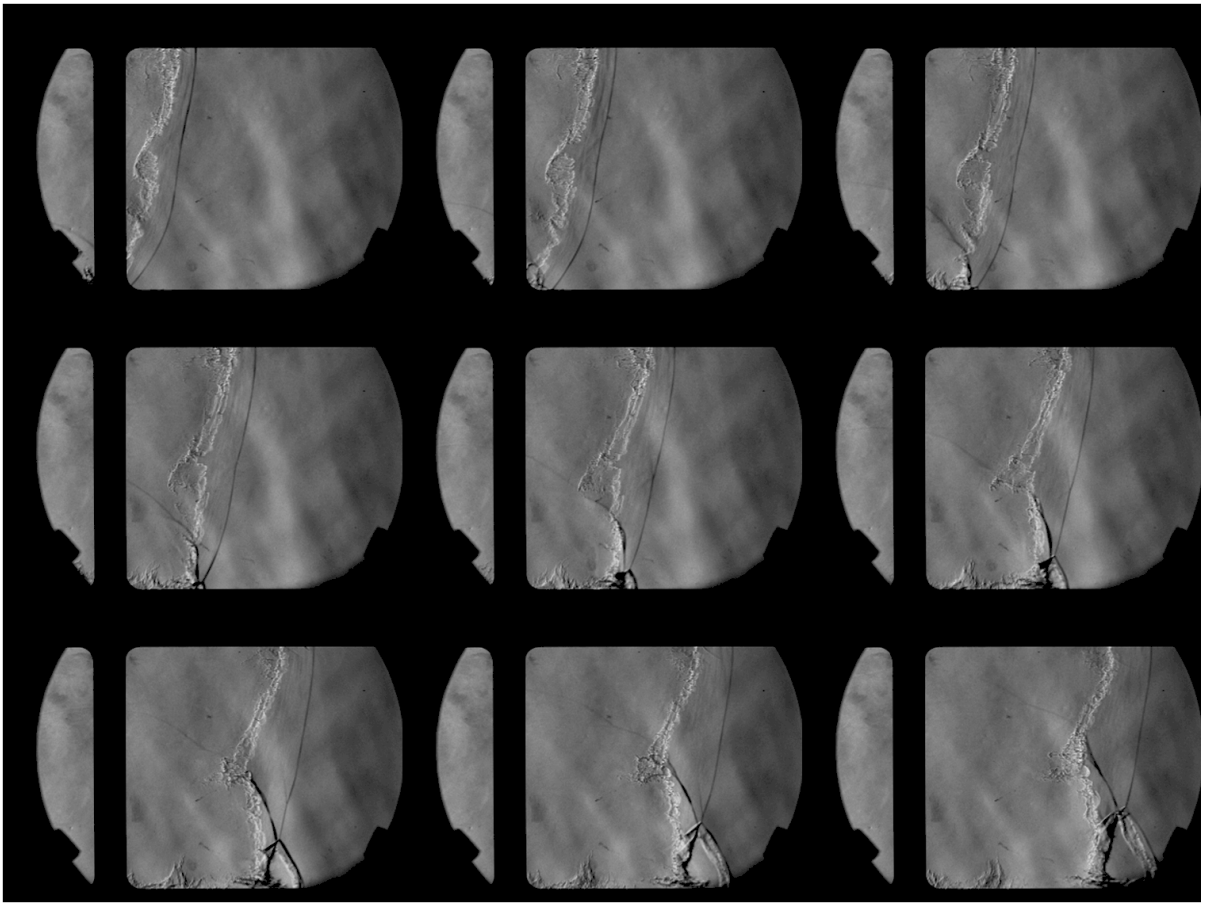

Figure G.23: Schlieren images of a flow field evolution for $p_0 = 12.3$ kPa and $T_0 = 300$K with an inter-frame delay of 12.97 μsec. *Test ID: CH4+O2-07-24-12(1.75psiTEST7)*

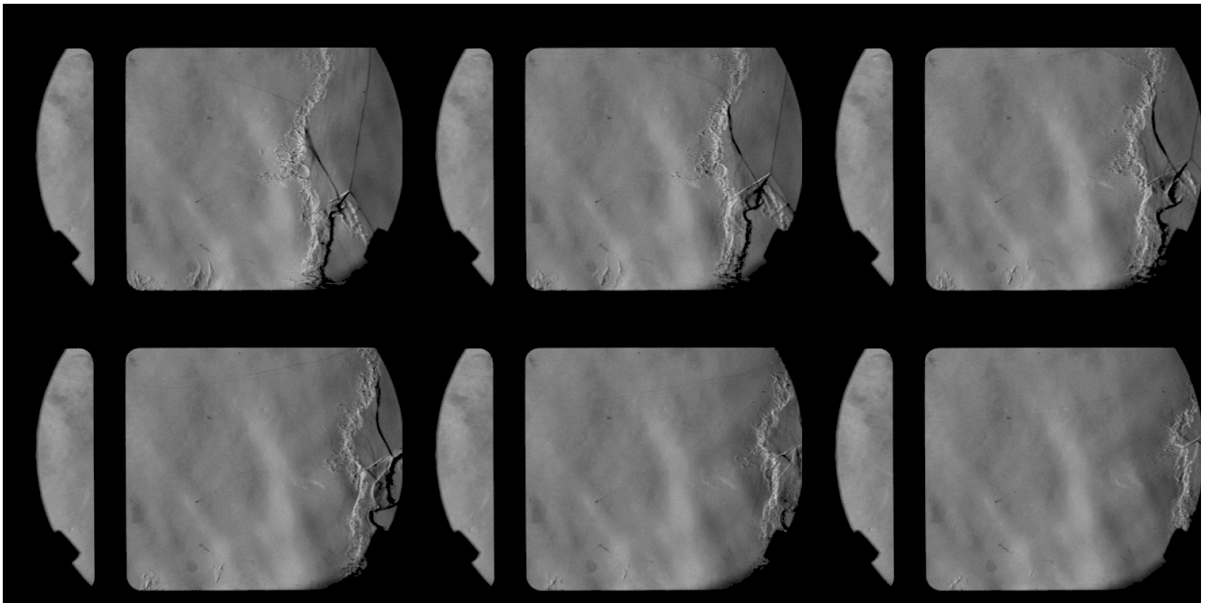

Figure G.24: Continuation of the flow field evolution shown in Figure G.23. *Test ID: CH4+O2-07-24-12(1.75psiTEST7)*

G.2.4 Detonation re-initiation regime using the half-cylinder obstacle

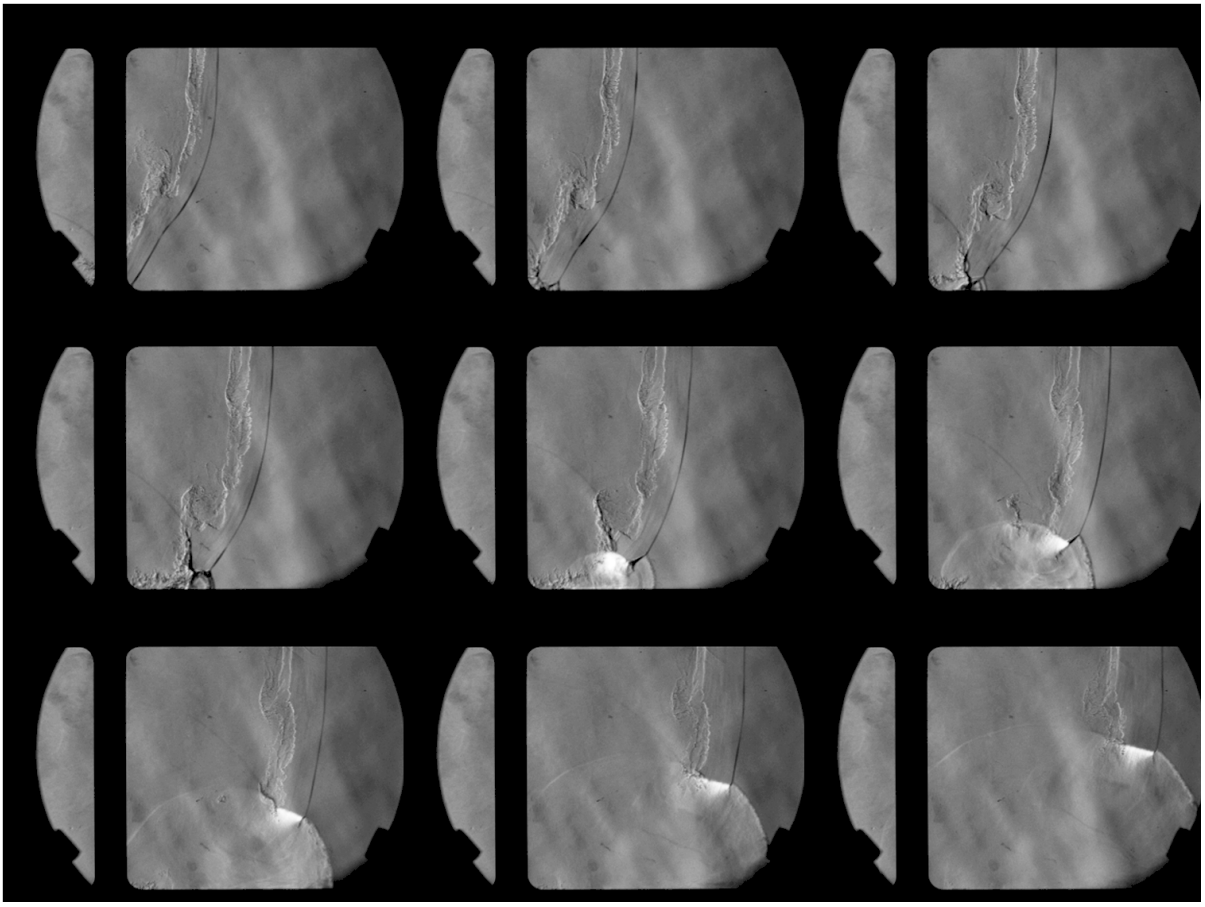

Figure G.25: Schlieren images of a flow field evolution for p_0 = 10.5 kPa and T_0 = 300K with an inter-frame delay of 12.97 μsec. *Test ID: CH4+O2-07-24-12(1.49psiTEST6)*

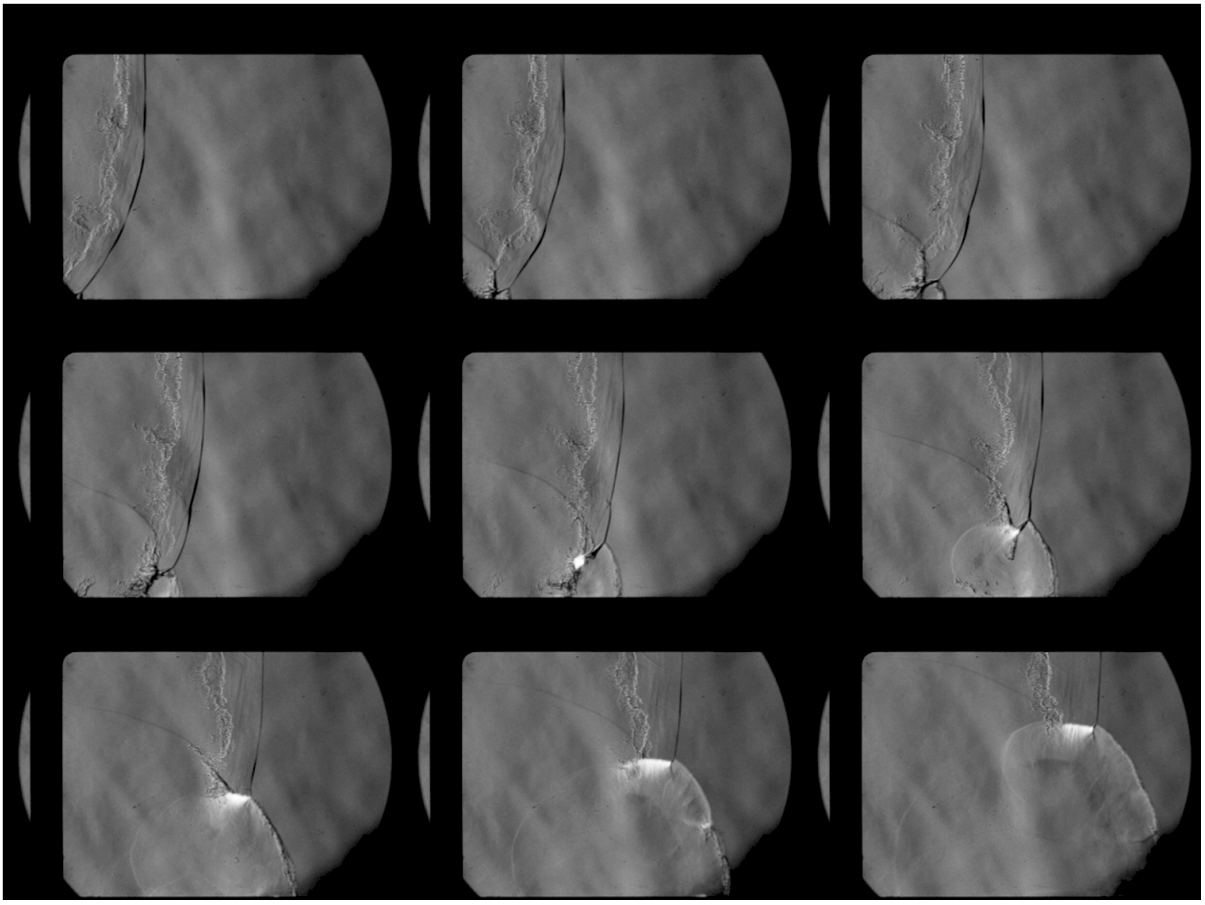

Figure G.26: Schlieren images of a flow field evolution for $p_0 = 10.5$ kPa and $T_0 = 300$K with an inter-frame delay of 12.97 μsec. *Test ID: CH4+O2-07-27-12(1.49psiTEST6)*

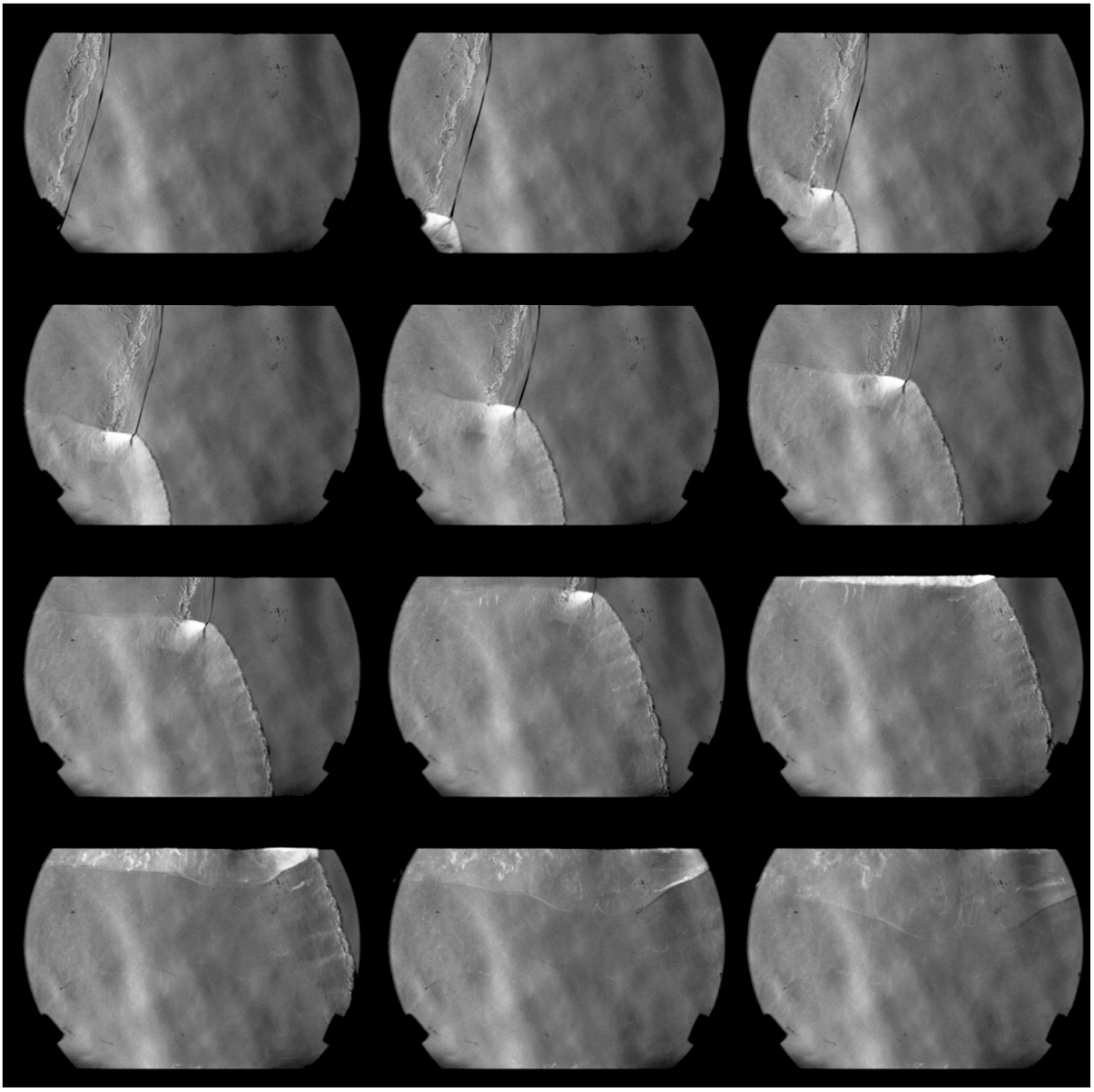

Figure G.27: Schlieren images of a flow field evolution for $p_0 = 12.3$ kPa and $T_0 = 300$K with an inter-frame delay of 12.97 μsec. *Test ID: CH4+O2-07-23-12(1.75psiTEST4)*

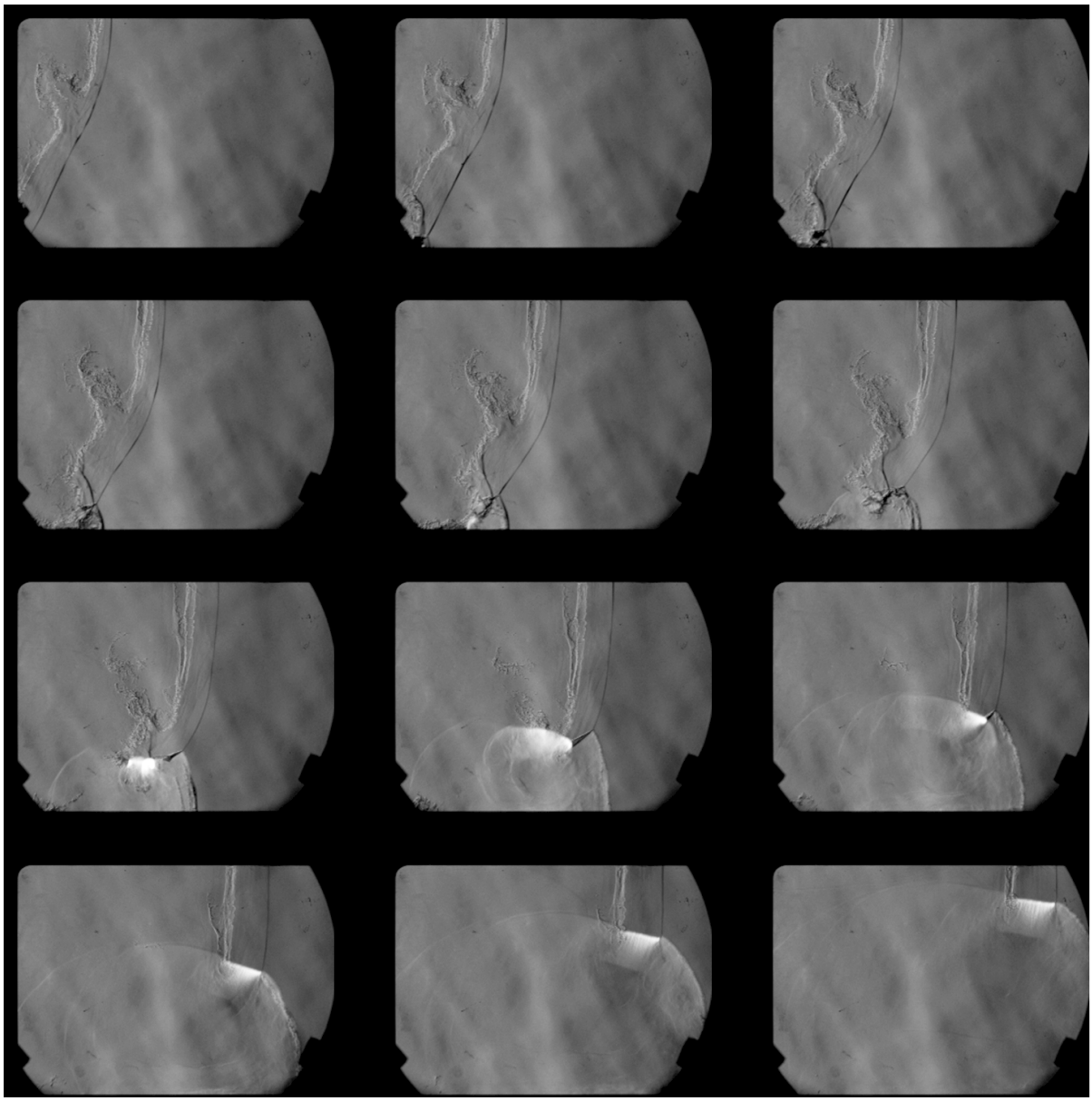

Figure G.28: Schlieren images of a flow field evolution for $p_0 = 12.3$ kPa and $T_0 = 300$K with an inter-frame delay of 12.97 μsec. *Test ID: CH4+O2-07-24-12(1.75psiTEST3)*

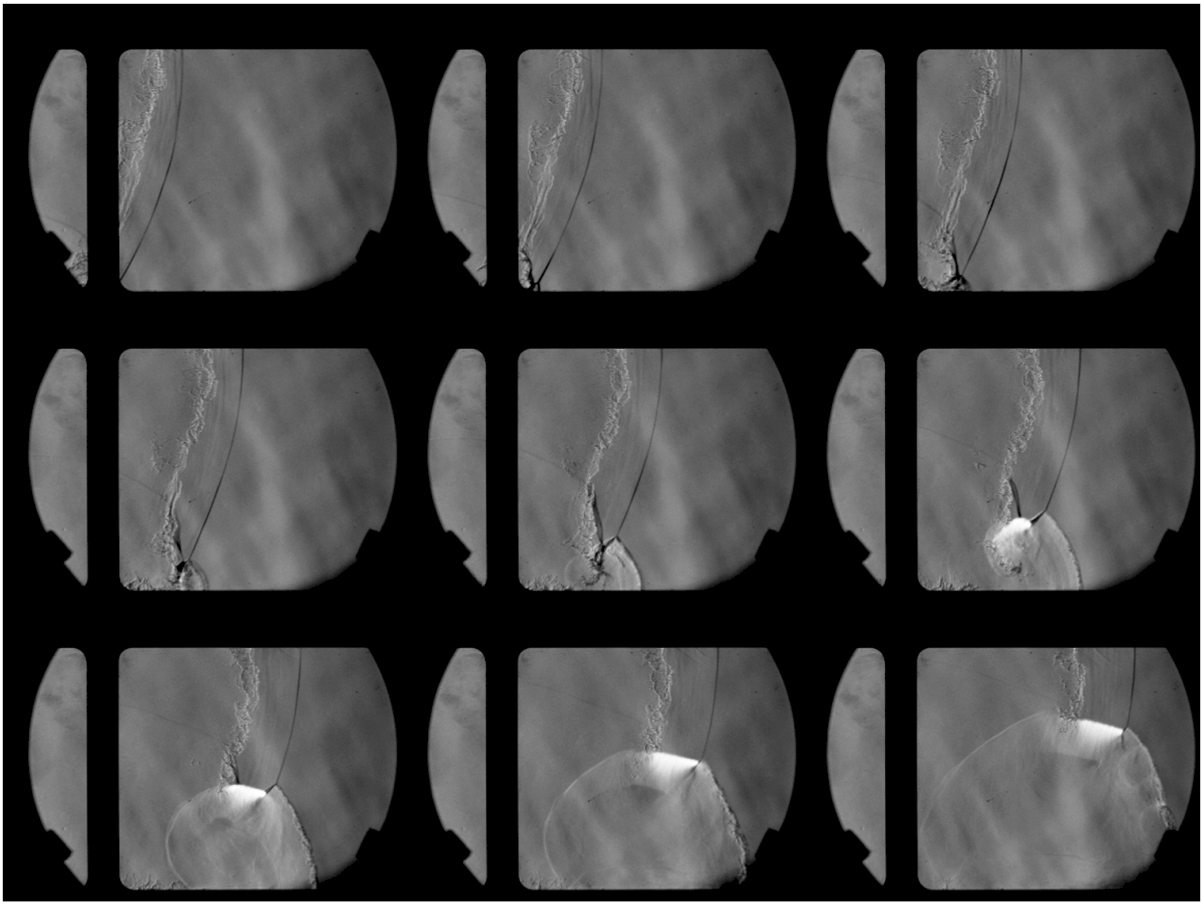

Figure G.29: Schlieren images of a flow field evolution for $p_0 = 12.3$ kPa and $T_0 = 300$K with an inter-frame delay of 12.97 μsec. *Test ID: CH4+O2-07-25-12(1.75psiTEST8)*

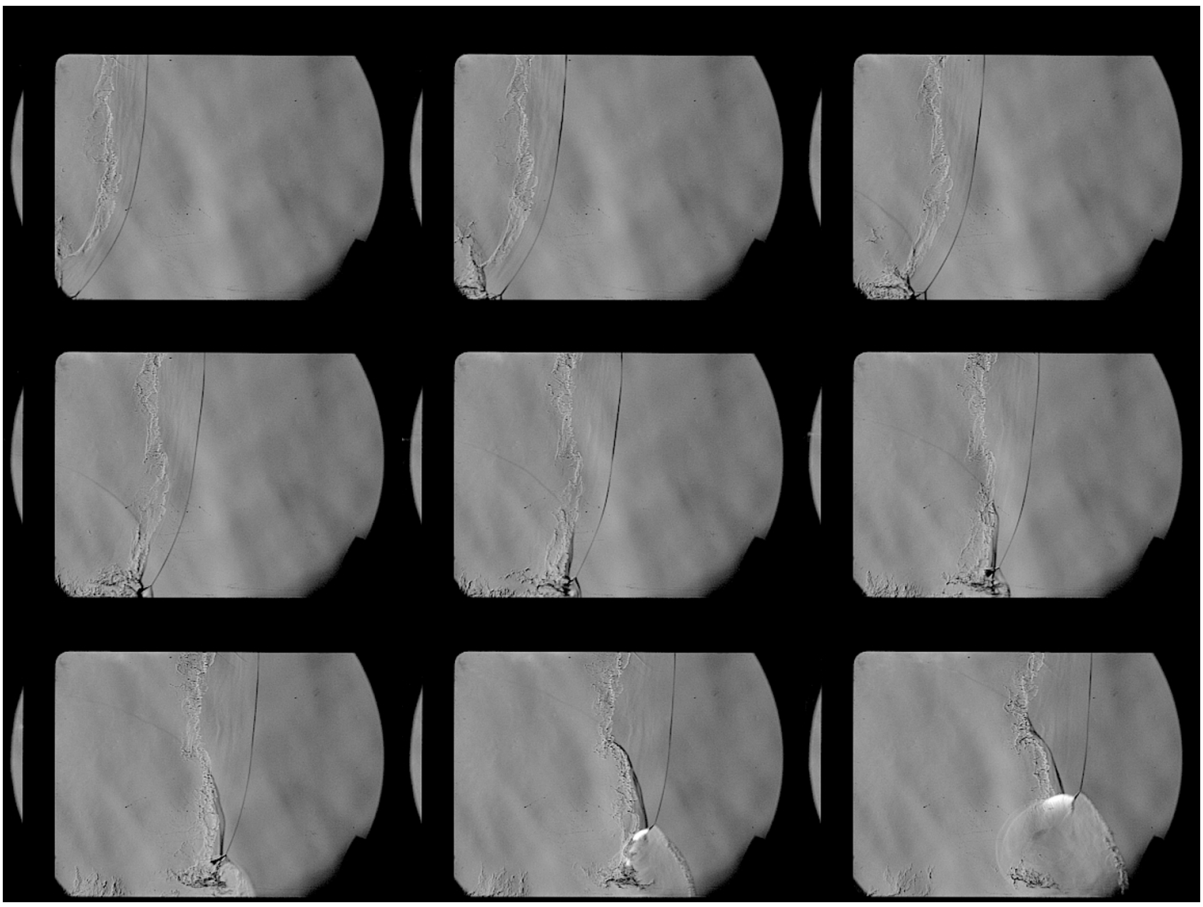

Figure G.30: Schlieren images of a flow field evolution for $p_0 = 11.9$ kPa and $T_0 = 300$K with an inter-frame delay of 12.97 μsec. *Test ID: CH4+O2-07-27-12(1.7psiTEST1)*

G.2.5 Detonation failure regime using the full-cylinder obstacle

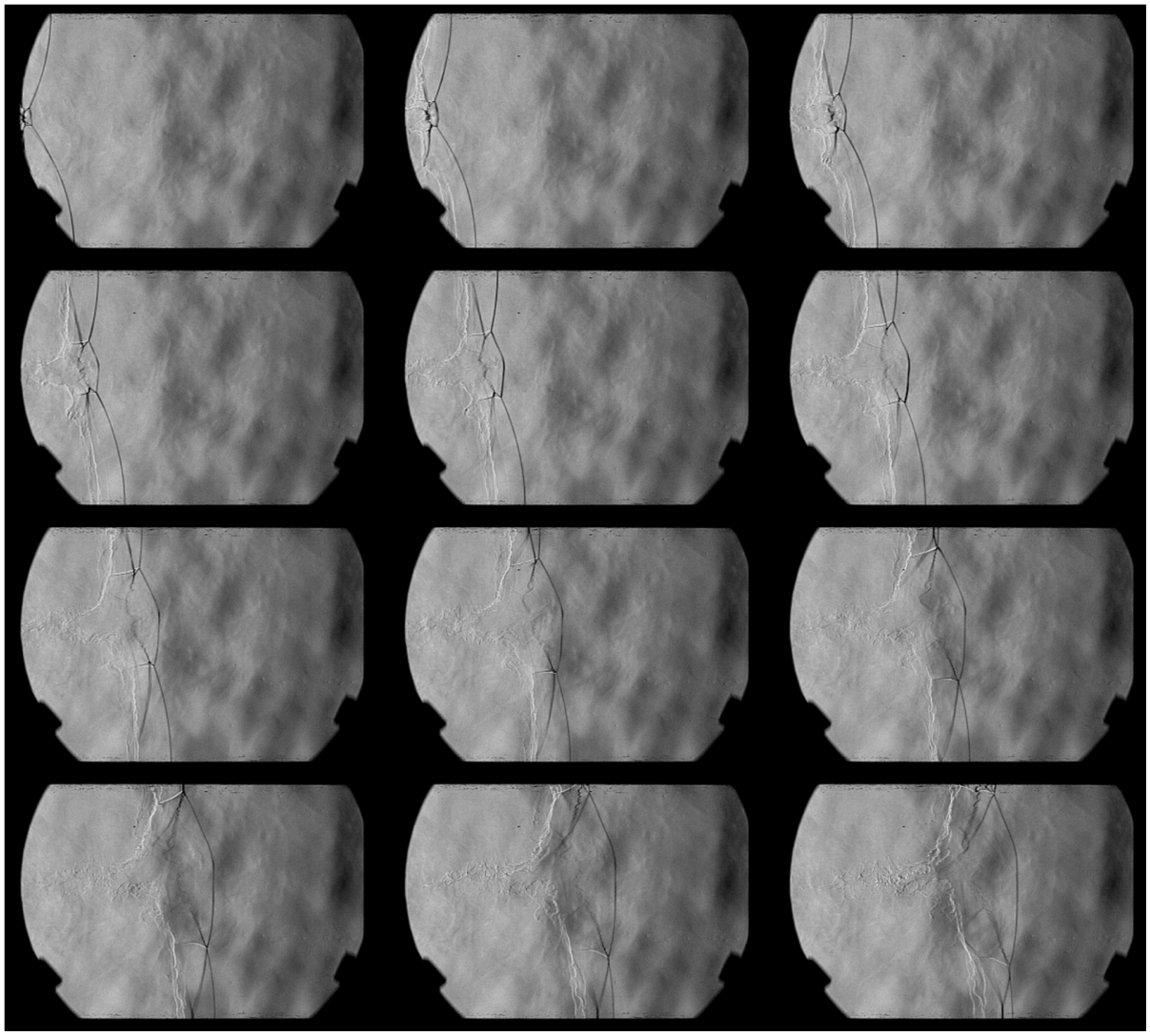

Figure G.31: Schlieren images of a flow field evolution for p_0 = 3.5 kPa and T_0 = 300K with an inter-frame delay of 11.53 μsec. *Test ID: CH4+O2-08-20-12(0.5psiTEST4)*

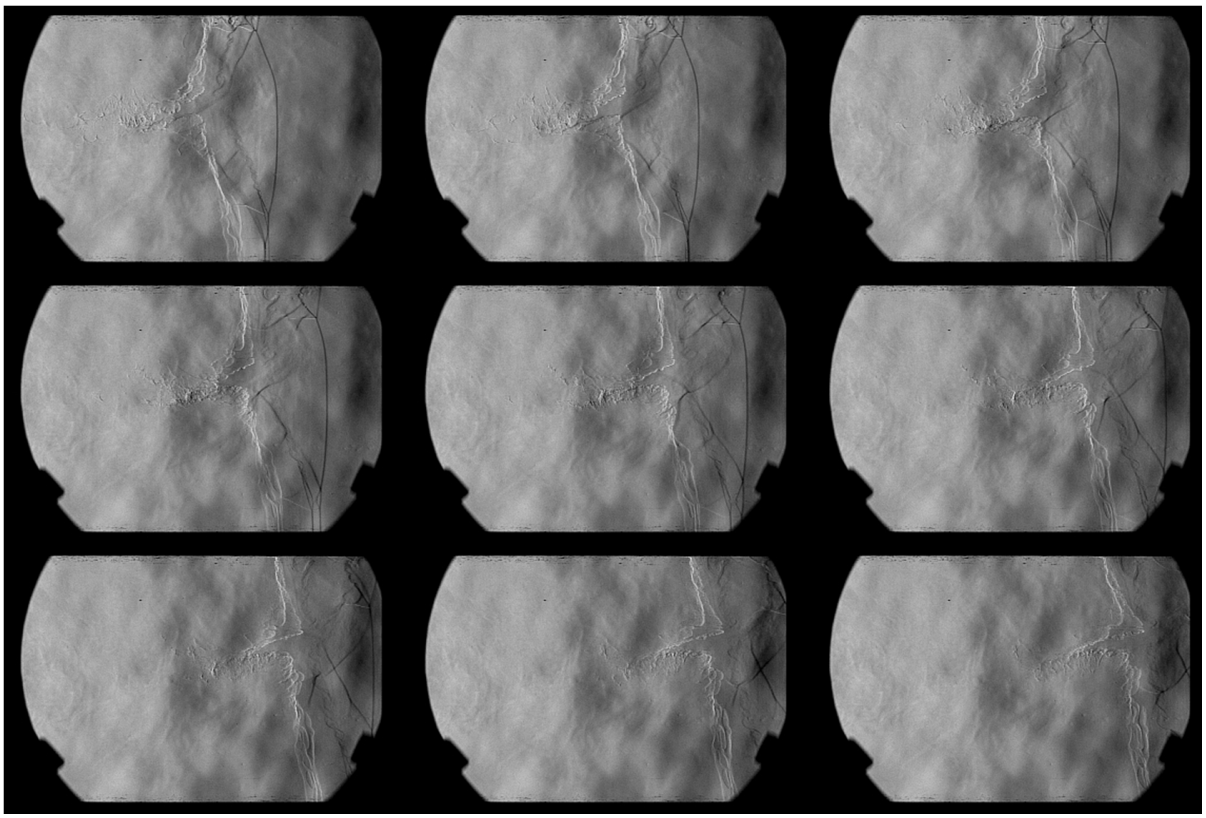

Figure G.32: Continuation of the flow field evolution shown in Figure G.31. *Test ID: CH4+O2-08-20-12(0.5psiTEST4)*

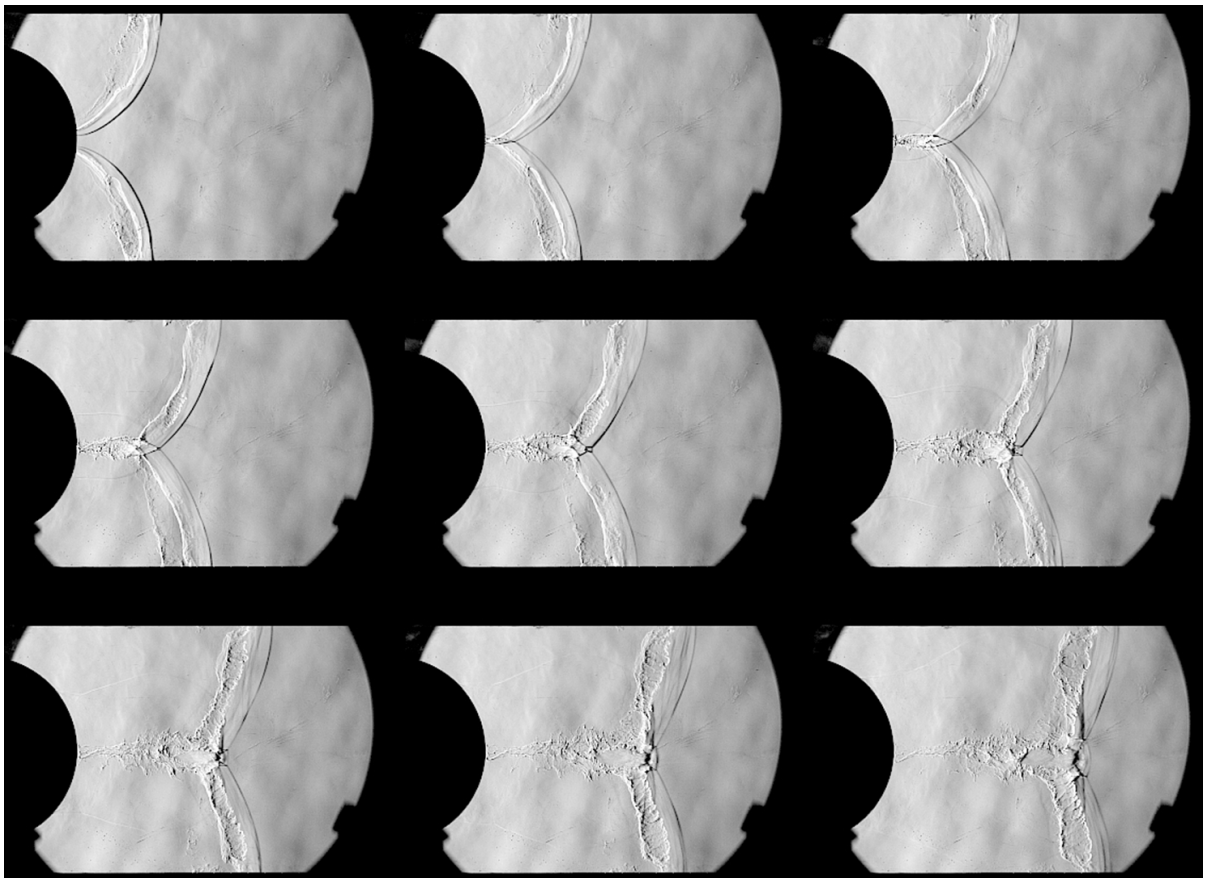

Figure G.33: Schlieren images of a flow field evolution for $p_0 = 9.8$ kPa and $T_0 = 300$K with an inter-frame delay of 12.97 μsec. *Test ID: CH4+O2-08-01-12(1.4psiTEST1)*

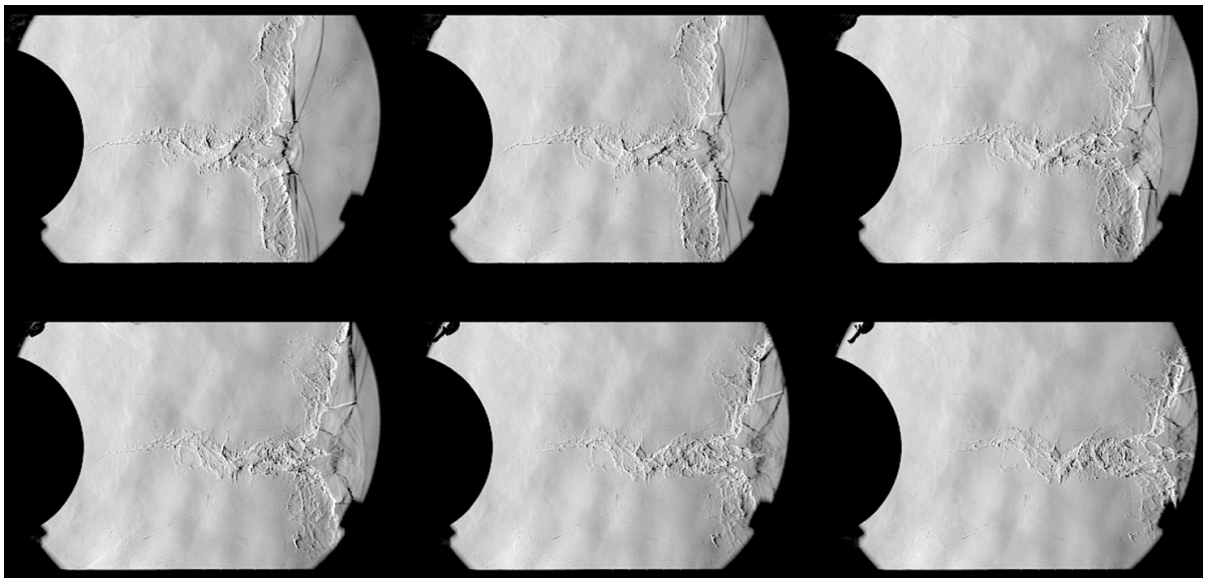

Figure G.34: Continuation of the flow field evolution shown in Figure G.33. *Test ID: CH4+O2-08-01-12(1.4psiTEST1)*

G.2.6 Hot spot re-ignition regime using the full-cylinder obstacle

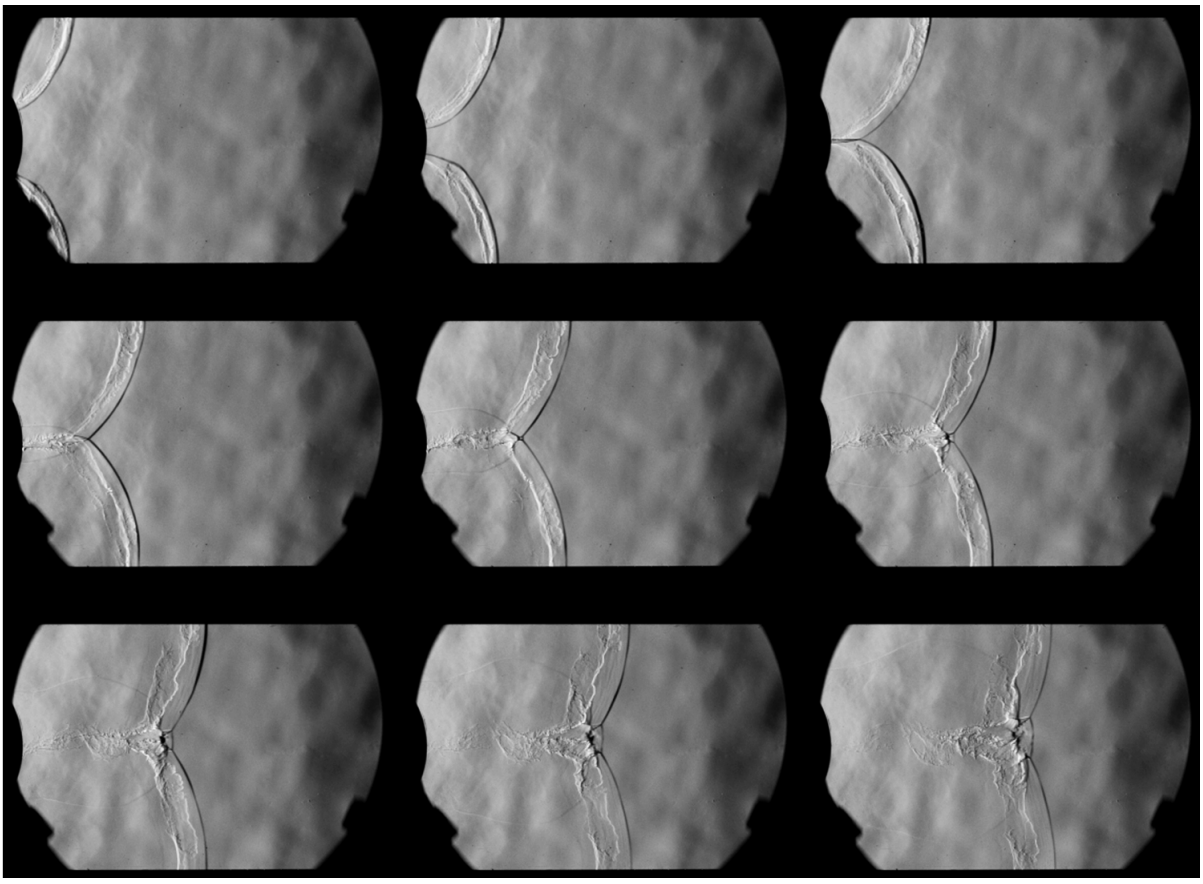

Figure G.35: Schlieren images of a flow field evolution for $p_0 = 5.5$ kPa and $T_0 = 300$K with an inter-frame delay of 12.91 μsec. *Test ID: CH4+O2-08-14-12(0.8psiTEST3)*

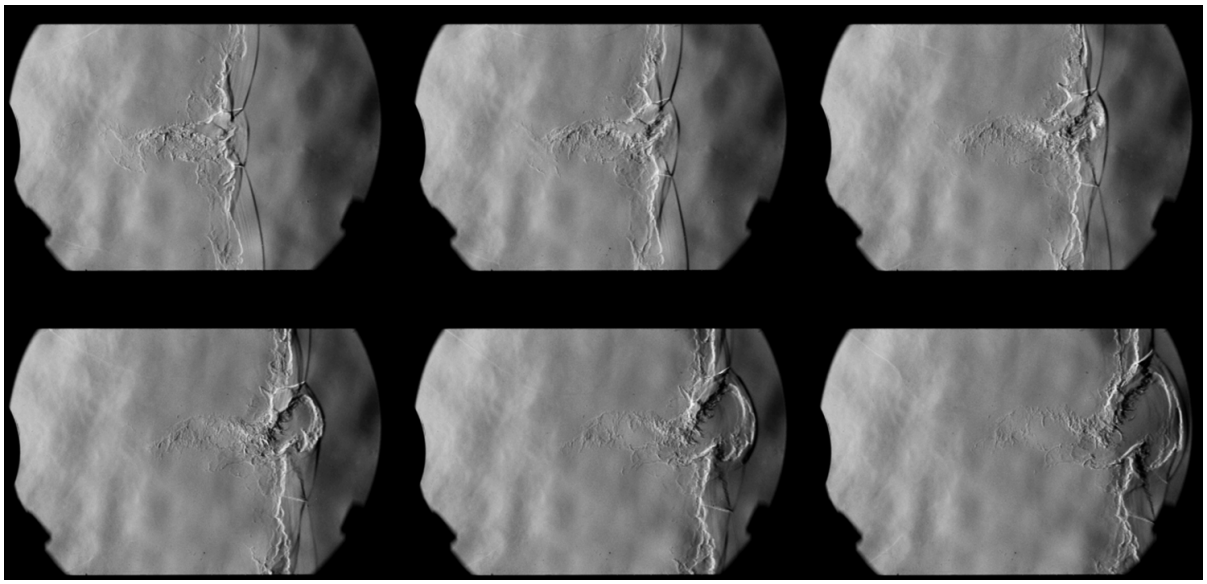

Figure G.36: Continuation of the flow field evolution shown in Figure G.35. *Test ID: CH4+O2-08-14-12(0.8psiTEST3)*

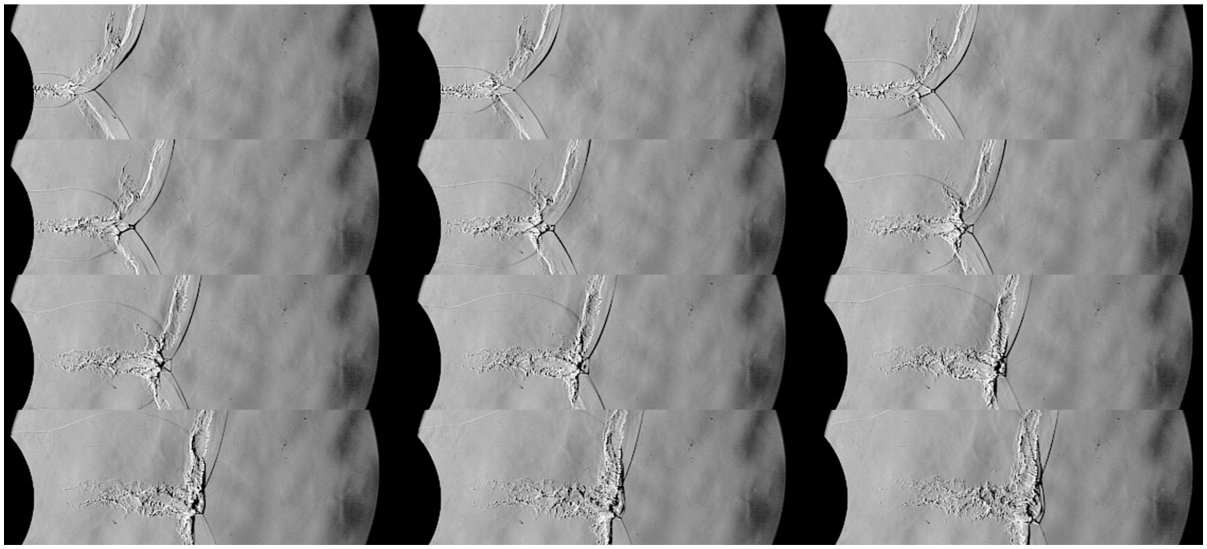

Figure G.37: Schlieren images of a flow field evolution for $p_0 = 10.5$ kPa and $T_0 = 300$K with an inter-frame delay of 6.03 μsec. *Test ID: CH4+O2-08-01-12(1.5psiTEST6)*

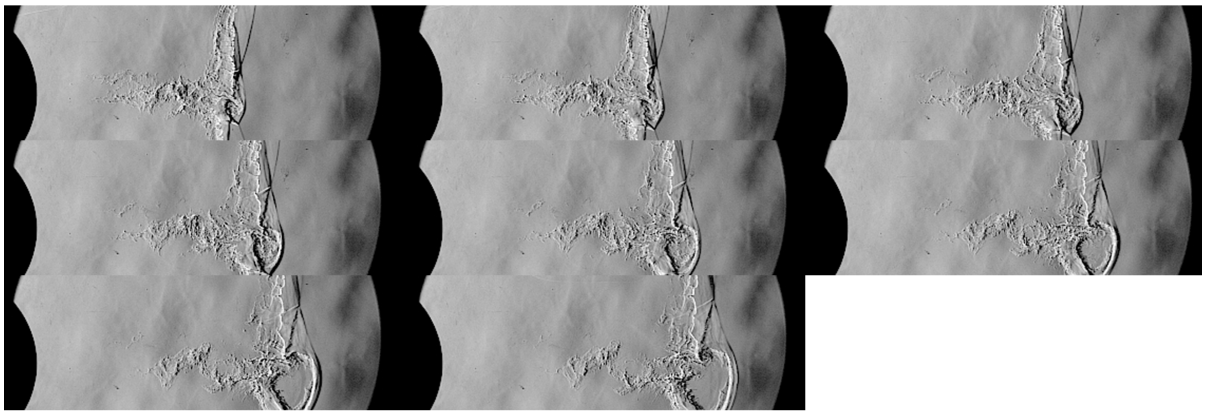

Figure G.38: Continuation of the flow field evolution shown in Figure G.37. *Test ID: CH4+O2-08-01-12(1.5psiTEST6)*

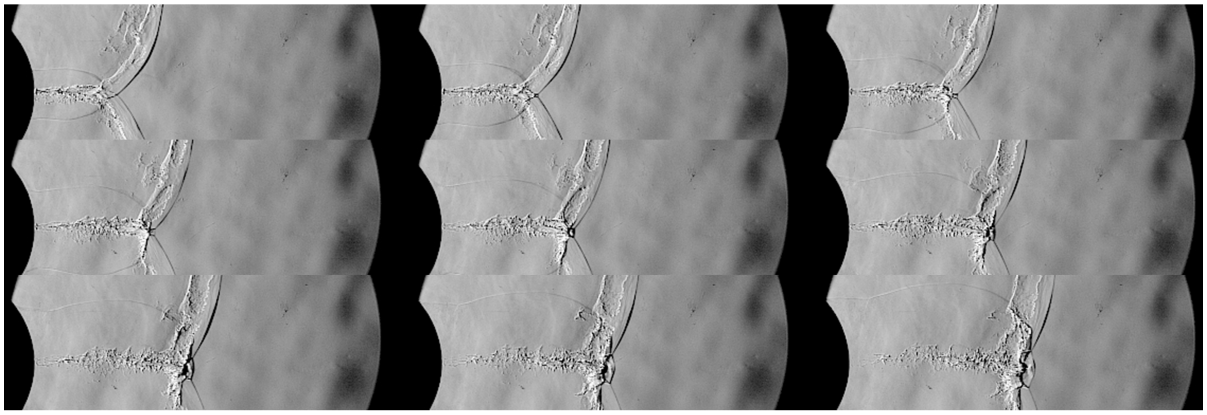

Figure G.39: Schlieren images of a flow field evolution for $p_0 = 10.5$ kPa and $T_0 = 300$K with an inter-frame delay of 6.03 μsec. *Test ID: CH4+O2-08-01-12(1.5psiTEST8)*

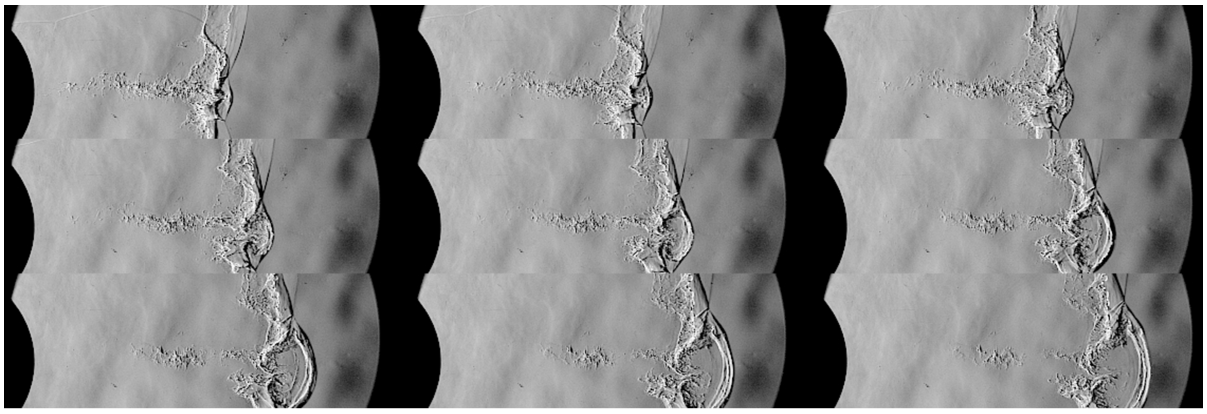

Figure G.40: Continuation of the flow field evolution shown in Figure G.39. *Test ID: CH4+O2-08-01-12(1.5psiTEST8)*

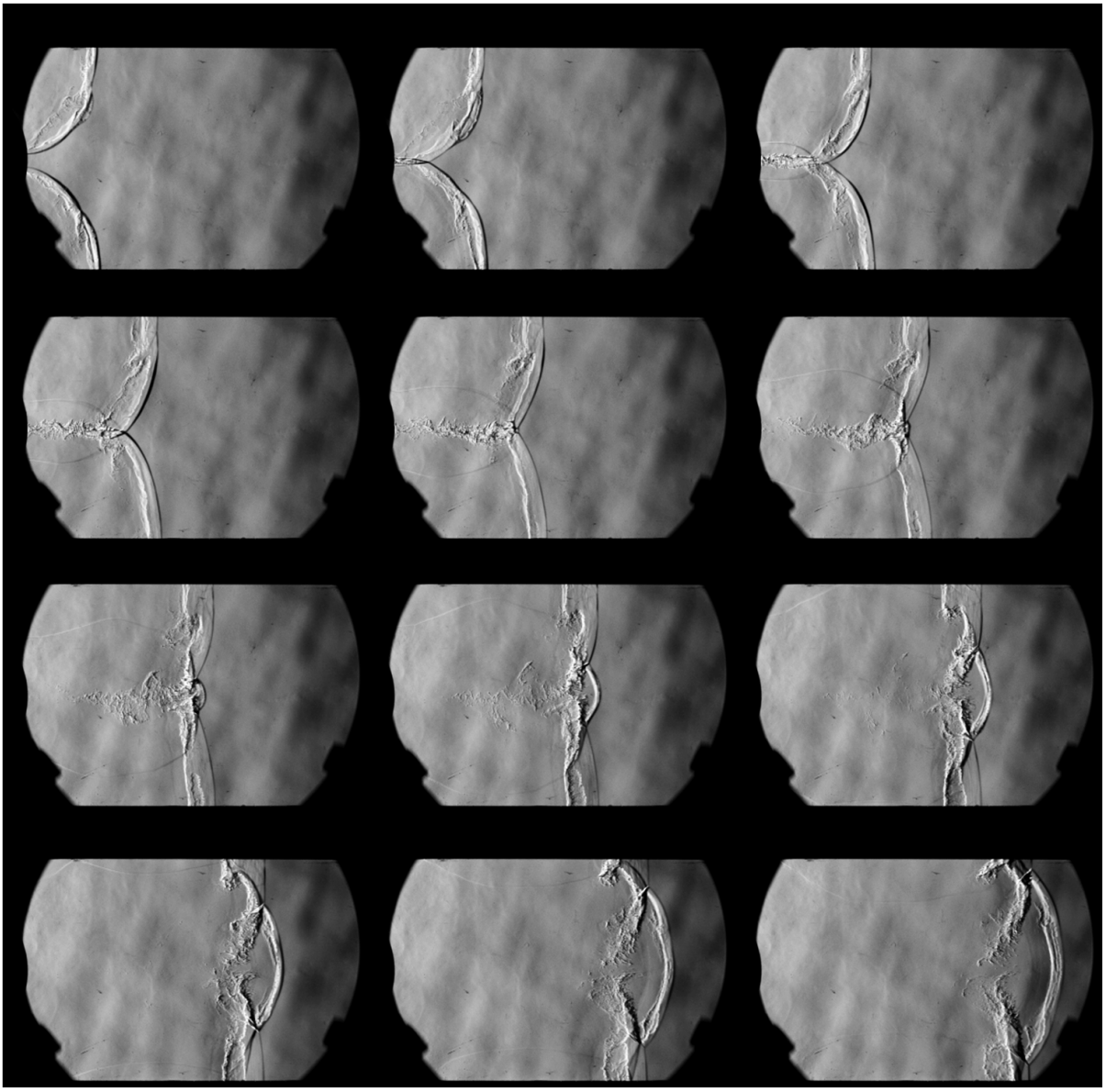

Figure G.41: Schlieren images of a flow field evolution for $p_0 = 9.8$ kPa and $T_0 = 300$K with an inter-frame delay of 12.97 μsec. *Test ID: CH4+O2-08-03-12(1.4psiTEST1)*

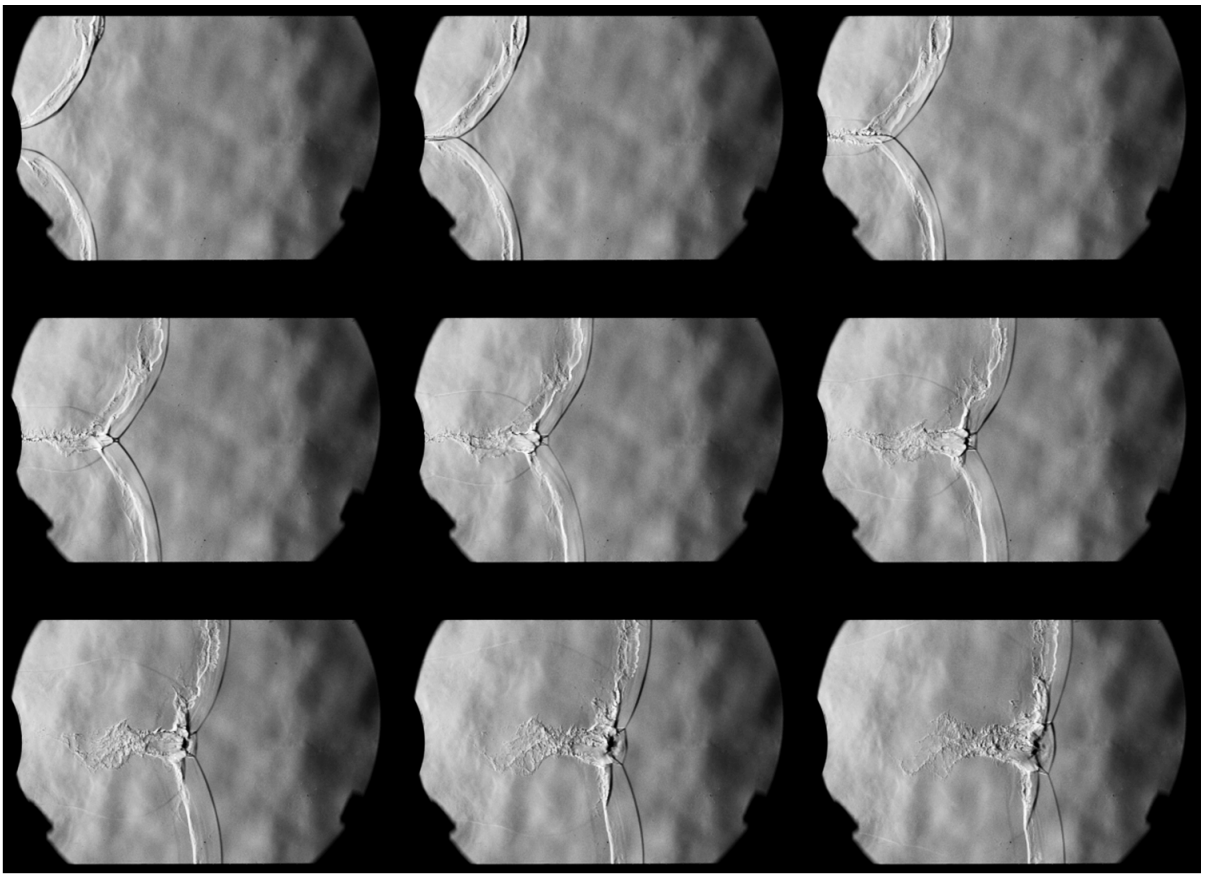

Figure G.42: Schlieren images of a flow field evolution for $p_0 = 7$ kPa and $T_0 = 300$K with an inter-frame delay of 12.91 μsec. *Test ID: CH4+O2-08-14-12(1.0psiTEST2)*

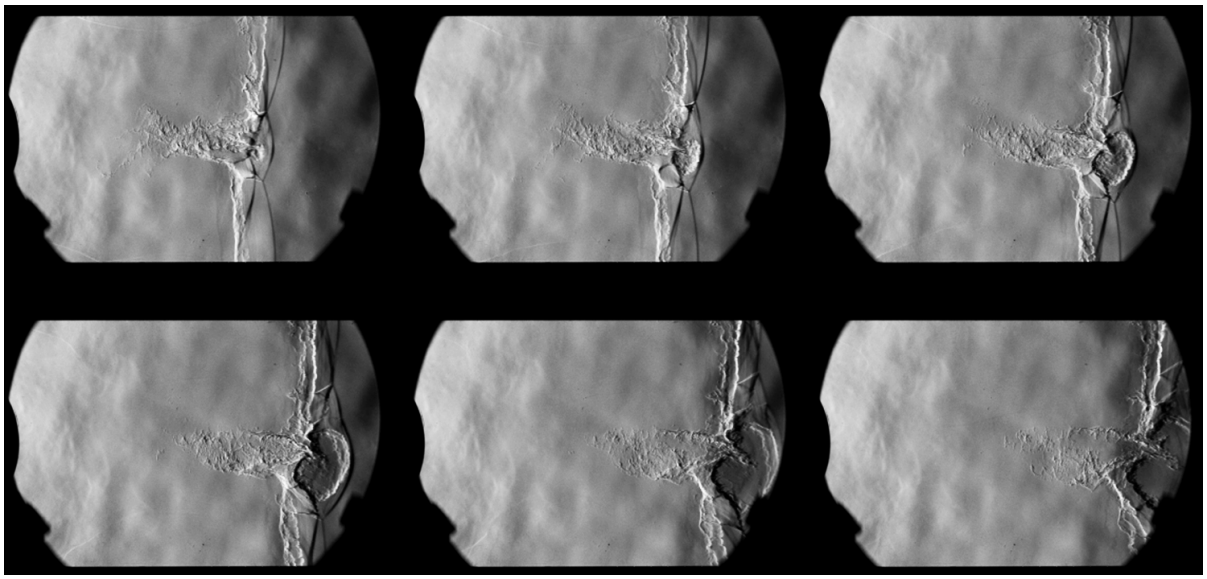

Figure G.43: Continuation of the flow field evolution shown in Figure G.42. *Test ID: CH4+O2-08-14-12(1.0psiTEST2)*

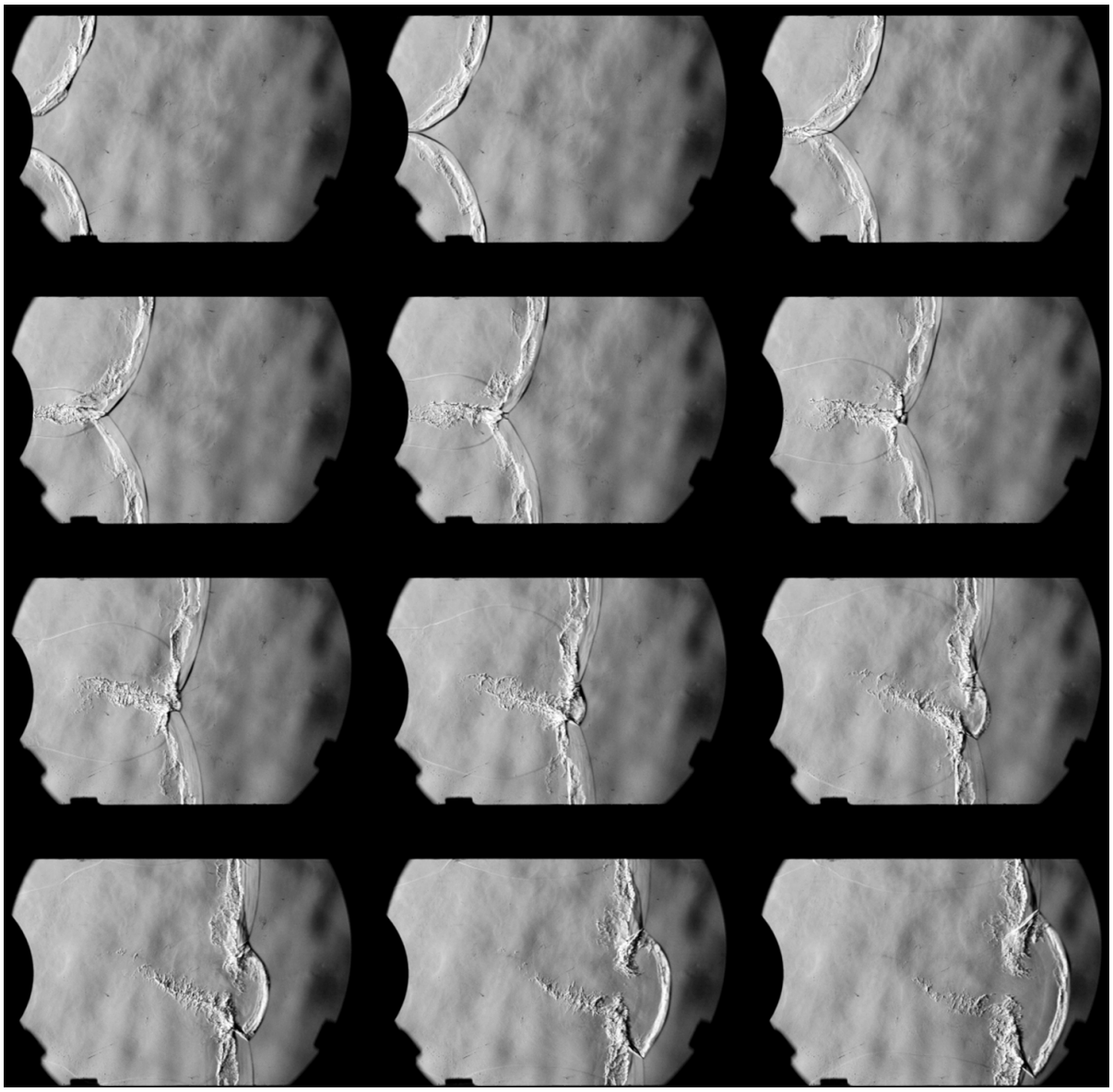

Figure G.44: Schlieren images of a flow field evolution for $p_0 = 14.0$ kPa and $T_0 = 300$K with an inter-frame delay of 12.97 μsec. *Test ID: CH4+O2-08-01-12(2.0psiTEST3)*

G.2.7 Detonation re-initiation regime using the full-cylinder obstacle

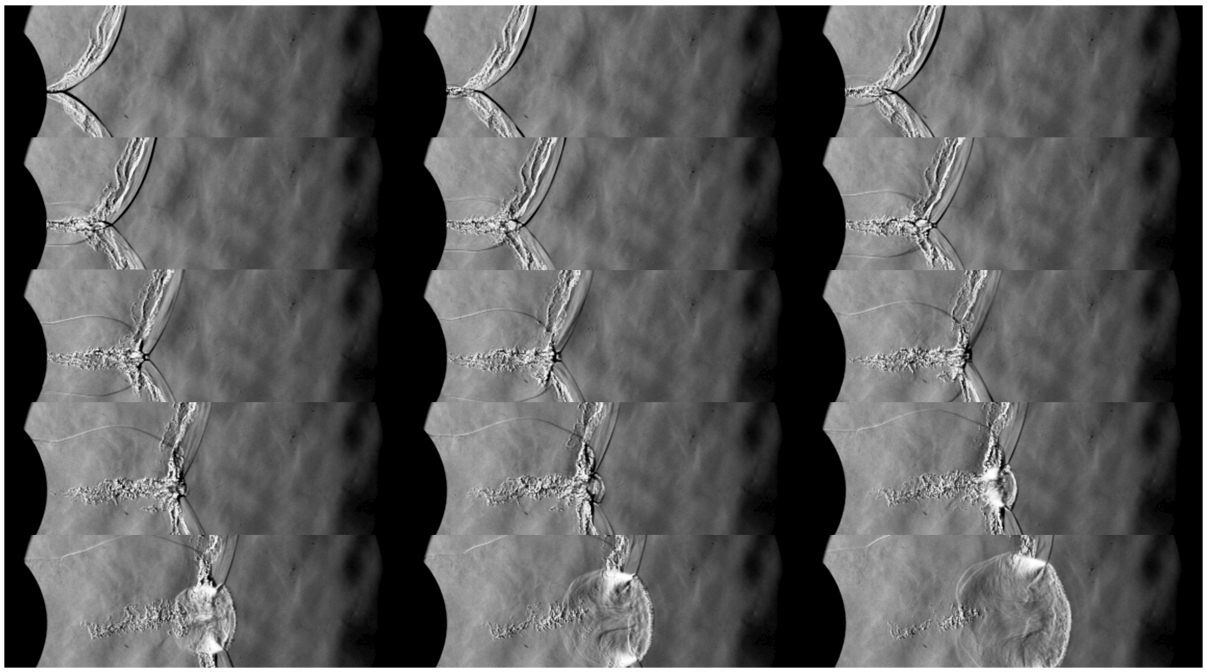

Figure G.45: Schlieren images of a flow field evolution for p_0 = 16.8 kPa and T_0 = 300K with an inter-frame delay of 6.03 μsec. *Test ID: CH4+O2-08-01-12(2.4psiTEST9)*

G.3 Schlieren images obtained from other experiments using the dual frame camera

Shown here are Schlieren images that were recorded using the double framing camera, from experiments that were not presented in the body of the report. Images for all regimes are shown below.

G.3.1 Detonation failure regime using the half-cylinder obstacle

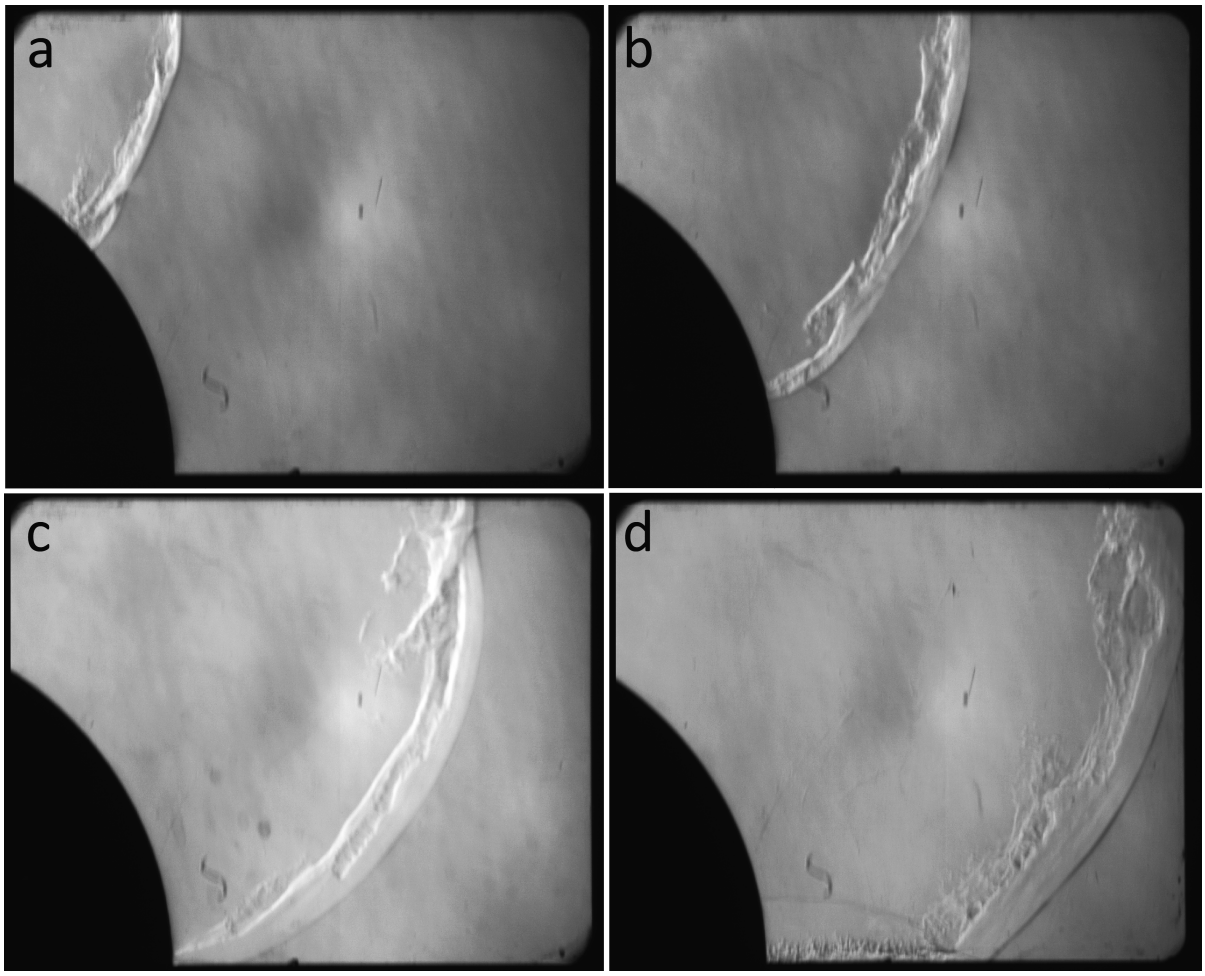

Figure G.46: Schlieren images for $p_0 = 5.5$ kPa and $T_0 = 300$K. *(a)Test ID: CH4+O2 - 08-4-11(0.85psi)5*; *(b)Test ID:CH4+O2 - 08-4-11(0.85psi)6*; *(c)Test ID: CH4+O2 - 08-4-11(0.85psi)8*; *(d)Test ID:CH4+O2 - 08-12-11(0.85psi)1*

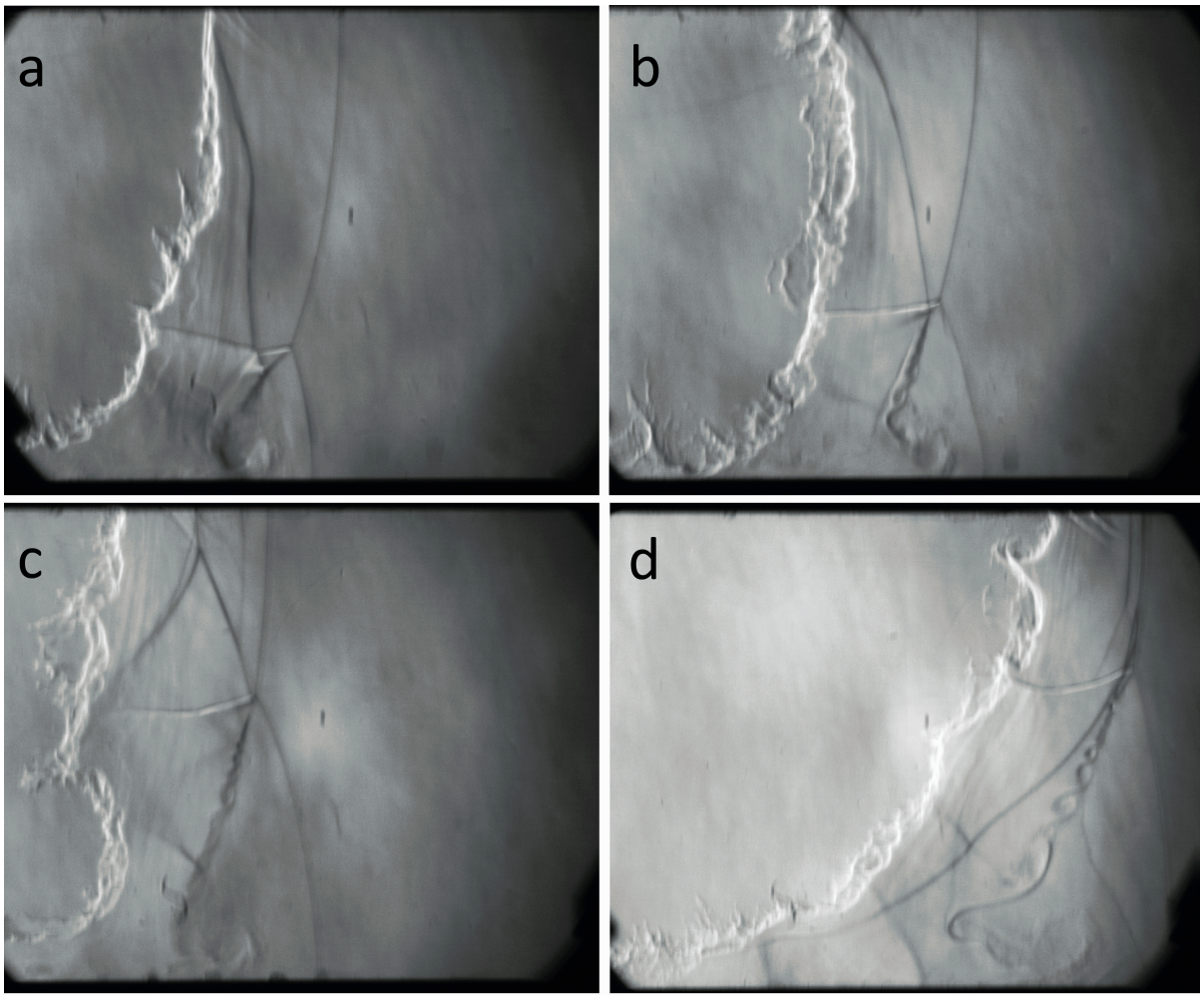

Figure G.47: Schlieren images for p_0 = 5.5 kPa and T_0 = 300K. *(a)Test ID: CH4+O2 - 07-27-11(0.85psi)2*; *(b)Test ID: CH4+O2 - 07-27-11(0.85psi)3*; *(c)Test ID: CH4+O2 - 07-27-11(0.85psi)5*; *(d)Test ID: CH4+O2 - 07-31-11(0.85psi)5*

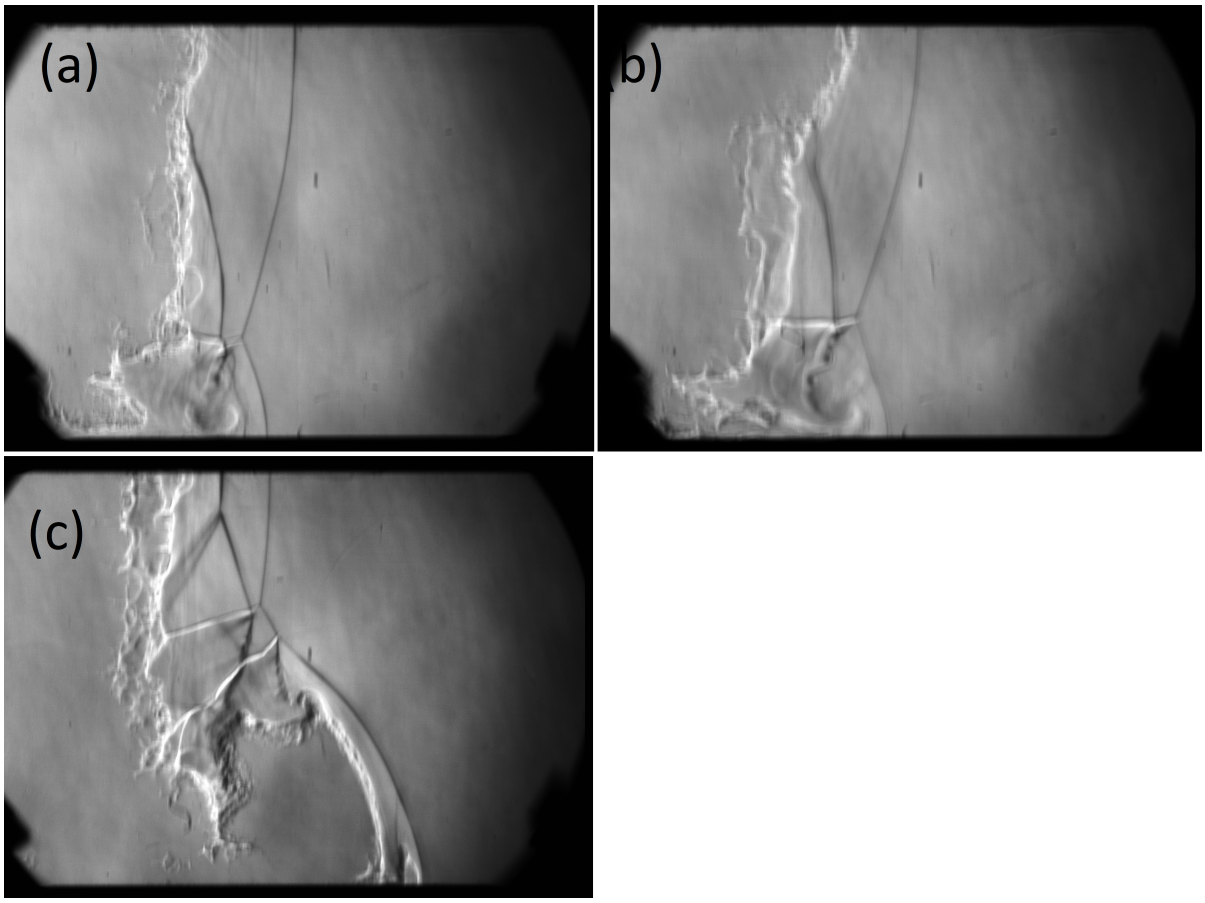

Figure G.48: Schlieren images for p_0 = 5.5 kPa and T_0 = 300K. *(a)Test ID: CH4+O2 - 08-24-11(0.85psi)11*; *(b)Test ID: CH4+O2 - 08-24-11(0.85psi)12*; *(c)Test ID: CH4+O2 - 07-31-11(0.85psi)4*

G.3.2 Hot spot re-ignition regime using the half-cylinder obstacle

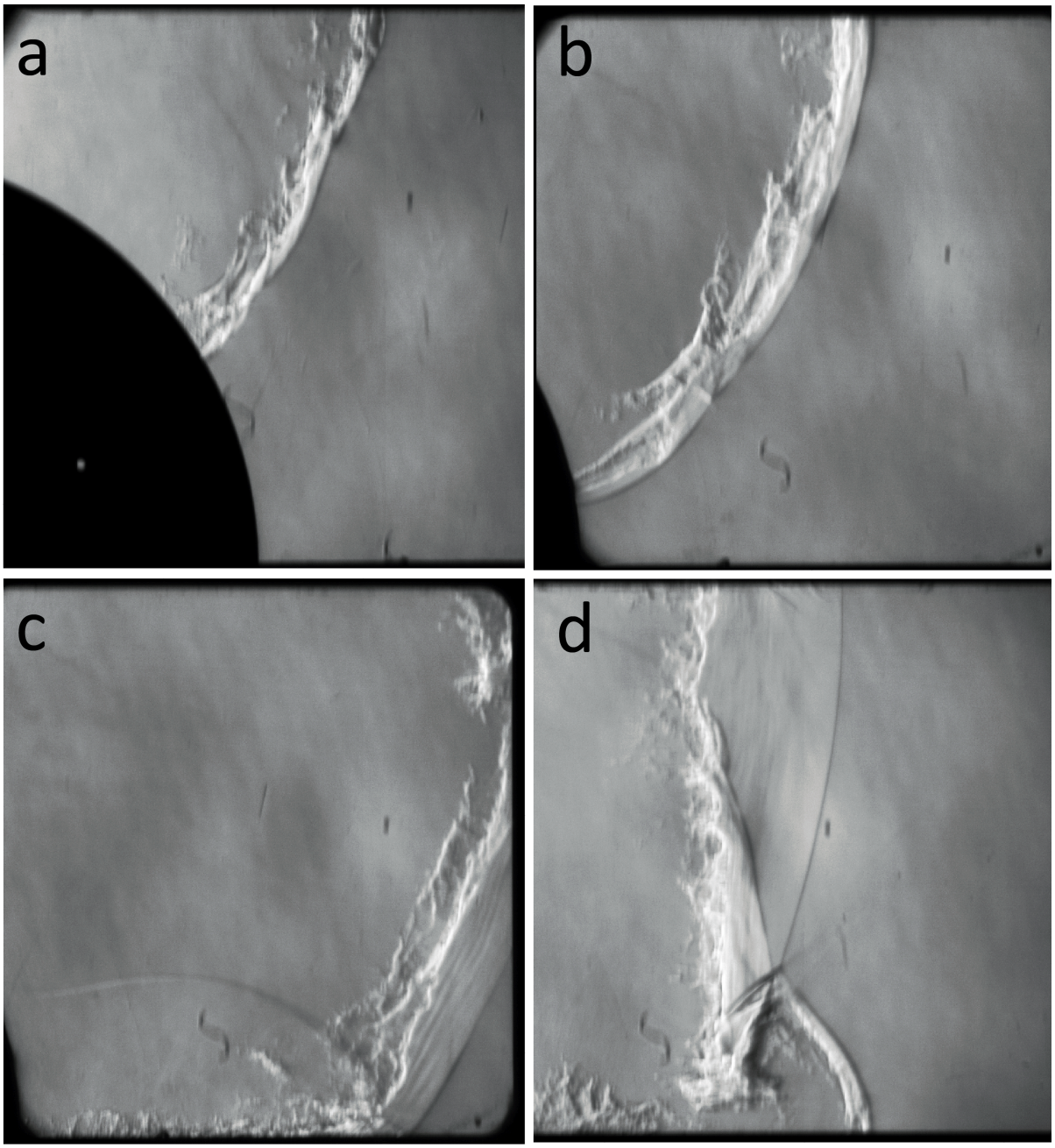

Figure G.49: Schlieren images for $p_0 = 10.5$ kPa and $T_0 = 300$K. *(a)Test ID: CH4+O2 - 08-24-11(1.49psi)2*; *(b)Test ID: CH4+O2 - 08-4-11(1.49psi)2*; *(c)Test ID: CH4+O2 - 08-4-11(1.49psi)4*; *(d)Test ID: CH4+O2 - 08-3-11(1.49psi)2*

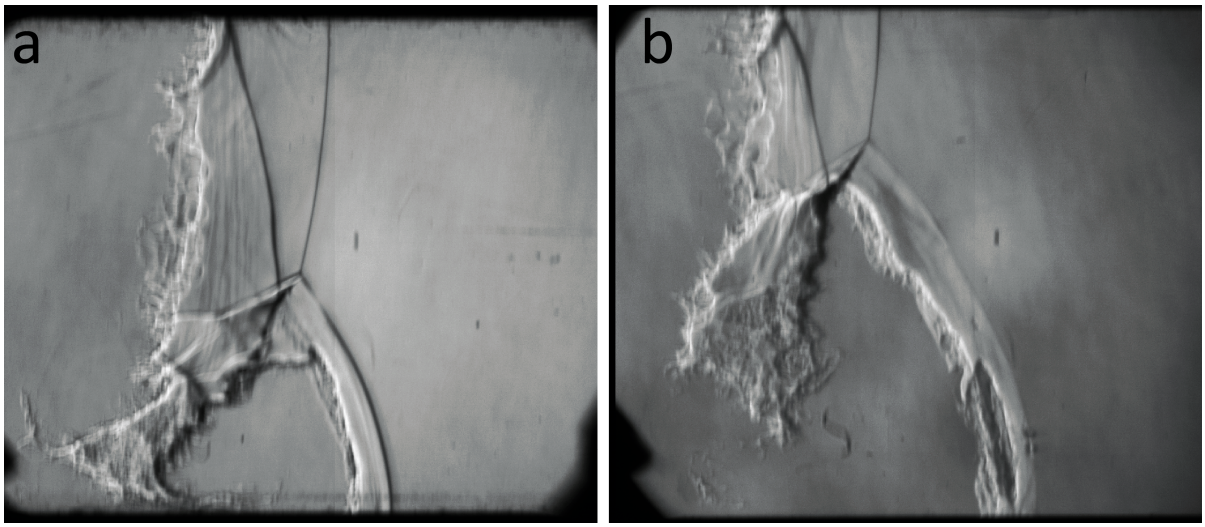

Figure G.50: Schlieren images for p_0 = 10.5 kPa and T_0 = 300K. *(a)Test ID: CH4+O2 - 05-10-11(1.49psi4)*; *(b)Test ID: CH4+O2 - 08-2-11(1.49psi)5*

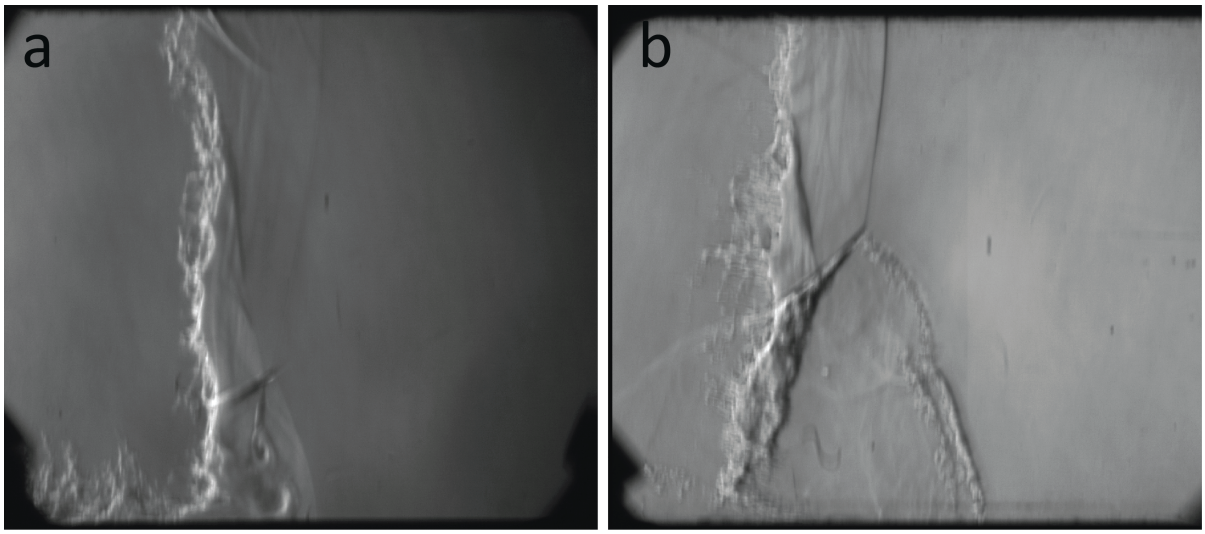

Figure G.51: Schlieren images for p_0 = 10.5 kPa and T_0 = 300K. *(a)Test ID: CH4+O2 - 08-26-11(1.49psi)3*; *(b)Test ID: CH4+O2 - 05-10-11(1.49psi3)*

G.3.3 Detonation re-initiation regime using the half-cylinder obstacle

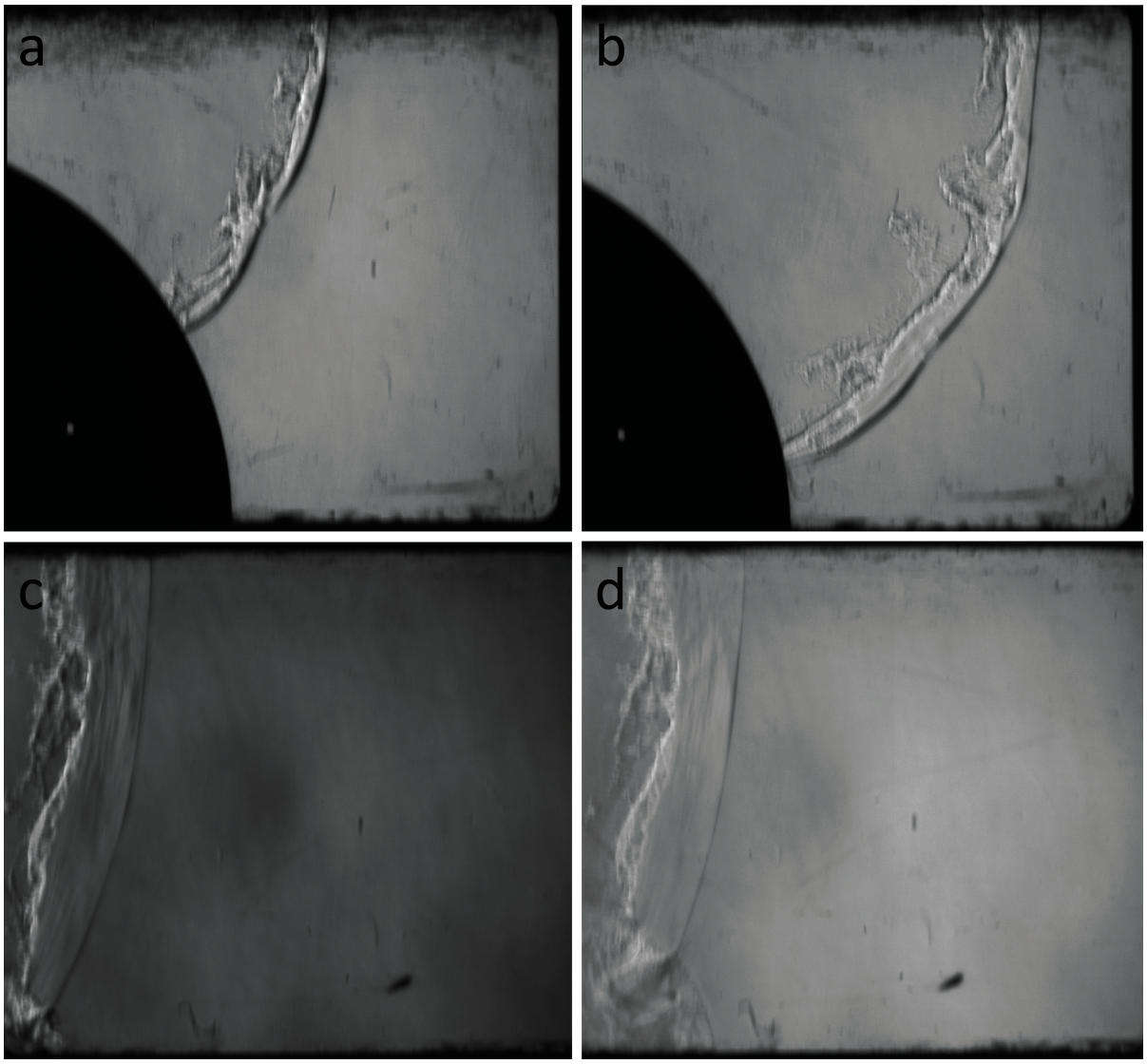

Figure G.52: Schlieren images for $p_0 = 12.0$ kPa and $T_0 = 300$K. *(a)Test ID: CH4+O2 - 03-13-11(1.72psi)5*; *(b)Test ID: CH4+O2 - 03-14-11(1.72psi)1*; *(c)Test ID:CH4+O2 - 03-12-11(1.71psi)2 (top frame)*; *(d)Test ID: CH4+O2 - 03-12-11(1.71psi)2 (bottom frame)*

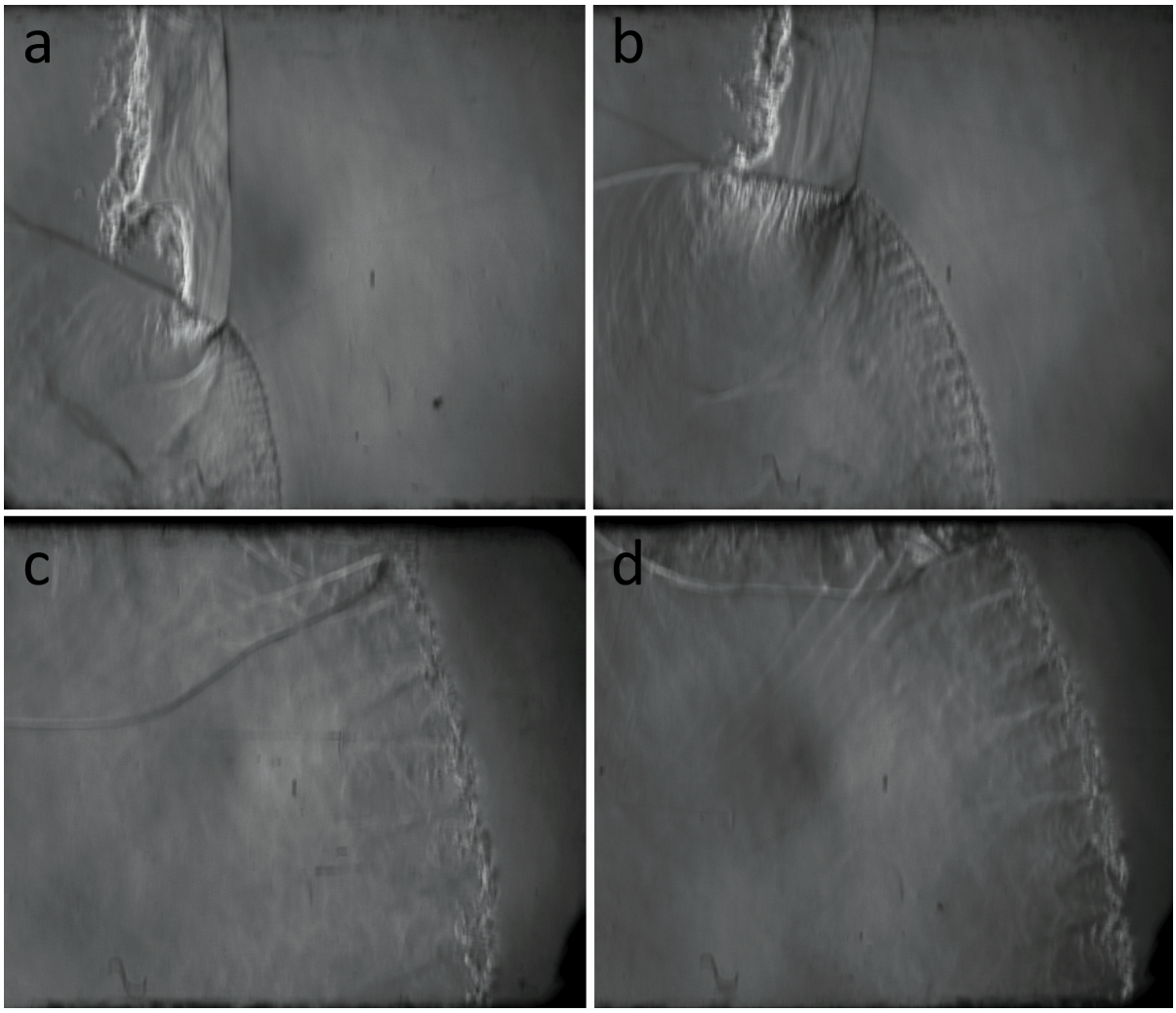

Figure G.53: Schlieren images for p_0 = 12.0 kPa and T_0 = 300K. *(a)Test ID: CH4+O2 - 03-12-11(1.72psi)7*; *(b)Test ID: CH4+O2 - 03-13-11(1.72psi)4*; *(c)Test ID: CH4+O2 - 03-13-11(1.72psi)3*; *(d)Test ID: CH4+O2 - 03-13-11(1.72psi)1*

References

[1] J. H. S. Lee. *The Detonation Phenomenon*. Cambridge University Press, 1st edition, 2008.

[2] J. E. Shepherd. Detonation in gases. *Proceedings of the Combustion Institute*, 32:83–98, 2009.

[3] V. A. Subbotin. Collision of transverse detonation waves in gases. *Combustion Explosion and Shock Waves*, 11(3):411–414, 1975.

[4] V. N. Gamezo, D. Desbordes, and E. S. Oran. Formation and evolution of two-dimensional cellular detonations. *Combustion and Flame*, 116:154–165, 1999.

[5] J. M. Austin. *The role of instability in gaseous detonations*. Ph.D. thesis, Department of Aerospace Engineering, California Institute of Technology, 2003.

[6] R.A. Strehlow. Detonation structure and gross properties. *Combustion Science and Technology*, 4:65–71, 1971.

[7] M. I. Radulescu, G. J. Sharpe, J. H. S. Lee, C. B. Kiyanda, A. J. Higgins, and R. K. Hanson. The ignition mechanism in irregular structure gaseous detonations. *Proceedings of the Combustion Institute*, 30:1859–1867, 2005. 30th International Symposium on Combustion JUL 25-30, 2004 University of Illinois Chicago, Chicago, IL.

[8] C.B. Kiyanda and A.J. Higgins. Photographic investigation into the mechanism of combustion in irregular detonation waves. *Shock Waves*, 2012.

[9] M. I. Radulescu, G. J. Sharpe, C. K. Law, and J. H. S. Lee. The hydrodynamic structure of unstable cellular detonations. *Journal of Fluid Mechanics*, 580:31–81, 2007.

[10] G. Ben-Dor. *Shock Wave Reflection Phenomena*. Springer, 2nd edition, 2007.

[11] Lee J. H and I. O Moen. The mechanism of transition from deflagration to detonation in vapour cloud explosions. *Progress in Energy and Combustion Science*, 6:359–389, 1980.

[12] P. Mach. *Bifurcating Mach shock reflections with application to detonation structure*. M.A.Sc. thesis, Department of Mechanical Engineering, University of Ottawa, 2011.

[13] H. Hornung. Regular and mach reflections of shock waves. *Annual Reviews Fluid Mechanics*.

[14] P. Collela and H.M. Glaz. Numerical modelling of inviscid shock flows of real gases. In Berlin Springer-Verlag, editor, *8th International Conference on Numerical Methods in Fluid Dynamics*, pages 175–182, 1984.

[15] R. Sorin, R. Zitoun, B. Khasainov, and D. Desbordes. Detonation diffraction through different geometries. *Shock Waves*, 19(1):11–23, 2009.

[16] K. Mazaheri, Y. Mahmoudi, and M. I. Radulescu. Diffusion and hydrodynamic instabilities in gaseous detonations. *Combustion and Flame*, 159:2138–2154, 2012.

[17] E. S. Oran, Weber J. W., Stefaniw E. I., M. H. Lefebvre, and J. D Anderson. A numerical study of a two-dimensional h2-o2-ar detonation using a detailed chemical reaction model. *The Combustion Institute*.

[18] H. D. Ng, M. I. Radulescu, A. J. Higgins, N. Nikiforakis, and J. H. S. Lee. Numerical investigation of the instability for one-dimensional chapman-jouguet detonations with chain-branching kinetics. *Combustion Theory and Modelling*, 9:385–401, 2005.

[19] G. J. Sharpe and M. I. Radulescu. Statistical analysis of cellular detonation dynamics from numerical simulations: one step chemistry. *Combustion Theory and Modelling*, 15:691–723, 2011.

[20] D. H. Edwards, G. O. Thomas, and M. A. Nettleton. The diffraction of a planar detonation wave at an abrupt area change. *Journal of Fluid Mechanics*, 95:79–96, 1979.

[21] E. Shultz. *Detonation diffraction through an abrupt area change*. Ph.D. thesis, Department of Aerospace Engineering, California Institute of Technology, 2000.

[22] M. Kamel. *An investigation of the diffraction of detonation waves around single cylinders*. M.A.Sc. thesis, Department of Mechanical Engineering, McGill University, 1993.

[23] A. Teodorczyk, J.H.S. Lee, and K. Knystautas. Propagation mechanism of quasi-detonations. In *Twenty Second Symposium (International) on Combustion*, volume 22, pages 1723–1731. The Combustion Institute, 1988.

[24] A. Teodorczyk, J.H.S. Lee, and K. Knystautas. The structure of fast turbulent flames in very rough, obstacle-filled channels. In *Twenty Third Symposium (International) on Combustion*, volume 23, pages 735–741. The Combustion Institute, 1990.

[25] S. Ohyagi, T. Obara, S. Hoshi, P. Cai, and T. Yoshihashi. Diffraction and re-initiation of detonations behind a backward-facing step. *Shock Waves*, 12(3):221–226, 2002.

[26] T. Obara, J. Sentanuhady, Y. Tsukada, and S. Ohyagi. Reinitiation process of detonation wave behind a slit-plate. *Shock Waves*, 18(2):117–127, 2008.

[27] M. I. Radulescu and B. M. Maxwell. The mechanism of detonation attenuation by a porous medium and its subsequent re-initiation. *Journal of Fluid Mechanics*, 667:96–134, 2011.

[28] M. Drolet. *Design of an experiment to study the instability of detonation waves*. Undergraduate thesis, Department of Mechanical Engineering, University of Ottawa, 2008.

[29] G.C. Maines. *Detonation re-initiation in the wake of a cylinder*. Undergraduate thesis, Department of Mechanical Engineering, University of Ottawa, 2011.

[30] G. S. Settles. *Schlieren and Shadowgraph Techniques*. Springer, corrected edition, 2006.

[31] M.I. Radulescu. *The propagation and failure mechanism of gaseous detonations: experiments in porous-walled tubes*. Ph.D. thesis, Department of Mechanical Engineering, McGill Univeristy, 2003.

[32] S. Laberge, R. Knystautas, and J.H.S. Lee. Propagation and extinction of detonation waves in tube bundles. *Progress in Astronautics and Aeronautics*, 153:381–396, 1993.

[33] S. Abid, G. Dupre, and C. Paillard. Oxidation of gaseous unsymmetrical dimethylhydrazine at high temperatures and detonation of udmh/o_2. *Progress in Astronautics and Aeronautics*, 153:162–181, 1991.

[34] M.D. Pedley, C.V. Bishop, F.J. Benz, C.A. Bennett, R.D. McClenagan, D.L. Fenton, R. Knystautas, J.H.S. Lee, O. Peraldi, G. Dupre, and J.E. Shepherd. Hydrazine vapour detonations. *Progress in Astronautics and Aeronautics*, 114:45–63, 1988.

[35] V.I. Manzhalei, V.V. Mitrofanov, and V.A. Subbotin. Measurement of inhomogeneities of a detonation front in a gas mixtures at elevated pressures. *Combustion, Explosion and Shock Waves (USSR)*, 10(1):89–95, 1974.

[36] R. Knystautas, J.H.S. Lee, and C.M. Guirao. The critical tube diameter for detonation failure in hydrocarbon-air mixtures. *Combustion and Flame*, 48(1):63–83, 1982.

[37] M. I. Radulescu and J. H. Lee. The failure mechanism of gaseous detonations: experiments in porous walled tubes. *Combustion and Flame*, 131:29–46, 2002.

[38] S. S-M. Lau-Chapdelaine. *Numerical simulations of detonation re-initiation behind an obstacle*. M.A.Sc. thesis, Department of Mechanical Engineering, University of Ottawa, 2013.

[39] D.A. Kessler, V.N. Gamezo, and E.S. Oran. Multilevel detonation cell structures in methane-air mixtures. *Proceedings of the Combustion Institute*, 33:2211–2218, 2011.

[40] V. N. Gamezo, Vasil'ev A. A., A. M. Khoklov, and E. S. Oran. Fine cellular structures produced by marginal detonations. In *Proceedings of the Combustion Institute*, volume 28, pages 611–617. The Combustion Institute, 2000.

[41] L. H. Cowell and A. H. Lefebvre. Influence of pressure on autoignition characteristics of gaseous hydrocarbon-air mixtures. *SAE Transactions*, 860068:12, 1986.

[42] C Gardner. *Experimental investigations of auto-ignition delay times and soot formation in gaseous fuel mixtures*. Ph.D. thesis, University of Wales, 2005.

[43] C.J. Goy, A.J. Moran, and Thomas G.O. Auto-ignition characteristics of gaseous fuels at representative gas turbine conditions. *ASME Paper*, 2001-GT-0051, 2001.

[44] J. Chao. *Critical deflagration waves that lead to the onset of detonation*. Ph.D. thesis, Department of Mechanical Engineering, McGill University, 2006.

[45] R. Knystautas and J.H.S. Lee. On the effective energy for direct initiation of gaseous detonations. *Combustion and Flame*, 27:221–228, 1976.

[46] S. Gordon and J. B McBride. *Computer program for calculations of complex equilibrium compositions and applications*.

[47] D. Goodwin. Cantera - an object-oriented software toolkit for chemical kinetics, thermodynamics, and transport processes. Last accessed - November 4, 2012. `http://code.google.com/p/cantera/`.

[48] G.P. Smith, D.M. Golden, M. Frenklach, N.W. Moriarty, B. Eiteneer, M. Goldenberg, C.T. Bowman, R.K. Hanson, S. Song, W.C. Gardiner Jr., V.V. Lissianski, and Z Qin. GRI-Mech 3.0. Last accessed - November 4, 2012. `http://www.me.berkeley.edu/gri_mech/`.

[49] D. Goodwin. Reactor networks. California Institute of Technology, 2004.

[50] D. Goodwin. One-dimensional flames. California Institute of Technology, 2004.